The Structure and Dynamics of an Environment Forming High-mass Stars

Toby John Terry Moore

Doctor of Philosophy

University of Edinburgh
1989

This thesis has been composed by me and consists entirely of my own work except where indicated in the text.

Toby John Terry Moore

September 1989

Abstract

A detailed investigation is presented of the physical environment associated with high-mass star formation. This is carried out by means of an in-depth multi-wavelength study of one such region in W75N. An analysis is made of the nature of the major embedded luminosity sources and the cloud core from which they have recently formed, from the hot dust very close to each object to the cold dust and molecular gas surrounding them. The dynamical relationship between the large molecular outflow and the ambient cloud is studied with regard to limitations that might be placed on plausible flow generation mechanisms. The details of the reflection nebulae associated with the mass outflows are interpreted in terms of the scattering properties of dust.

A recently-formed stellar cluster has been found, associated with the known signs of high-mass star formation in W75N (compact HII regions, OH and H_2O masers, CO outflow etc.). The main heating source and origin of the molecular outflow is identified and found to be very deeply embedded ($A_V > 90$ mag). Imaging near-infrared polarimetry, millimetre-wave molecular line spectroscopy and submillimetre continuum observations at scales of 0.01 to 0.2 pc have shown no disk or torus structure in the dense obscuring material around this source. However, circumstantial evidence exists in the near-infrared colours for significant amounts of dusty material close to the major luminosity sources. Therefore very small-scale (few $\times 100$ A.U.) disk-like formations may exist and play an important dynamical rôle.

The large molecular outflow in W75N is found to be unable to overcome the gravitational binding force of the large surrounding core unless the flow is initially highly collimated. The lobes of high-velocity gas possess a large degree of collimation, probably induced through confinement by the ambient material, but the outflow as a whole is irregular and possibly multipolar and appears to be intrinsically largely isotropic. The flow lobes are not wind-blown bubbles but are filled with high velocity molecular material. The driving mechanism is most likely to be a massive, semi-isotropic stellar wind but there could still be a cylindrically symmetrical, rotation-driven mechanism acting close to the star.

Of the two reflection nebulae in the region the largest and brightest is associated with the blue-shifted molecular outflow lobe. Features in the nebula, similar to those in other such objects, are consistent with scattering from large grains which pro-

duce diffraction-affected and strongly forward-biased scattering patterns. It is shown that large grains should dominate the scattering in the near-infrared, regardless of the detailed grain size distribution. The ubiquitous suppression of backward-directed reflection lobes in bipolar sources may be caused by forward scattering and not by large obscuring disks. A smaller reflection nebula surrounds the less luminous source IRS-2, indicating a limited-scale outflow from this object also. Hydrogen recombination line ratios in IRS-2 are consistent with current models of massive, partly-ionised stellar winds.

Acknowledgments

I must firstly thank my supervisors Matt Mountain and Peter Brand for all their practical help and guidance. Thanks are also due to the many staff of the Astronomy Department of the University of Edinburgh and of the Royal Observatory who have given their help and time with friendliness and generosity. It is a pleasure to acknowledge both the SERC, for financial support and for funding my half-dozen observing trips, and the ROE, for providing such excellent facilities without which the struggle would have been considerably more arduous. A special thanks also to Jim Emerson for his patience during the last nine months.

Among the many friends made during my stay in Edinburgh, who made the whole business a pleasure and kept my mind (mostly) off my cold feet (but not off my old age), I'll take the risk of singling out Paul, Neil, Andrew, Stuart, Steve, J.D. and Claire and hope the others will understand. An extra thanks to Claire for helping out so often when it probably should have been the other way around. A special mention is due to Phil Puxley for being such an excellent mate right from the start and for so rarely running out of energy, enthusiasm and humour.

More personal thanks must go to my Mum and Bill Boyle for always being there to help in a tight spot and for always assuming I knew what I was doing, even when I didn't. Above all, thanks to Júlia who gave up friends, family and sunshine to live in cold, damp poverty in a very foreign country. She has had to put up with the worst of the stress, anxiety and loneliness and is now waiting – hopefully not for long – for some good to come of it.

For my Dad,

who would have been proud.

Table of Contents

Chapters :

Appendices :

Chapter 1

Introduction

The main concerns of this thesis are to probe the physical conditions in the molecular cloud environment in which high-mass stars have recently formed. Of especial interest are the mutual interactions between the embedded young stars and their parent cloud and what conclusions might be drawn from these concerning the condition of the stars themselves.

There are two basic ways in which such an investigation can be tackled. The first is to observe a representative group of sources, compare the results and see in what ways they are similar and in what ways they differ. Thus it may be possible to find common properties that are intrinsic to the star formation process and properties that are dependent upon variables such as mass and environmental conditions (e.g. Linke & Goldsmith 1980, Bally & Lada 1983). The second method is to make a detailed study of a single object and produce a comprehensive picture of the prevailing physical conditions (e.g. Garden 1986). Information gained by this process can be used to update or amend general theories, meant to apply to all sources, developed from the first technique. Thus in fact the two methods are complementary and require each other to be effective. The bulk of this thesis is a study of the second kind, involving a detailed multi-wavelength investigation of W75N.

The majority of observational work on star formation has naturally concentrated on low-mass stars, since these have a relatively long evolutionary timescale and emerge from their obscuring layers of placental material still in a primitive state far from the Main Sequence. High-mass stars, on the other hand, develop very rapidly (see below) and reach the Main Sequence while still heavily enshrouded by the parent cloud core. Consequently, high-mass young stellar objects (YSOs) are difficult to observe directly and intrinsic properties such as surface temperature and surface activity are almost

impossible to measure. The only intrinsic parameter that may be easily observed is the luminosity, since the extinguishing dust efficiently converts optical and UV photons into far-infrared and submillimetre radiation, which then readily escape from the cloud. It is into this waveband that the majority of the luminosity of deeply embedded sources is emitted (e.g. Evans 1981).

The study of the actual formation of stars has been limited by the failure of observers to find a single unambiguous example of a true protostar, which (as defined by Wynn-Williams 1982) is still in the process of accumulating its eventual total mass and whose only heat source is the accreting material. The reason for this is probably an unfortunate combination of the intrinsic faintness of low-luminosity objects, which should be both relatively plentiful and long-lived, with the rare and short-lived nature of the more luminous high-mass protostar. Consequently, the observational study of star formation is often the study of the early stages of stellar evolution, carried out in the hope that knowledge of the conditions in and around YSOs will constrain the possible paths of protostellar development. Other experimental workers approach the problem from the opposite side and attempt to follow the development of the molecular cloud cores in which stars form.

It is worth noting here that the term 'protostar' tends to be used to describe many different stages in the life of a young star. This classification can be applied to anything from cold, pre-collapse condensations within cloud cores, through the accreting, pre-nuclear burning objects which are heated by mass infall, to any star which is sufficiently obscured to be only detectable at infrared wavelengths. Throughout this introduction, 'protostar' will apply only to objects which have yet to begin nuclear fusion but which may be internal heated by accretion.

The study of early stellar evolution has progressed rapidly in the last decade, with the development of new millimetre-wave and infrared instrumentation and the building of the large new millimetre telescopes. The success of the Infrared Astronomical Satellite (IRAS) mission also played a major part by producing a (virtually) all-sky survey in the mid- and far-infrared. Since it is in these wavebands that cool sources and deeply embedded stars emit most of their energy, it was at last possible with IRAS to look for young objects using their own characteristic emission rather than through, for example, radio continuum surveys which might be biased toward the more evolved sources.

The understanding of the nature of YSOs was at first shaken and then considerably

advanced by the unexpected discovery (Zuckerman *et al.* 1976, Kwan & Scoville 1976) of major mass outflows, the subsequent evidence that many such outflows were highly anisotropic (e.g. Snell, Plambeck & Loren 1980) and the realisation that vigorous mass loss is a developmental process common to all young stars.

Many basic questions still remain to be answered which are vital to our complete understanding of the star formation process. For example: What is the mechanism that generates the outflows and at what stage in the star-formation process is it triggered? What causes the bipolarity of most flows? What is the effect of the energetic flows on the ambient medium? Is star formation stopped or is it triggered elsewhere in the cloud? What stops the outflow eventually? Do flows halt the accretion process or are infall and outflow contemporary phenomena and if so, are they causally linked? What part do disks play in producing or collimating the flows? What causes the mass distribution observed, i.e. what decides the final mass of a star?

In the rest of this introduction current ideas are reviewed on the process of star formation and the associated phenomena, some of which attempt to answer the questions above. The generation and collimation of outflows is also discussed, their relationship to dense disk structures and the possible role of outflows in regulating stellar mass and in shedding angular momentum in the contracting cloud cores. Also discussed is one other aspect of the natural history of young stars, infrared reflection nebulae. A number of excellent reviews are available in the literature which explore aspects of these subjects in more detail (e.g. Wynn-Williams 1982; Lada 1985; Shu, Adams & Lizano 1987; *Protostars and Planets II* ed. D.C. Black & M.S. Matthews, Tuscon: Univ. Ariz. Press, 1985.)

1.1 Current Ideas of Star Formation

1.1.1 Clouds and Cloud Cores

Most of the molecular gas in the Galaxy is contained in Giant Molecular Clouds (GMCs) with masses between 10^5 and 10^6 $M_\odot$ and sizes of a few $\times$ 10 pc (Solomon *et al.* 1979) and GMCs are the principal sites of of active star formation. These GMCs have an internal hierarchical structure, being made up of loose aggregates of smaller molecular clouds of mass $\sim 10^3 - 10^4$ $M_\odot$, size $\sim 2 - 5$ pc and density $10^8 - 10^9$ m^{-3}. These smaller clouds are gravitationally bound within the GMC, moving with relative velocities of several kms^{-1}, about equal to the virial speed of the complexes (Cassen,

Shu & Terebey 1985). In turn, these constituent molecular clouds contain small denser subregions or cloud cores (Myers & Benson 1983). The apparent sizes and densities of the cores depend on the molecule and the transition used to observe them (Myers, 1985) but, those measured in NH_3 have $M \sim 1$ $M_\odot$, $n > 10^{10}$ m^{-3}, $R < 0.1$ pc and $T \sim 10$ K and almost thermal linewidths. The cores appear to be embedded in massive envelopes of a few $\times$ 100 $M_\odot$ (Perault *et al.* 1985). It is these clumps in which star formation occurs. GMCs appear to form by the aggregation of small units, through collisions or by gravitational instabilities in the Galactic disk (Elmegreen 1989), the latter theory explaining the appearance of self-gravitating clouds on all scales from 10^3 to 10^7 $M_\odot$.

The clumps within GMCs appear to be supported by turbulence and magnetic fields since their Jeans masses are only a few $M_\odot$, much less than the masses of the clumps. If they were not so supported, the clumps would all tend to collapse and the star formation rate would be much higher than observed (Zuckerman & Palmer 1974). In addition, there is evidence that magnetic fields play a critical part in cloud support, since turbulent energy should be dissipated quickly and since ordered fields (and hence little distorting turbulence) are indicated by polarisation studies of dark clouds (see the discussions by Shu, Adams & Lizano 1987 and Cassen *et al.* 1985). Magnetic support can occur both perpendicular to the field direction and parallel to it, by means of propogating Alfvén waves. Magnetic fields also explain the generally low rotation rates ($\Omega \sim 1$ kms^{-1} pc^{-1}) in molecular clouds and in small ammonia-traced cores in such regions as Taurus (Shu, Adams & Lizano and references therein) by rotational coupling of the dense cores to the surrounding cloud by magnetic braking.

1.1.2 From Cloud Cores to Protostars

Current theories on the formation of protostars from self-gravitating gas clumps predict that the process bimodally separates into low-mass and high-mass star-formation, determined by the mass of the clump and the strength of the internal magnetic field.

Since the ionisation fraction inside a molecular cloud is thought to be low ($\sim 10^{-7}$ at densities of $\sim 10^{10}$ m^{-3} – see Shu, Adams & Lizano 1987), magnetic fields and the associated charged particles can drift relative to the neutral molecules in the gas (Mestel & Spitzer 1956). The neutral particles are only supported against gravity by the frictional drag of the ions trapped in the magnetic field. This drift is known as ambipolar diffusion and dominates the initial gravitational contraction of a cloud core

when the cloud mass is below the critical value ($M_{\rm crit}$) that can be supported by the combination of magnetic field and turbulent pressure. In this situation the field tends to decay towards the background level and the cloud core condenses quasi-statically, producing a small, dense, isothermal core within an extended envelope (Cassen, Shu & Terebey 1985). The extended envelope may be flattened if support along the field lines is significantly less than in the lateral direction. If the mass of the contracting cloud is significantly less than its Jeans mass, it should fragment (also quasi-statically) into many individual cores.

After a time of $10^6 - 10^7$ yr, depending on the amount of internal turbulence (Lizano & Shu 1989), the core becomes sufficiently centrally-condensed that gravitational collapse must occur. The collapse begins at the centre and propogates outward at the sound speed and an accreting protostar is formed. The time scale for the runaway collapse phase is much shorter ($\sim 10^5$ yr) than that for the contraction phase. This collapse appears to have occurred within at least half of the cores in Taurus (Beichman *et al.* 1986). If the core has significant rotation, a centrifugally-supported nebular disk will form in addition to the protostar, the disk having radial density distribution $\rho \propto r^{0.5}$ (Adams & Shu 1986). The star-forming efficiency ($M_{STARS}/(M_{STARS}+M_{GAS})$) within a molecular cloud is also affected by the bimodal formation process. The long timescale of the contraction phase for low-mass core formation creates a very low efficiency (e.g. $\sim 2\%$ in the Taurus-Auriga dark cloud complex, Wilking & Lada 1985 and references therein). The gravitational collapse of the cores, having a very short timescale, will then not be synchronised throughout the cloud and individual new stars will have time to ignite, turn on energetic winds and disrupt nearby potential star-forming cores.

If the initial cloud mass is greater than $M_{\rm crit}$, then self-gravity overwhelms the magnetic and turbulent support (even without weakening of the field through ambipolar diffusion) and collapse occurs straight away, taking the magnetic field with the matter. If there any flow of material along the field lines, the cloud will flatten and produce internal regions with super-critical mass-to-flux ratios which can collapse independently. Thus we might expect massive clouds to fragment and form close-knit groups of star-forming cores (Shu, Adams & Lizano 1987) on a short, well-synchronised timescale leading to efficient star formation (as found, for example, in ρ Oph. ($\sim 25\%$) and NGC 7023 (30–50%), Wilking & Lada 1985). The super-critical mass situation may arise in agglomerated GMCs which would then efficiently produce stars. If the

cores are heated during the process then the Jeans mass increases and higher mass stars may be formed.

The gravitational collapse of a core proceeds isothermally while it is still optically thin. The increase in density at the centre is stopped only when an optically thick protostar is formed (with mass $10^{-3} - 10^{-2}$ $M_\odot$). This protostar then continues to grow hydrostatically (after the dissociation of H_2) by accreting gas and dust from the still-infalling cloud. Internal changes in the protostar take place on the time scale GM_*^2/R_*L_* (the Kelvin-Helmholtz time T_{K-H}) which is the time taken to reach thermal equilibrium. However, the infall rate is not dependent on the central mass (Shu, Adams & Lizano 1987). Therefore for massive protostars, T_{K-H} will be less than the infall time scale and the star will reach the Main Sequence while still gaining mass. In a low-mass protostar, T_{K-H} is large and accretion may have finished well before the star reaches the Main Sequence. It is for this reason that low-mass stars emerge from their parent clouds still in a primitive state, while their high-mass cousins may spend a large fraction (if not all) of their Main Sequence life deeply obscured. During the early life of a low-mass protostar, the luminosity from the accretion shock between the infalling material and the protostar ($L = GM\dot{M}/R_*$) may dominate the internal luminosity of the source. However, this luminosity may be significantly reduced from the spherical infall value if the gravitational energy is stored as rotational energy in a disk.

1.1.3 End of Accretion and Beginning of Outflow

One of the fundamental problems on theoretical studies of star formation has been to determine the process that selects the final mass of the new star by halting accretion. This problem is also central to the question of outflow generation, since it is likely that the same mechanism is responsible. Lizano & Shu (1989) have concluded, from a detailed three-dimensional model, that the initial conditions do not determine the final mass.

When the central temperature of the protostar reaches approximately 1×10^6 K, deuterium-burning fusion processes begin. In the model of Stahler *et al.* (1980), with an infall rate of 10^{-5} $M_\odot$ yr^{-1}, deuterium ignition occurs when the protostellar mass is about 0.3 $M_\odot$ and a convection zone is formed in the new star which spreads to occupy most of the stellar volume by the time the mass reaches 0.5 $M_\odot$. As described by Cassen, Shu & Terebey (1985) and Shu, Adams & Lizano (1987), convection may combine with differential rotation in the star to produce a dynamo action generating

magnetic activity. This magnetic activity can then release stored rotational energy, converting it into intense surface activity. There is much observational evidence of violent surface activity in intermediate- and low-mass pre-Main Sequence stars, such as P-Cygni emission-line profiles, reversed P-Cygni profiles, significant irregular variability and possible large starspots (see Rydgren & Cohen 1985). Surface phenomena may generate massive mechanically-driven stellar winds which are then responsible for terminating the infall and for powering the large-scale molecular outflows.

Radiation pressure might be able to halt spherically symmetric infall, where $L_*/M_* \gtrsim 700(\mathrm{L}_\odot/\mathrm{M}_\odot)$ (Shu, Adams & Lizano 1987), but this is true for all Main Sequence stars larger than about 7 $\mathrm{M}_\odot$ and therefore cannot be occurring. It is more likely, then, that infall is generally highly non-spherical and that accretion proceeds via disks which block most of the stellar radiation. However, infall is most likely to be terminated by stellar winds not photons since the molecular outflow momenta measured are always factors of 3–5 larger than carried by all photons emitted by the central star (Lada 1985).

There is empirical evidence that the cloud cores associated with low-mass star formation have rather low temperatures ($\sim$ 10 K, Myers & Benson 1983), while those near OB stars are significantly warmer (see Wynn-Williams 1982). If the temperature differences precede the initial formation of stars in the host cloud, the mass infall rates in the warmer clouds will have been higher, since $\dot{M} \propto a^3$ where $a \propto \sqrt{T}$ is the thermal sound speed (Cassen, Shu & Terebey 1985). The rate of mass accumulation affects the timing of deuterium ignition in the protostar, since a higher infall rate gives the newly-accreted material less time to radiate its energy. The outer layers will thus be hotter and more expanded and the ratio R_*/M_* will be higher. Since the central temperature in the star is inversely proportional to R_*/M_*, a higher mass is reached before deuterium starts to burn. If the protostellar mass reaches about $2\,\mathrm{M}_\odot$ before deuterium burning is started, a large convection zone will not form, since the larger envelope will be able to transmit the extra luminosity radiatively and remain stable (Cassen, Shu & Terebey 1985). In this case it is not clear what mechanism can be invoked to terminate the mass accumulation in the largest stars.

Significant heating of the cloud core gas in regions of high column density can occur during the ambipolar diffusion process (Lizano & Shu 1987). This may explain why the gas appears to be hotter than the surrounding dust in the ρ Ophiuchus cloud (Loren, Sandqvist & Wootten 1983, Wilking & Lada 1983) where the cores have $A_\mathrm{V} \sim$

100 mag. It also fits well with the lower gas temperatures of the star-forming region in Taurus (10 – 11 K) which contains no stars more massive than $2\,M_{\odot}$, where cores have $A_V \sim 10$ mag and ambipolar diffusion would add little extra heating over that produced by cosmic rays.

1.2 The Outflow Phenomenon

Since the discovery of molecular molecular material moving at high velocities in the Orion-KL region (Zuckerman *et al.* 1976), it has become apparent that the systematic outflow of energetic ($10^{36} - 10^{40}$ J) molecular gas is a characteristic phenomenon of the early stages of stellar development and a fundamental part of the star-forming process (see the reviews by Lada 1985, Snell 1985). High spatial resolution studies of the large-scale (0.1 – 1 pc) molecular outflows have shown that most are highly anisotropic or bipolar, often with very large degrees of collimation (first noted by Snell, Loren & Plambeck 1980). Molecular outflows occur in all YSOs of all masses and appear to be closely related to other energetic phenomena, such as the extremely narrow optical jets that originate very close to low-mass YSOs (e.g. Mundt & Fried 1983, Reipurth *et al.* 1986). Other associated phenomena are: the Herbig-Haro objects which are closely associated with optical jets (see the review by Schwartz 1983 and Mundt 1985) and trace the energetic shocks produced when the outflow or jet strikes the ambient medium, H_2O masers, which often have high velocities relative to the exciting source (Lada 1985), and bipolar or cometary infrared and optical reflection nebulae (see below).

1.2.1 Outflow Generation

From a determination of the energetics of a sample of molecular outflow sources, Bally & Lada (1983) concluded that the momenta contained in the high-velocity gas was too large *in all cases* to be powered by a radiation-driven wind. The only way radiation pressure could drive the outflows would be if photons were scattered 100 – 1000 times before escaping from the cloud, but this is unlikely, especially since a number of known outflow sources (e.g. T Tauri) are visible objects. Bally & Lada did, however, find that the total luminosity of the central embedded objects was roughly correlated with, but always greater than, the outflow mechanical luminosity. Hence the central stars possess sufficient energy to power the flows. It is also likely that the physics of the

driving mechanism is the same in all cases and that the flows are steady and not explosive events (Lada 1985).

The most plausible explanation for the production of large-scale molecular outflows is that they are momentum-driven by energetic stellar winds from YSOs. Evidence for such winds, especially in less obscured low-mass YSOs, is extensive. For example, blue-shifted absorption features in broad optical Hα lines from T Tauri stars (or P-Cygni profiles) indicate mass outflow and steady wind activity. Velocity-resolved spectroscopy of hydrogen recombination lines (e.g. Simon *et al.* 1981, Persson *et al.* 1984). The large masses and low velocities (with respect to the stellar winds) of the molecular outflows is consistent with their being material swept up by winds. Further, theoretical modelling of the intense recombination lines and optically thick line ratios from low- and intermediate-mass objects (e.g. Simon *et al.* 1983, Natta, *et al.* 1988) predict massive, mass-losing winds (with $\dot{M} \simeq 10^{-8} - 10^{-6}$ $M_\odot$ yr^{-1}) which may contain a large neutral mass component which is not directly detected.

It has been thought (see Lada 1985 and references therein) that much of the material constituting molecular outflows is confined to a thin swept-up shell around a cavity evacuated by the stellar wind and that flows may be energy-driven by an expanding bubble of hot, diffuse gas occupying the cavity. This interpretation was supported by high spatial resolution observations of CO in L1551 (Kaifu 1985) showing an apparent cavity inside a shell-like flow. However, more recent observations in ^{13}CO suggest that there is a considerable amount of molecular material in the interior of the L1551 flow (C.V.M. Fridlund, personal communication, see also Chapter 3).

The main rival mechanisms are centrifugally-driven (Pudritz & Norman 1983, 1986) or magneto-hydrodynamically-driven flows (Uchida & Shibata 1985) which draw energy from large ($\sim$ 0.1 pc) disk structures around the central stars. These models are very attractive in that they simultaneously provide a ready-collimated outflow while providing a means for the protostar-disk system to shed large amounts of angular momentum. However, as pointed out by Shu, Adams & Lizano (1987), there are mechanical problems in these large-disk models in that the disks have very low specific energy and need to be very massive ($\gtrsim$ 100 $M_\odot$) to drive the flows. Furthermore, the models predict very high accretion rates from the disk to the protostar due to the reaction by the magnetic field on the disk material. On the grounds of specific energy the model of Draine (1983), which has a spinning protostar (with $\sim 10^6$ times more energy per kg) as the engine for a magneto-hydrodynamic flow, is preferable.

It is not clear, on observational grounds, whether large coherent disk structures, of the type needed for the above models, exist in fact. Claims to have detected such structures in molecular line data (e.g. L1551: Kaifu *et al.* 1984; S106: Bieging 1984) have been subsequently challenged (Batlra & Menten 1985, Moriarty-Schieven *et al.* 1987, Barsony *et al.* 1989). It is clear that flattened structures can be left over from the initial gas distribution in the star forming cloud, or from contraction along ordered field lines (Lizano & Shu 1989). Such flattened clouds may be laterally supported by magnetic tension or may be relics of the tendency for bipolar flows to remove large amounts of material in the polar regions and leave equatorial gas largely untouched. Before claiming to have found a disk of any size it is important to establish rotational support with velocities $v \sim \sqrt{GM/r}$ greater than the internal sound speed in the disk. The existence of small disks ($\sim$ 100 A.U.) around stars has much support, however. The emergent spectra from low-mass and intermediate-mass YSOs appear to fit well with those predicted for star-disk systems, often with significant accretion-generated luminosity (Adams, Lada & Shu 1987). Direct observations have also seemed to confirm the existence of such disks, with masses up to $\sim$ 0.3 $M_\odot$ (e.g. Beckwith *et al.* 1984, Grasdalen *et al.* 1984, Moneti *et al.* 1987).

1.2.2 Outflow Collimation

There are two possible reasons for the high level of collimation observed in molecular outflows. Either the generating wind is itself highly collimated, intrinsically or by physical interactions very close to the star, or the wind/flow is initially isotropic or semi-isotropic and is channelled into elongated lobes by the density distribution in the ambient cloud. The latter process has been proposed and modelled by, for example, Cantó *et al.* (1981), Königl (1982) and Torrelles *et al.* (1983) The dominance of external influences is supported by the large range in collimation factors observed in outflows (Lada 1985), suggesting variations in physical structure from cloud to cloud. In addition, observations of emission lines from T Tauri winds indicate that the winds are probably isotropic and not initially directed (Mundt, Stocke & Stockman 1983). It has also been noted that molecular outflow lobes, despite being highly collimated, are rather thick near the origin which implies a large initial opening angle for the flow close to the source (Snell *et al.* 1984, see also Chapter 3).

Alternatively, the observations of narrow optical jets from YSOs trace highly collimated outflows very close ($\sim$ 100 A.U.) to the stellar surface (see Lada 1985

and references therein). It seems, therefore, that two collimation processes may be occurring with very different scale sizes. Very close to a young star, non-spherically symmetric circumstellar matter (i.e. a small, thick disk) may create a narrow jet from an intrinsically spherical wind by confining it everywhere except at the rotational poles. The subsequent development may then be either spatial (as outlined by Lada 1985) or temporal (as proposed by Shu, Adams & Lizano 1987). In the former scenario, a jet may expand nearly freely after leaving the influence of the circumstellar disk, possible with a large opening angle if it has picked up ambient gas and slowed significantly. Subsequent encounters with denser parts of the cloud core may then produce pressure re-confinement and collimation on interstellar scales ($\gtrsim$ 0.1 pc), where the flow has a large cross-section. If the flow development occurs in time, the jet may begin very highly collimated as it breaks out of the central core material (at the rotational poles or at any weak point). The dense matter would then be gradually eaten away, leaving only equatorial gas and dust, as the flow widens and becomes nearly isotropic. It may be reconfined by continuing infall in the off-axis direction or more simply propogate faster at the flow 'head' where interaction with the cloud is less oblique and ram pressure is greater (Königl 1982)

1.2.3 Effect of Outflows on the Ambient Cloud

As has been mentioned above, the appearance energetic outflows in regions of recent star formation is likely to have some significant effect on the star-forming efficiency within the cloud. The flows may have time to disrupt the contraction of nearby cores in clumps forming low-mass stars, where star-formation is otherwise a virtually continuous process.

The large masses of observed flows suggests that they are mostly made up of gas swept up from the ambient medium. The formation of denser groups of massive stars in more active regions may thus be closely followed by the rapid sweeping out of the remaining cloud gas by very energetic outflow action to leave visible OB associations and open clusters.

Molecular outflows may also be a source of turbulent energy input into molecular clouds. ^{12}CO self-absorption features have been observed that have a correspondence to the spatial distribution of the outflow lobes (e.g. Lada & Gautier 1982). This may indicate a significant effect on the bulk dynamics of the cloud by the flow. However, it is not certain that the mechanical energy of the flows can be efficiently converted to

random kinetic energy in order to contribute significantly to the turbulent support of the cloud (see the discussions by Lada 1985 and Shu, Adams & Lizano 1987).

1.3 Infrared Reflection Nebulae

Closely associated with the other manifestations of the star formation process are the optical and infrared reflection nebulae. These nebulae are extended regions of surface brightness in which the emission is generally highly polarised (frequently up to $\sim 50\%$). Infrared reflection nebulae are almost always identified with molecular outflows from young sources and may also have elongated structure which mirrors that of the known high-velocity CO (e.g. Lenzen, Hodapp & Solf 1984, Joyce & Simon 1986). The observed high degrees of polarisation can only be produced by scattering off dust grains and the polarisation vectors are always arranged in a generally centro-symmetric pattern around the illuminating source (Lenzen 1987). This pattern is consistent with single scattering, in which the electric vector of the scattered polarised light lies perpendicular to the scattering plane (except in certain unusual circumstances, such as in scattering from dielectric particles, Bastien & Ménard 1988).

Scattering from material arranged in a bipolar morphology in young sources was first proposed by Elsässer & Staude (1978) to explain highly-polarised infrared emission. However, this was only later associated with bipolar molecular outflows (e.g. Heckert & Zeilick 1984). Yamashita *et al.* (1987), modelling the variation of surface brightness and polarisation fraction in GGD27 IRS, found that the pattern was consistent with scattering from the surface of a paraboloid shell and not from material in the volume of the lobe. More detailed models were constructed by Bastien & Ménard (1988), who also explained the linear polarisation pattern (perpendicular to the outflow direction) often found close to illuminating sources (e.g. Scarrott, Draper & Warren-Smith 1989, but see the discussion therein) as due to multiple scattering in a dense disk around the source.

Large dense disks surrounding the central source have often been invoked to explain the asymmetry common in reflection nebulae (e.g. Castelaz *et al.* 1986). It is often found that nebulae are unipolar or 'cometary' or that one lobe of a bipolar source is much weaker than the other. Without exception it is the reflection lobe corresponding to the red-shifted flow that is suppressed, and this has been explained as due to tilted disks or tori obscuring the further lobes of otherwise symmetrical sources. How-

ever, as discussed in Chapter 6, this effect can be explained by strong forward-directed scattering from large dust grains and there is no requirement for large disks.

It seems that infrared reflection nebulae are created by the molecular outflows from YSOs, which sweep out regions of reduced density in the surrounding molecular cloud and/or deposit shells of swept-up dusty material beyond the original limits of the dense core. This then creates a path by which shorter-wavelength photons from the central object can escape and be scattered towards the observer, while the source itself remains heavily or completely obscured along the direct line of sight. Analysis of the scattered light may provide information relevant to the physical conditions very close to high-mass YSOs which are otherwise unobservable.

References

Adams, F.C. & Shu, F.H., 1986. *Astrophys. J.*, **308**, 836.

Adams, F.C., Lada, C.J. & Shu, F.H., 1986. *Astrophys. J.*, **312**, 788.

Bally, J. & Lada, C.J., 1983. *Astrophys. J.*, **265** 824.

Barsony, M., Scoville, N.Z., Bally, J. & Claussen, M.J., 1989. *Astrophys. J.*, **343**, 212.

Bastien, P. & Ménard, F., 1988. *Astrophys. J.*, **326**, 334.

Batrla, W. & Menten, K.M., 1985. *Astrophys. J. Lett.*, **298** L19.

Beckwith, S., Zuckerman, M.F., Skrutskie, M.F. & Dyck, H.M., 1984. *Astrophys. J.*, **287**, 793.

Beichman, C.A., Myers, P.C., Emerson, J.P., Harris, S., Mathieu, R.D., Benson, P.J. & Jennings, R.E., 1986. *Astrophys. J.*, **307**, 337.

Bieging, J.H., 1984. *Astrophys. J.*, **206**, 591.

Cantó, J., Rodriguez, L.F., Barral, J.F. & Carral, P., 1981. *Astrophys. J.*, **244**, 102.

Cassen, P., Shu, F.H. & Terebey, S., 1985. In *Protostars and Planets II*, ed. D.C. Black & M.S. Matthews, p. 448. Tuscon: Univ. Ariz. Press.

Castelaz, M.W., Hackwell, J.A., Grasdalen, G.L. & Gehrz, R.D., 1986. *Astrophys. J.*, **300**, 406.

Elmegreen, B.G., 1989. *Astrophys. J. Lett*, **342**, L67.

Elsässer, H. & Staude, H.J., 1978. *Astr. Astrophys.*, **70**, L3.

Evans, N.J., 1981. In *Infrared Astronomy, IAU Symp. No. 96*, ed. C.G. Wynn-Williams & D.P. Cruickshank. p. 107. Dordrecht: Reidel.

Garden. R.P., 1986. *PhD Thesis*, Edinburgh University.

Grasdalen, G.L., Strom, S.E., Strom, K.E., Capps, R.W., Thompson, D. & Castelaz, M., 1984. *Astrophys. J. Lett.*, **283**, L57.

Heckert, P.A. & Zeilick, M., 1984, *Astron. J.*, **90**, 1379.

Joyce, R.R. & Simon, T., 1986. *Astron. J.*, **91**, 113.

Kaifu, N., Suzuki, S., Hasegawa, T., Morimoto, M. & Inatani, J., 1984. *Astr. Astrophys.*, **134**, 7.

Kaifu, N., 1985. In *Star-Forming Regions, IAU Symp. No. 115*, ed. M. Peimbert, J. Jugaku, p.275. Dordrecht: Reidel.

Königl, A., 1982. *Astrophys. J.*, **261**, 115.

Kwan & Scoville, N.Z., 1976. **210**, L39.

Lada, C.J. & Gautier, T.N., 1982. *Astrophys. J.*, **261**, 161.

Lada, C.J., 1985. *Ann. Rev. Astr. Astrophys.*, **23**, 267.

Lenzen, R., Hodapp, K.W. & Solf, J., 1984, *Astr. Astrophys.*, **137**, 202.

Lenzen, R., 1987, *Astr. Astrophys.*, **173**, 124.

Linke, R.A. & Goldsmith, P.F., 1980. *Astrophys. J.*, **235**, 437.

Lizano, S. & Shu, F.H., 1987. In *NATO/ASI Physical Processes in Interstellar Clouds*, ed. M. Scholer, Dordrecht: Reidel.

Lizano, S. & Shu, F.H., 1989. *Astrophys. J.*, **342**, 834.

Loren, R.B., Sandqvist, A. & Wootten, A., 1983. *Astrophys. J.*, **270**, 620.

Mestel, L. & Spitzer, L., 1956. *Mon. Not. R. astr. Soc.*, **116**, 503.

Moneti, A., Forrest, W.J., Pipher, J.L. & Woodward, C.E., 1988. *Astrophys. J.*, **274**, 677.

Moriarty-Schieven, G.H., Snell, R.L., Strom, S.E. & Grasdalen, G.L., 1987. *Astrophys. J. Lett.* **317**, L95.

Mundt, R. 1985. In *Protostars and Planets II*, ed. D.C. Black & M.S. Matthews, p. 414. Tuscon: Univ. Ariz. Press.

Mundt, R. & Fried, J.W., 1983. *Astrophys. J. Lett.*, **274**, L83.

Mundt, R. Stocke, J. & Stockman, H.S., 1983. *Astrophys. J.*, **263**, L73.

Myers, P.C. & Benson, P.J., 1983. *Astrophys. J.*, **266** 309.

Myers, P.C., 1985. In *Protostars and Planets II*, ed. D.C. Black & M.S. Matthews, p. 81. Tuscon: Univ. Ariz. Press.

Natta, A., Giovanardi, C. & Palla, F., 1988. *Astrophys. J.*, **332**, 921.

Perault, M. Falgarone, E. & Puget, J.L., 1985. *Astr. Astrophys.*, **152**, 371.

Persson, S.E., Geballe, T.R., McGregor, P.J., Edwards, S. & Lonsdale, C.J., 1984. *Astrophys. J.*, **286**, 289.

Pudritz, R.E. & Norman, C.A., 1983. *Astrophys. J.*, **274**, 677.

Pudritz, R.E. & Norman, C.A., 1986. *Astrophys. J.*, **301**, 571.

Reipurth, B., Bally, J., Graham, J.A., Lane, A.P. & Zealey, W.J., 1986. *Astr. Astrophys.*, **164**, 51.

Rydgren, A.E. & Cohen, M. 1985. In *Protostars and Planets II*, ed. D.C. Black & M.S. Matthews, p. 371. Tuscon: Univ. Ariz. Press.

Scarrott, S.M., Draper, P.W. & Warren-Smith, R.F., 1989. *Mon. Not. R. astr. Soc.*, **237**, 621.

Schwartz, R.D., 1983. *Ann. Rev. Astr. Astrophys.*, **21**, 209.

Shu, Adams & Lizano, S., 1987. *Ann. Rev. Astr. Astrophys.*, **25**, 23.

Simon, M., Righini-Cohen, G., Fischer, J. & Cassar, L., 1981. *Astrophys. J.*, **251**, 552.

Snell, R.L., 1985. In *Star-Forming Regions, IAU Symp. No. 115*, ed. M. Peimbert, J. Jugaku, p.213. Dordrecht: Reidel.

Snell, R.L., Loren, R.B. & Plambeck, R.L., 1980. *Astrophys. J.*, **239**, L17.

Snell, R.L., Scoville, N.Z., Sanders, D.B. & Erickson, N.R., 1984. *Astrophys. J.*, **284**, 176.

Solomon, P.M., Sanders, D.B. & Scoville, N.Z., 1979. In *The Large Scale Characteristics of Galaxies, IAU Symp. No. 84*, ed. W.B. Burton, p. 35. Dordrecht: Reidel.

Stahler, S.W., Shu, F.H. & Taam, R.E., 1980. *Astrophys. J.*, **242**, 226.

Torrelles, J.M., Rodriguez, L.F., Cantó, J., Carral, P., Mercaide, J., Moran & Ho, P.T.P., 1983. *Astrophys. J.*, **274**, 214.

Uchida, Y., & Shibata, K., *Publ. astr. Soc. Japan*, **37**, 515.

Wilking, B.A. & Lada, C.J., 1983. *Astrophys. J.*, **274**, 698.

Wilking, B.A. & Lada, C.J., 1985. In *Protostars and Planets II*, ed. D.C. Black & M.S. Matthews, p. 297. Tuscon: Univ. Ariz. Press.

Wynn-Williams, G., 1982. *Ann. Rev. Astr. Astrophys.*, **20**, 587.

Yamashita, T., Sato, S., Nagata, T., Suzuki, H., Hough, J.H., McLean, I.S., Garden, R. & Gatley, I., 1978. *Astr. Astrophys.*, **177**, 258.

Zuckerman, B., & Palmer P., 1974. Ann. Rev. Astr. Astrophys., **12**, 279.

Zuckerman *et al.*, 1976. *Astrophys. J.*, **209**, L137.

Chapter 2

Discovery of New Near-infrared Sources and Reflection Nebulosity in W75N

The original observations in the series covering the source W75N were single-detector maps at 10-arcsec and 20-arcsec resolution, intended to find the infrared counterparts of the HII/OH maser and the source of the known molecular hydrogen line emission. Physical information on the ionisation of the surrounding gas and the depth of foreground material was then obtained by continuum colour photometry and spectroscopy of the newly-found objects.

The work contained in this chapter was done in collaboration with C.M. Mountain, T. Yamashita & M.J. Selby and is published in Moore *et al.* 1988: *Mon. Not. R. astr. Soc.*, **234**, 95. The majority of the observations were obtained during PATT allocation U/H/11, with additional data provided by the UKIRT Service Observing Programme.

Summary

Near infrared observations around the OH maser source in W75N reveal new embedded sources, an infrared reflection nebula and extended molecular hydrogen emission. The brightest 2-μm continuum source, IRS-1, may be either a peak in the reflection nebula or a self-luminous object, although the former requires very large near infrared continuum and recombination brightnesses from the true luminosity source. Confirmation of either model requires observations with higher spatial resolution. A second source, IRS-2, is a very young object with strong recombination lines but no accompanying 5GHz continuum emission. Photometry indicates a visual extinction of ~ 34 mag towards IRS-2. The source of luminosity in the reflection nebula has a ZAMS stellar type between B0.5 and O7 or equivalent, and is probably coincident with the ultracompact HII region and OH maser source W75N(OH).

Molecular hydrogen v=1–0 S(1) emission was mapped in a slightly undersampled 1.5 × 2 arcmin area. The total reddened luminosity detected in the line is ~ 0.3 $L_\odot$. Energetics calculations show that either UV photons or CO outflow mechanical energy are sufficient to account for the H_2 emission by fluorescence or shock-excitation. H_2 line ratios fall between the values expected for the two mechanisms, suggesting that both may contribute.

Simple dynamical timescales suggest that the various sources in this region are the result of coeval formation, if a North-South density gradient of around 10 per cent may be assumed in the original cloud.

2.1 Introduction

W75N is a bipolar CO outflow source and infrared-luminous region of recent star formation with an integrated IRAS SKYFLUX luminosity of over 10 $L_\odot$. It is embedded in a large molecular cloud with average radial velocity near +9 kms^{-1}, at a distance of 2 kpc (Dickel, Dickel & Wilson 1978) and is part of the Cygnus-X complex of dense molecular clouds. There are a number of radio, infrared and molecular line sources associated with the W75N region and Dickel, Dickel & Wilson (1978), who have mapped the large scale structure of this area in ^{12}CO and ^{13}CO, suggest that these sources may be the products of an interaction between the W75N and nearby DR-21 molecular clouds.

The region contains a bright OH maser source W75N(OH) identified with a faint ultracompact HII region, HII(B), lying 25 arcsec to the South and 15 arcsec to the West of a more extended HII region, HII(A) (Habing *et al.* 1974; Haschick *et al.* 1981). HII(A) coincides with a 20-μm emission peak (Wynn-Williams, Becklin & Neugebauer 1974) and is also a source of molecular hydrogen emission (Fischer, Righini-Cohen & Simon 1980). However HII(B), relatively less studied in the infrared, is also close to a high-velocity H_2O maser (Genzel & Downes 1977) and to the peak of the far-infrared emission that probably dominates the luminosity of this region (detected at 53 μm by Harvey, Campbell & Hoffmann 1977). It has been shown that HII(B) is also a source of molecular hydrogen emission (Mountain *et al.* 1985b).

Fischer *et al.* (1985) have reported ^{12}CO J=1–0 line profiles from W75N with a full width at 0.1K antenna temperature of about 35 kms^{-1} . This satisfies the criterion of Lada (1985) defining the presence of a high-velocity cold molecular outflow, i.e. that

the full width at $T_A^*(^{12}CO) = 0.1$ K should be greater than 10 kms^{-1} . These authors also mapped the region in the high velocity wings of ^{12}CO and discovered an apparently lightly collimated bipolar outflow centred near to the HII(A) and HII(B) sources, and extending out to about 1.2 pc from it.

In this chapter near-infrared observations of the W75N region are presented, including a 8-arcsec resolution 2.2-μm continuum map covering a 64 × 48 arcsec area centred near to W75N(OH). This map reveals a cluster of previously unobserved near-infrared continuum sources and an extensive 2-μm reflection nebula. Using photometry and Brackett line detections we estimate the extinction towards these sources and discuss the detailed structure of the region and the nature of the individual objects found. An undersampled map of molecular hydrogen v=1-0 S(1) detections is also presented covering a 1.5 × 2 arcmin area. The strength, distribution and location of the emission is discussed in comparison with excitation models and the constraints they place on the energetics of the source.

2.2 Observations and Results

All observations were made on the 3.8m United Kingdom Infrared Telescope (UKIRT) on Mauna Kea, Hawaii. 4-μm spectroscopy was done with a 5-arcsec aperture using the cooled grating spectrometer CGS2 as part of the UKIRT Service Observing Programme of October 10, 1986. The 2-μm mapping, photometry and spectroscopy were carried out with the UKIRT CVF spectrophotometer UKT-9 during three half nights on the $28^{th} - 30^{th}$ of July 1985. Photometry was done in a 7.8-arcsec beam for the UKIRT filter set J, H, K, and L′ and in a 5-arcsec beam for M. The H_2, v=1–0 S(1) line was mapped with a 'Queensgate' 2-μm Fabry-Perot etalon with a resolution of $\sim$ 120 kms^{-1}, used in an uncollimated f/36 beam in front of UKT-9 with a 19.6-arcsec sky aperture. Sky chopping was used in all observations, the beams being separated $\sim$ 130 arcsec east-west. The telescope pointing was accurate to about 3 arcsec throughout the observations.

Spectrometric and flux calibrations were obtained using NGC 7027 and standard stars from the UKIRT standards list. We assumed a line strength, in H_2 v=1–0 S(1), of $(2.5 \pm 0.5) \times 10^{-15}$ Wm^{-1} for NGC 7027, obtained by integrating the map of Beckwith *et al.* (1980) over the 19.6-arcsec aperture used for the 2-μm spectroscopic observations.

The 2.2-μm continuum flux density map, made on a 4-arcsec grid with the 7.8-

arcsec circular beam, is shown in Fig. 2.1. The offset centre is at $20^h36\ ^{rmm}50.^s5 + 42°26'56'' \pm 2$ arcsec (1950). This is the peak of the 2-μm emission, and is about 3 arcsec south and 6 arcsec east of the position of W75N(OH). The image has been slightly smoothed using a 2D Gaussian function with a sampling radius equivalent to the beam size. The map reveals a small cluster of previously undetected near infrared sources which we have designated (in order of 2-μm brightness) IRS-1, IRS-2, IRS-3. The latter two sources are pointlike while IRS-1 appears extended by $\sim$ 15 arcsec towards the Southeast, with other slight extensions to the West and Northeast. Fig. 2.1 also shows the existence of diffuse 2-μm emission extending over almost the whole area covered by the map, with low-level emission ($< 2 \times 10^{-15}$ Wm^{-2} μm^{-1} per beam) extending beyond the limits set by our observations.

Results of photometry measurements are given in Table 2.1 and Fig. 2.2 for IRS-1, IRS-2, IRS-3 and a representative point in the extended nebula at offset 20 arcsec east, 12 arcsec north. IRS-1 and IRS-2 are highly reddened, IRS-2 having an H–K = 3.5 and K–L′ = 3.8, and typical points in the nebula have H–K $\simeq$ 2.3, similar to IRS-1. Flux calibrations were obtained using standard stars and the measurements of absolute flux from Vega by Mountain *et al.* (1985a). Brα and Brγ line strengths toward IRS-1 and IRS-2 are listed in Table 2.2. Two 2.05-μm to 2.30-μm CVF spectra taken at separate points in the extended nebula are displayed in Figs. 2.3(a) and 2.3(b) and each clearly shows the v=1–0 S(1) (2.122 μm), v=1–0 S(0) (2.223 μm) and v=2–1 S(1) (2.248 μm) lines of molecular hydrogen.

To determine the extent and magnitude of the molecular hydrogen emission in the vicinity of HII(B) the v=1–0 S(1) line was mapped with a circular 19.6-arcsec beam on a 20-arcsec grid. At each point the line and continuum contributions were measured by stepping the Fabry-Perot (FP) off the line centre to a suitable continuum point, determined from initial CVF and FP scans. The total line-plus-continuum integration time per point was 8 sec. The S(1) line strengths are accurate to about 20 per cent, most of the error arising from uncertainties in the calibration. The results are shown in Fig. 2.4, overlayed on the 6-cm VLA map of Haschick *et al.* (1981). The H emission is extended on a scale of order 120 arcsec which subtends about 1.2 pc at 2kpc. The S(1) peak flux in Fig. 2.4 agrees well with 3×10^{-16} Wm^{-2}, obtained from the CVF spectrum taken at IRS-1 with the same aperture.

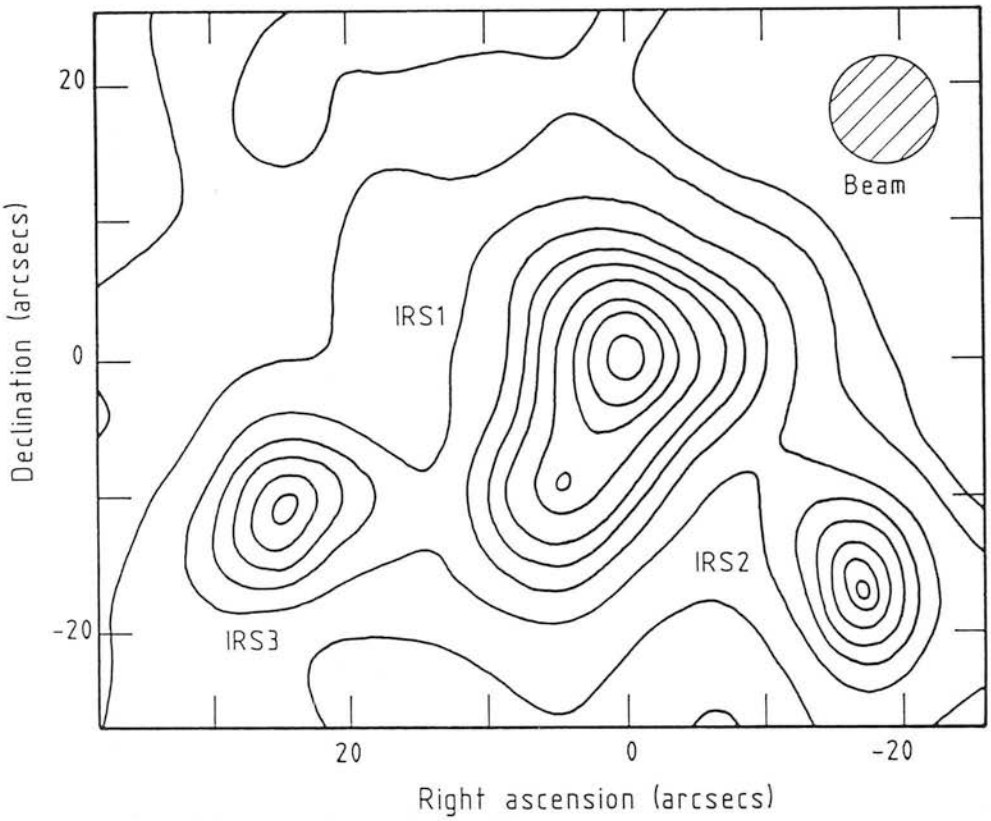

Figure 2.1: K continuum map. Contours are at 2, 4, 10, 20, 30,... 80 $\times 10^{-15}$ $Wm^{-2}\,\mu m^{-1}$ per 7.8-arcsec beam. The offset centre is at $20^h36^m50^s.5$; $+42°26'56''$ (1950). The map is oversampled at 4-arcsec intervals.

Table 2.1: 1-μm to 5-μm Photometry

SOURCE	OFFSET /arcsec		MAGNITUDE J	H	K	L′	M	Implied A_V (from J–H)
IRS-1	0	0	14.0	11.3	9.2	7.0	–	25
IRS-2	−16	−16	16.4*	12.8	9.3	5.5	4.3	≥ 34
IRS-3	+24	−12	12.7	10.9	9.6	–	–	17
diffuse nebula	+20	+12	17.6*	15.0	12.7	–	–	≥ 24

* 3σ upper limit.
– indicates that no measurement was made.

Table 2.2: Recombination Line Strengths

SOURCE	Observed line fluxes $/10^{-16}$ Wm^{-2}	
	Brγ: 2.166 μm (20-arcsec beam)	Brα: 4.052 μm (5-arcsec beam)
IRS-1	1.0 (±0.2)	1.2 (±0.2)
IRS-2	1.2 (±0.2)	9.5 (±0.5)

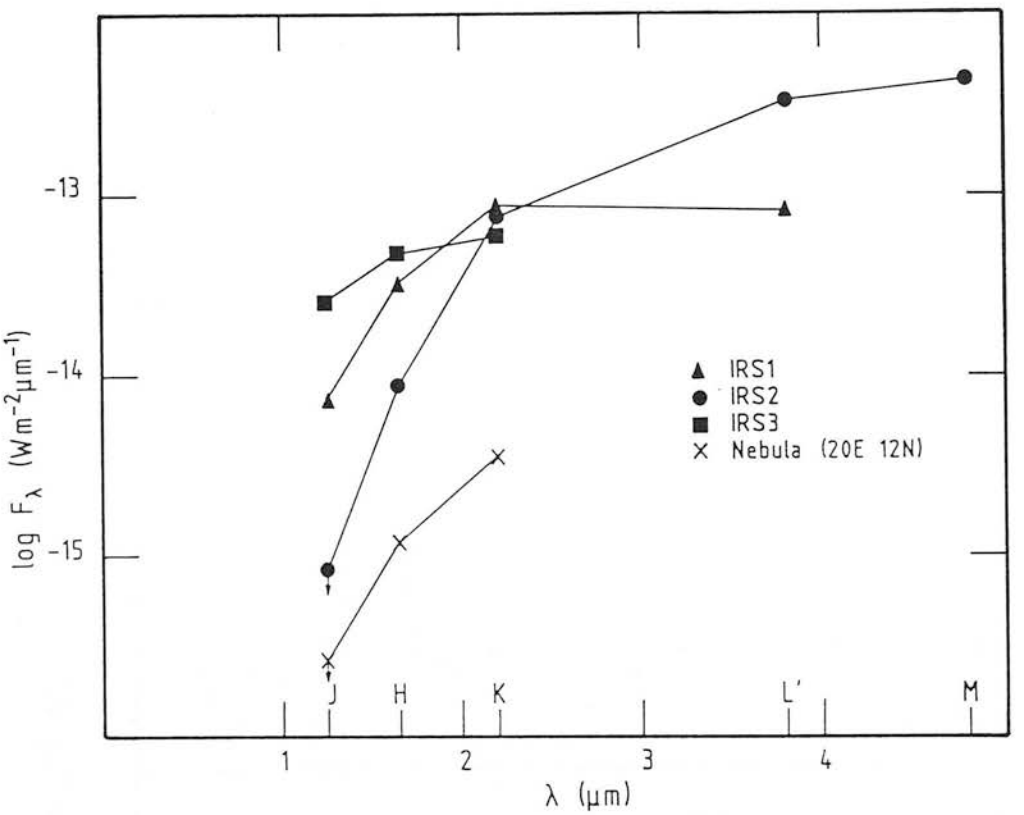

Figure 2.2: Results of J H K L′ & M photometry towards IRS-1, IRS-2, IRS-3 and a position in the diffuse nebula. The J measurements of IRS-2 and the diffuse nebula are upper limits. Typical 1σ errors are around 10 per cent.

Table 2.3: Calculated parameters for the source illuminating IRS-1

	Pre-reflection:				$\log_{10}(N_{Ly})$	ZAMS	M_K
Albedo	J–H	A_v(J–H)	Brα/Brγ	A_v(Case B)	(from Brα)	type	/mag
Draine & Lee	2.9	27	37 ($\pm$9)	33–40	48.2 $\pm$30%	O8	–9.3
unity at all λ	2.7	25	10 ($\pm$3)	13–22	47.0 $\pm$30%	B0/B0.5	–7.4

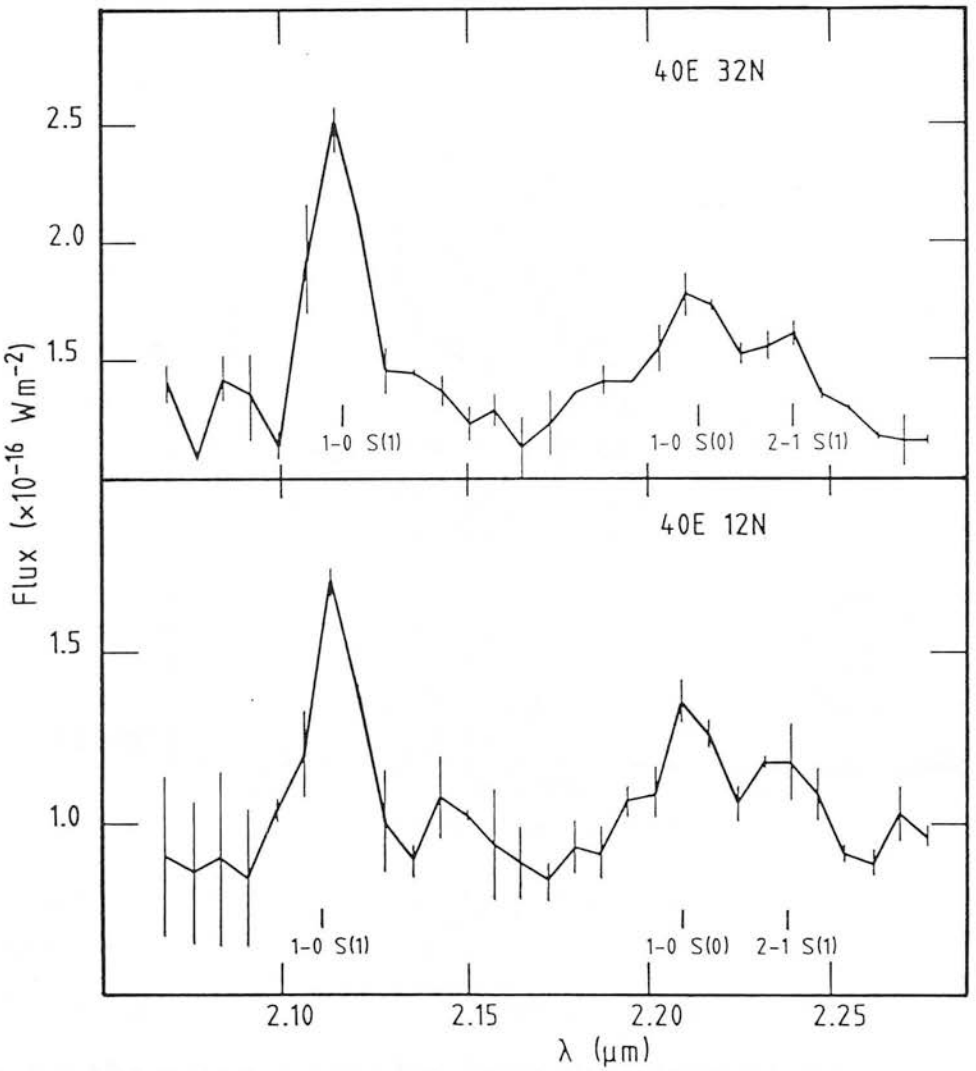

Figure 2.3: 20-arcsec resolution 2.05-μm to 2.30-μm spectra showing molecular hydrogen lines originating from two points in the continuum reflection nebula.

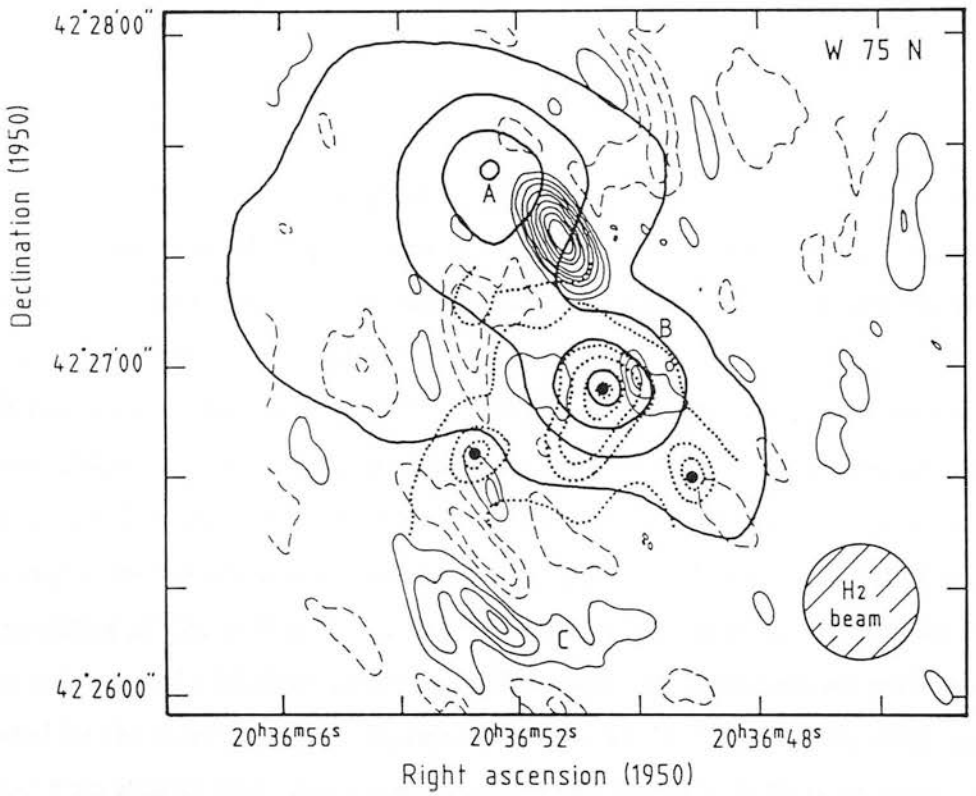

Figure 2.4: Map of the v=1–0 S(1) line of molecular hydrogen (thick contours) superposed on the 6-cm radio continuum map of Haschick *et al.* (1981). Contour levels are at 0.3, 1.1, 1.9 and 2.7 $\times 10^{-16}$ Wm^{-2} per 19.6-arcsec beam. The sampling grid is 20 arcsec $\times$ 20 arcsec. Dotted contours show the 2-μm continuum from Fig. 2.1.

2.3 Discussion

2.3.1 Compact Continuum Sources and Diffuse Nebula

The low-level, diffuse 2-μm continuum emission in Fig. 2.1 clearly arises from an infrared reflection nebula. The alternative possibility of extended free-free emission is excluded since the 2-μm CVF spectra (Figs. 2.3(a) and 2.3(b)) show an absence of Brγ recombination lines in the nebula, and since no complementary extended radio emission is observed (Haschick *et al.* 1981 & Fig. 2.4). This conclusion is supported by continuum polarisation observations at 2 μm by Yamashita *et al.* (1988) revealing polarisation fractions of up to 50 per cent throughout the region of Fig. 2.1. Strong polarisation (20 per cent) was observed towards the K continuum peak, IRS-1, hinting that this may actually be a bright portion of the reflection nebula and not the source of illumination. The extended appearance of IRS-1 in Fig. 2.1 may indicate the presence of separate associated sources or patchy extended emission to the West, Northeast and especially towards the Southeast of the peak.

If IRS-1 were a hot ($T > 10,000$ K) self-luminous source then the J–H colour of 2.7 mag (Table 2.1) would imply a visual extinction of $A_V \simeq 25$ mag. Hence the Brα detected in a 5-arcsec beam towards IRS-1 would require a total Lyman continuum luminosity from the associated ionising source of 3.7×10^{45} ($\pm$30 per cent) photons s^{-1} (assuming 10^4 K, 10^{10} m^{-3} and Menzel's Case B: Brockelhurst 1971; Giles 1977). This is indicative of a B1/B0.5 ZAMS star (Thompson 1984), compatible with the type predicted for the star ionising HII(B) (Haschick *et al.* 1981). However, the displacement of IRS-1 from HII(B) (Fig. 2.4) is significantly larger than the RMS telescope pointing error making it difficult to conclude that the two sources are the same; the HII region may coincide instead with the slight Western extension of IRS-1. The 2-μm peak is therefore more likely to be associated with a separate cluster member or with bright, extended emission.

No small-beam Brγ flux is available to examine properly the Brγ/Brα intensity ratio towards IRS-1. The line was detected in a 20-arcsec aperture during these observations, but one cannot say if the emitting source is IRS-1, HII(B), extended reflected emission in the nebula or a combination of these. If the emission were solely from a single point source at IRS-1, the observed Brackett line ratio would be highly anomalous, being close to unity even without dereddening corrections. This makes it more likely that the Brα flux is contaminated by HII(B), or that the measured recombination

lines are due to extended scattered emission in the nebula. Considering also the 20 per cent polarisation fraction observed toward IRS-1 (Yamashita *et al.* 1988), one might argue that the source is dominated by, or is purely, reflected light. In this case the illuminating object is considerably extinguished at 2 μm, and would be most probably associated with the ionizing source in or near HII(B). This location is consistent with the pattern of polarisation vectors observed in the nebula (Yamashita *et al.* 1988).

Since the assumption of a single point source at IRS-1 creates problems in interpreting the recombination line ratio, one should also examine whether the source can plausibly consist of scattered light. The main difficulty with such an analysis is the assumption of a suitable scattering efficiency or grain albedo for the reflecting material. Estimated parameters for a source at HII(B) illuminating IRS-1 are shown in Table 2.3 for two contrasting cases. The first uses the theoretical graphite/silicate mix albedos calculated by Draine & Lee (1984) and the second assumes 100 per cent scattering efficiency, independent of wavelength. The 'pre-reflection' values of J–H colour and implied visual extinction (columns 1 & 2) are not greatly affected either way, but the Brγ/Brα ratio and its associated extinction estimate are strongly altered by adopting the Draine & Lee albedos, as these fall rapidly between 2 μm and 4 μm. Thus the J–H photometry should provide a more reliable extinction estimate, especially since the source is identified in this case with a hot ionising star. With better line data it would be possible to say more about the grain scattering properties in this wavelength range.

A flat albedo produces a Case B reddening estimate from the Brγ/Brα ratio which is too small in comparison with A_V(J–H), while the estimate obtained from the Draine & Lee results is rather too high (columns 3 & 4). An intermediate 2-μm/4-μm albedo ratio of $\sim$ 1.6 would provide better agreement; however, if a significant fraction of the reddening occurs within the reflecting material itself, optical depth effects will distort the J–H colour and the Brγ/Brα ratio.

Columns 5 & 6 of Table 2.3 contain Case B Lyman continua and associated ZAMS spectral types for a source at HII(B), calculated from the Brγ towards IRS-1 and assuming a projected displacement from IRS-1 of 6 arcsec (reddening corrections are taken from the J-H colours and the Draine & Lee 4-μm albedo is taken to be 0.06). In the first case the predicted spectral type is consistent with the IRAS far infrared luminosity of the region but not with the 5-GHz continuum measurements of Haschick *et al.* (1981), which imply an ionising source for HII(B) of B0.5; the ionisation required by a high, flat albedo is much more compatible with these radio data.

One may estimate the apparent K magnitude of the central source by using Hubble's relation for reflection nebulae, in the form given by Castelaz et al. (1985) (which assumes 100 per cent scattering efficiency at the wavelength in question):

$$m_*(\lambda) = -2.75 + m'_{neb}(\lambda) - 5log_{10}\theta$$

Here $m_*(\lambda)$ is the derived apparent magnitude (at wavelength λ) of the illuminating star, $m'_{neb}(\lambda)$ is the measured surface brightness of a point in the nebula (in mag/arcsec^2) and θ is the distance between nebula and source in arcsec. This formula yields the absolute K magnitudes for the illuminating object given in the final column of Table 2.3. The value of –9.3 obtained using the Draine & Lee 2 μm albedo of 0.22 is implausibly bright, since the total IRAS luminosity of the whole W75N region is 1.3×10^5 $L_\odot$. The latter luminosity, if from a dominant single source, limits the ZAMS spectral type to O7 at most, with absolute K magnitude of around –4.3. This problem may be resolvable in terms of a source with a low effective temperature (*i.e.* a few thousand K) which could be separate from the ionising star. If the majority of the extinction occurs before reflection, it is also possible that the 2-μm source photosphere is spatially extended on a 0.01 – 0.1 pc scale and that the solid angle correction contained in Hubble's relation is inapplicable. However, the corrections available are only just sufficient and must be viewed with caution; we cannot fully account for the Brα luminosity needed for reflection which remains (in the Draine & Lee case) about an order of magnitude too large in comparison to the 5-GHz flux measurement of Haschick *et al.* (1981). To correct for this requires a continuum optical depth of ~ 2.5 at 5GHz which is not unusual in ultracompact HII regions of the kind studied by Garay, Reid & Moran (1985), but may be hard to accept in a considerably larger object such as this. The assumption of a high and roughly constant albedo for this dense cloud-core environment appears to obviate the bulk of the foregoing problems; however, this produces a disagreement between extinction estimates which is opposite to that expected from optical depth effects within extended reflecting material.

It is clear that the present data will not allow positive conclusions to be drawn on the nature of IRS-1 and it may be that the situation is confused by the presence of multiple sources coexisting in a very small region. Further observations are certainly necessary, including high spatial resolution maps of the continuum polarisation and mid infrared emission plus small-beam Brγ observations around IRS-1 and HII(B).

IRS-2 is a deeply embedded, pointlike source with J–H > 3.6 implying $A_V \geq 34$

mag along the line of sight. An ionization rate of $(3.8 \pm 0.4) \times 10^{46}$ s^{-1} is implied by the Brα flux (3.0×10^{-15} Wm^{-2}, de-reddened according to Rieke & Lebofsky (1985), and is equivalent to the Lyman flux expected from a ZAMS B0.5 – B0 star (Thompson 1984). However, no 5-GHz continuum source has been detected at the position of IRS-2 to a 2.7 mJy limit (Haschick *et al.* 1981 and Fig. 2.4). Standard Case B recombination theory predicts a radio continuum flux density of $\sim$ 120 mJy at 5GHz from an optically thin ionised region producing this amount of Brα emission.

As IRS-2 appears unresolved, no beam-size correction has been applied to the Brα/Brγ intensity ratio. Comparing the diffuse 2-μm continuum emission nearby IRS-2 with that at IRS-1, contamination of the large-beam Brα measurement by scattered photons should be an order of magnitude less than the observed flux. The line intensity ratio for IRS-2 is thus 8 ± 1.5, implying a Case B extinction of $A_V = 12 - 17$ mag, much lower than the value obtained from the J–H colour. If the J–H extinction value is correct, then the intrinsic Brα/Brγ ratio is around 0.8 (*cf* the usual Case B value of 2.82). Anomalous recombination line ratios are predicted by Simon *et al.* (1983) for very young, medium to low luminosity sources due to self-absorption of the Brα line in very dense ionised material. IRS-2 thus appears to be an extremely young, highly reddened stellar source, possibly having a very compact ionised region with a high continuum optical depth at cm wavelengths.

Little information has been gained on the third near-infrared source, IRS-3, except that it appears to be a somewhat less reddened ($A_V \simeq 17$ mag from the J–H colour), point-like luminosity source. It is, however, close to an enhancement in the radio continuum map of Haschick *et al.* (1981), (see Fig. 2.4) but no recombination line observations were made toward this object.

2.3.2 H_2 Emission

By integrating over the map in Fig. 2.4, the total observed luminosity in the v=1–0 S(1) line obtained is $\sim$ 0.3 $L_\odot$. Using the arguments of Beckwith *et al.* (1980) and Fischer *et al.* (1985) and assuming that most of the H_2 vibrational radiation results from cooling behind an isothermal shock, then the power radiated in these lines should be approximately equal to the rate at which bulk energy is deposited in the gas. From the results of Fischer *et al.* (1985) the total energy in the CO flow should be $\sim 1 \times 10^{40}$ J. If the flow has been steady, its age (t_f) is $\sim 2.3 \times 10^4$ yr, and the total H_2 energy radiated in all lines (taking the vibration-rotation temperature as $T_{v-r} = 2000$K)

during this time is $\sim 1 \times 10^{39}$ J. This assumes that the total power emitted in all H_2 lines is 10–17 times that in the v=1–0 S(1) line (Shull & Hollenbach 1978). Thus the ratio of total energies is:

$$(\text{Total } H_2 \text{ luminosity} \times t_f)/(\text{CO flow energy}) \sim 0.1$$

Hence the outflow is energetic enough to power the H_2 emission by shock excitation. For this ratio to exceed unity, there would have to be an average 2-μm extinction of > 2.5 mag across the whole region, and the likelihood of this is linked to the previous discussion of the nature of IRS-1. However, there are many assumptions made in calculating this ratio, as discussed by Fischer *et al.* (1985), and before the molecular line emission can be ascribed to post-shock cooling it is necessary to examine other excitation mechanisms.

As the line emission appears predominantly near an infrared reflection nebula, it is necessary to examine the possibility that the H_2 could be fluorescent, as reported by Gatley *et al.* (1987) in the visual reflection nebula NGC 2023 and by Sellgren (1986) for other visual reflection nebulae. Following the argument of Longmore, Robson & Jameson (1986), about 1 per cent of the total luminosity of a B0.5 star will be emitted in the non-ionizing 912 - 1108 Å range responsible for fluorescence in H_2. If 75 per cent of the emitted photons go into heating dust and the conversion efficiency into 1–0 S(1) photons is about 2 per cent (Black & Dalgarno 1976; Black & van Dishoeck 1987), then the total energy in the 2.122-μm line should be about $1.3\,L_\odot$. If the star is hotter than B0.5, then this figure increases rapidly. In fact, we observe ~ 0.3 $L_\odot$. and so fluorescent emission is energetically feasible. The short-fall in the observed emission could be due to a higher UV absorption rate by dust or missed emission due to under-sampling, but is most likely to be accounted for by extinction.

Calculations by Black & Dalgarno (1976) for fluorescent H_2 predict [2–1 S(1)]/[1–0 S(1)] and [1–0 S(0)]/[1–0 S(1)] line ratios of 0.52 and 0.64, respectively. These values are generally consistent with the results of the more detailed strong field models of Black & van Dishoeck (1987). From the spectra in Fig. 2.3, the observed ratios are 0.3 ± 0.1 and 0.5 ± 0.1. Assuming a shock velocity of $V_s \sim 15$ kms^{-1} and a density $n(H_2) \sim 3 \times 10^{11}$ m^{-3} (Chapter 4) the H_2 shock-heated models of Kwan (1977) and Shull & Hollenbach (1978) give values of 0.2 for both ratios. The present data fit rather better to the UV fluorescence model, but not sufficiently so to rule out shock-excitation. The low ratios may suggest that the observed spectra are a 'mixture' of fluorescent

and shock heated gas. Until further observations are made and more sophisticated H_2 excitation codes developed it may be difficult to unambiguously differentiate between the two mechanisms from limited line ratio studies. The presence of a second strong peak coincident with the larger HII(A) seems to point toward fluorescent emission there, due to UV radiation from the B0.5 ionizing star (Haschick *et al.* 1981) or to non-ionizing radiation from HII(B) impinging on enhanced density material surrounding HII(A).

2.3.3 Cluster Evolution and Morphology

W75N contains a cluster of young sources, spread over a region about 0.6 pc in size, which appear to display a sequence in relative age. The more extended, less embedded and so probably more evolved HII region, HII(A) appears in the north, the more compact OH maser source HII(B) is central, and on the south end of this 'line' is the very young BN-type object, IRS-2 (see Fig. 2.4).

To examine if these sources are the result of sequential or coeval formation we can calculate the dynamical ages (τ_d) of the HII regions assuming an expansion rate of the order of the thermal sound speed $\sim$ 10 kms^{-1} (Ho, Haschick & Israel 1981), this also being the apparent expansion velocity of the maser spots near HII(B), (Baart *et al.* 1986). This gives, for HII(A): $\tau_d \sim 8 \times 10^3$ yr; HII(B): $\tau_d \sim 4 \times 10^3$ yr and for IRS-2: $\tau_d < 10^3$ yr. The upper limit on the IRS-2 age is calculated assuming the maximum size an optically thick 4.9-GHz emission region can have without being detected on the VLA map of Haschick *et al.* (1981) (0.1 arcsec or $\sim$ 200 A.U.), allowing for a departure from the assumed sound speed up to a factor $\sim$ 5 (Ho, Haschick & Israel 1981). If these age differences are the result of sequential star formation, the formation times (τ_f) would have to be of the same order as the differences in dynamical age.

An upper limit to the formation time can be set by the placental cloud free-fall time (τ_{ff}) as given by Ho, Haschick & Israel (1981):

$$\tau_f > \tau_{ff} = 4.3 \times 10^{10} n(H_2)^{-0.5} \text{ yr.}$$

The differences in the observed dynamical timescales are $\sim 4 \times 10^3$ yr, requiring substantial pre-formation densities greater than 10^{14} m^{-3}, whereas the observed central density in the W75N region is only about 3×10^{11} m^{-3} (Chapter 4) and there is no reason to suppose this figure was significantly higher in the past. Density inhomogeneities

or a density gradient of only 10 per cent of the present day value could, however, have produced formation times that differ by the range of observed dynamical ages. This suggests that the initial collapse to form these objects occurred at the same time, with differences in their dynamical ages resulting from a shallow north-south density gradient.

2.4 Conclusions

1. Near-infrared observations of W75N have revealed a number of embedded objects in a region $\sim$ 0.6 pc in extent, close to the ultra-compact HII region and OH maser source. Surrounding them is an extensive infrared reflection nebula.

2. The brightest 2-μm source, IRS-1, may be a reflection peak in the nebula, but this model requires a large excess near-infrared continuum and recombination line luminosity from a purely stellar source coincident with the OH maser. It is possible to reconcile this excess with the total IRAS luminosity of the region by assuming that the source has a considerably extended photosphere with a temperature of only a few thousand degrees, but the required recombination line output remains difficult to explain. The opposing conclusion that IRS-1 is a real source or a cluster of sources is equally probable, based on the present data. The limits on the ZAMS spectral type of the central source are B0.5 to O7.

3. The second brightest 2-μm continuum source, IRS-2, is highly reddened ($A_V \geq$ 34 mag) with a large recombination line flux although it has no associated 5-GHz continuum emission. This object appears to be extremely young, possibly possessing a very dense and compact ionized region.

4. The extended molecular hydrogen v=1–0 S(1) emission has an observed luminosity of $\sim$ 0.3 $L_\odot$. This can be accounted for by the post-shock cooling energy available from the CO flow in W75N. However the H_2 line ratios and energetics suggest a significant UV-fluorescence component to the excitation.

5. The dynamical ages of the HII regions are surprisingly small and differ by only a few percent of possible free-fall formation times. This might be explained by coeval formation in a shallow density gradient (*sim*10 per cent over the region) running north-south.

References

Baart E.E., Cohen, R.J., Davies, R.D., Norris, R.P. & Rowland, P.R., 1986. *Mon. Not. R. astr. Soc.*, **219**, 145.

Beckwith, S., Neugebauer, G., Becklin, E.E., Matthews, K., Persson, S.E., 1980. *Astr. J.*, **85**, 886.

Black, J.H. & van Dishoeck, E.F., 1987. *Astrophys. J.*, **322** yyy.

Black, J.H. & Dalgarno, A., 1976. *Astrophys. J.*, **203**, 132.

Brocklehurst, M., 1971. *Mon. Not. R. astr. Soc.*, **153**, 471.

Castelaz, M.W., Hackwell, J.A., Grasdalen, G.L., Gehrz, R.D. & Gullixson, C., 1985 *Astrophys. J.*, **290**, 261.

Dickel, J.R., Dickel, H.R. & Wilson, W.J., 1978. *Astrophys. J.*, **223**, 840.

Draine, B.T. & Hyung Mok Lee, 1984. *Astrophys. J., 285*, 89.

Elmegreen, B.G. & Lada, C.J., 1977. *Astrophys. J., 214*, 725.

Fischer, J., Righini-Cohen, G. & Simon, M., 1980. *Astrophys. J. (Letts)*, **238**, L155.

Fischer, J., Sanders, D.B., Simon, M. & Solomon, P.M., 1985. *Astrophys. J.*, **293**, 508.

Garay, G., Reid, M.J. & Moran, J.M., 1985. *Astrophys. J.*, **289**, 681.

Gatley, I., Hasegawa, T., Suzuki, H., Garden, R., Brand, P., Lightfoot, J., Glencross, W., Okuda, H. & Nagata, T., 1987. *Astrophys. J., (Letts)*, **318**, L73.

Genzel, R. & Downes, D., 1977. *Astr. Astrophys. Suppl.*, **30**, 145.

Giles, K., 1977. *Mon. Not. R. astr. Soc.*, **180**, 57P.

Habing, H.J., Goss, W.M., Matthews, H.E. & Winnberg, A., 1974. *Astr. Astrophys.*, **35**, 1.

Harvey, P.M., Campbell, M.F. & Hoffmann, W.F., 1977. *Astrophys. J.*, **211**, 786.

Haschick, A.D., Reid, M.J., Burke, B.F., Moran, J.M. & Miller, G., 1981. *Astrophys. J.*, **244**, 76.

Ho, P.T.P., Haschick, A.D. & Israel, F.P., 1981. *Astrophys. J.*, **243**, 526.

Kwan, J., 1977. *Astrophys. J.*, **216**, 713.

Lada, C.J., 1985. *Ann. Rev. Astr. Astrophys.*, **23**, 267.

Longmore, A.J., Robson, E.I. & Jameson, R.F., 1986. *Mon. Not. R. astr. Soc.*, **221**, 589.

Mountain, C.M., Leggett, S.K., Selby, M.J., Blackwell, D.E. & Petford, A.D., 1985a. *Astr. Astrophys.*, **151**, 399.

Mountain, C.M., Selby, M.J., Zadrozny, A. & Hartquist, T.W., 1985b. *Mon. Not. R. astr. Soc.*, **216**, 13P.

Norris, R.P., Booth, R.S., Diamond, P.J. & Porter, N.D., 1982. *Mon. Not. R. astr. Soc.*, **201**, 191.

Rieke, G.H. & Lebofsky, M.J., 1985. *Astrophys. J.*, **288**, 618.

Sellgren, K, 1986. *Astrophys. J.*, **305**, 399.

Shull, J.M. & Hollenbach, D.J., 1978. *Astrophys. J.*, **220**, 525.

Simon, M., Felli, M., Cassar, L., Fischer, J. & Massi, M., 1983. *Astrophys. J.*, **266**, 623.

Thompson, R.I., 1984. *Astrophys. J.*, **283**, 165.

Thompson, R.I., 1987. *Astrophys. J.*, **312**, 784.

Wynn-Williams, C.G., Becklin, E.E. & Neugebauer, G., 1974. *Astrophys. J.*, **187**, 473.

Yamashita, T., Sato, S., Tamura, M., Suzuki, H., Gatley, I., Hough, J.H., Mountain, C.M. & Moore, T.J.T., 1988. *Mon. Not. R. astr. Soc.*, **233** 899.

Chapter 3

Molecular Line Observations of the Core and Outflow in W75N

After the discovery of new heating sources in W75N, high resolution molecular line observations were required to investigate the detailed structure in the dense material close to the newly-formed stars, to identify the source of the known high-velocity CO outflow and to study the interactions of the outflow with the ambient cloud core material.

The observational study in the following chapter is part of a collaboration with C.M. Mountain and T. Yamashita and was partly made during PATT allocation M/M/81 and partly during time awarded on the Nobeyama 45-m telescope.

Summary

High-resolution (15 to 20 arcsec) observations of the CO outflow in W75N reveal an apparently well-collimated but complex spatial structure. The flow appears to be multi-polar with structure and degree of collimation dominated by interactions with the inhomogeneous material of the cloud core. The main red-shifted flow lobe appears to split and diverge after an interaction with a large clump of dense gas in its path. The total mass of outflowing gas is calculated as $\gtrsim 100$ $M_\odot$. The internal structure of the outflow is not that of a molecular shell around a hot, expanding bubble; molecular gas fills the flow channels. The outflow is therefore most likely to be momentum-driven by an energetic stellar wind.

CS observations of the cloud core show a large, massive condensation as found in the submillimetre continuum with mass $\simeq 2700$ $M_\odot$ and mean density $n(H_2) \simeq 2 \times 10^{11}$ m^{-3}. There are no signs of a large interstellar toroid around the outflow source, or of a significant rotation in the existing core. However, the large core mass is sufficient to provide gravitational confinement of the outflow and to cause large-scale (re-)collimation of an initially isotropic or freely expanding flow. Morphological

features in the core correspond directly to others in the multipolar CO outflow, forming channels and obstacles for the high-velocity gas.

The distribution of emission from the rare isotope $C^{18}O$ in the central region shows two massive condensations of roughly equal size and mass (350 $M_{\odot}$) within the larger CS core. One of these centres corresponds to the submillimetre continuum peak and outflow source, the other has no associated continuum source and may be at a very early evolutionary stage

3.1 Introduction

A number of molecular line studies of star forming regions have provided direct evidence of large ($\sim$ 0.1-pc), disk-like or toroidal structures of dense molecular gas and dust surrounding young bipolar outflow sources (e.g. Kaifu *et al.* 1984; Hasegawa *et al.* 1984; Torrelles *et al.* 1984; Little *et al.* 1985; Jackson, Ho & Haschick 1988). These formations are thought to have causal connections with the high velocity flows; however, the precise dynamical relationship between the apparent disks and the outflows is not known. The observed flattened structures may simply be fossil remnants of a density distribution produced by non-spherically symmetric contraction of the original cloud in the presence of rotation or anisotropic magnetic support (see Lizano & Shu 1989). In this case, the flattened core may still provide collimation for the outflow through gravitational or inertial confinement. On the other hand, collimation of the flow may occur at much smaller scales through the confining action of 'circumstellar' (as opposed to 'interstellar') material (cf the detection of an elongated circumstellar dust envelope in L1551 IRS5: Moneti *et al.* 1988 and the narrow jet originating very close to HH 34: Reipurth *et al.* 1986). There have also been strong suggestions that the outflows themselves may be generated and powered by the energy released from a rotating and contracting magnetized small-scale accretion disk (e.g. Shibata & Uchida 1986; Pudritz & Norman 1983). Such models are attractive in that they provide a mechanism for simultaneously providing a ready-collimated flow and for shedding angular momentum in the contracting protostar and disk. It is also thought that disks may prolong the mass accretion process in a new star well beyond the point at which it would otherwise be stopped after the onset of hydrogen burning (Shu, Adams & Lizano 1987).

The massive bipolar molecular outflow from W75N was mapped in the J=1–0 transition of CO by Fischer *et al.* (1985) (hereafter F85) at approximately 1-arcmin

resolution. They found high velocity material with a large and apparently lightly-collimated bipolar morphology, the blue- and red-shifted lobes overlapping by a large fraction. These observations enabled estimates of the mass, momentum and energy in the outflow and of its apparent age, but had insufficient spatial resolution to pick out a candidate source from the three compact ionisation centres resolved by Haschick *et al.* (1981).

Little data exists on the dense core surrounding the outflow source except for a low-resolution map of HCN emission by Morris *et al.* 1974. The W75N and neighbouring DR21 molecular clouds were studied in very low resolution CO observations by Dickel, Dickel & Wilson (1978) who postulated that the newly-formed sources in both clouds could be the consequence of a collision between these two large formations.

3.2 Observations

Observations of the 115 GHz J=1–0 transition of ^{12}CO, CS (J=1–0) at 49 GHz and CS (J=2–1) at 98 GHz were made with the 45m telescope of Nobeyama Radio Observatory (NRO), Japan. The two CS transitions were measured simultaneously, along with the 48-GHz C^{34}S (J=1–0) line, by directing the two linearly polarised components of the signal into separate receivers. The signal was then split into 2 high resolution (40-kHz) and 2 low resolution (250-kHz), separately-tuned, 2048-channel acousto-optical spectrometers for each required line. The CS emission was mapped on a regular 15-arcsec grid over an area of approximately 4 × 3 arcmin. The telescope beam was approximately Gaussian in profile with half-power size of 36 ± 1 arcsec at 49 GHz and 18 ± 1 arcsec at 98 GHz, and so the CS maps are over-sampled in J=1–0 and somewhat undersampled in J=2–1. The CO (J=1–0) observations were made on a 10-arcsec grid in a 2 × 2 arcmin square region around the emission peak, almost fully-sampling in the 16-arcsec beam, and on a 15-arcsec grid in the outer regions of the map.

For both CS and CO observations, the sky emission was subtracted by position-switching to an emission-free region at $20^{h}37^{m}09^{s}.8$ $+42°34'13''$ (1950). The off-position was observed once for every 3 to 4 on-source measurements. Maps were built up by rastering in Right Ascension and then repeated, scanning in Declination to minimise the possible effects of variations in calibration between scans (which might be affected by short-term variations in sky opacity etc). As a further safeguard against this problem, a reference position close to the source peak was observed at the beginning

of each 1-D scan to ensure consistent internal calibration within the maps. Absolute calibration was carried out automatically using a rotating hot load in the beam before each raster. The telescope software yielded results in the T_A^* or corrected antenna temperature scale. T_A^* is corrected for rear spillover and atmospheric losses (see Kutner & Ulich 1981 for definitions of the major temperature scales used in molecular line studies). The Shottky diode receivers employed provided single-sideband system temperatures of 600K – 1000K at 115 GHz, 500K – 700K at 49GHz and 700K – 1,000K at 98 GHz. Pointing observations were made every 1 to 2 hours by observing the nearby 80GHz SiO maser in NML Cyg.

^{13}CO and $C^{18}O$ (J=1–0) at 110 GHz were measured during January, 1987 with the NRO 45-m, employing the same observing techniques. The ^{13}CO map covered the same sampling grid observed in ^{12}CO while $C^{18}O$ was observed on a 10-arcsec grid in the central region of the cloud core. System temperatures were 500 – 550 K.

^{12}CO and ^{13}CO (J=2–1) at 230 GHz and 220 GHz and CS (J=7–6) at 343 GHz were observed during May 1988 at the James Clerk Maxwell (JCMT) 15-m telescope on Mauna Kea, Hawaii. Two separate, dual-polarisation, Schottky diode receivers were used for the 230 and 343 GHz bands. As with the NRO 45-m, position-switching was used (to the same off position), but with one sky measurement for every on-source position to compensate for the greater sky instability at higher frequencies. A single (330-kHz per channel) AOS was used to analyse the signal, giving 0.3 kms^{-1} resolution at 343 GHz and 0.4 kms^{-1} at 230 GHz. System temperatures were between 800 K and 900 K at 230 GHz, 900 K – 1,000 K at 220 GHz and 3,000 K – 5,000 K at 343 GHz. The half-power beam sizes at 230 and 343 GHz were 21 and 15 arcsec, respectively. Again the CO (J=2–1) maps followed the original ^{12}CO (J=1–0) sampling. The CS (J=7–6) line was mapped on an undersampled 10-arcsec grid in a 15-arcsec beam. Accurate pointing was maintained by observations of the peak position in W75N itself. Calibration was performed internally, observing hot and cold loads about twice per hour. A summary of the observations is shown in Table 3.1.

3.3 Results

The line profiles at the reference positions are displayed in Figs 3.1 (CS), 3.2 (CO, ^{13}CO, $C^{18}O$ J=1–0) and Fig. 3.3 (CO, ^{13}CO J=2–1). These profiles are the results of averaging the flux reference taken during each raster scan. Except for ^{12}CO (J=1–0),

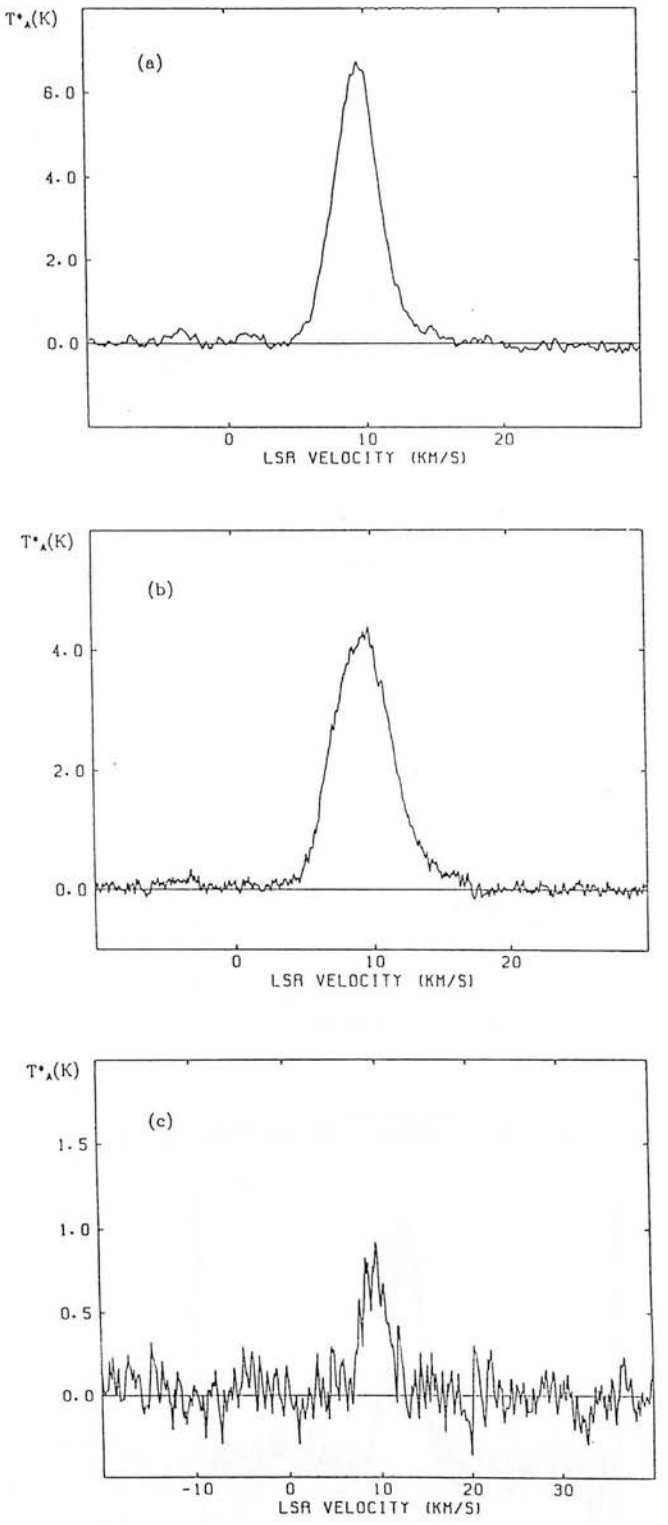

Figure 3.1: (a) CS (J=1–0), (b) CS (J=2–1) and (c) $C^{34}S$ (J=1–0) line profiles at the central map position. The total on-source integration time was 11 minutes for the CS lines, 9 minutes for the $C^{34}S$ line.

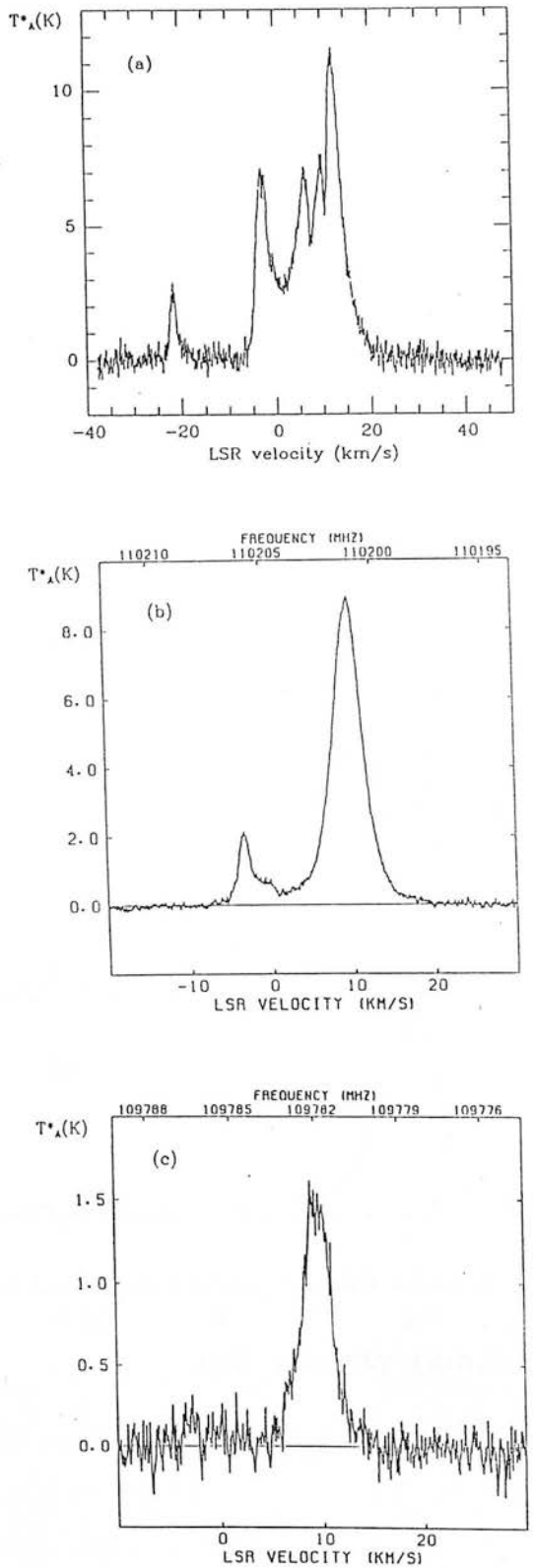

Figure 3.2: (a) ^{12}CO, (b) ^{13}CO and (c) $C^{18}O$ (J=1–0) spectra. The ^{12}CO reference position was at offset (–39, +3) arcsec from the map centre. Total on-source integration times: 11 minutes (^{12}CO), 23 minutes (^{13}CO) and 5 minutes ($C^{18}O$).

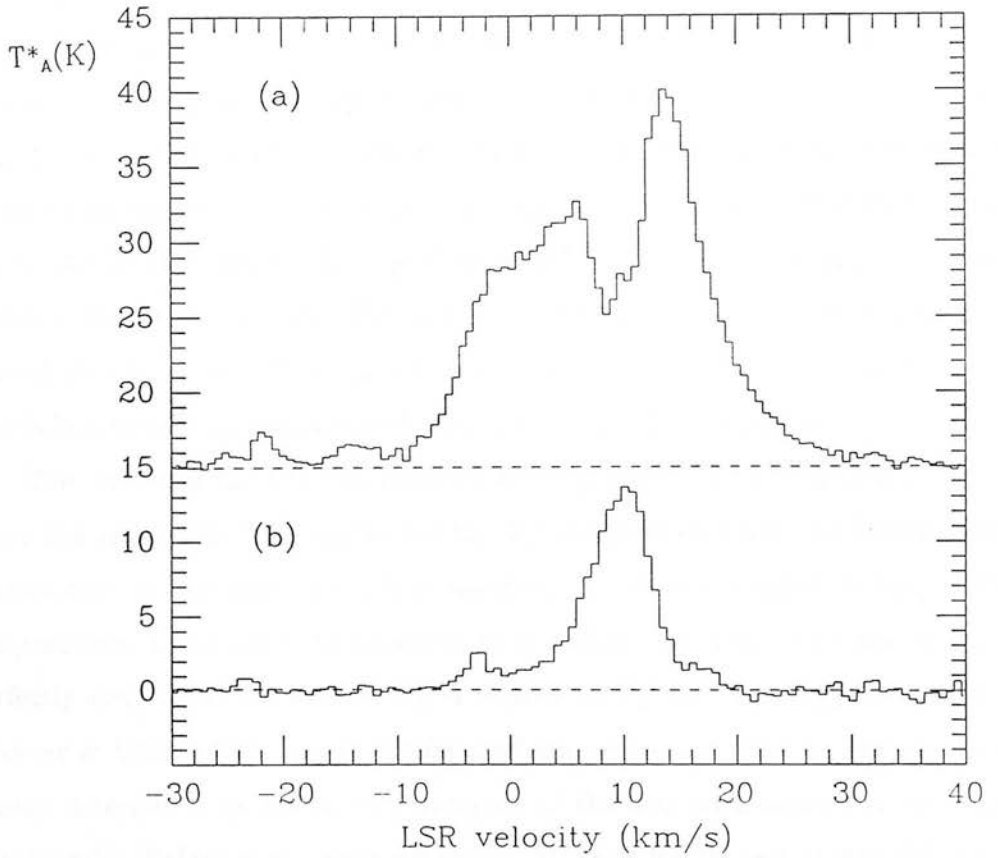

Figure 3.3: (a) ^{12}COand (b) ^{13}CO (J=2–1) spectra at the central reference position. Total on-source integration time: 7 minutes.

which was at offset (−39, +3), all reference positions were at the map centre. The number of co-adds and hence the resulting noise levels varies in these spectra. $C^{34}S$ (J=1–0) was only detected at the central reference position after coadding 27 20-s scans.

All the maps presented in this chapter have offset centre: $20^h36^m50^s.0$ $+42°27'01''$ (1950), which is close to the position of the compact HII region and OH maser source HII(B) (see Chapter 2). Spectra are given in terms of velocity with respect to the local standard of rest (V_{LSR}). The cloud core of W75N has a velocity of approximately +9.5 kms^{-1} in this frame of reference. A linear baseline has been subtracted from each spectrum before inclusion in the maps.

Figs 3.4 and 3.5 contain the integrated CS (J=1–0) and (J=2–1) maps, respectively, while Figs 3.6 and 3.7 show the velocity-channel maps obtained in these transitions and display the velocity structure in the cloud core. In order to compare the J=2–1 and J=1–0 results the effective resolution of the former was degraded to 36 arcsec by averaging, with Gaussian weighting, each point over neighbouring pixels to match the 49 GHz beam. A map of the ratio of integrated line brightness temperatures is shown in Fig. 3.8. Fig. 3.9 is the integrated CS (J=7–6) emission in the central 50 × 50 arcsec. The signal-to-noise ratio of the CS(J=7–6) observations were insufficient to provide useful velocity information in this transition.

The results of the CO observations are displayed in Figs 3.10 to 3.17. All maps and spectra in this chapter use the T_A^* temperature scale. To derive telescope-independent source parameters it is necessary to know the intrinsic line brightness temperatures T_b as would be observed by a perfect telescope above the atmosphere, perfectly coupled to the source. T_b is related to T_A^* via $T_b = T_R^*/\eta_c = T_A^*/(\eta_{fss}\eta_c)$ (Kutner & Ulich 1982). η_{fss} is the forward scattering and spillover efficiency (and is mainly determined by the surface accuracy of the dish with respect to the observed wavelength). Values of η_{fss} were 0.8 (for JCMT at 230GHz and at 343 GHz) 0.7 (for the 45-m at 49 GHz) and 0.4 (for the 45-m at 98 and 115 GHz). The source coupling efficiency η_c remains close to unity for source sizes comparable to or larger than the beam and, since this is the case in most of the present data, it is assumed that $\eta_c = 1$. This assumption will be most inaccurate at high velocities in the CO outflow and will result in under-estimates of T_b. The rms pointing uncertainty was determined to be $\lesssim 5$ arcsec at both telescopes throughout the observations.

Table 3.1: Observations summary

Line	GHz	date	telescope	beam	η_{fss}
^{12}CO (J=1–0)	115.271	1986 May	NRO	16″	0.4
^{12}CO (J=2–1)	230.538	1988 May	JCMT	23″	0.8
^{13}CO (J=1–0)	110.201	1987 Jan	NRO	16″	0.4
^{13}CO (J=2–1)	220.399	1988 May	JCMT	23″	0.8
C^{18}O (J=1–0)	109.782	1987 Jan	NRO	16″	0.4
CS (J=1–0)	48.991	1986 May	NRO	36″	0.7
CS (J=2–1)	98.981	1986 May	NRO	18″	0.4
C^{34}S (J=1–0)	48.207	1986 May	NRO	36″	0.7

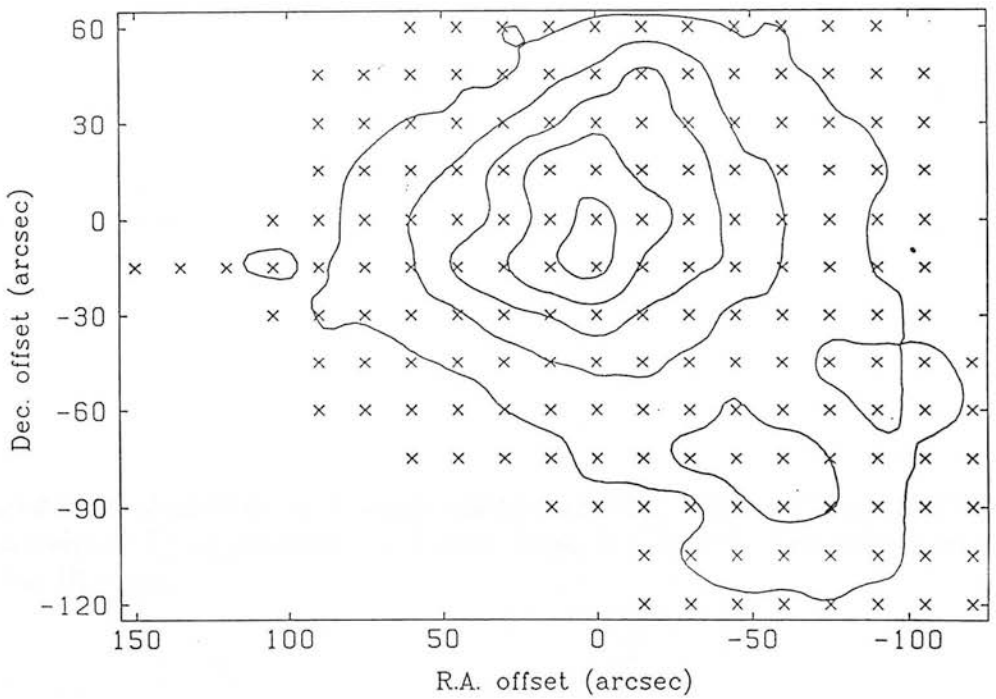

Figure 3.4: CS (J=1–0) emission integrated between V_{LSR} = 5 and 13 kms^{-1}. Contours are in units of T_A^* at intervals of 5 K.kms^{-1}from 5 K.kms^{-1}. The half-power beam size for this line was 36 arcsec. The observed points are marked.

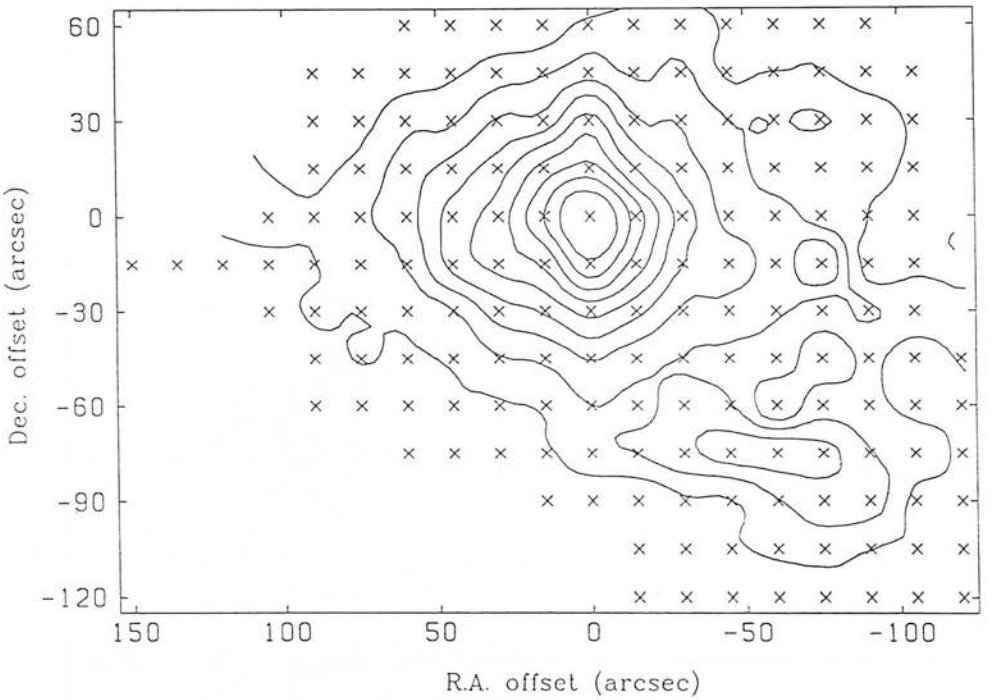

Figure 3.5: CS (J=2–1) emission integrated between V_{LSR} = 5 and 13 kms^{-1}. Contours are in units of T_A^* at intervals of 2 K.$kms^{-1}$from 3 K.kms^{-1}. The half-power beam size was 18 arcsec.

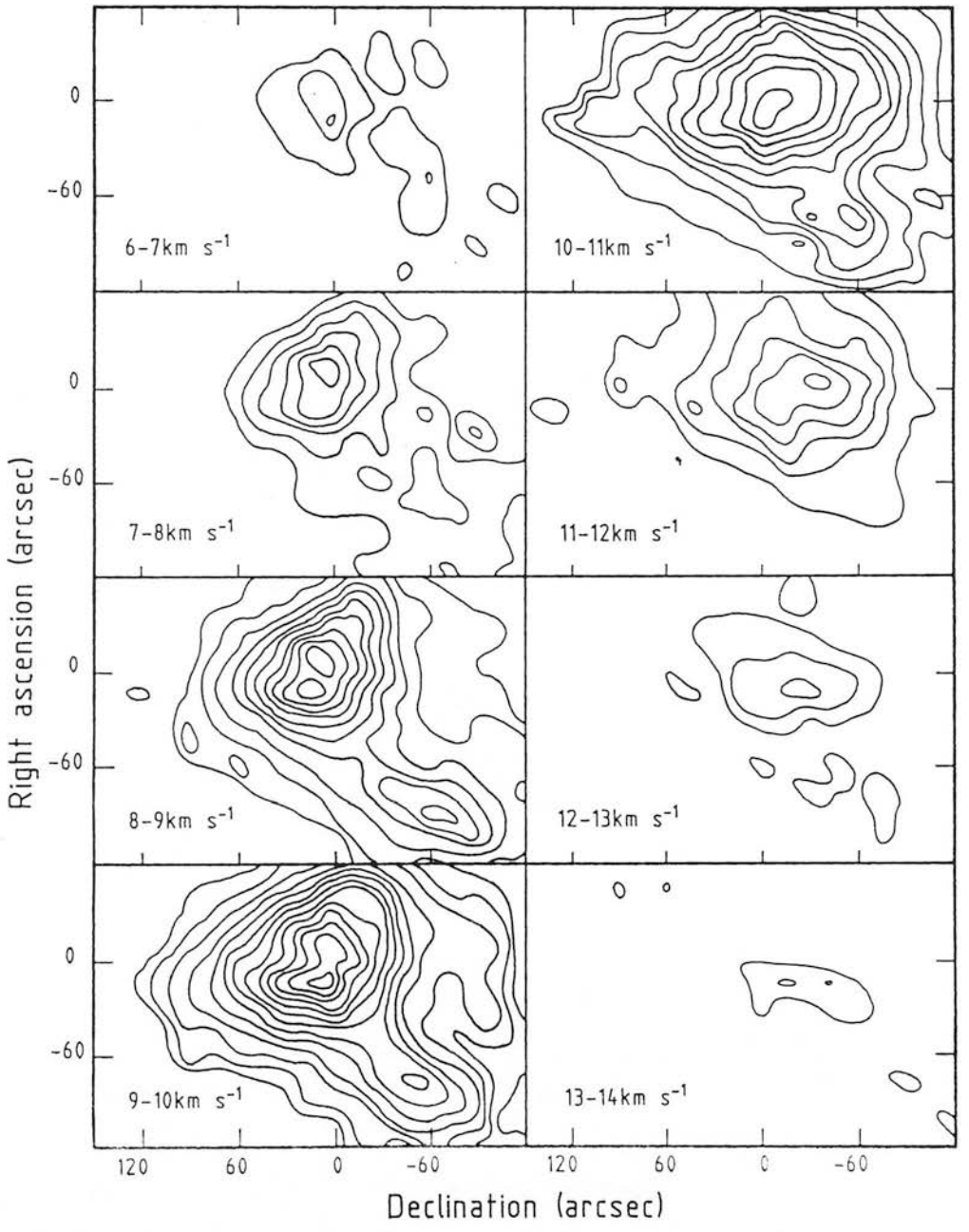

Figure 3.6: Velocity-channel maps in CS (J=1–0) emission. The velocity interval is 1 kms^{-1} from V_{LSR} = 6 – 7 $kms^{-1}$to V_{LSR} = 13 – 14 kms^{-1}. Contours are in units of T_A^*at intervals of 0.5 $K.kms^{-1}$ from 0.5 $K.kms^{-1}$.

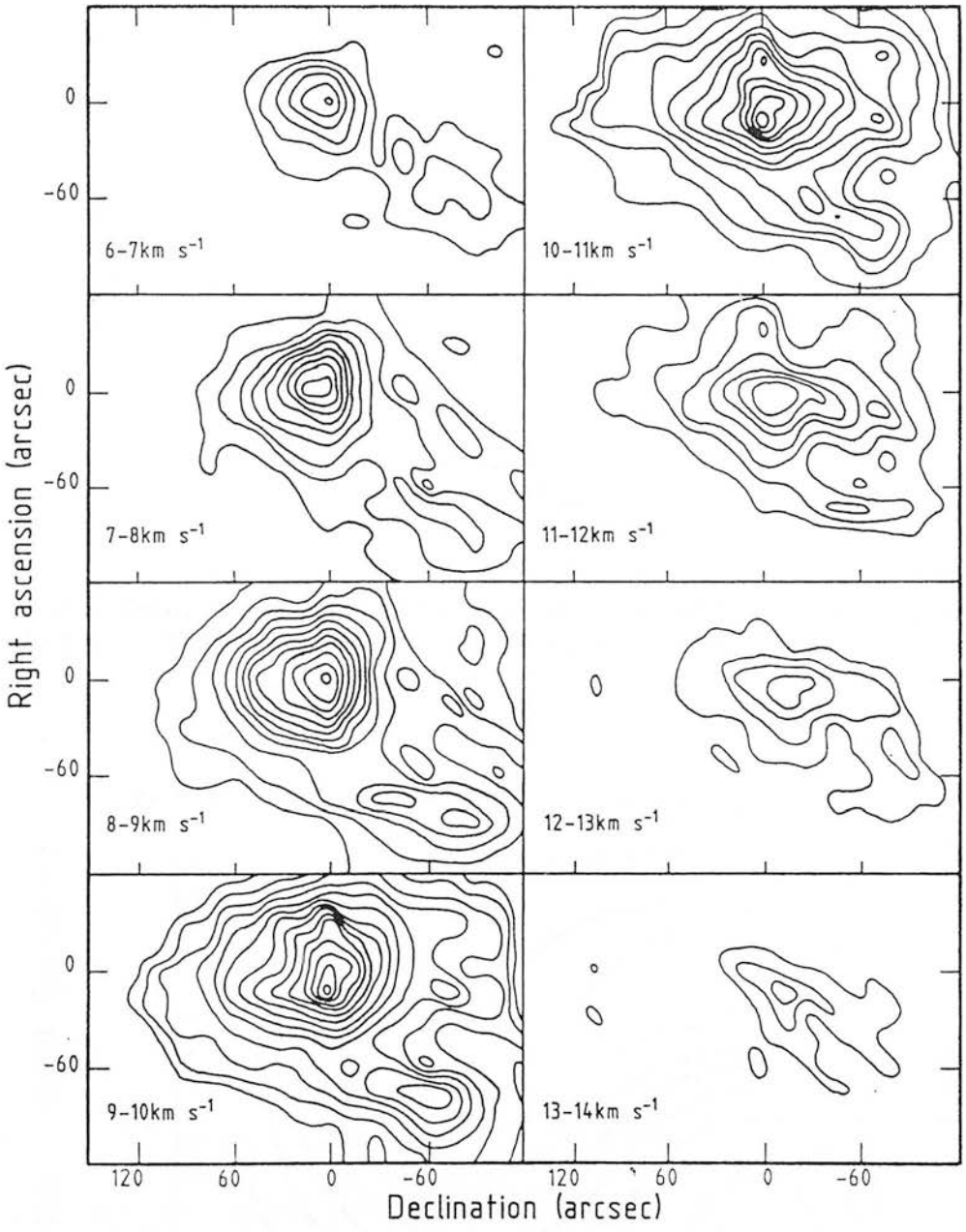

Figure 3.7: Velocity-channel maps in CS (J=2–1) emission. The velocity interval is 1 kms^{-1} from V_{LSR} = 6 – 7 $kms^{-1}$to V_{LSR} = 13 – 14 kms^{-1}. Contours are in units of T_A^*at intervals of 0.3 $K.kms^{-1}$ from 0.3 $K.kms^{-1}$.

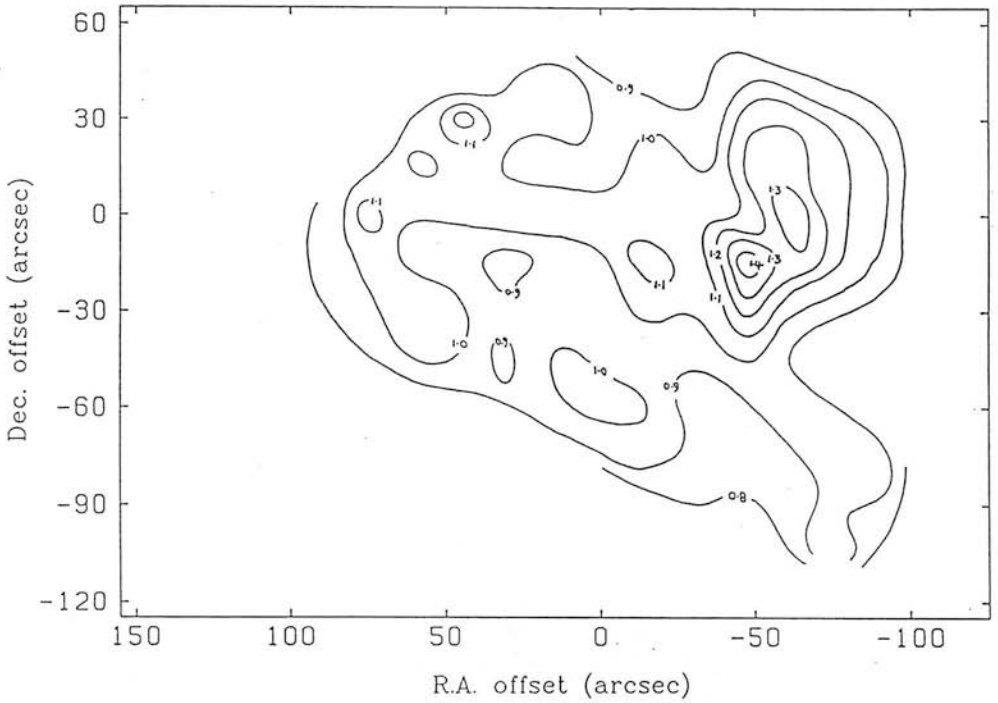

Figure 3.8: Spatial distribution of the ratio of integrated brightness temperatures $\int T_b(J=2\text{–}1) \div \int T_b(J=1\text{–}0)$. Contours are at intervals of 0.1 from 0.8.

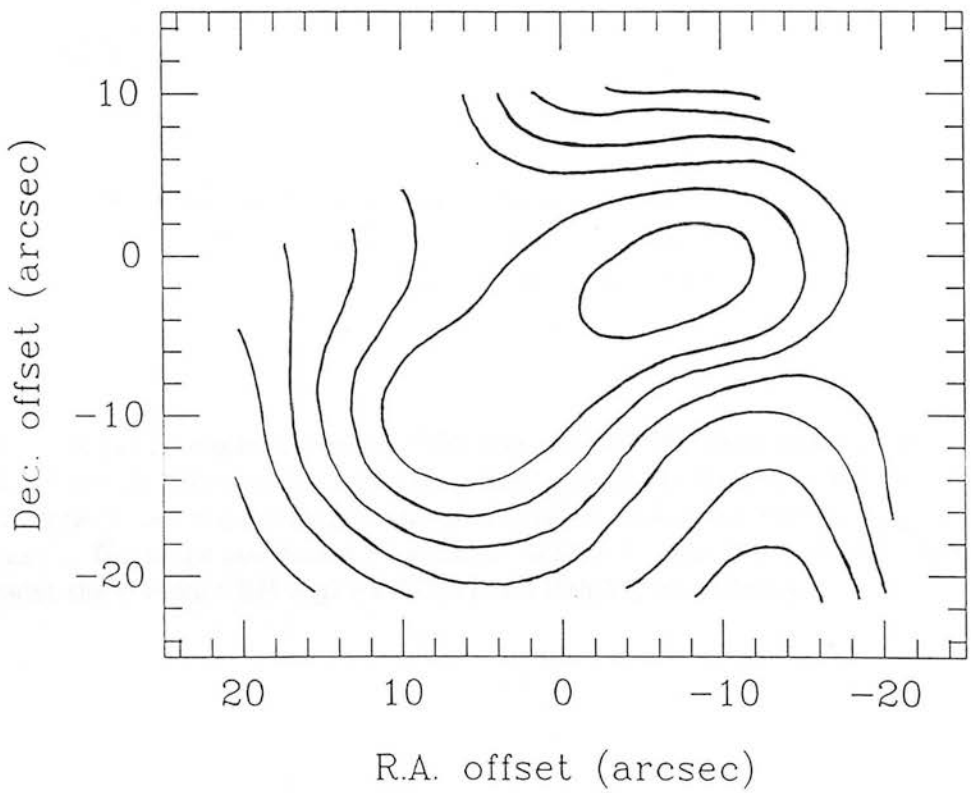

Figure 3.9: Map of the integrated CS (J=7–6) emission in the central area. Contours are in units of T_A^*, at intervals of 5 K.kms^{-1} from zero.

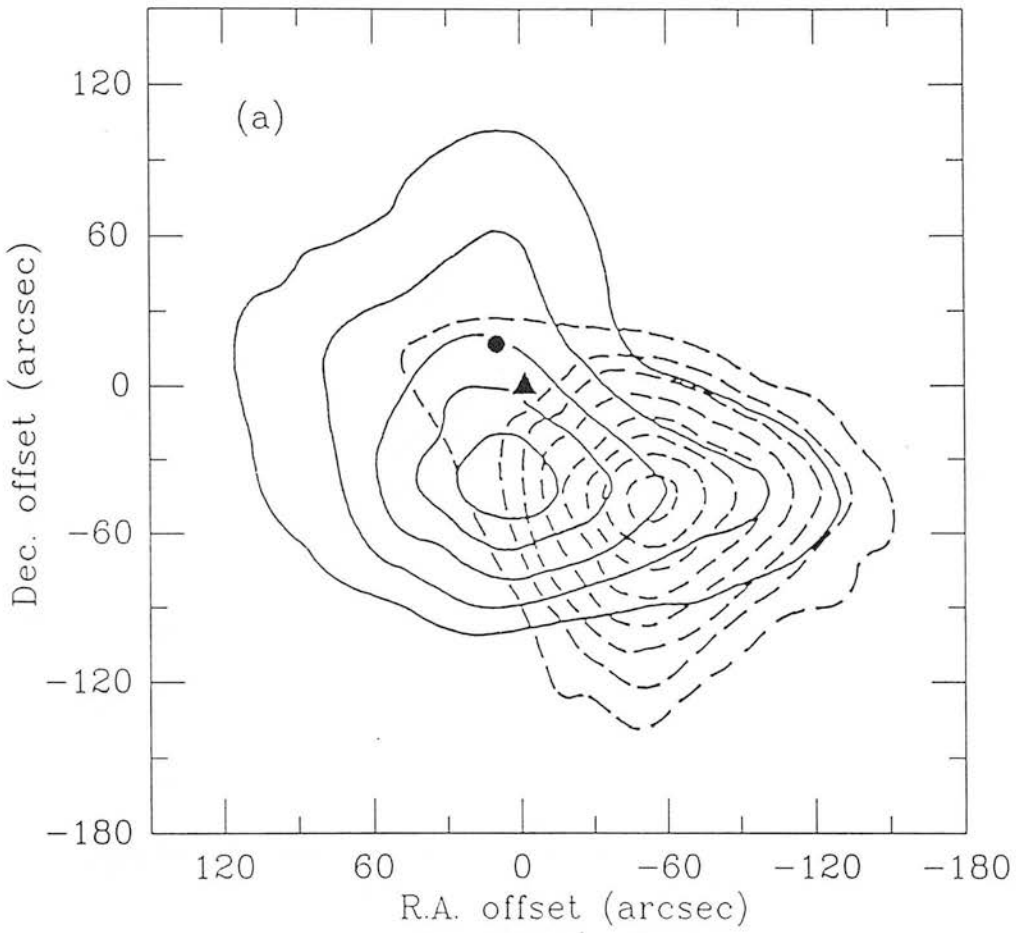

Figure 3.10: (a) 1-arcmin resolution ^{12}CO map of the W75N outflow from Fischer *et al.* (1985) (F85) The blue-shifted emission (solid contours) is integrated between V_{LSR} = 1 and 5 kms^{-1} and the red-shifted emission (broken contours) between V_{LSR} = 17 and 20 kms^{-1}. Contours are drawn at 3,4,5,.... K.kms^{-1}. The filled triangle and circle represent the compact HII regions HII(B) and HII(A), respectively.

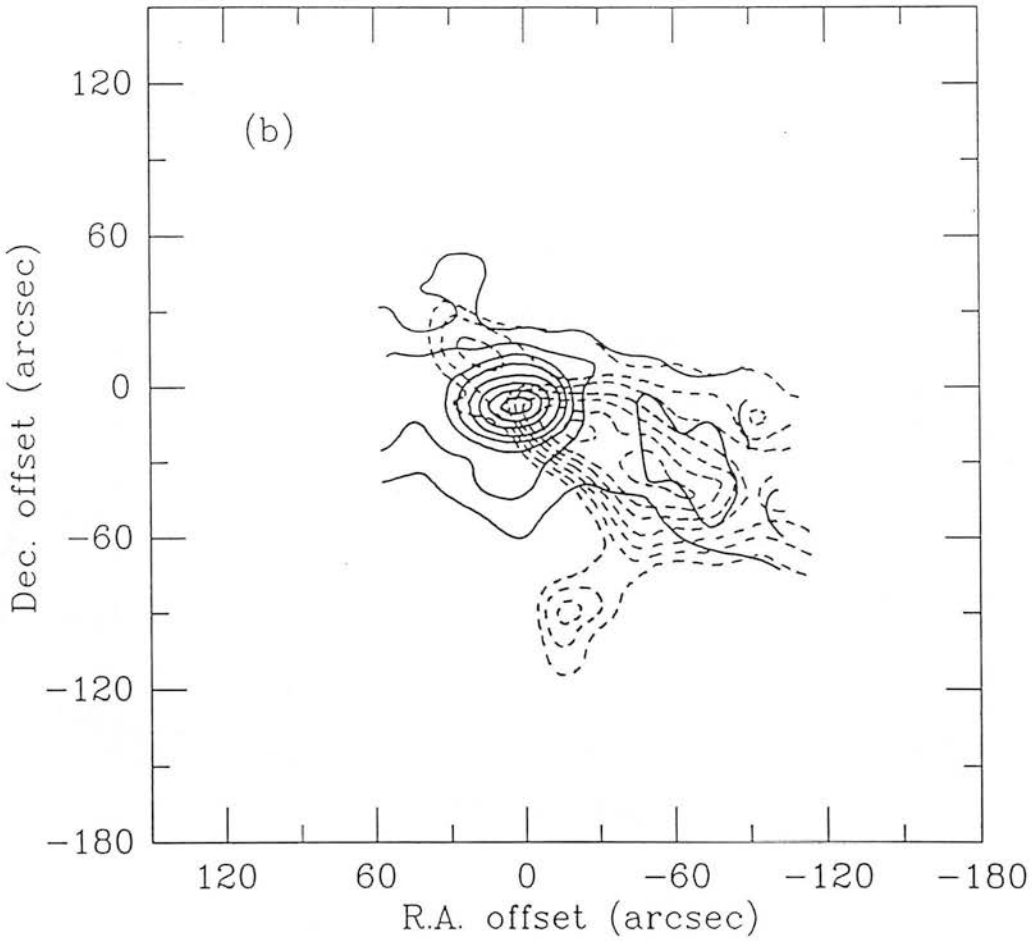

Figure 3.10: (b) 15-arcsec resolution ^{12}CO map from the present data. The integration limits are the same as for (a). Contours are at 2,4,6,.... K.kms^{-1}(blue) and 2,3,4,..... K.kms^{-1}(red).

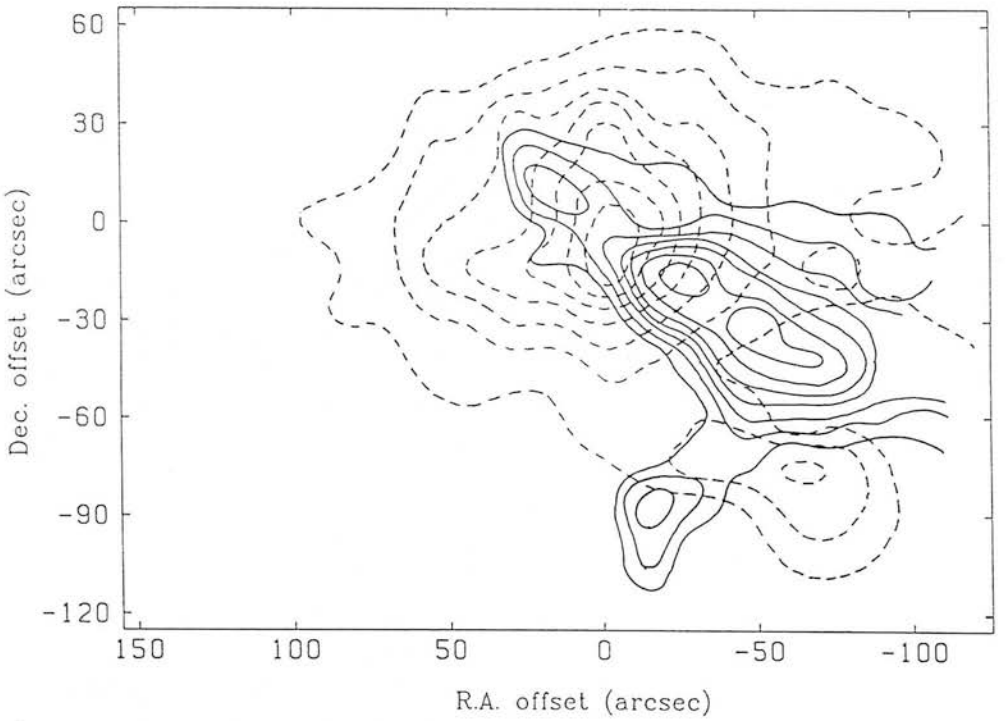

Figure 3.11: CS (J=2–1) emission from V_{LSR} = 9 to 10 kms^{-1} (cloud rest velocity; dashed contours) superimposed on red-shifted ^{12}CO contours (solid; as in Fig. 3.10) to display the corresponding physical features in the outflow and dense core.

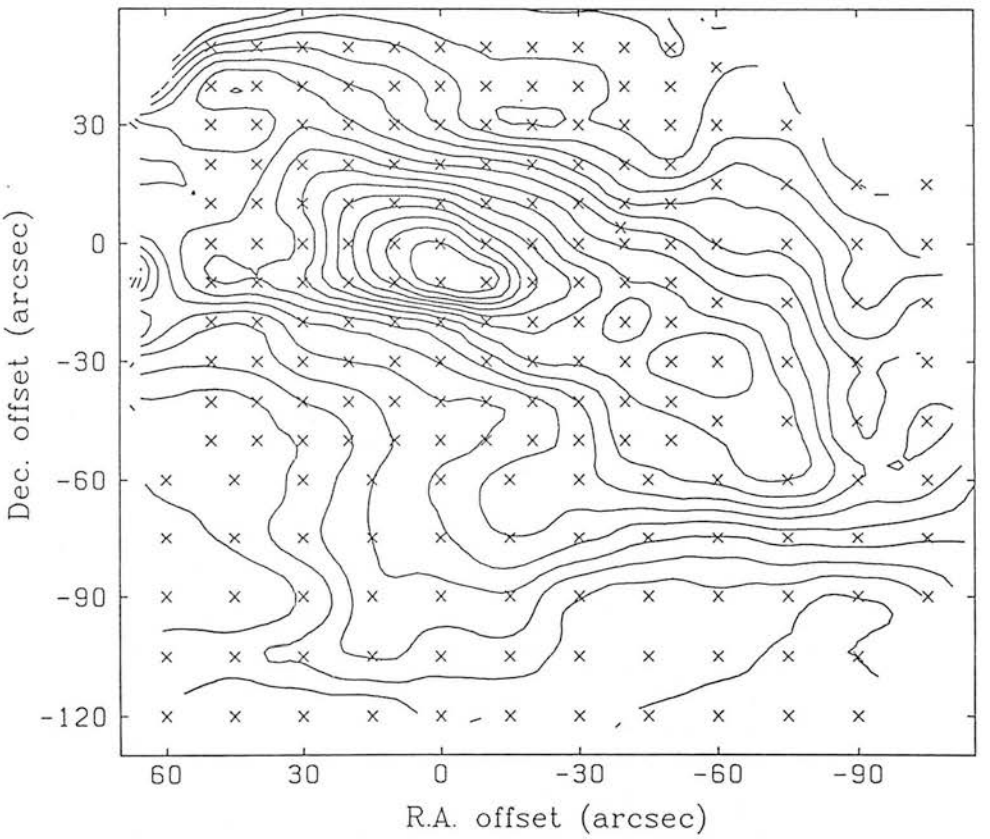

Figure 3.12: Total integrated ^{12}CO (J=1–0) emission ($V_{LSR} = 2 - 30$ kms^{-1}). Contours are at intervals of 5 K.kms^{-1}from 30. The half-power beam size for ^{12}CO (J=1–0) was 16 arcsec.

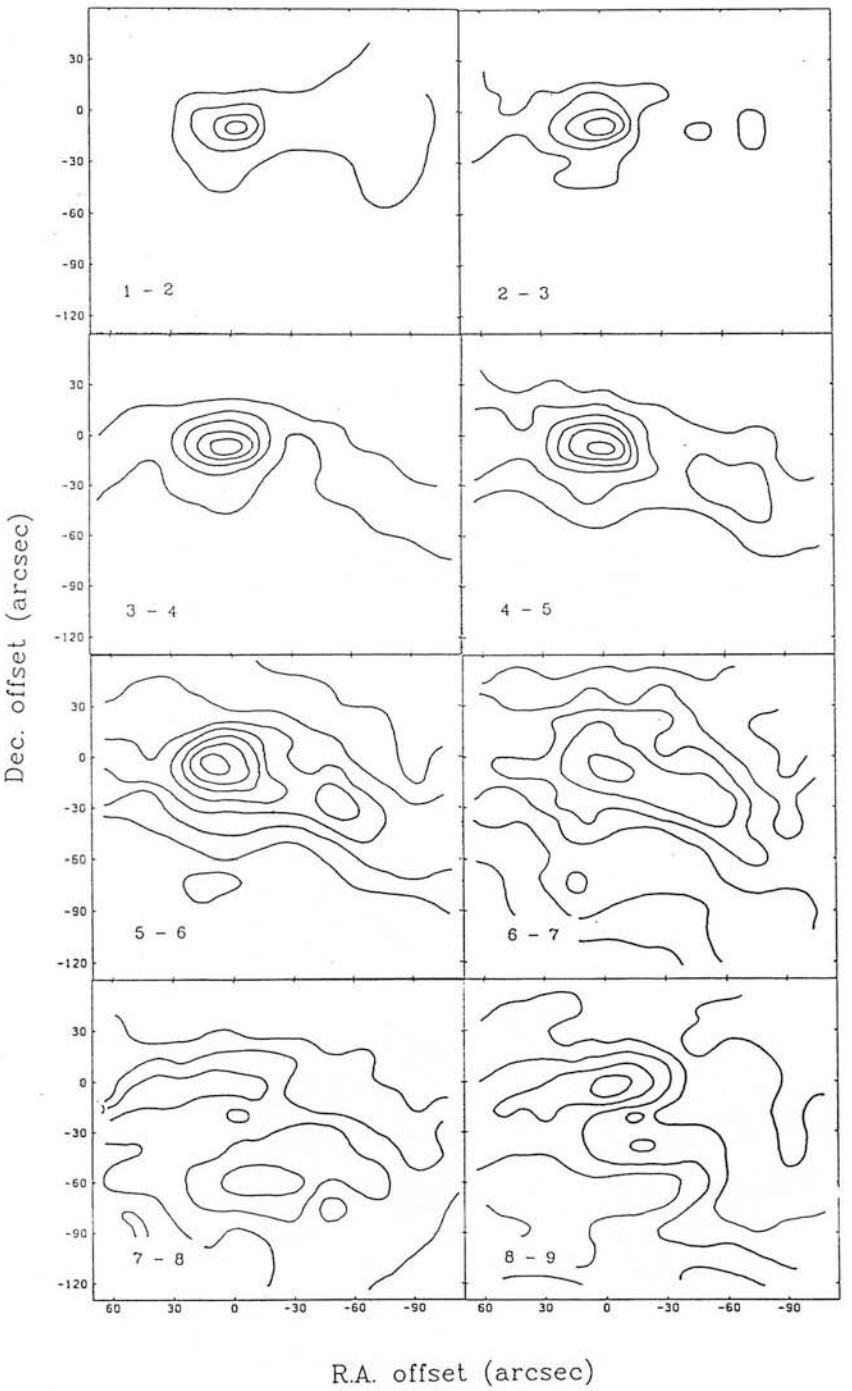

Figure 3.13: ^{12}CO (J=1–0) velocity-channel maps. (a) Channels of width 1 kms^{-1} from V_{LSR} = 1 to 9 kms^{-1}. Contours are drawn at intervals of 1K from 1K, except for the 7 – 8 kms^{-1} and 8 – 9 kms^{-1} maps, where the base is 3K.

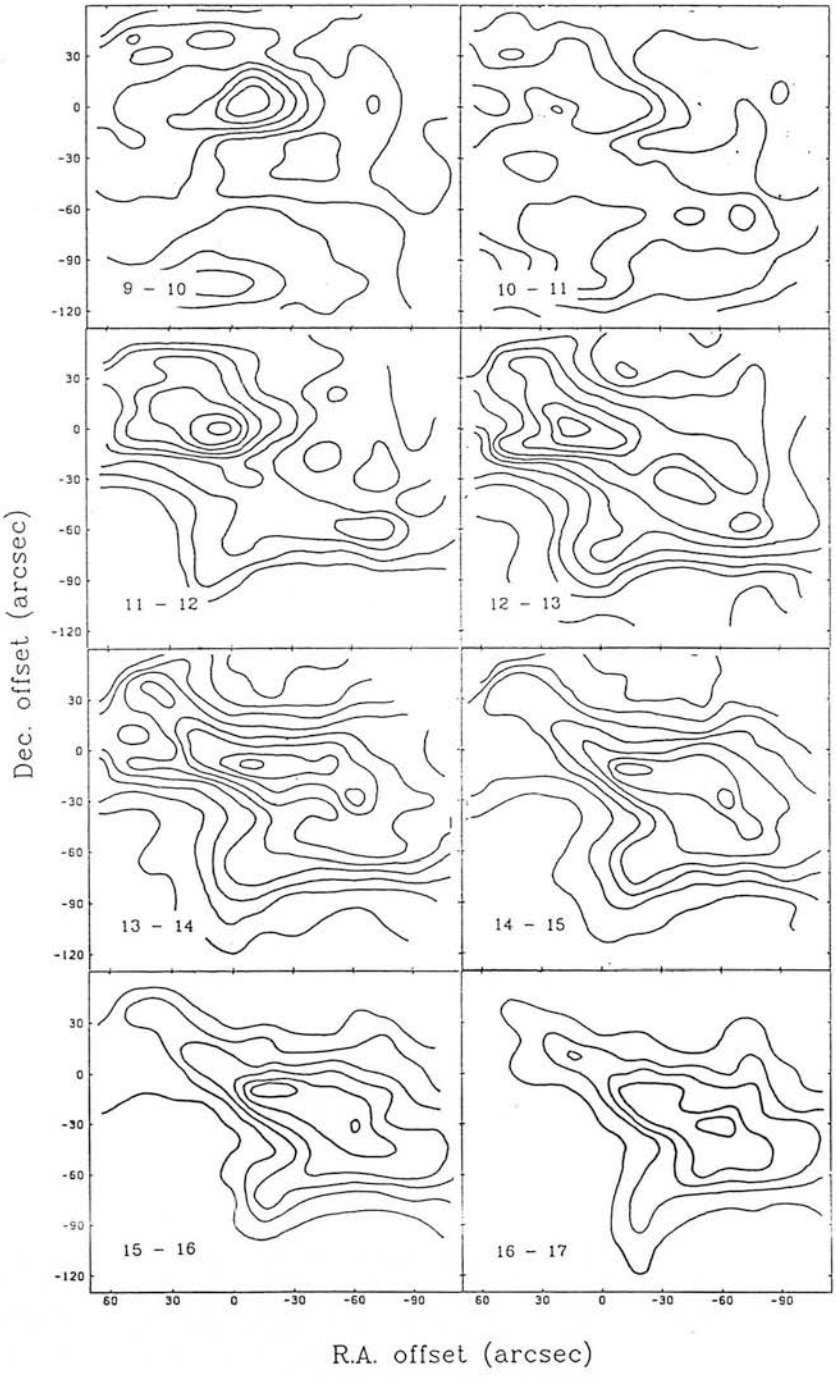

Figure 3.13: ^{12}CO (J=1–0) velocity-channel maps. (b) From V_{LSR} = 9 to 17 kms^{-1}. Contours are as in (a) except for the channels at 9 – 10, 10 – 11, and 11 – 12 kms^{-1}, where the base is 4K.

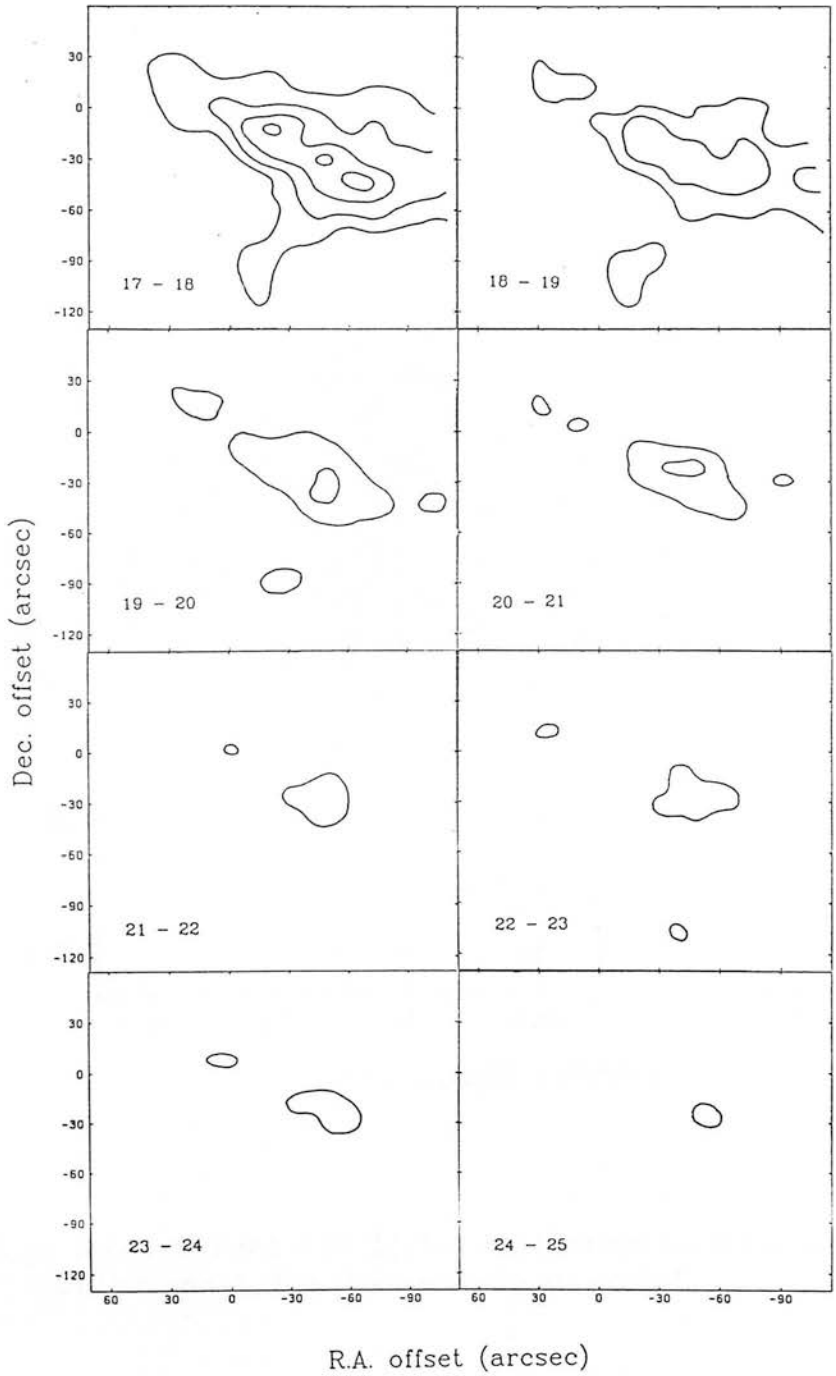

Figure 3.13: ^{12}CO (J=1–0) velocity-channel maps. (c) V_{LSR} = 17 to 25 kms^{-1}. Contours as in (a).

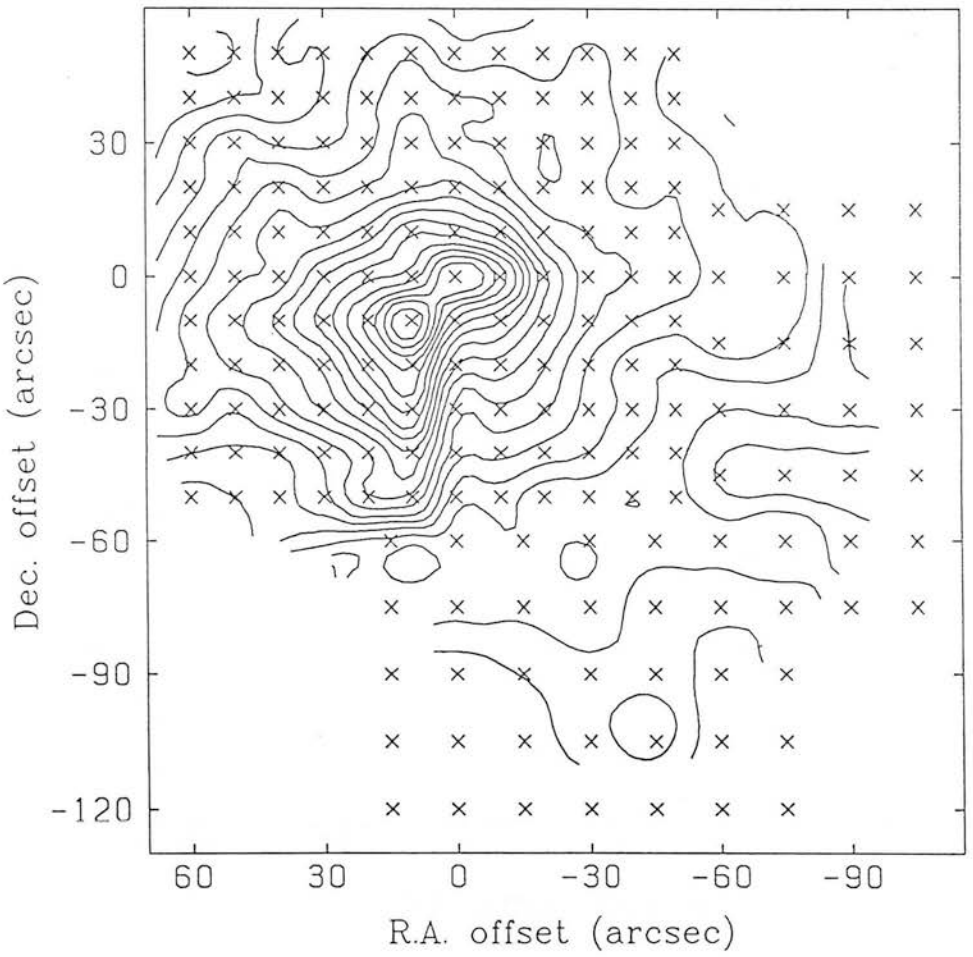

Figure 3.14: Total integrated ^{13}CO T_A^*(J=1–0). Contours are drawn at intervals of 2 K.kms^{-1} from 10 K.kms^{-1}. The observed points are marked.

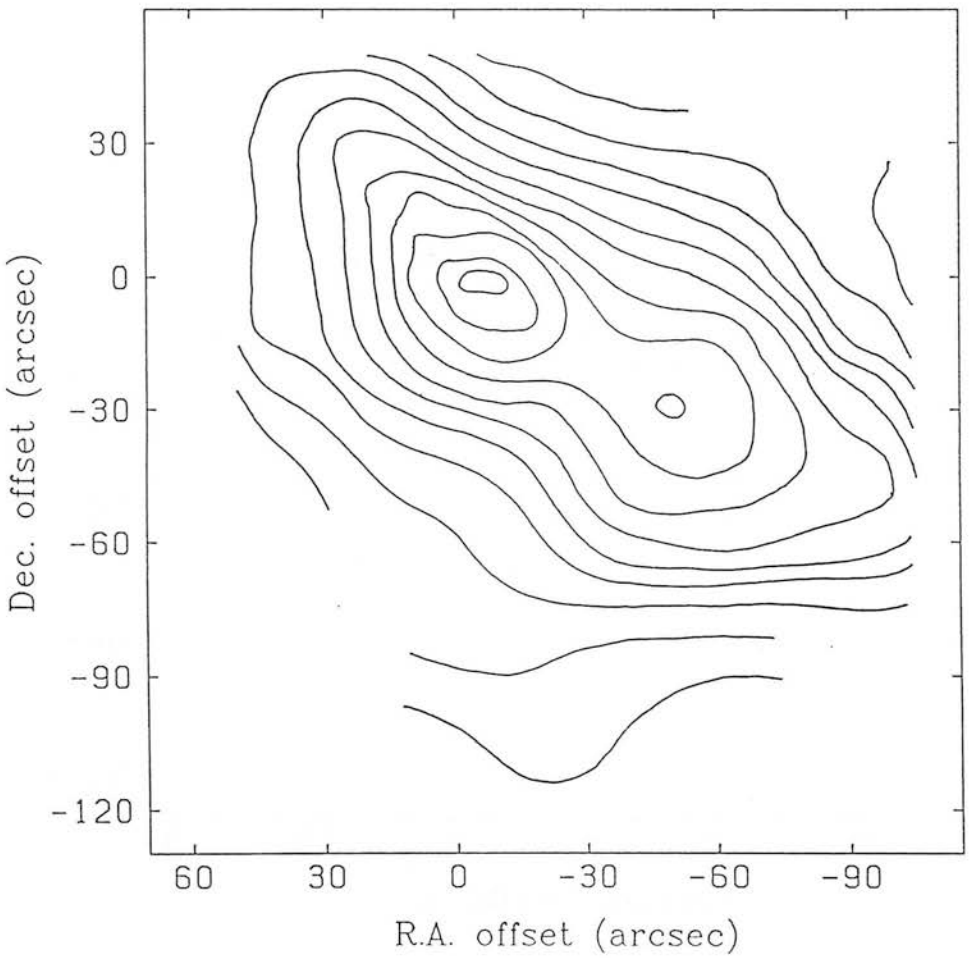

Figure 3.15: Total integrated ^{12}CO $T_A^*(J=2-1)$. Contours are at intervals of 20 K.kms^{-1} from 80 K.kms^{-1}. The half-power beam size for this line was 23 arcsec.

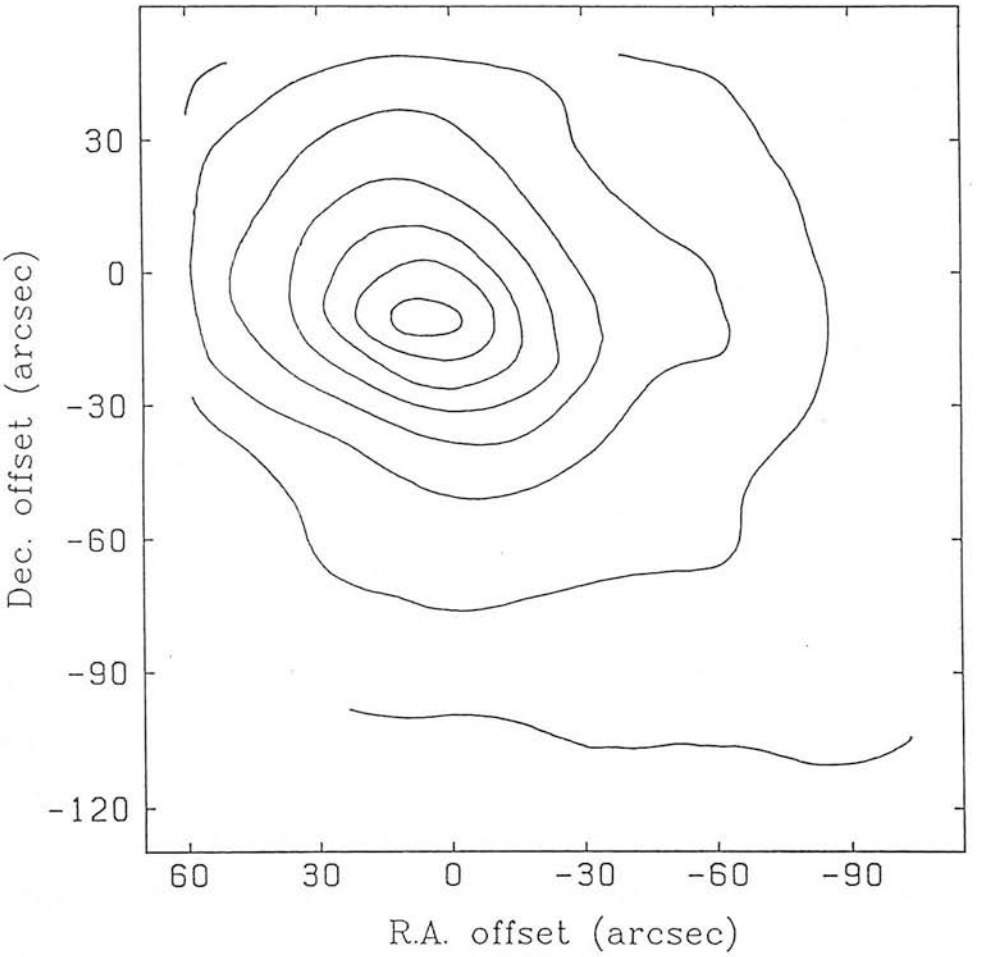

Figure 3.16: Total integrated ^{13}CO $T_A^*(J=2-1)$. Contours are at intervals of 10 K.kms^{-1} from 20 K.kms^{-1}.

3.4 Discussion

3.4.1 CS Morphology

The cloud core of W75N, as traced by CS line emission is relatively large, with respect to other similar sources. The observed half-power size of the main core is approximately 70 arcsec in both RA and Dec (Figs 3.4 & 3.5), which is subtended by 0.7 pc at the accepted distance of 2kpc (Dickel, Dickel & Wilson 1978). This indicates that densities high enough to excite significant quantities of CS to the lower J states ($n(H_2) \gtrsim 2\times10^{11}$ m^{-3}) persist over a large area, instead of being localised around individual objects.

The most notable feature in the CS maps, apart from the main core, is a large, virtually independent condensation towards the southwest. This clump is almost coincident with a spur or secondary flow branching from the main red-shifted lobe of the CO outflow (Fig. 3.11) and there may be a causal relationship between these unusual features. The southwestern clump also appears to form the southern limb of a sheath of dense material around the main red flow. It may thus consist of material separated from the main cloud core and piled up by the impacting high velocity gas. The northern limb of the sheath is less prominent but can be recognised in the velocity-channel map at the cloud rest velocity (Fig. 3.7). The main core component peaks very close to the position of the OH maser source HII(B) which is also the likely origin of the CO outflow (Fig. 3.10).

In the velocity channel maps shown in Fig. 3.6 and 3.7 the emission at the local cloud velocity (9–10 kms^{-1}) clearly resembles the integrated emission maps of Figs 3.4 & 3.5. Local enhancements appear either side of the main CO flow channel to the southwest of the peak and, in the J=2–1 map, to the northeast where a second localised red-shifted outflow component is located. The J=2–1 emission shows up physical features with more clarity than the J=1–0 due to a combination of higher spatial resolution and a higher critical density for the former transition which thus tends to trace denser material. At slightly blue-shifted velocities (7–8 kms^{-1}) the emission in the southwest becomes more uniform across the outflow channel and suggests the front surface of an expanding cone-like structure of dense gas around the outflow.

The velocity dispersion of the CS-traced material is rather small, and little emission appears outside ±3 kms^{-1} from the cloud rest velocity. However, at red-shifted velocities outside this range, low-level emission was detected within the southwestern outflow channel (Figs 3.6, 3.7), indicating the presence of a small amount of dense

material moving in the main red flow lobe. At about +2 kms^{-1} from the cloud rest velocity, the CS emission peak begins to shift to the southwest, towards the main red-shifted outflow channel. The emission tends to follow the walls of the channel at first, leaving a void in the centre and mirroring the pattern of the low-velocity CO in the same region. As the relative velocity increases, the emission shifts towards the centre of the channel. This pattern very clearly represents the acceleration of dense material ablated from the walls of a cavity by the low-density, high-velocity gas of the outflow. The fastest gas, located in midstream, emits rather weakly and has probably been disrupted during the acceleration process, leaving a lower proportion of dense gas able to produce significant CS emission.

As with the CO flow morphology, all the blue-shifted dense material traced by CS appears localised around the source position, indicating a trajectory close to the line of sight. At 8–9 kms^{-1} the southwestern clump appears as two separate components. This gives the appearance that the condensation is somewhat disrupted and in the process of breaking up but this is unlikely to be happening (see §3.4.6) and this morphology is more probably due to a line opacity effect, especially since it occurs close to the line centre velocity.

There is no sign, in the CS velocity-channel maps (Figs 3.6 & 3.7), of any systematic spatial shift that might indicate significant rotation of the core. A shallow northwest-southeast gradient in the larger-scale W75 cloud was identified by Dickel, Dickel & Wilson (1978), but the variation from this gradient over the area covered by the current observations would be significantly less than 1 kms^{-1}. There is no evidence, either in the shape of the core or in the velocity structure, for any large disk or toroid formations such as are often associated with CO outflows (e.g. L1551: Kaifu *et al.* 1984, GGD 27: Yamashita *et al.* 1989, G35.2N: Little *et al.* 1985). It is becoming apparent that such large structures may have little to do with the formation or collimation of molecular outflows and that very high degrees of flow collimation can be achieved where no large disk is present (e.g. in NGC 2071: Snell *et al.* 1984; NGC 2024: Richer *et al.* 1989). The large, flattened and often rotating structures that have been observed are more likely to be passive vestiges of the early density distribution in the cloud and/or the results of ablation by an already collimated flow. If disks do play an active rôle in outflow collimation or even formation, then they are likely to do so on the scale of the circumstellar structures around young low-mass stars (the existence of which is supported by indirect evidence: e.g. Moneti *et al.* 1988, Grasdalen *et al.* 1984,

Beckwith *et al.* 1984, 1989), and of the very narrow, optically visible jets originating very close to similar (but especially low-mass) objects (e.g. Reipurth *et al.* 1986).

3.4.2 CS Radiative Transfer Analysis

Throughout this chapter, the main analysis of of the molecular line data is done using the assumption of local thermodynamic equilibrium (LTE) in which the rotational levels of the molecule are taken to be thermalised, i.e. populated according to the Boltzmann distribution. In the case of CS, comparative reference is made to approximate results predicted by existing models of radiative transfer through a large velocity gradient (LVG) (i.e. Linke & Goldsmith 1980), although there is evidence that LVG modelling may be inappropriate where velocity dispersions in the dense gas are less than $\sim 10 - 15$ kms^{-1}pc^{-1} (Irvine, Goldsmith & Hjalmarson 1987: hereafter, IGH), which is considerably larger than that indicated by the CS line widths in W75N (Fig. 3.1). Further, it appears from the observations that the transitions in the dominant isotope are significantly optically thick and hence that the LVG assumptions are not valid over much of the line (see below).

The large electric dipole moment of the CS molecule which makes it an excellent probe of high density gas (with critical densities of 2×10^{10} m^{-3} and above) also means that the rotational levels may be sub-thermally populated over significant regions of a source. However, the mean densities in the W75N core, suggested by analysis of the submillimetre continuum emission (Chapter 4), are above the J=2–1 critical density (2×10^{11} m^{-3}). The inaccuracies involved, and the differing estimates obtained through LVG modelling, are in any case overwhelmed by the large uncertainty in the relative abundance of the molecule ($n(\mathrm{CS})/n(\mathrm{H_2}) = X(\mathrm{CS})$). Garden (1986), in a study of the DR21 cloud and outflow, finds largely similar predictions of the physical parameters from LTE and LVG models, but it is clear that DR21 is a considerably more energetic outflow source than W75N and the velocity gradients in the cloud core may be appropriately large for LVG models to apply.

The detection of the isotopic line of C^{34}S (J=1–0) at the central position (corresponding to the maser source HII(B)) allows an estimate of the optical depth in the main isotopic line. If the two species are assumed to have the same excitation temperature,

$$\frac{T_A^*(\mathrm{CS})}{T_A^*(\mathrm{C^{34}S})} = \frac{1 - e^{-\tau_{\mathrm{CS}}}}{1 - e^{-\tau_{\mathrm{C^{34}S}}}} = \frac{1 - e^{-R\tau_{\mathrm{C^{34}S}}}}{1 - e^{\tau_{\mathrm{C^{34}S}}}} \tag{3.1}$$

where $R = \tau_{CS}/\tau_{C^{34}S}$ is equal to the relative isotopic abundance of the $C^{34}S$ species. If R is very large compared to the observed line ratio, as is usually the case with CO and ^{13}CO, then its assumed value does not significantly affect the calculated value of τ. However, in W75N the peak line ratio, 10 ± 3, and the integrated line ratio, 9.7 ± 0.3, are comparable to the expected isotopic abundance (the solar system value is $R \simeq 23$) and the assumed value of R becomes important. Using the above relation and $R = 23$, the predicted value of the J=1–0 line-centre optical depth at the central source position is $\tau(\text{CS } 1\text{–}0) = 2.2 \pm 0.9$.

If we know the excitation temperature (T_{ex}) of the line emission, it is possible to investigate the optical depth from the ratio of $T_A^*(2\text{–}1)$ to $T_A^*(1\text{–}0)$, even though the present data introduce extra problems related to the different beam sizes for the two transitions. After convolving the map of integrated J=2–1 emission to an effective resolution of 36 arcsec and taking account of the differing antenna efficiencies at the two frequencies, the peak brightness temperature ratio $T_b(2\text{–}1)/T_b(1\text{–}0)$ is 1.0 ± 0.2 at the central position. Taking $T_{ex}(2\text{–}1) = T_{ex}(1\text{–}0) = T_{dust} = 29$K from Chapter 4, the optical depth ratio $\tau(2-1)/\tau(1-0)$ is predicted to be 3.5, since

$$\frac{\tau_{21}}{\tau_{10}} = 2\frac{(1 - e^{-h\nu_{21}/kT_{ex}})}{(e^{h\nu_{10}/kT_{ex}} - 1)} \tag{3.2}$$

(see Appendix A) which represents the optically thin limit to the brightness temperature ratio and otherwise tends to unity with increasing optical depth. Then by applying Eqn. 3.1 with $R = 3.5$ and $\tau_{C^{34}S}$ substituted by τ_{10}, the predicted line temperature ratio is 1.1, in agreement with that observed. However, in parts of Fig. 3.8, the T_b ratio falls below unity even though the lines are strongly detected. This may be a sign that a line-of-sight temperature gradient in the internally-heated cloud is affecting the relative line strengths and distorting the line ratio (see Cantó *et al.* 1987). In fact the optical depth in the J=1–0 line is well within the range of values (1–3) most sensitive to such distortions.

Having obtained a value for the line optical depth, a preliminary calculation of the mass of the dense, CS-traced cloud core can be made by considering the integrated emission from the entire source. From Appendix A, the beam-averaged CS column density at each point is estimated from the J=1–0 antenna temperatures as follows:

$$\overline{N}_{CS} \simeq \frac{1.75 \times 10^{16}}{(1 - e^{-2.35/T_{ex}})} \left(\frac{\tau_{10}}{1 - e^{-\tau_{10}}}\right) \int \frac{1}{\eta} T_A^*(V) dV. \tag{3.3}$$

If $\tau_{10} = 2.2$, the CS column density at position (0, 0) is 5.4×10^{18} m^{-2}, taking T_{ex} at the central position to be 29K, to be consistent with the dust temperature measured in Chapter 4. IGH find consistent values of X(CS) in the range $(3.9 - 10) \times 10^{-9}$ from Galactic sources. The mean value of their results is $7(\pm 3) \times 10^{-9}$, which yields a molecular hydrogen column density of 7.7×10^{26} m^{-2}.

There is evidence in the C^{18}O data (§3.4.5.2; Fig. 3.21) that T_{ex} in the molecular gas away from the central source falls to 10K – 15K. Hence, taking $T_{ex} = 15$K as an effective temperature characteristic of the whole core, a total core mass of 2900 ($\pm$1200) $M_\odot$ is obtained by summing $\overline{N}_{CS}$ over Fig. 3.4. This result is quite consistent with the cloud core mass obtained from submillimetre continuum observations in Chapter 4 (1900 $M_\odot$, using a single-temperature model), small adjustments in the effective T_{ex} and X(CS) taking care of any residual discrepancy. It should be noted that this result for the core mass assumes that the value of τ_{10} found at (0, 0), where a C^{34}S measurement is available, is applicable to the whole core, so introducing an unquantified error. The justification for this crude assumption lies in the persistently low values of $T_b(2\text{–}1)/T_b(1\text{–}0)$ in Fig. 3.8 which should rise to between 2 and 3 if the optical depth in the line were significantly reduced in other parts of the cloud core.

The same method applied to the J=2–1 map produces a CS column density estimate at (0, 0) of 5.2×10^{18} m^{-2}, since

$$\overline{N}_{CS} \simeq \frac{8.61 \times 10^{15} e^{2.35/T_{ex}}}{(1 - e^{-4.7/T_{ex}})} \left(\frac{\tau_{21}}{1 - e^{-\tau_{21}}} \right) \int \frac{1}{\eta} T_A^*(V) dV. \tag{3.4}$$

The corresponding total core mass estimate is 2500 $M_\odot$. The assumptions therefore produce quite consistent results for $\overline{N}_{CS}$ at the map centre (to which they more specifically apply) and for the total core mass from both J=2–1 and J=1–0 data. It is not possible explicitly to calculate the variation in T_{ex} across the core or to find a comparative value of T_{ex}(J=2–1) using the present data, since we have no information on C^{34}S(J=2–1) or the spatial variation of C^{34}S(J=1–0).

In an inhomogeneous medium the beam-filling factor f gives an indication of the clumpiness of the material. The value of f can be calculated directly from the definition of line brightness temperature, via:

$$f_{ij} = \frac{T_b}{\frac{h\nu_{ij}}{k}[(e^{h\nu_{ij}/kT_{ex}} - 1)^{-1} - (e^{h\nu_{ij}/kT_{bg}} - 1)^{-1}](1 - e^{-\tau_{ij}})} \tag{3.5}$$

where T_{bg} is the temperature of the cosmic microwave background. For CS(J=1–0) this expression becomes:

$$f_{10} = \frac{T_A^* / \eta_{fss} \eta_c}{[2.35(e^{2.35/T_{ex}} - 1)^{-1} - 1.69](1 - e^{-\tau_{10}})}. \quad (3.6)$$

$f_{10} = 1$ for a uniform source that fills the beam. If $T_{ex} = 15$K, the values of both f_{10} and f_{21} at (0, 0) in Figs 3.4 and 3.5 are 0.75 (this result depends on the assumed excitation temperature and f is larger at smaller values of T_{ex}).

The brightness temperature ratio map of Fig. 3.8 shows low values localised around the southwestern CS condensation, to the northwest of the central peak and along a ridge to the east of the centre. These areas are most probably regions of either reduced excitation (lower T_{ex}) or increased optical depth. Since no continuum source has been detected within the southwestern condensation in either the near- or mid-infrared (Chapter 5) it is likely that the dust temperature here is lower than in the heated core, say 10–20 K. Support for high optical depths to the east of the main central peak can be found in the presence of a second eastern peak in the rare isotope $C^{18}O$ (J=1–0) (Fig. 3.17). In consistent fashion, the regions of increased CS (2–1)/(1–0) trace the channels of the two main red-shifted CO outflow lobes, where the flows have removed large amounts of core material, reducing the gas column density and optical depth, and/or shock-heated the nearby dense gas. Evidence of shock-heating within the outflow cavities is available from the detection of near-infrared H_2 lines in the corresponding regions (see Chapter 2)

A simple comparison of the above LTE results with the predictions of a LVG model for the dense gas can be made by examining Fig. 3 of Linke & Goldsmith (1980). At $T_{ex} = 20$K, a line brightness temperature of $\sim$ 8K and a (2–1)/(1–0) ratio (R_{21}) close to 1 indicate a density of about 8×10^{10} m^{-3} and $X(CS)/(\mathrm{dV/dr}) \simeq 3 \times 10^{-10}$ (kms^{-1} pc^{-1})$^{-1}$. From the line widths in Figs 3.3 & 3.4, dV/dr in the W75N core is 7–8 kms^{-1} pc^{-1}, so the predicted CS abundance is $X(CS) \simeq 2 \times 10^{-9}$, which is less than the lowest value reported by IGH and a factor of 3 below the value assumed above. IGH observe that low derived abundances are a feature of the application of LVG models to sources without velocity gradients over 10–15 kms^{-1} pc^{-1} in which optical depths remain high over much of the line. The predicted density is also lower than the mean LTE figure (3×10^{11} m^{-3} at (0, 0)), since, under LVG assumptions, $R_{21} \simeq 1$ indicates sub-critical excitation of J=2. Lower values of R_{21} mean lower densities from the model, while

higher values mean higher densities but considerably lower CS abundances. At higher T_{ex}, the LVG-predicted densities decrease further, while the values of $X(CS)$ increase.

Taking T_{ex} = 29 K and $\tau_{10} = 2.2$, the assumption of thermalisation of the rotational levels up to J=7 would imply an optical depth in J=7–6 of 80. However, the true optical depth is probably less than this, because the columns over which the J=7–6 and J=1–0 transitions are excited are not comparable. The critical density for J=7–6 is $\sim 2 \times 10^{13}$ m^{-3} and it is only above this value that the line emission is $\propto N_{CS}$. On the other hand, the critical density may be less significant in the case of high optical depth where radiative trapping will contribute significantly to the excitation. It is likely in any case that only the inner regions of the core contribute to the J=7–6 emission and this is borne out by the limited extent of the detectable emission in Fig. 3.9 compared to that in Fig. 3.4 & 3.5 (J=1–0 and J=2–1). It is clear that without knowledge of the density and temperature structure of the core it is difficult to compare directly the J=7–6 data with the lower transitions examined above. A lower limit to the column density of CS in which J=7 is significantly populated can, however, be obtained from

$$\overline{N}_{CS}^{76} \gtrsim \frac{2.50 \times 10^{15} \times e^{49.4/T_{ex}}}{(1 - e^{-16.5/T_{ex}})} \int \frac{1}{\eta} T_A^*(V) dV. \qquad (3.7)$$

(Appendix A) which is accurate in the optically thin limit. This yields $\overline{N}_{CS}^{76} \gtrsim 1.4 \times 10^{17}$ m^{-2} and $N_{H_2} \gtrsim 2.1 \times 10^{25}$ m^{-2} at position (0, 0), if T_{ex} = 29K is still applicable. From Fig. 3.9 the physical linear size of region emitting J=7–6 is $\sim 1/3.5$ of that of the 1–0 and 2–1 core. The column density ratio therefore lies somewhere between this value and unity, depending on the radial density distribution in the cloud. For instance, if N^{76}/N^{10} were equal to 0.6 (in a somewhat somewhat centrally peaked distribution) and if LTE were still appropriate, τ_{76} would be $\lesssim 34$ since T_{ex} = 29K now probably constitutes a lower limit to the effective excitation temperature.

An analysis of the CS data in each velocity channel enables the calculation of the mass, energy and momentum of the W75N core material for comparison with the outflow energy and momentum input and with the gravitational binding energy of the dense gas and the embedded stars. These three quantities are calculated through the three moments:

$$M = \sum_V m(V), \quad P = \sum_V m(V)V, \quad E = \frac{1}{2} \sum_V m(V)V^2$$

where $m(V)$ is calculated from $T_A^*(V)$ in the same way as before. The current $C^{34}S$ profile (Fig. 3.5) does not have sufficient signal-to-noise to calculate optical depth corrections to $m(V)$ in the wings of the line (i.e. outside ± 2 kms^{-1} from the line centre), but CS/$C^{34}S$ ratios of between 9 and 12 occur in the line core. Hence, assuming optical depths in CS(J=1–0) of 2 to 2.5 for V_{LSR} between 8 and 11 kms^{-1} and < 1 otherwise, the above expressions yield $M = 2700$ $M_\odot$, $P = 5.3 \times 10^{36}$ kg.ms^{-1} (2700 $M_\odot$kms^{-1}) and $E = 4.8 \times 10^{39}$ J. The mass value is in good agreement with the cruder estimate above and is probably more accurate, as it takes into account the inevitable reduction in optical depth in the line wings. The momentum and kinetic energy estimates are lower limits, since the velocities used are projections along the line of sight and some of the material apparently at V = 0 will also be in motion. If the velocity field in the dense gas were completely isotropic (i.e. as in the case of uniform expansion or contraction or completely random motion) and there were no significant distribution of speeds between constituent clumps, the above momentum estimate would be 0.64, and the kinetic energy 0.5, of their true values. Under the assumption of a Gaussian density distribution, the gravitational binding energy in the CS-traced core can be estimated from the expression in §4.4.4. If the embedded stars within the core contribute about 200 $M_\odot$, a mass of $\sim$ 2700 $M_\odot$ in the core itself means a gravitational binding energy of $\sim 5 \times 10^{40}$ J. Given that the worst potential underestimate of E above is little more than a factor of two the core appears to be gravitationally bound, despite signs of expansion in the outer layers.

3.4.3 CO Line Profiles

The ^{12}CO (J=1–0) spectrum shown in Fig. 3.2 has a number of interesting characteristics. This complex line profile is a mixture of separate emission and self-reversal features. The peak at $V_{LSR} = -3$ kms^{-1} is emission from the DR-21 Giant molecular cloud which occupies the same line of sight as the W75 cloud over a large region. DR-21 is thought to be immediately behind the W75 cloud, the two possibly in collision (Dickel, Dickel & Wilson 1978), although Garden (1986) places DR-21 much further away, at 5 kpc. The DR-21 cloud is very large; emission at this velocity is present across the whole mapped area even though the main embedded heating sources are around 18 arcmin to the southwest.

Emission from W75N is centred at $V_{LSR} = +9.5$ kms^{-1}. At the present sensitivity (0.4 K per 0.1-kms^{-1} channel) red-shifted material is detected out to $V_{LSR} = +35$

kms^{-1}. A very strong blue-shifted wing merges with the –3 kms^{-1} component long before reaching $T_A^* = 0$ K and it is not possible to say how far the blue wing of the W75N J=1–0 line extends into the DR-21 contamination. The low-velocity line 'core' (which is essentially emission from the ambient cloud) is affected by two strong, narrow self-absorption features at $V_{LSR} = +8.5$ and $V_{LSR} = +10.0$ kms^{-1}, or –1.0 and +0.5 kms^{-1} from the cloud rest velocity. Such features, which are common in ^{12}CO emission lines from Galactic sources, are caused by large columns of overlying cool material (Loren *et al.* 1981). There thus appears to be two such components, one slightly red-shifted, perhaps still moving inward towards the cloud core as a vestige of the original cloud collapse, and one outward towards the observer. The blue-shifted absorption component may be related to the signs of expansion in CS observations (§3.4.1.1) and caused by the energy input of the high-velocity flow. The weak J=1–0 line at $V_{LSR} = -22$ kms^{-1} is an unrelated, probably diffuse cloud along the line of sight.

^{12}CO (J=2–1) follows the general features of the J=1–0 line except that the W75N blue wing falls less steeply and appears to merge smoothly with the DR-21 component. Both the $V_{LSR} = -22$ kms^{-1} and DR-21 components appear to be relatively weak, with respect to the emission from W75N, when compared to the corresponding J=1–0 lines. This is consistent with emission from low-temperature gas, far from any heating sources. The self-absorption lines are still present, but have merged, perhaps due to the lower velocity resolution of the J=2–1 observations.

The ^{13}CO (J=1–0) central line profile has extremely low noise, and shows a central cloud component clear of self-reversal. The red-shifted wing is detected out to $V_{LSR} = +20$ kms^{-1} but once again the blue wing is considerably stronger and does not fall to zero before merging with the DR-21 emission. This profile shows that a separate feature may be present at $V_{LSR} \simeq -1$ kms^{-1}, appearing as a shoulder on the DR-21 line and contributing to the strong emission on the blue side of W75N. In fact the expected narrow –3 kms^{-1} line seems to sit upon a wide emission pedestal, possibly indicating significant turbulent motion within the background cloud. Beyond the DR-21 component, emission appears to continue at the $\sim$ 0.15 K level out to about $V_{LSR} = -8$ kms^{-1}. This may be the continuation of the blue wing of the W75N line which would then extend to –17 kms^{-1} from the cloud rest velocity, compared to $\sim$ 10 kms^{-1} for the red-shifted wing. Blue wing emission clearly belonging to W75N can be followed to $V_{LSR} \simeq 1$ kms^{-1}. The ^{13}CO (J=2–1) line, as for the ^{12}CO profile, has a relatively

weak DR-21 component. Compared to the J=1–0 line, the signal-to-noise ratio in the wings is rather poor and the red line wing is not significantly detected beyond +16 kms^{-1}. The blue wing, however, is very strong in this transition. The evidently large column density of blue-shifted gas suggests again that motion in the blue outflow is close to the line of sight. The very strong blue wing can also be seen in the $C^{18}O$ (J=1–0) line where the profile is still clearly asymmetric. Even in this rare isotopic transition, the DR-21 cloud is marginally detected at around $T_A^* = 0.2$ K.

3.4.4 ^{12}CO & ^{13}CO Outflow Morphology

In comparison with the $\sim$ 1-arcmin resolution CO (J=1–0) map made of the W75N molecular outflow by F85 (Fig. 3.9), the 15-arcsec resolution of the present observations reveal a much more localised high-velocity flow with a large, well-collimated red-shifted lobe extending towards the southwest and compact blue-shifted emission concentrated near the central position. The spatial origin of the outflow is also much more easily identified and occurs close to the compact HII region and OH maser source HII(B) (see Chapter 2). Since it is also the dominant heating source (Chapter 5) and the most deeply embedded object in the region (Chapter 6), HII(B) is the most likely physical source of the outflow.

Although the integrated line-wing maps of Fig. 3.12 show well-separated red- and blue-shifted lobes, it is clear that the outflow in W75N does not have a simple bipolar structure. A secondary spur attached to the main red-shifted lobe appears coincident with the large, dense, CS-traced condensation to the southwest of the main cloud core. The possibility that this spur of fast-moving gas is caused by the division of the larger flow after an interaction with the dense clump is supported by the detection of near-infrared H_2 lines on its northern edge, suggesting shocked gas at the interface (T.J.T. Moore, unpublished data). An alternative explanation would be that, since there is some blue-shifted emission to the northwest of the CS clump, a second, smaller bipolar outflow may be operating from a source within the clump itself. However, this is made less plausible by the lack of any continuum source within the CS condensation (Chapters 4 & 5). In addition, the blue-shifted emission is somewhat diffuse and is most likely associated with the expanding shell of swept-up gas around this flow, as seen in CS.

The main red-shifted outflow lobe is approximately 100 × 50 arcsec (1.0 × 0.5 pc) in extent and contains material with projected velocities up to at least +15 kms^{-1}

from the cloud rest velocity (at the present 3σ detection limit of $T_A^* = 0.6$K). There is no corresponding, oppositely-directed blue outflow lobe with similar dimensions. Localised high-velocity material is present in the opposite direction to the main red flow, but it is also red-shifted (at +2 to +3 kms^{-1}). Most of the blue-shifted material is concentrated in a small region near to the central position and, remaining virtually unchanging at all velocities (Fig. 3.13), is probably moving close to the line of sight. To a large extent, the blue-shifted emission and the northeastern red outflow are coincident on the plane of the sky.

Superimposed red and blue emission has been seen in other CO outflows (e.g. B335, Hirano *et al.* 1988) and is conventionally interpreted as due to flows with longitudinal axes orientated close to the plane of the sky and with significantly large opening angles. The expected emission from such objects has been modelled by Cabrit & Bertout (1986). However, if the blue- and red-shifted material observed here are part of a single outflow lobe, the opening angle must be very large ($\gtrsim 100°$) perpendicular to the plane of the sky while remaining quite small ($\sim 20°$ to $30°$) in the complementary direction. If the observed opening angle were similar to that along the line of sight, then the inclination of the outflow axis would need to be very small and the true CO velocities extremely high (approximately ten times those observed). In such a case, however, one would expect to see an extended morphology and lower column density (§3.4.5.1) in the blue-shifted flow. Instead, it is possible that there are in fact three separate major outflow lobes which originate close to the source, plus a subsidiary minor lobe forming the southwest spur.

The multi-polar outflow model is reminiscent of that used by Barral *et al.* (1982) to explain observations of NGC 6302, in which the outflow may begin as either bipolar or isotropic close to the central source, but further out the structure becomes dominated by interactions with an inhomogeneous cloud core, finding its way out along the steepest density gradients and becoming multi-lobed in the process. In this model there is no rôle for a large interstellar ($\gtrsim 0.1$ pc) disk in the collimation of the outflow, and any collimation induced on smaller scales by the circumstellar material may be lost. However, supersonic outflows can remain or become well-collimated through de Lavall funnelling via a density gradient in the ambient medium (Königl 1982) or by simple gravitational or pressure confinement.

In the ^{13}CO (J=1–0) emission, integrated over all velocities, a large ridge is seen (Fig. 3.14) extending from near the central source position towards the south.

Since this feature does not appear in ^{13}CO (J=2–1) (Fig. 3.16), it is not clear whether it is a real physical feature or an artifact. 'Scanning effects' can easily occur in maps made up of linear scans, if the calibration or sky opacity change momentarily during one raster. However, the ^{13}CO maps are made up of both vertical and horizontal scans and careful examination of the raw data has revealed no strong evidence of such a problem. Some circumstantial evidence exists that the feature is real, however. In the integrated CS (J=7–6) map (Fig. 3.9), although the noise levels are high, there appears to be strong emission in the same region. This would indicate very warm dense material exists here and the ^{13}CO ridge may thus be part of the compressed boundary between the blue-shifted outflow and the surrounding cloud. The ^{13}CO (J=2–1) transition may have a significant optical depth in this region and not probe the deeper structure. Further observations are necessary to investigate this matter.

Even though the lower velocity contours are strongest at the edges of the outflow, the main red lobe shows no sign of a shell-like density cross-section used to model bipolar flows by, for example, Kaifu (1985) and (Snell & Schloerb 1985). At higher velocities, the strongest emission occurs in the centre of the outflow channel, suggesting a filled structure within the fast-moving gas. Similarly, new observations of L1551 have shown that large amounts of molecular material in fact exist in what were apparent cavities, which may have appeared because of saturation effects in the ^{12}CO observations (C.V.M. Fridlund personal communication). The velocity-channel maps in Fig. 3.13 show that the emission peak shifts away from the source along the flow with increasing velocity. This is frequently the case in CO outflows (A similar velocity structure was found in the single-lobed outflow in NGC 2024 by Richer *et al.* 1989) and may be indicative of continuous acceleration of the material in the main body of the outflow (e.g. by nozzle effects induced by the surrounding density gradient). On the other hand, the apparent acceleration may merely represent the history of a flow in which the earliest periods of mass loss were the most energetic.

At small red-shifted velocities (+2 to +4 kms^{-1}), strong CO emission begins to appear along the edges of the main southwestern flow channel; at first close to the southwestern CS condensation, which delineates the southern edge, and then along the northern edge as well with a definite cavity in the region between. As velocities increase, the strongest emission slips along the northern limb of the outflow channel and begins to move into the channel itself, occupying it fully by about +8 kms^{-1}. This velocity structure was also observed in CS and indicates a slow-moving shell of

material around a much faster and less dense central flow. It appears, therefore, either that the fast flow is in the process of breaking off and accelerating many dense clumps of material from the ambient cloud, which are then gradually disrupted and move into the main flow, or that the flow has a shell of compressed gas around it which has acquired a significant component of momentum in the flow direction.

Similarly, the northeastern red lobe shows evidence of a limb-brightened shell structure at lower velocities ($V_{\rm LSR}$ = +12 to +13 kms^{-1}) in the J=1–0 transition, while emission from faster moving material in this flow is present out to at least $V_{\rm LSR}$ = +25 kms^{-1} occupying the central area of the flow channel.

3.4.5 CO Radiative Transfer Analysis

3.4.5.1 ^{12}CO and ^{13}CO: The Outflow

The analysis of the emission from the high-velocity gas in the CO outflow lobes has been done under LTE assumptions. Such an approach is the general rule in CO observational studies since the low dipole moment and the consequently low critical density ($n(\rm H_2) \simeq 2 \times 10^3$ m^{-3} for ^{12}CO J=1–0) mean that that thermalisation of the lower rotational levels is easily achieved at the densities prevalent in all molecular clouds ($n(\rm H_2) \gtrsim 10^9$ m^{-3}). Although LVG analysis might at first seem more appropriate in the fast-moving gas, ubiquitously high opacities observed even in high-velocity ^{12}CO (e.g. Plambeck, Snell & Loren 1983; Margulis & Lada 1985) mean that the LVG assumptions of radiative decoupling are not generally satisfied.

It is important to try to use low optical depth transitions in calculating values of the excitation temperature to minimise distortions that may be caused by line-of-sight temperature gradients (see Cantó *et al.* 1987). For example, if the optical depth in the lines employed is significant, an inwardly decreasing temperature variation can depress the ratio T_A^*(2–1)/T_A^*(1–0). This occurs because the opacity of the J=1–0 line is generally smaller then that of J=2–1 and the former will probe deeper regions with higher temperatures. Unfortunately, this effect cannot be securely guarded against when using ^{12}CO and ^{13}CO to calculate optical depth, since the ^{12}CO line will be optically thick out to quite high velocities in the wings. However, the presence of spatial variations in T_{ex} across an outflow may help betray any significant line-of-sight gradients.

In the inner wings of the line ($V_{\rm LSR} = 7-14$ and $14-20$ kms^{-1}), both transitions

of ^{12}CO and ^{13}CO were detected. By integrating the antenna temperatures in these velocity intervals, mean optical depths of ^{13}CO J=2–1 (τ_{21}) and J=1–0 (τ_{10}) were calculated at each position using the appropriate version of Equation 3.1:

$$\frac{T_A^*(^{12}CO)}{T_A^*(^{13}CO)} = \frac{1 - e^{-R\tau}}{1 - e^{-\tau}}.$$

where $R = \tau(^{12}CO)/\tau(^{13}CO)$ is the relative isotopic abundance $n(^{12}CO)/n(^{13}CO)$. The Solar System value of R is 89, but values as low as $\sim$ 40 have been employed (Dickman 1978). However, the derived value of τ is not sensitive to R when $T_A^*(^{12}CO) \div T_A^*(^{13}CO) \ll R$ (i.e. where $\tau \gtrsim 3$). This common method of calculating τ assumes that the same excitation temperature is appropriate for both ^{12}CO and ^{13}COand this may be a source of error, since high ^{12}CO optical depths and consequent radiative trapping may have a significant effect on the level populations in the majority isotope. In addition, as mentioned above, the derived values may be affected by temperature gradients along the line of sight.

In using the above equation and in converting later from ^{13}CO to H_2 column densities, a conservative isotopic abundance of 50 was adopted, bearing in mind the possibility that the ^{13}CO abundance may have been enhanced by fractionation effects in the original undisturbed cloud (see the discussion by Van Dishoeck & Black 1988). The choice of this factor and that of the ^{12}CO abundance relative to molecular hydrogen introduce approximately a factor of two uncertainty in the final values of mass, momentum and energy in the outflow.

^{13}CO (J=1–0) optical depths in the 1–7 kms^{-1} range in the vicinity of the blue outflow are found to be generally between 0.1 and 0.25, indicating ^{12}CO (J=1–0) optical depths in this velocity interval between about 5 and 15. These are similar values to those obtained in the inner ^{12}CO wings of a number of similar sources by Margulis & Lada (1985). The signal-to-noise levels in the red-shifted line wing (14–20 kms^{-1}) are considerably lower than in the blue wing and so the derived optical depths are less reliable. In general, however, values of τ_{10} are between 0.05 and 0.1 in the main red lobes. In these regions, the ^{12}CO line may be only marginally optically thick ($\tau \sim 3 - 5$).

Although noise levels in the J-2–1 transitions were too high to derive the excitation temperature as a function of position from the ratio of optical depths (Equation 3.2),

T_{ex} was obtainable direct from the ^{13}CO (J=1–0) line antenna temperature and the optical depth, via the definition of line brightness temperature T_b (Appendix A):

$$T_{ex} = \frac{h\nu/k}{\ln[1 + (1 - e^{-\tau})h\nu/kT_b]} \tag{3.8}$$

where T_b is $T_A^*/\eta_c\eta_{fss} \simeq T_A^*/0.4$, for J=1–0. In this way, a velocity-averaged T_{ex} was calculated at each position and the results are displayed in Figs. 3.18 and 3.19. The very large column density peak near the origin in the map of blue-shifted material is consistent with the conclusion that the major blue flow lobe axis is orientated close to the line of sight. Since the line optical depths appear to change very slowly across the region in both red and blue line wings, the spatial distribution of T_{ex} closely follows that of T_A^*. Values range from 6K to 16K in both major flow lobes, and are higher towards the central regions of each component. The derived temperatures are a factor of two lower than the arbitrary 25K adopted by F85, and a factor of three less than the central cloud core dust temperature (30K: Chapter 4). Snell *et al.* (1984) also find that T_{ex} in the high-velocity gas of similar sources was less than or roughly equal to that of the nearby undisturbed molecular gas. This suggests that the observed CO lies away from the accelerating shocks (presumably at the cloud-flow boundary).

The above method of obtaining T_{ex} assumes a beam filling factor of unity everywhere (see §3.4.2). By integrating over position as well as velocity, it was found that the ratio τ_{21}/τ_{10} in the flow regions varied generally between 1 and 2.5. Such values imply T_{ex} between 6K and 20K for both line wings, in good agreement with the values derived from the antenna temperatures. This indicates that the beam filling factor is actually quite high and that the molecular gas is not significantly clumped in the outflows at these velocities. For the reasons mentioned above, line-of-sight temperature gradients can affect the derived filling factor (Cantó *et al.* 1987), but an artificially increased value requires a gradient which is decreasing into the cloud or flow lobe. The spatial variations observed (Fig. 3.18) show higher T_{ex} in the central regions of the flow, hence any resulting distortion ought to favour low derived filling factors.

With the mean T_{ex} calculated in the same velocity ranges as τ, the beam-averaged column density $\overline{N}(^{13}CO)$ was calculated at each position from $T_A^*(V)$ (J=1–0), τ_{10} and T_{ex} in each 1-kms^{-1} velocity channel using

$$\overline{N}(^{13}CO) = \frac{2.4 \times 10^{18}}{(1 - e^{-5.28/T_{ex}})} \int \frac{1}{\eta} T_A^*(V) dV \left(\frac{\tau_{10}}{1 - e^{-\tau_{10}}}\right) \quad . \tag{3.9}$$

Summing the results over the approximate areas of the separate flow lobes and over velocity, the values for the mass, momentum and kinetic energy were calculated from the moments

$$M = \sum_V \mathrm{N}(V), \quad P = \sum_V \mathrm{N}(V)V, \quad E = \frac{1}{2}\sum_V \mathrm{N}(V)V^2$$

and the results are listed in Table 3.2. The momentum and energy values derived in this way are lower limits to the true figures since the inclination of the outflow direction is not taken into account. The mass is also a lower limit because there may be significant amounts of slow-moving gas (or gas whose projected velocity is low) overlapping the ambient cloud emission component. The abundance of ^{12}CO relative to H_2 was taken as 6×10^{-5} (IGH) and the ratio of total gas mass to that of hydrogen was assumed to be 1.36 (Hildebrand 1983).

In the outer part of the red-shifted line wing (i.e. beyond $V_{\rm LSR} = 20$ kms^{-1}) ^{13}CO was not detected. It was therefore necessary to calculate column densities from the ^{12}CO line intensities without knowing the precise optical depth or excitation temperature at these velocities. In order to do this it was assumed that the values of T_{ex} in the $V_{\rm LSR} = 14-20$ kms^{-1} range would approximate sufficiently well to the temperatures in the faster-moving gas and that the optical depths would be small. Low optical depths ($\tau_{10} \lesssim 3$) are suggested by the values found in the inner wing. The resulting error is in any case small, since this velocity range does not contribute a significant fraction of the total mass ($\sim 0.4\%$), momentum ($\sim 1\%$) energy ($\sim 3\%$) in the red-shifted gas. The strong emission at $V_{\rm LSR} \simeq -3$ kms^{-1} from the DR-21 cloud contaminates the high-velocity blue-shifted line wing and it is impossible to estimate with accuracy the true W75N contribution beyond $V_{\rm LSR} = +1$ kms^{-1}. However, the latter point suggests that the mass, momentum and energy calculated in the $V_{\rm LSR} = 1-7$ kms^{-1} range do not seriously underestimate the totals in the blue-shifted gas.

The total mass of gas in the outflow is found to be ~ 100 $M_\odot$. This can be compared to the figure of 130 $M_\odot$ obtained by F85 using somewhat cruder methods and a factor of two higher excitation temperature. The total momentum and energy are found to be smaller than the previous results because of the adoption of a mass-weighted mean flow velocity (§3.4.6).

The red-shifted outflow components can be traced morphologically from about $V_{\rm LSR} = +12$ kms^{-1} in the ^{12}CO velocity maps (Fig. 3.13), which is where the ^{12}CO

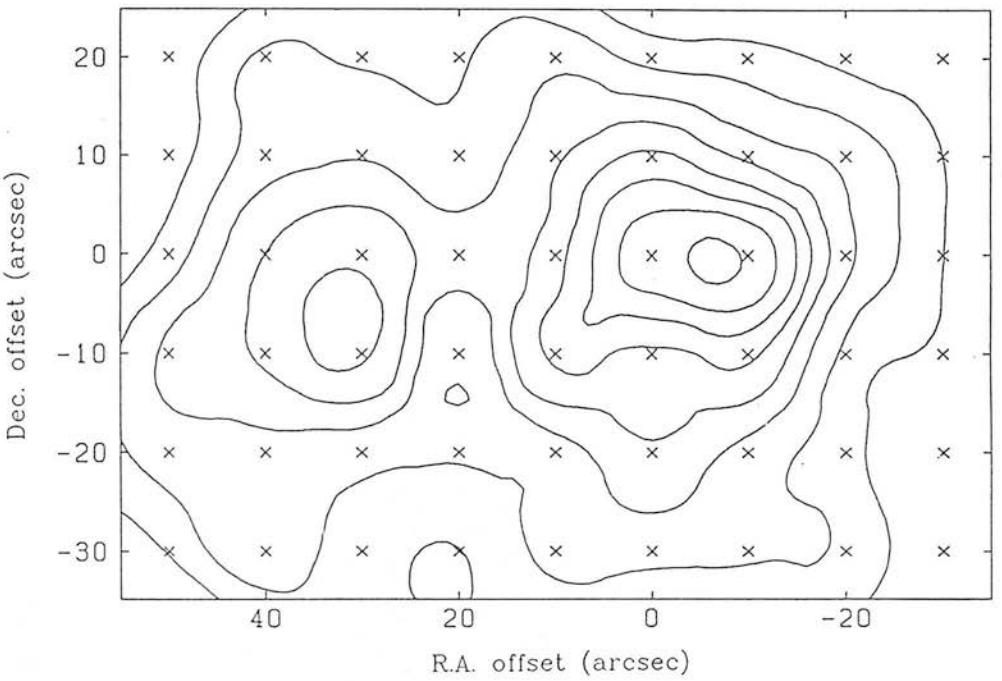

Figure 3.17: $C^{18}O$ T_A^*(J=1–0) in the central area integrated between V_{LSR} = 4 and 15 kms^{-1}. Contours are at intervals of 0.5 from 2 $K.kms^{-1}$.

Table 3.2: Mass, Momentum and Energy in the high-velocity outflow

V_{LSR} /kms^{-1}	Component	Mass / $M_\odot$	Momentum /$kg.kms^{-1}$	Energy /J
1–7	Blue	31.9	2.7×10^{35}	6.3×10^{38}
12–14	Main Red	28.8	2.0×10^{35}	3.5×10^{38}
	N.E. Red	11.3	7.5×10^{34}	1.3×10^{38}
	Red Spur	1.9	1.3×10^{34}	2.1×10^{37}
14–20	Main Red	20.2	2.6×10^{35}	8.6×10^{38}
	N.E. Red	5.3	6.8×10^{34}	2.3×10^{38}
	Red Spur	1.8	2.4×10^{34}	8.5×10^{37}
20–30	Main Red	0.3	8.8×10^{33}	6.0×10^{37}
	N.E. Red	0.1	2.8×10^{33}	2.0×10^{37}
	Red Spur	~ 0	7.4×10^{32}	4.2×10^{36}
Totals	Blue	31.9	2.7×10^{35}	6.3×10^{38}
	Main Red	49.3	4.7×10^{35}	1.3×10^{39}
	N.E. Red	16.7	1.5×10^{35}	3.8×10^{38}
	Red Spur	3.7	3.8×10^{34}	1.1×10^{38}
Grand Total		101.6	9.3×10^{35}	2.4×10^{39}

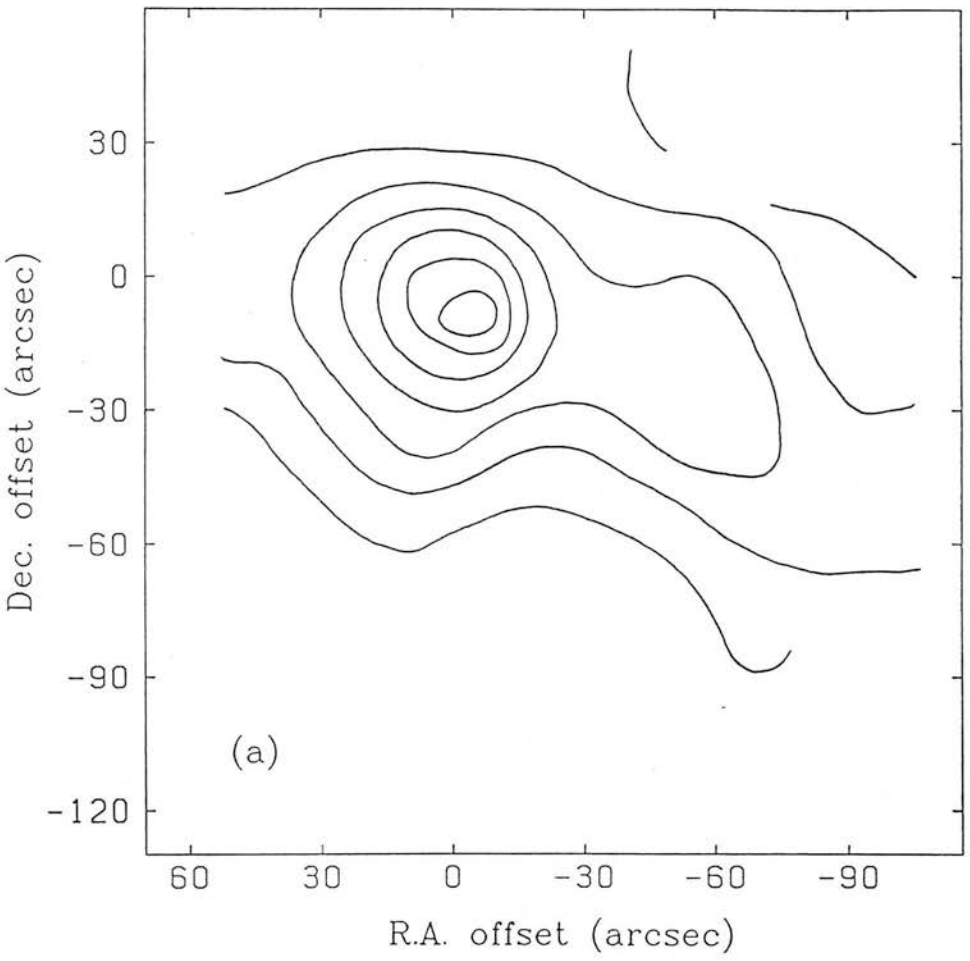

Figure 3.18: T_{ex} distribution in the ^{13}CO line wings: (a) $V_{LSR} = 1-7\,kms^{-1}$. Contours are at intervals of 2K from 4K.

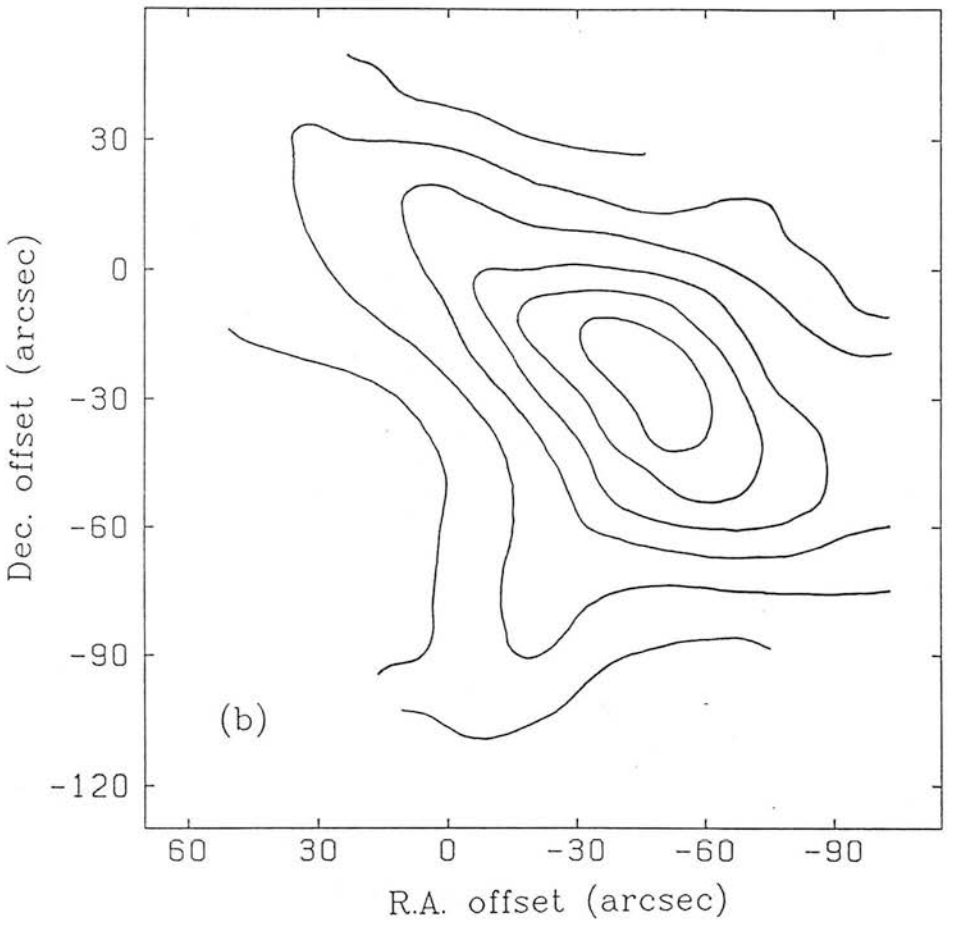

Figure 3.18: T_{ex} distribution in the ^{13}CO line wings: (b) $V_{LSR} = 14 - 20$ kms^{-1}. Contours are at intervals of 2K from 4K.

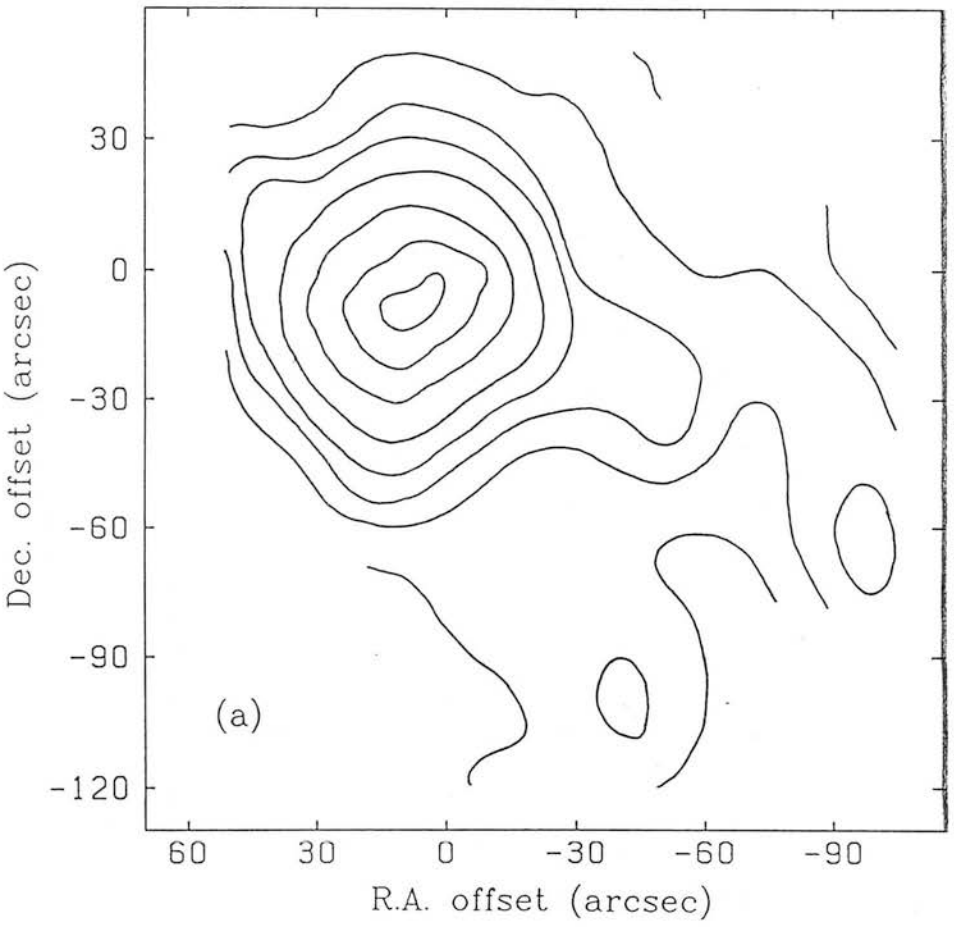

Figure 3.19: (a) Velocity-dependent $\overline{N}(^{13}CO)$ distribution for $V_{LSR} = 1 - 7$ **kms**$^{-1}$. Contours (6, 12, 18, 24, 36, 60, 90 and 120) $\times 10^{18}$ m^{-2}.

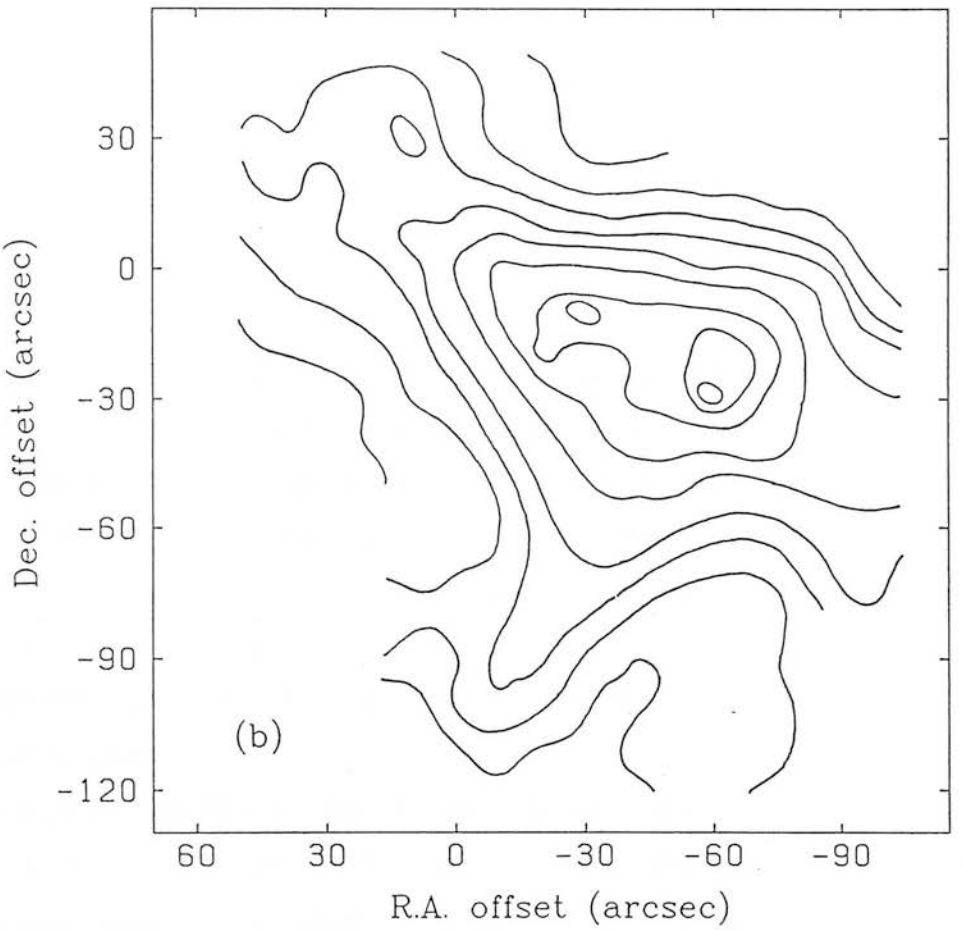

Figure 3.19: (b) Velocity-dependent $\overline{N}(^{13}CO)$ distribution for V_{LSR} = 14 – 20 kms^{-1}. Contours at (3, 6, 12, 18, 24,....) $\times 10^{18}$ m^{-2}.

(J=1–0) self-absorption and the velocity extent of the emission component from the ambient cloud (as determined by the CS line widths: Fig. 3.1) end. However, the ^{12}CO (J=2–1) self-absorption features affect the line out to $V_{\rm LSR} \simeq 14$ kms^{-1}. Therefore, in the region 12 – 14 kms^{-1} which contains a significant fraction of the outflow mass, τ and T_{ex} can only be calculated for the J=1–0 transition.

3.4.5.2 C^{18}O: The Core

The map of integrated C^{18}O (J=1–0) emission (Fig. 3.17) shows for the first time the true structure of the dense inner regions of the W75N core, since this is the first set of observations in reliably optically thin transition. The most obviously striking feature of the integrated T_A^* map is that there are two major column density peaks. The western maximum corresponds to the peak position in CS (J=1–0) and (J=2–1) (Figs 3.4 & 3.5) and in the submillimetre continuum (Chapter 4) as well as to the probable dominant luminosity and outflow source, HII(B). The second condensation, whose integrated C^{18}O strength in a 15-arcsec beam (5.8 ± 0.2 K.kms^{-1}) is comparable to that of the 'central' source (6.1 ± 0.2 K.kms^{-1}), appears about 40 arcsec to the west and 10 arcsec south of the latter. It is not explicitly observed in any other line or in the continuum, although a ridge to the east of the main CS peak (Figs 3.4 & 3.5) may be associated, as may be a small extension in the same direction in the 350-μm continuum (Chapter 4).

The nearest known continuum source is the near-infrared object IRS-3 (Chapter 2) which is about 10 arcsec to the south. This is unlikely to be a heating source within the clump, however, since it is the least reddened of the major 2-μm objects in the region. Mid-infrared observations (Chapter 5) only detected faint emission at the position of IRS-3 at 10 μm and its spectrum appears to fall rapidly to longer wavelengths. The interesting possibility remains that this clump is as massive and dense as as that containing the dominant luminosity source (see below), but is without a central star and therefore may be a very unevolved protostellar core.

The double isotope ratio ^{13}CO/C^{18}O is somewhat uncertain. The value found in dark clouds is close to the terrestrial figure of 5.5 (Dickman, McCutcheon & Shuter 1979) but the ratio in Giant Molecular Clouds is found to be a factor 2–4 higher (Taylor & Dickman 1989). Other studies show values in the region of 10 in large star-forming regions (Lis & Goldsmith 1989; Penzias 1981; Penzias 1983) but Taylor and Dickman suggest that the true value is between 4 and 6 in all sources and that the derived

column density ratios are distorted in GMCs by the effects of turbulent clumping on beam-filling factor for the different isotopes. Since the latter postulation is still somewhat speculative and the effects of fractionation in enhancing ^{13}CO and of selective photoionisation in reducing $C^{18}O$ are unquantified in a large cloud containing multiple ionising sources, we adopt a $^{13}CO/C^{18}O$ abundance ratio of 10. This is consistent with the observed integrated T_A^* ratio (10 ± 1) in the $-3 kms^{-1}$ DR-21 emission component. The integrated T_A^* ratio of 6.3 ± 0.2 in the western peak (Fig. 3.17) gives an optical depth of 0.11 ± 0.01 (from equation 3.1). The corresponding ^{13}CO (J=1–0) emission optical depth is 1.1 and the J=2–1 transition must therefore be considerably optically thick ($\tau \sim 3$). This is contrary to the common assumption that ^{13}CO is reliably optically thin everywhere. $C^{18}O$, therefore, is the only molecular transition so far observed in W75N which probes the true column density structure in the core. The noise levels obtained in $C^{18}O$ (J=1–0) ($\Delta T_A^* = 0.13$ K, rms, per 0.1 kms^{-1} channel) are, however, insufficient to provide information on the velocity structure in the central core.

Under the assumption of LTE, and where $\tau \ll 1$, the beam-averaged column density of $C^{18}O$ is given by

$$\overline{N}_{C^{18}O} = \frac{2.42 \times 10^{18}}{(1 - e^{-5.23/T_{ex}})} \int \frac{1}{\eta} T_A^*(V) dV. \qquad (3.10)$$

Taking $T_{ex} = 30$K in the core material and $\eta = \eta_{fss} = 0.4$, we obtain $\overline{N}_{C^{18}O} = 2.3 \times 10^{20}$ m^{-2} and 2.2×10^{20} m^{-2} for the column density towards the western and eastern peaks, respectively. With a relative abundance of $C^{18}O$ to H_2 of $X(C^{18}O) \simeq 1.2 \times 10^{-7}$ the corresponding H_2 column density values are 1.8×10^{27} m^{-2} and 1.9×10^{27} m^{-2}. Summing over the area covered by Fig. 3.17 we find a total gas mass of approximately 1,000 $M_\odot$. This is a little lower than the mass derived from the 350-μm continuum observations of Chapter 4, which cover a similar area but is within the combined uncertainties in both values. This total mass seems to divide equally between the two $C^{18}O$ emission centres which have approximately 350 and 330 $M_\odot$ in a 30×30 arcsec area around each peak, the remaining mass being made up of more diffuse surrounding material.

Using the ratio of integrated optical ^{13}CO and $C^{18}O$ emission between $V_{LSR} = 7 kms^{-1}$ and $12 kms^{-1}$, the velocity-averaged $C^{18}O$ optical depth was calculated at each point observed in $C^{18}O$ (Fig. 3.20). It was then possible to estimate the excitation temperature variation from T_A^* and τ as was done for the CO line wings (§3.4.5.1;

Equation 3.8). The results are shown in Fig. 3.21. It can be seen that T_{ex} falls towards the edges of the map (i.e. away from the heat sources) where it has values of 10K – 15K.

The most immediately obvious feature in the T_{ex} map is the small area of very high values $\sim$ 30 arcsec to the southeast of the central position. This is specifically caused by the strong ridge in the ^{13}CO map (Fig. 3.13) coinciding with weak C^{18}O emission. Since the antenna temperature ratio is large, the derived optical depth is very small in this area and this in turn produces very large estimates of T_{ex}. Since it is not clear whether the ^{13}CO ridge is real or an artifact it is not certain either that the T_{ex} peak is genuine. However, the area of high temperatures is virtually coincident with the large infrared reflection nebula which is associated with the blue-shifted outflow lobe (Chapter 6). If the ^{13}CO ridge were real then the high T_{ex} values may reflect high kinetic temperatures arising in shocked gas at the flow boundary. The lack of a corresponding rise in C^{18}O antenna temperature is difficult to explain unless a UV field were present, selectively photo-dissociating C^{18}O (predicted by van Dishoeck & Black 1988), but such an explanation should wait for confirmatory ^{13}CO observations.

3.4.6 The Interaction of the CS Core and the CO Outflow

The mass-weighted mean velocity in the CO outflow is <V>. = (total mass) $\div$ (total momentum) = 4.6 kms^{-1}. Since the maximum detected flow velocity (in ^{12}CO J=1–0) is $\sim$ 20 kms^{-1}, this shows that the great majority of the flowing material is moving relatively slowly. This can also be seen in Table 3.1, which shows more mass in the $V_{\rm LSR} = 12 - 14$ kms^{-1} interval than in all the rest of the red-shifted flow. The length scale <L> of the outflow, as estimated from the main red-shifted lobe, is $\sim$ 0.5 pc. Therefore the characteristic timescale $\tau_{\rm flow}$ is <L> $\div$ <V>$\simeq$ 1 $\times$ 10^5 yr. This is considerably longer than the estimate of F85 (2.3 $\times$ 10^4 yr), mainly because of their assumption that the maximum detected velocity (21 kms^{-1}) characterises the outflow. 10^5 yr is quite long compared to other similar flows (e.g. Snell *et al.* 1984) which may mean that the W75N outflow is in a well-advanced evolutionary state.

An estimate of the gravitational binding force in the whole cloud core can be obtained assuming a Gaussian density distribution (see Chapter 4 and Appendix B). In this case, a core mass of 2000 M$_\odot$ and an approximate effective central stellar mass of 200 M$_\odot$ implies a binding force of around 3 $\times$ 10^{24} N (taking a half-power size of 0.4 pc for the core). The mean rate of momentum deposition by the outflow into the

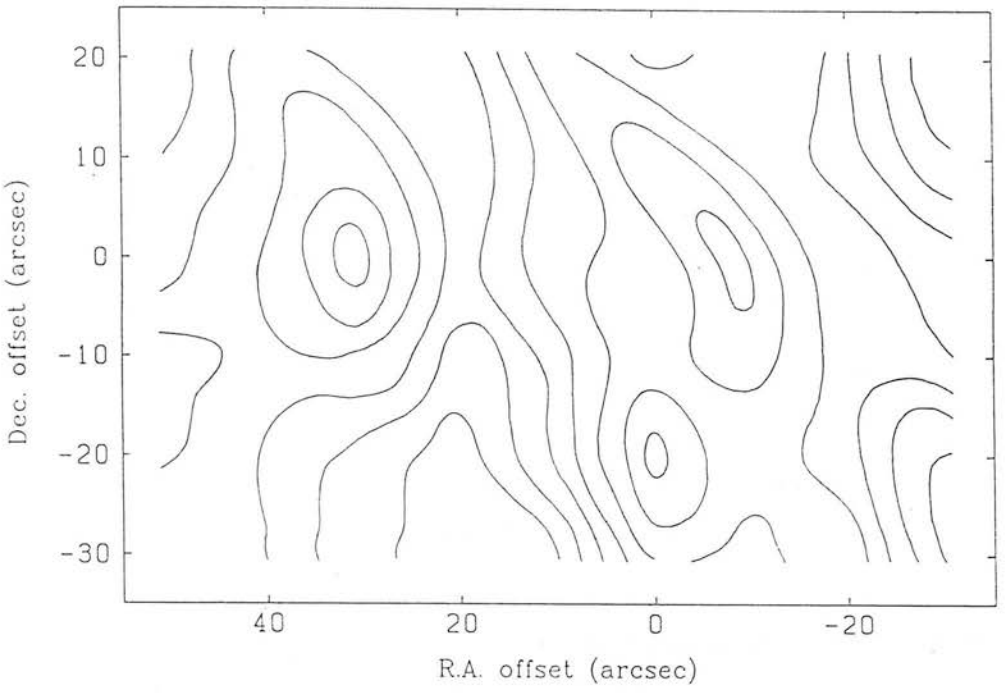

Figure 3.20: τ_{10} distribution for integrated $C^{18}O$ (J=1–0). Contour levels are at intervals of 0.2 from 0.2.

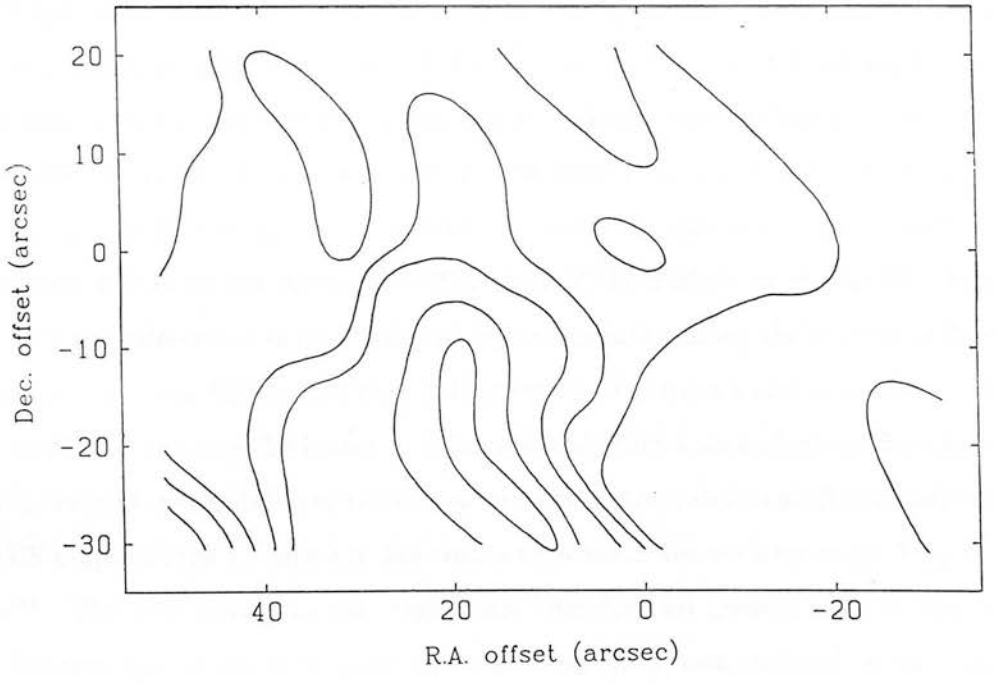

Figure 3.21: T_{ex} distribution for integrated $C^{18}O$ (J=1–0). Contour levels are at 15, 20, 25, 50 and 75K.

ambient cloud is given by (total momentum)/$\tau_{\rm flow}$ = 2.7×10^{23} N. This is at least an order of magnitude smaller force than that binding the cloud. Therefore, if the outflow is initially isotropic or nearly so soon after leaving the source, then the cloud core can easily contain the outflow and provide a mechanism for collimating, or re-collimating, it on a large scale without the action of any large regular structure such as a dense toroid. There is some morphological that the outflow is at least semi-isotropic before interacting with the ambient cloud, since the flow appears to have a large cross-section very soon after leaving the source. Hence, even if the driving wind (or other driving mechanism) is intrinsically bipolar or if significant collimation is induced by circumstellar material close to the star, it must acquire a very large opening angle, as if expanding freely, immediately after leaving the environs of the source. Also, the outflow is obviously not classically bipolar and appears to have multiple lobes emerging over a large range of angles, which is suggestive of an initially spherical flow finding its way out along the steepest gradients in an inhomogeneous density distribution. Königl (1982) modelled flow propagation in this situation and found that strongly directed supersonic jets could form through a de Lavall acceleration mechanism, even in a mass-conserving outflow.

The important point to note is that W75N possesses a highly collimated outflow (with special reference to the main red-shifted component) arising without the action of any large interstellar disk or toroid of similar scale. The collimation appears to arise naturally through confinement by the ambient cloud. Interstellar disks are therefore not necessary to the formation of collimated bipolar outflows and are unlikely to be dynamically active structures. Small-scale disks, on the other hand, may play an important rôle in determining the initial state of the outflow or the driving wind.

Since the detection of near-infrared H_2 line emission along the northern edge of the large southwestern CS clump (Fig. 3.4) suggests that a dramatic interaction with the CO outflow is causing the latter to bifurcate and form a secondary outflow spur, it is worth examining the ability of the clump to remain integrated in such a situation. From the CS maps of Figs 3.4 and 3.5, the clump appears in the velocity range $V_{\rm LSR} = 7 - 12$ kms^{-1}. The line widths in this region are therefore no greater than in the bulk of the CS core and so no high speed mass motions have been induced in the clump by the impacting material. Integrating T_A^* over this velocity interval and over the spatial extent of the clump, a mass estimate of $\sim$ 300 $M_\odot$ is obtained (assuming T_{ex} = 20K and $\tau_{10}(^{13}CO) = 2$); this indicates a binding force of $\sim 2 \times 10^{23}$ N. The force imposed

by the impinging flow is difficult to quantify, since the fraction of the flow that might be intercepted by the clump is uncertain. However, making a conservative estimate of 1/5 for this fraction, the force imposed may be up to $\sim 3 \times 10^{22}$ N. It therefore seems that, unless the outflow inclination to the plane of the sky is less than about 10°, the clump is quite capable of remaining intact under such an interaction and of forcing the high-velocity gas to flow around it. The corresponding momentum in the impinging flow is approximately 1×10^{35} kg.ms^{-1} (50 M$_\odot$kms^{-1}) and the apparent 'turbulent' momentum in the clump is $\sim 9 \times 10^{32}$ kg.ms^{-1} (0.45 M$_\odot$kms^{-1}). It is therefore clear that very little momentum transfer is taking place and the flow must be striking at a shallow angle and is deflected (by pressure in a heated layer at the interface) rather than driving into the clump. This may also explain why no significant radial bulk motion has been induced in the bound clump.

3.5 Conclusions

High spatial resolution observations of CO show that the large outflow in W75N is quite highly collimated. The velocity-dependant morphology of the outflow suggests that it may be multi-lobed or highly asymmetric. The outflow structure consists of dense, slow-moving material in a shell surrounding more diffuse high-velocity gas in the central flow channels. The total mass of flowing gas is $\sim$ 100 M$_\odot$. The CO excitation temperatures are somewhat higher in the central flow regions than at the edges but are comparable to the temperatures in the ambient gas ($\sim$ 15K). The force due to the impact of the outflow is not sufficient to overcome the gravitational binding force in the cloud core. The dense core may thus be entirely responsible for the large-scale collimation of the flow on scales $\gtrsim$ 0.1 pc and the structure and dynamics of the outflow are dominated by density inhomogeneities in the cloud.

A large ($\sim$ 2000 M$_\odot$) dense core was detected in CS emission. The core is gravitationally bound and there are signs of both coherent expansion and contraction in the self-absorption features in the ^{12}CO lines. The distribution of J=1–0 emission from the rare isotope C^{18}O in the central regions shows that there are two massive cores. The western condensation corresponds to the submillimetre continuum peak and the probable source of the outflow. The eastern core is previously undiscovered and, having no associated continuum source, may be a very young protostellar condensation.

A red-shifted spur appears to break from the larger red-shifted flow lobe at a

position where the flow interacts with a large CS-traced clump of dense material. The mass in the clump is sufficient to have withstood disruption during the lifetime of the flow and appears to have caused the outflow to split and diverge.

References

Barral, J.F., Cantó, J., Meaburn, J. & Walsh, J.R., 1982. *Mon. Not. R. astr. Soc.*, **199** 817.

Beckwith. S., Zuckerman, M.F., Skrutskie, M.F. & Dyck, H.M., 1984. *Astrophys. J.*, **287**, 793.

Cabrit, S. & Bertout, C., 1986, *Astrophys. J.*, **307**, 313.

Cantó, J., Rodriguez, L.F. & Anglada, G., 1987. *Astrophys. J.*, **321** 877.

Dickel, J.R., Dickel, H.R. & Wilson, W.J., 1978, *Astrophys. J.*, **223**, 840.

Dickman, R.L., McCutcheon, W.H. & Shuter, W.L.H. 1979, *Astrophys. J.*, **234**, 100.

Fischer, J., Sanders, D.B., Simon, M. & Solomon, P.M., 1985, *Astrophys. J.*, **293**, 508.

Garden, R.P., 1986, PhD Thesis, University of Edinburgh.

Grasdalen, G.L., Strom, S.E., Strom, K.M., Capps, R.W., Thompson, D. & Castelaz, M., 1984. *Astrophys. J.Lett.*, **283**, L57.

Haschick, A.D., Reid, M.J., Burke, B.F., Moran, J.M. & Miller, G., 1981, *Astrophys. J.*, **244**, 76.

Hildebrand, R., 1983, *Q. J. R. astr. Soc.*, **24**, 267.

Hirano, N., Kameya, O., Nakayama, M. & Takakubo, K., *Astrophys. J. Lett.*, **327**, L69.

Irvine, W.M., Goldsmith, P.F. & Hjalmarson, Å, 1987. in *Interstellar Processes*, D.J. Hollenbach & H.A. Thronson eds, Reidel.

Kaifu, N., Suzuki, H., Hasegawa, T., Morimoto, M., Inatani, J., Nagane, K., Miyazawa, K., Chakada, Y., Kanzawa, T. & Akabane, K., 1984, *Astr. Astrophys.*, **134**, 7.

Königl, A., 1982. *Astrophys. J.*, **261**, 115.

Kutner, M.L. & Ulich, B.L., 1981, *Astrophys. J.*, **250**, 341.

Leung, C.M., 1976. *Astrophys. J.*, **209**, 75.

Linke, R.A. & Goldsmith, P.F., 1980, *Astrophys. J.*, **235**, 437.

Lis, D.C. & Goldsmith, P.F., 1989, *Astrophys. J.*, **337**, 704.

Little, L.T., Dent, W.R.F., Heaton, B., Davies, S.R. & White, G.J., 1985, *Mon. Not. R. astr. Soc.*, **217**, 227.

Lizano, S. & Shu, F.H., 1989. *Astrophys. J.*, **342**, 834.

Loren *et al.* 1981. *Astrophys. J.*, **245**, 495.

Margulis, M., & Lada, C.J., 1985, *Astrophys. J.*, **299**, 925.

Moneti, A., Forrest, W.J., Pipher, J.L. & Woodward, C.E., 1988. *Astrophys. J.*, **274**, 677.

Moore, T.J.T., Mountain, C.M., Yamashita, T. & Selby, M.J., 1988, *Mon. Not. R. astr. Soc.*, **234** 95.

Moriarty-Schieven, G.H., Snell, R.L., Strom, S.E. & Grasdalen, G.L., 1987 *Astrophys. J.Lett.*, **317**, L95.

Morris, M., Palmer, P., Turner, B.E. & Zuckerman, B., 1974. *Astrophys. J.*, **191**, 349.

Penzias, A.A., 1981, *Astrophys. J.*, **249**, 518.

Penzias, A.A., 1983, *Astrophys. J.*, **273**, 195.

Pudritz, R.E. & Norman, C.A., 1983. *Astrophys. J.*, **274**, 677.

Reipurth, B., Bally, J., Graham, J.A., Lane, A.P. & Zealey, W.J., 1986. *Astr. Astrophys.*, **164**, 51.

Richer, J.S., Hills, R.E., Padman, R. & Russell, A.P.G., 1989. *Mon. Not. R. astr. Soc.*, in press.

Sato, S., Nagata, T., Nakajima, T., Nishida, M., Tanaka, M. & Yamashita, T., 1985, *Astrophys. J.*, **291**, 708.

Shibata, K. & Uchida, Y., 1986, *Publ. astr. Soc. Japan*, **38**, 631.

Shu, F., Adams F.C. & Lizano, S., 1987. *Ann. Rev. Astron. Astrophys.*, **25**, 23.

Snell, R.L., Scoville, N.Z., Sanders, D.B. & Erikson, N.R., 1984, *Astrophys. J.*, **284**, 176.

Taylor, D.K. & Dickman, R.L. 1989, *Astrophys. J.*, **341**, 293.

Wynn-Williams, C.G., Becklin, E.E. & Neugebauer, G., 1974, *Astrophys. J.*, **187**, 473.

Yamashita, T., Sato, S., Tamura, M., Suzuki, H., Kaifu, N., Takano, T., Mountain, C.M., Moore, T.J.T., Gatley, I. & Hough, J.H., 1987, *Publ. astr. Soc. Japan*, **39**, 809.

Yamashita, T., Sato, S., Tamura, M., Suzuki, H., Gatley, I., Hough, J.H., Mountain, C.M. & Moore, T.J.T., 1988, *Mon. Not. R. astr. Soc.*, **233** 899.

Chapter 4

Submillimetre Continuum Observations of AFGL 2591 and W75N

The complex radiative transfer and a priori assumptions of molecular abundances caused quite large uncertainties in the CS line analysis of the W75N dense core. Observations were therefore made, at similar spatial resolution, of the thermal emission from cool dust at submillimetre wavelengths, where the radiation is almost guaranteed to be optically thin and the emission mechanism is simple. In order to check the reliability of the mass-tracing properties of CS, a comparative study was done of AFGL 2591 in which molecular line data appeared to show an elongated structure suggesting the type of large interstellar disk evidently missing in W75N.

The observations contained in the following chapter were made during PATT allocation U/L/17 and are part of a collaboration with C.M. Mountain and T. Yamashita.

Summary

350-μm, 800-μm and 1100-μm continuum observations have been made (with angular resolutions of between 20 arcsec and 1 arcmin) around the bipolar molecular outflow sources AFGL 2591 and W75N. The cloud cores, as traced by emission from cool ($\sim$ 30 K) dust, are spatially resolved in both cases but show little physical structure which can be convincingly related to the molecular outflows. The AFGL 2591 cloud core is found to be approximately 0.25pc by 0.1pc in size and contains 300 to 500 $M_\odot$ of material. The mean space density in the central regions is at least 4.7×10^{11} m^{-3}. The calculated mass is probably not sufficient to provide large-scale confinement and collimation, even if the outflow were initially isotropic, and other evidence suggests that significant collimation occurs on much smaller scales. Since the observed morphology of this core appears to depend on which emission mechanism is used to trace gas

column density, care may be necessary when interpreting large, elongated structures in other sources as interstellar disks.

In W75N, an extended, roughly symmetrical cloud core is found, in which the dominant heating source is the OH maser and compact HII region HII(B). Either a single-component or a dual-component model of the dust temperature can satisfactorily account for the observed submillimetre emission. These two models predict a cloud core mass in the region of 1800 to 2500 $M_{\odot}$ and an average density of $(4.5-6.0)\times 10^{11}$ m^{-3} . The large derived masses are consistent with a region heated by a cluster of embedded young sources. There is no evidence in the observations of any > 0.2 pc sized disk structure surrounding the outflow source in W75N. The mass in the large cloud core is found to provide sufficient gravitational force to confine and collimate the CO outflow on large scales. A single submillimetre grain emissivity law, proportional to λ^{-2}, is consistent with the observations.

4.1 Introduction

Past studies in molecular lines have reported observations of large ($\sim$ 0.1-pc), possibly rotating, dense interstellar disks or toroids around bipolar outflow sources (e.g. Kaifu *et al.* 1984; Hasegawa *et al.* 1984; Torrelles *et al.* 1984; Little *et al.* 1985; Jackson, Ho & Haschick 1988). However, the morphological appearance of the putative disk structures is not always consistent when observed in different molecules or transitions (see Moriarty-Schieven *et al.* 1987). This tendency is probably indicative of complex molecular excitation or formation conditions. By contrast, continuum emission at submillimetre wavelengths is commonly accepted as a reliable tracer of dust (and hence gas) column density, since optical depths are generally low and the emission mechanism is simple (Hildebrand 1983). The following chapter therefore presents submillimetre continuum measurements of AFGL 2591 and W75N, which are both at distances of about 2 kpc (Dickel, Dickel and Wilson 1978 and Merrill & Soifer 1974), in order to investigate the cloud core structure around these two outflow sources, with reference to the outflows themselves, and to obtain estimates of the basic physical parameters for comparison with the existing molecular line data.

AFGL 2591 is one of the most well-studied galactic star-forming regions, first attracting attention for its BN-like infrared spectrum (Merrill & Soifer 1974). The source also shows large near-infrared polarisation fractions, with a vector pattern that

suggests scattering by dust above and below a dense disk lying perpendicular to the CO outflow (Hodapp 1984; Sato *et al.* 1985). Recent mapping observations of CS transitions (Yamashita *et al.* 1987) show asymmetric structures of dense material around AFGL 2591 on scales of 1 arcmin. The dense cloud core material traced by CS (J=1–0) was shown to be elongated in a north-south direction; however, the higher contours of CS (J=2–1) appeared to show some extension along a roughly east-west axis as well as signs of a velocity gradient in that direction. A similar velocity gradient was previously found by Takano *et al.* (1986) in lower resolution NH_3 observations. Since the only available observations of the extensive CO outflow from AFGL 2591 are the ~ 1 arcmin resolution map of Lada *et al.* (1984) which do not reveal a convincing outflow direction, it is difficult to define an expected axis for any associated molecular disk.

W75N is an outflow and OH maser source that has been rather less well studied in the past. Wynn-Williams *et al.* (1974) detected a 10-μm and 20-μm continuum source close to the more extended northern HII region, HII(A) (using the nomenclature of Haschick *et al.* 1981), while Harvey, Campbell & Hoffman (1978) found emission between 53 μm and 175 μm peaking around 30 arcsec further south, a position later discovered to coincide with a compact HII region and maser source HII(B). A small group of reddened near-infrared sources was found close to HII(B) in Chapter 2, along with extended molecular hydrogen emission possibly associated with the CO outflow first studied by Fischer *et al.* (1985). Recent measurements at much higher resolution (Chapter 3) have revealed this flow to be strongly collimated, but with an irregular large-scale structure. Also in Chapter 3, observations of the high-density tracer CS showed a large cloud core surrounding all the major sources. This core contained no sign of a large disk structure associated with the CO flow, but was able to confine and collimate the large-scale molecular outflow. The structure of the outflow appeared to be determined principally by interactions with the inhomogeneous density distribution in the dense ambient gas.

2-μm continuum polarisation observations have been made by Yamashita *et al.* (1988), revealing a near-infrared reflection nebula around the embedded objects. Follow-up high-resolution imaging polarimetry has also been done (Chapter 6), the pattern of polarisation vectors indicating an illuminating source associated with HII(B). photometric analysis of the scattered near-infrared light indicates considerable amounts of hot dusty material exists very close to the illuminating source.

4.2 Observations and Results

The observations were made during 1987, July 14, 15 and 17, using the 3.8m U.K. Infrared Telescope (UKIRT) in Hawaii, with the ^{3}He-cooled, single-element bolometer system UKT14. A 21-mm aperture at 350-μm gave a 20-arcsec beam on the sky and at 1100-μm a 65 mm aperture gave approximately 1-arcmin resolution. An east-west chopper throw of 150 arcsec was used and a pointing accuracy of $\sim$ 3 arcsec rms was maintained throughout the observations by frequent visual observations of nearby positional standards. Sky transmission and flux calibration were obtained from repeated observations of Uranus, Jupiter and Saturn. Absolute calibration errors are estimated at around 10 per cent at 1100 μm, 15 per cent at 800 μm and 35 per cent at 350 μm. The majority of these uncertainties arise from the calculation of atmospheric extinction; corresponding mean statistical errors were 0.7 Jy, 1.8 Jy and 15 Jy, respectively, after $\sim$ 40s net integration time per position.

Figs 4.1 to 4.4 show the spatial distribution of the submillimetre continuum in the two sources. Asymmetric structure is resolved in the strong 350-μm emission from AFGL 2591 (Fig. 4.1) with clear elongation along a northwest-southeast axis. At 1100 μm (Fig. 4.2), extended structure is partially resolved in the low-level emission. A slice along the elongated axis of the 350-μm source is shown in Fig. 4.3, with a fitted Gaussian profile. This fit implies a half-power size of 33 ± 6 arcsec and thus a physical size of 26 ± 7 arcsec, when deconvolved from a perfect 20-arcsec Gaussian beam. The short axis half-power best fit is 23 ± 2 arcsec, which deconvolves to 11^{+4}_{-6} arcsec. However, while the long axis fit has a good reduced χ^2 statistic of 0.6, that along the short axis has $\chi^2 = 9$, indicating a poor fit. The strong 350-μm emission appears to be essentially unresolved in the northeast-southwest direction with low flux levels extending towards the north. Best fits of Gaussian profiles to the 1100-μm emission from AFGL 2591 give half-power sizes of 52 ± 4 ($\chi^2 = 2.5$) and 49 ± 2 ($\chi^2 = 5$), in the north-south and east-west directions, respectively.

A fully-sampled map of the strong 350-μm emission from W75N is presented in Fig. 4.4 along with the results of measurements at 800 μm and 1100 μm; positional offsets are given in arcsec from $20^h36^m50^s.0$ $+42°26'59''$ (1950). At 350 μm the edge of the emission was not found: at the boundaries of the map the mean surface brightness is about one sixth of the peak and detected with a signal-to-noise ratio close to 7. The map shows extended emission that is roughly symmetrically distributed, with no sign

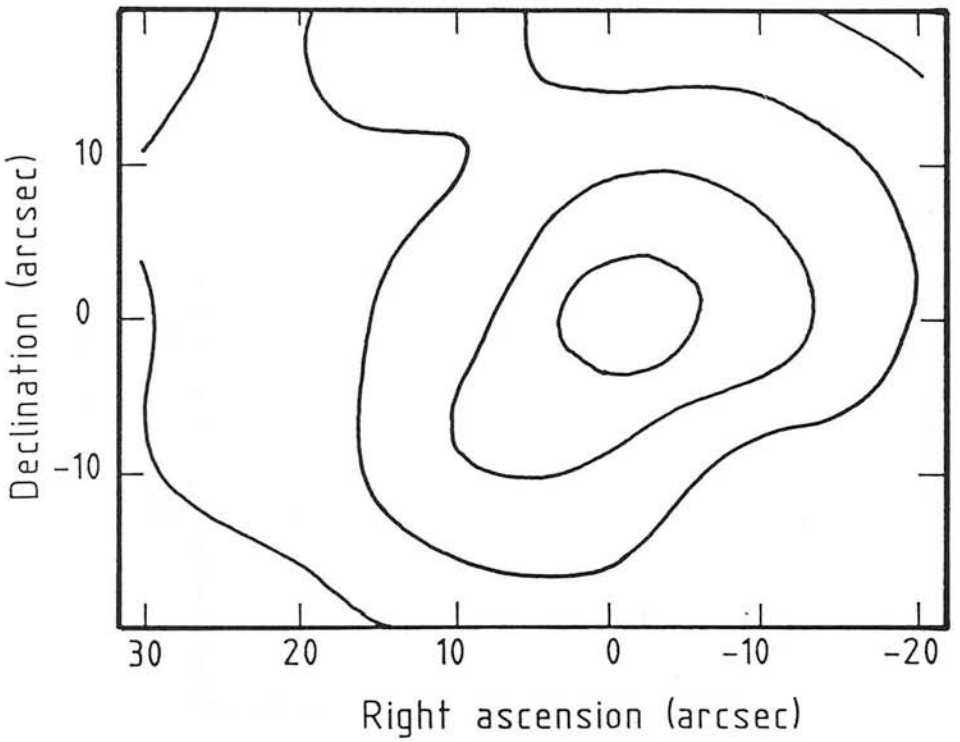

Figure 4.1: The 350-μm continuum at 20 arcsec resolution in AFGL 2591. The map is sampled at 10-arcsec intervals and the offset centre is $20^{h}27^{m}35.^{s}8, +40°01'14''$ (1950). Contours are at 30, 60, 90 and 120 Jy per beam.

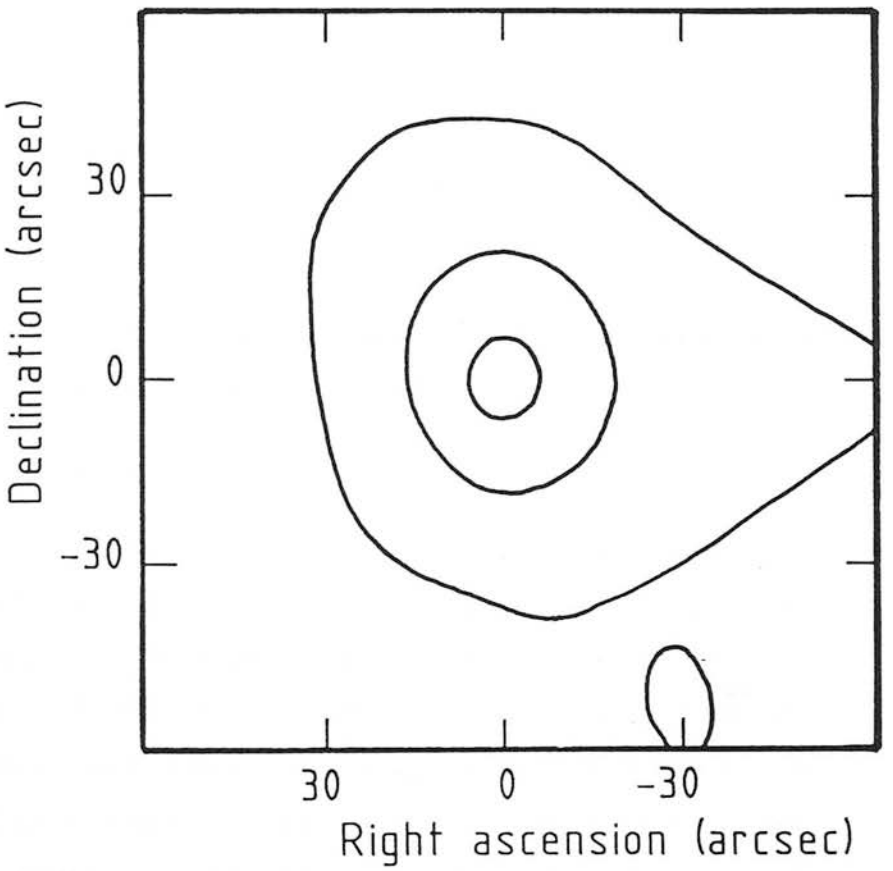

Figure 4.2: 1100-μm continuum map of AFGL 2591 with 1 arcmin resolution and a 30-arcsec sampling grid. The offset centre is the same as in Fig. 4.1 and contours are at 2.4, 4.8 and 7.2 Jy per beam.

of any 0.2-parsec- scale disk structure with which to associate the bipolar CO outflow. Cuts across the peak in RA and Dec yield better Gaussian fits to the data at 800-μm than at 350 μm, the former having a reduced χ^2 value of 2.8 as opposed to ~ 8 in the latter. The best-fit curves have full widths at half maximum (FWHM) of 64 ± 1 arcsec (RA) and 61 ± 1 arcsec (Dec), peaking at offset (−4, +1). The 1100-μm distribution produces a good Gaussian fit ($\chi^2 = 0.4$) with FWHM 78 ± 3 arcsec (RA) and 82 ± 3 arcsec (Dec), peaking at offset (+3, +2).

4.3 Discussion

4.3.1 Source Geometry and Strength

4.4.1.1 AFGL 2591

If we were to assume that the source has an overall gaussian shape, we could deconvolve the true source flux density from the 350-μm map by

$$S_\nu = S_\nu(peak) \times \left(\frac{\Omega_s + \Omega_b}{\Omega_b} \right)$$

Here, Ω_s and Ω_b are the source and beam solid angles, respectively, and S_ν(peak) is the peak value in the surface brightness (flux density per beam) map. This method yields $S_\nu = 144 \times 1.71 = 250 \pm 100$ Jy for AFGL 2591 which is in very good agreement with that measured by Rieke *et al.* (1973) in a 63-arcsec beam. Unfortunately, the above method is rather unreliable in the present case since the source is neither well-resolved nor well-approximated by a Gaussian in the northeast-southwest (short axis) direction.

In order to avoid the errors involved in *a priori* assumptions of the source shape, the deconvolved source flux densities are estimated by simply removing the oversampling factor in the maps. If the beam is taken to be Gaussian and the sampling frequency is equal to half the full width at half maximum, this factor is 4.51 (see Appendix C). The flux density per beam, integrated over the 350-μm map of AFGL 2591 (Fig. 4.1) is 1477 Jy. The total flux density in the map is therefore $1477/4.51 = 330 \pm 100$ Jy which is still in good agreement with Rieke *et al.* (1973). This estimate contains an unquantified error associated with the assumption of a perfect Gaussian beam but not that introduced by presupposing a Gaussian source as well.

The deconvolved AFGL 2591 flux density at 1100 μm is similarly determined to be 9 ± 2 Jy. This is hardly different from the observed peak value of 8.5 Jy, indicating an unresolved source in the larger beam, although there is evidence in Fig. 4.2 for

some extended low-level emission towards the north and west. The deconvolved total flux densities for AFGL 2591 at each observed wavelength are given in Table 4.1.

The elongated shape of the AFGL 2591 core (as observed at 350 μm), centred as it is on the probable outflow source, is a morphology that is instantly suggestive of a large edge-on disk structure. This is made more plausible by considering that the flux distribution is unresolved in the direction of the minor axis, and the true axis ratio must be as high as 2:1 or even 3:1. However, as discussed in §4.4.3, the evidence from other observations does not tend to support this explanation.

4.4.1.2 W75N

At submillimetre wavelengths the individual embedded sources in the W75N region, identified in Chapters 2 & 6, are swamped by emission from the cooler dust of the surrounding cloud core (Fig. 4.4) and do not appear as individual peaks, although there is sufficient spatial resolution in the present 350-μm observations. Within the pointing accuracy of the observations, the continuum radiation at all three observed wavelengths peaks at the position of HII(B), as does that at 53 μm (Harvey, Campbell & Hoffman 1978). HII(B) is evidently the dominant luminosity source within the W75N cloud core, since the maximum of the continuum flux distribution occurs in the far-infrared (Fig. 4.6). HII(B) is also the likely source of the bipolar molecular outflow in the region, from 15-arcsec resolution CO observations (see Chapter 3).

The general shape of the W75N cloud core is symmetrical, resembling the inner regions of the core as traced by CS rotational transitions (Chapter 3). There is no indication of structure related to the large CO outflow in the region. If a large disk were present it must be orientated nearly face-on to the observer, but this is not borne out by the near-infrared observations (Chapters 2 & 2) which indicate a very large column of material ($A_V \gtrsim 90$ mag) towards the central source. Source flux densities, calculated in the same way as for AFGL 2591, are listed in Table 4.1. The value at 350 μm for is likely to be an underestimate, since some significant emission was lost outside the mapped area.

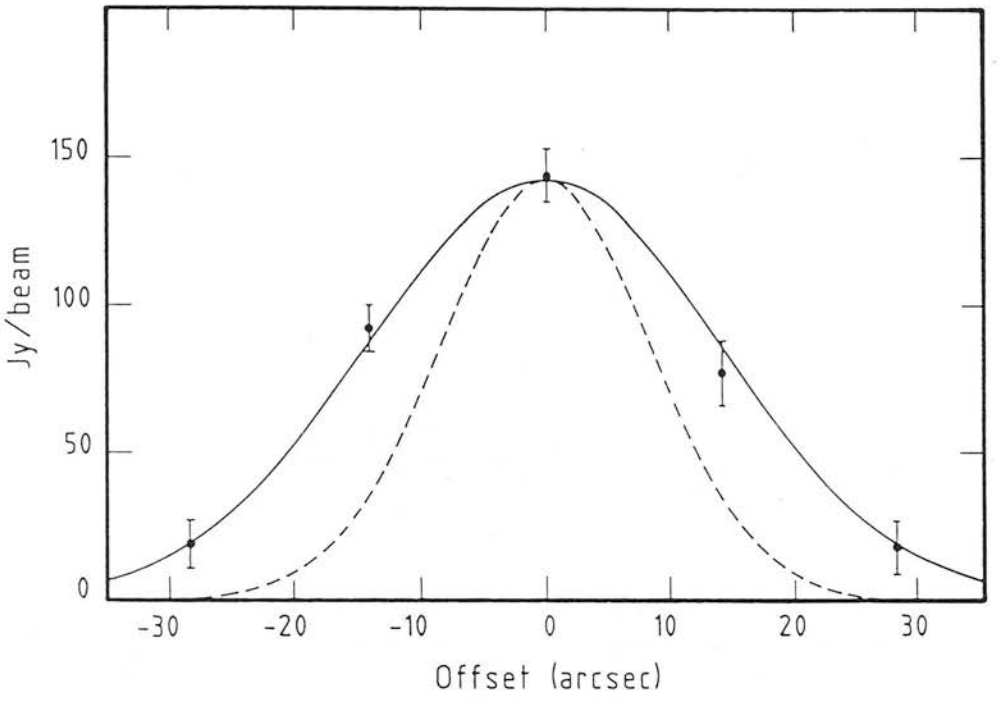

Figure 4.3: A northwest-southeast slice through the offset centre in Fig. 4.1. The solid curve is the best-fit gaussian for the data and the dashed curve is a gaussian with FWHM = 20 arcsec, representing the 350-μm beam. Error bars show statistical uncertainties. Southeast is to the left.

Table 4.1: Deconvolved Submillimetre Continuum Strengths

Object	Integrated Source Flux Density /Jy		
	$S_\nu(350\,\mu\mathrm{m})$	$S_\nu(800\,\mu\mathrm{m})$	$S_\nu(1100\,\mu\mathrm{m})$
AFGL 2591	330 ± 100	–	9 ± 2
W75N	1170 ± 440	92 ± 18	23 ± 4

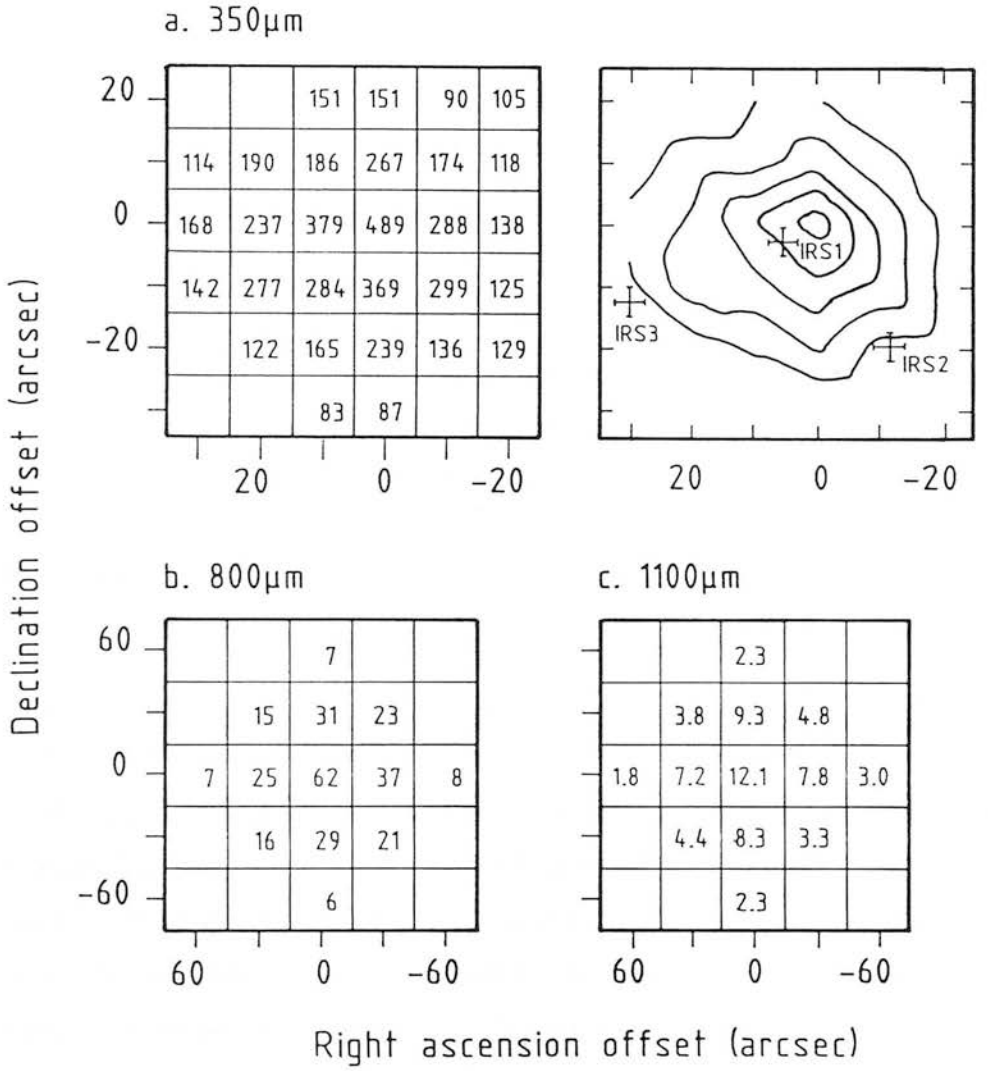

Figure 4.4: (a) Fully-sampled 350-μm map of the central region around W75N HII(B). Contours are at intervals of 75 Jy per 20-arcsec beam, from 150 Jy per beam. The offset centre is at $20^{h}36^{m}50.^{s}0, +42°26'59''$, the position of the compact HII region HII(B). The error bars indicate the positions of the three bright near-infrared sources found in Chapter 2(b) and (c) 800-μm and 1100-μm flux densities observed at 30-arcsec intervals around the position of HII(B), with a $\sim$ 1-arcmin beam.

4.3.2 Dust Temperature

4.4.2.1 AFGL 2591

In AFGL 2591, $S_{350} = 330$ Jy and $S_{1100} = 9$ Jy give a 350 μm/1100 μm colour temperature of only about 18 K (assuming an emissivity law $\propto \lambda^{-2}$). However, using IRAS SKYFLUX data, points at wavelengths longer than 60 μm fit well to a single-temperature grey body (again with λ^{-2} emissivity) at 36 K (Fig. 4.5), with no evidence of a significant cold (< 20 K) dust component affecting the long wavelength emission. We therefore adopt 36 K as the representative dust temperature, and assume that the emissivity follows a λ^{-2} law at both 350 μm and 1100 μm. Although evidence has been found in favour of a significant change in grain emissivity between 350 μm and 1100 μm (Gear, Robson & Griffin 1988) in similar objects, we lack a mid-wavelength point for AFGL 2591 and so adopt the simplifying assumption of a single law.

4.4.2.2 W75N

The integrated continuum data for W75N at wavelengths longer than 100 μm can be fitted with a single-temperature, 29K grey body function (Fig. 4.6(a)). Alternatively, if the 60-μm point is included in the fit, it is possible to use a "central" warm component ($T_{\rm d} = 35$ K, $\tau_{350} = 0.03$) plus an "outer" cool component ($T_{\rm d} = 19$ K, $\tau_{350} = 0.09$) to reproduce the data (Fig. 4.6(b)). Such a model can be viewed as a crude approximation of a temperature gradient, and thus as a somewhat more physical representation of a cloud core heated internally by a number of embedded sources. The justification for including the 60-μm point in the fit to longer wavelengths is the 53-μm map of Harvey, Campbell & Hoffman (1978) in which emission also peaks close to HII(B) and extends over a similar area to the 350-μm map in Fig. 4.4. This implies that the 50-μm continuum traces the same dusty material as the observed submillimetre wavelengths. In contrast, the continuum at 20 μm has been found to peak towards the northern HII region HII(A) (Chapter 5), and traces a quite different mass and temperature component. The fits in Fig. 4.6 also assume a single emissivity law $\propto \lambda^{-2}$, which is consistent with the present data. The large calibration error at 350 μm renders it difficult to determine whether the emissivity exponent changes appreciably between 800 μm and 1100 μm. On the other hand the possibility mentioned above, that the derived 350-μm flux density is somewhat underestimated, makes such a steepening unlikely in W75N.

The comparable quality of the single- and dual-component fits to the observations illustrates the difficulty in finding a unique physical explanation for long-wavelength data in many cases. Thus we have used both models to estimate the molecular hydrogen column density and total gas mass in the W75N cloud core and, as will be seen in the following section, the results are similar enough to provide a reliable and convincing picture of the density conditions in the cloud. Since the full extent of the diffuse 350-μm radiation is not known, I have used the approximate observed area of the strong emission (50 × 50 arcsec) to define a nominal source size. The assumed size will affect the estimates of mean optical depth, space density and column density, but not that of the final mass.

4.3.3 Column Density, Space Density and Mass

Mean optical depths at the different wavelengths and temperatures were calculated by comparison of the deconvolved source flux density, $S_\nu(\lambda)$, to the flux density, $\Omega_s B_\nu(\lambda, T_d)$ from a black body with the same solid angular size Ω_s and with a temperature equal to the derived dust temperature T_d, by

$$1 - e^{-\tau} = \frac{S_\nu(\lambda)}{\Omega_s B_\nu(\lambda, T_d)}.$$

Upper limits to the source dimensions are given by the observed half-power sizes (33×23 arcsec in the case of AFGL 2591). If the deconvolved 350-μm source flux density is 330 Jy and if $T_d = 36$ K is a suitable representative temperature as obtained in §5.3.3, then we obtain $\tau_{350} \geq 0.05$ for this source.

In order to convert dust optical depths to hydrogen column densities, $N(\mathrm{H})$, we employ a simplified version of the relation used by Mezger *et al.* (1987), i.e.

$$N(\mathrm{H}) = \frac{1.43 \times 10^{24}}{b} \times \lambda^2(\mu\mathrm{m}) \times \tau_\lambda \ \mathrm{m}^{-2}$$

which predicts the total column density of hydrogen nuclei and assumes a grain emissivity proportional to $\lambda^{-2.0}$. b is a measure of the dust cross-section and takes some value in the empirically determined range $1 < b < 3.4$. Adopting $b = 1.9$ in concordance with Hildebrand (1983) and assuming all the hydrogen is in molecular form, the values of $N(\mathrm{H_2})$ and average space density $n(\mathrm{H_2})$ are calculated and listed in Table 4.2.

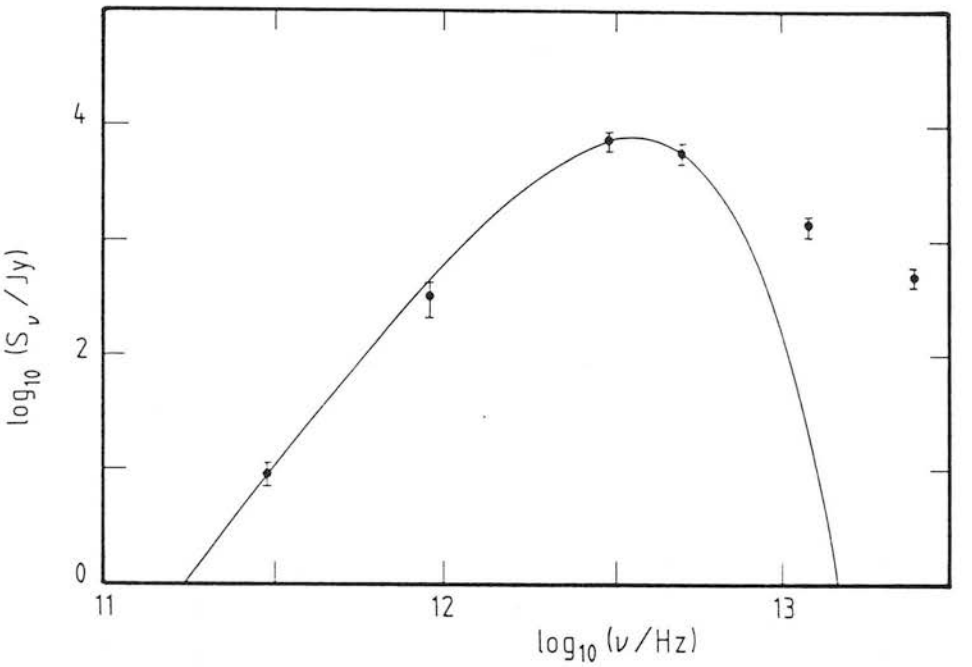

Figure 4.5: Data for AFGL 2591 at wavelengths greater than 12 μm. The 12-μm to 100-μm points are taken from IRAS SKYFLUX maps. The fitted curve is a single temperature grey body function with grain emissivity $\propto \lambda^{-2.0}$ and T = 36 K.

Table 4.2: Derived Cloud Core Parameters (single temperature models)

Object	λ / μm	τ_λ	$N(H_2)$ /10^{27} m^{-2}	M_{core} / $M_\odot$	$n(H_2)$ /10^{11} m^{-3}
AFGL 2591	350	≥ 0.05	2.3	300 ± 100	2.3
	1100	$\geq 2.9 \times 10^{-3}$	1.3	500 ± 100	0.9
W75N	350	0.088	4.1	1700 ± 600	4.0
	800	0.022	5.3	2200 ± 400	5.3
	1100	0.009	4.1	1700 ± 200	4.1

Table 4.3: Derived W75N Core Parameters (dual temperature model)

λ / μm	$S_\nu(\lambda, 35K)$ /Jy	$S_\nu(\lambda, 19K)$ /Jy	τ_λ	$N(H_2)$ /10^{27} m^{-2}	M_{core} / $M_\odot$	$n(H_2)$ /10^{11} m^{-3}
350	680	490	0.125	5.8	2400 ± 900	5.8
800	45	47	0.029	7.1	2900 ± 500	7.0
1100	11	12	0.012	5.5	2200 ± 300	5.5

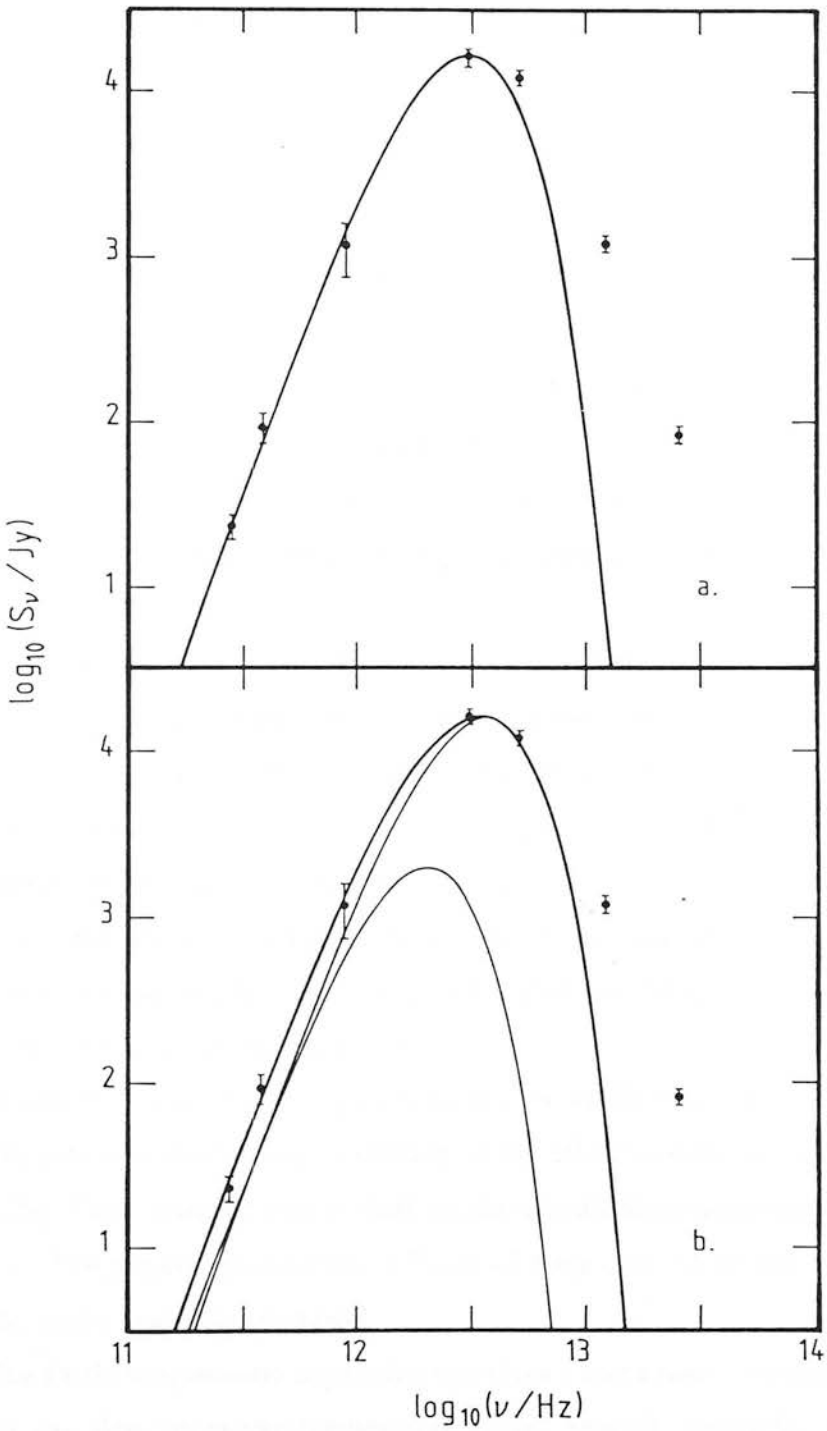

Figure 4.6: (a) Single temperature grey-body fit to the continuum spectrum of W75N. The grain emissivity exponent is taken as 2.0. The fit is to points with $\lambda \geq 100\,\mu$m, giving $T_{\rm d} = 29$ K and $\tau(350\text{ m}) = 0.09$. (b) Two-temperature model of W75N with $T_{\rm d} = 35$ K, $\tau(350\text{ m}) = 0.04$ and $T_{\rm d} = 19$K, $\tau(350\,\mu\text{m}) = 0.09$, including $\lambda = 60\,\mu$m in the fit.

If the optical depth is small, the masses of the cloud cores can be more directly derived from the source flux densities without having to take account of the source size. Since $M \simeq \Omega_s D^2 N(\mathrm{H}) \times m_\mathrm{H} \times \mu_\mathrm{H}$, using $\tau_\lambda \simeq S_\nu(\lambda)/\Omega_s \mathrm{B}_\nu(\lambda, T)$ and the conversion to hydrogen column density given above, it follows that

$$M(\lambda, T) \simeq 8.4 \times 10^{-6} \times \left(\frac{D}{1\mathrm{kpc}}\right)^2 \times \left(\frac{\lambda}{1\,\mu\mathrm{m}}\right)^2 \times \left(\frac{S_\nu}{1\mathrm{Jy}}\right) \times \left(\frac{10^{11}\mathrm{Jy/Sr}}{\mathrm{B}_\nu}\right) \quad \mathrm{M}_\odot.$$

The uncertainty involved in assuming a source size does not, therefore, affect the total mass estimates for the cloud cores. The ratio of total gas mass to hydrogen mass (μ_H) is taken as 1.36 and a distance of 2 kpc is assumed for both W75N and AFGL 2591 (Merrill & Soifer 1974; Dickel, Dickel & Wilson 1978). In both cases the three-dimensional source geometries are assumed to be roughly the solids of revolution arising from the observed 2-dimensional morphologies and the internal density is taken to be constant.

The mass of 1000 $\mathrm{M}_\odot$ calculated from CS data by Yamashita *et al.* (1987) for the AFGL 2591 core is approximately twice that obtained from the 1100-μm data which, in turn, is larger than the 350-μm estimate. The former discrepancy can be accounted for by the somewhat larger observed size of the core in the CS line, or by uncertainties in the relative molecular abundance and the value of b, above. Since low-level emission is present at the edges of the region sampled at 350 μm and the 1100-μm observations cover a considerably larger area, there is some evidence for a diffuse dust component exterior to the densest part of the core.

In the dual-temperature approximation for W75N, the source flux density is separated into two components according to the relative contributions inferred from Fig. 4.6(b). Two corresponding optical depths are calculated separately and added to obtain τ_λ. The physical parameters in Table 4.3 were then calculated in the same way as for the single-temperature model.

The single-temperature approximation gives a mean mass estimate of 1800 ± 400 $\mathrm{M}_\odot$ and the alternative two-temperature model, roughly simulating a temperature gradient in the core, predicts 2500 ± 600 $\mathrm{M}_\odot$. The errors quoted here are observational, and the factor of ~ 2 uncertainty in the dust optical depth to gas column density conversion is left implicit. The two mass estimates are not statistically consistent, as they arise from the same data and their errors are dominated by the same calibration uncertainties, and yet they are similar enough to give a reliable figure for the core

mass. If the source is approximated by a homogeneous sphere of diameter 50 arcsec, the mean molecular hydrogen density is 4.5 or 6.0×10^{11} m^{-3}. The large mass estimate is consistent with a cluster of young sources heating an extended core region. As with AFGL 2591, the corresponding value obtained from CS observations ($\sim$ 2700 $M_{\odot}$, see Chapter 3) is consistent with both submillimetre continuum estimates, given its large uncertainty (approximately a factor of two).

4.3.4 Relevance of Associated Molecular Observations

The CS(J=1–0) emission in AFGL 2591 has a completely separate morphology from the submillimetre continuum, being extended in the north-south direction (Yamashita *et al.* 1987). This appears to reflect the large-scale (0.5pc – 1pc) structure in the outer regions of the AFGL 2591 cloud core, where the density is around the critical value of $n_{\rm crit} \simeq 4 \times 10^{10}$ m^{-3} for the J=1–0 line. The J=2–1 transition of the same molecule, however, has an apparently mixed form. The low-level emission follows the J=1–0 north-south orientation, while the high-level contours are elongated roughly east-west. The higher resolution in the latter observations also picks out a velocity gradient aligned roughly east-west which may be related to that found by Takano *et al.* (1986) in NH_3. The morphology of the J=2–1 emission may reflect the tendency of this line to trace denser material ($n_{\rm crit}$ of the J=2–1 line is $\sim 2 \times 10^{11}$ m^{-3}) or may simply be a consequence of the smaller beam at this transition. The higher optical depth of J=2–1 means that the shape of the central core structure is not completely revealed, despite spatial resolution comparable to our 350-μm data.

High-resolution NH_3 observations of AFGL 2591 (Torrelles *et al.* 1989) do not appear to show any large solid structure in the warm central regions of the cloud. On the contrary, these observations seem to reveal an internally heated cavity, presumably swept out by the bipolar outflow, with large temperature gradients in the surrounding material. This conclusion is strongly supported by the observations of Forrest & Shure (1986) who also identified a bubble or cavity at near-infrared wavelengths. This cavity is coincident with the region of strong 350 μm emission, which cannot therefore be delineating a large coherent disk structure. Temperature variations within the dense material may dominate over column density in determining the observed intensity distribution.

Following Gear *et al.* (1986), we can make a simple determination of the ability of the cloud cores to collimate the associated molecular outflows, by comparing the

gravitational binding force in the dense material with the integrated momentum flux in the high-velocity gas. The rate of momentum deposition by an outflow is

$$F_f \sim \frac{M_f V_f^2}{r_f}$$

where M_f, V_f and r_f are the mass, velocity and length of the outflow lobes, respectively. The binding force on a core of mass M_c with a Gaussian density distribution of half-maximum size $r_{1/2}$ and containing a central source of mass M_* is given by

$$F_c = GM_c \frac{((2\ln 2)M_* + 0.25M_c)}{r_{1/2}^2}$$

(see Appendix B) which must be greater than F_f for a static core in order to confine an initially isotropic, momentum-conserving wind.

In the case of AFGL 2591, for a single central source of total luminosity 9×10^4 $L_\odot$ (implying $M_* \sim 20$ $M_\odot$) and known CO flow parameters (Lada *et al.* 1984), the disk would provide confinement if the total mass in the flow were less than 50 $M_\odot$. By following Snell *et al.* (1984) we can estimate a value for the flow mass of $\sim 25 \times \tau/(1 - e^{-\tau})$ $M_\odot$, from the ^{12}CO observations of Lada *et al.* (1984). Since the mean optical depth in the line wings may well reach values of $\tau \simeq 8$ or more (by comparison with Margulis & Lada 1985), it is clear that the large-scale core structure observed at 350 μm in AFGL 2591 is unlikely to provide significant collimation of the CO flow on 0.1pc - 0.2pc scales.

The high-resolution near-infrared maps obtained by Forrest & Shure (1986), supported by recent NH_3 observations with the VLA (Torrelles *et al.* 1989), point to an elongated cavity in the cloud close to, and heated internally by, the IR source. Such a cavity is likely to have been created by the outflow itself which must then be collimated on much smaller scales ($\lesssim$ 0.01pc). In such a situation, the specific momentum flux in the outflow is increased and the possibility of confining the flow on large scales is diminished even further.

In the case of W75N, a core mass of around 2,000 $M_\odot$ and an effective embedded stellar mass of $\sim$ 200 $M_\odot$ would provide containment of an initially isotropic outflow with $F_f \ll 3\times10^{24}$ N. From the analysis in Chapter 3 the total force on the cloud due to the outflow is $\gtrsim 2\times10^{23}$ N. This means that, unless the majority of the outflow material is moving with a trajectory inclined less than about 10° to the plane of the sky, the core material presents an effective barrier to the passage of the flow. Hence, the anisotropic large-scale flow structure is probably produced through physical confinement by the

dense core as it finds its way out of the cloud. If the outflow were initially collimated on much smaller scales ($\ll$ 0.1pc), the specific momentum flux delivered to the cloud material would be much higher and the flow would push a straight path through the cloud much more easily. However, the irregular appearance of the CO outflow argues that any such intrinsic collimation was lost close to the source (see Chapter 3).

4.4 Conclusions

We have resolved the cloud core structure around the outflow sources W75N and AFGL 2591 as traced by the submillimetre continuum emission from cool ($\sim$ 30K) dust. In W75N, the gravitational binding force in the cloud core is capable of confining and collimating the large-scale outflow. In AFGL 2591, the observed cloud core mass is not capable of effective constraint of the associated molecular outflow by this means.

The central mass distribution in AFGL 2591 is elongated in a northwest-southeast direction. From observations at 350 μm, this region is about 0.25 $\times$ 0.1 pc in size, contains 300 $M_\odot$ to 500 $M_\odot$ of material and is apparently centred on the IR source and probable outflow centre. Despite the morphology, there is little evidence to identify this asymmetrical structure as a disk or torus causally connected to the bipolar outflow. There is evidence from high-resolution near-infrared and NH_3 line data that significant collimation occurs on much smaller scales close to the source. The mean density in the central core is at least 5×10^{11} m^{-3}. The 1100-μm emission from AFGL 2591 is rather compact but also shows evidence of an extended, diffuse envelope surrounding the central dense zone.

In W75N, the dense cloud core is extended on a scale of $\sim$ 0.5 pc, is roughly symmetrical and shows no evidence of disk structure larger than 0.2 pc which one might associate with the coincident CO outflow. The dominant heating source in the area appears to be the compact HII region and OH maser HII(B). The integrated continuum emission beyond 60 μm can be represented by either a single 29 K dust temperature or a dual-temperature (19 K and 35 K) composite model. The latter approximation is more physically appropriate since it accommodates the known 53-μm source morphology, which indicates an origin within the same mass component as longer wavelength emission, and since it represents more satisfactorily the likely presence of a temperature gradient. The two models predict total cloud core masses of 1800 and 2500 $M_\odot$, respectively. The corresponding mean particle densities in a

0.5-parsec sphere are 4.5 and 6.0×10^{11} m^{-3}. The large mass estimate is consistent with the heating of an extended region by a cluster of embedded young sources, but is insufficient to have a significant effect on the collimation of the high-velocity outflow. A single-exponent submillimetre grain emissivity law, proportional to λ^{-2}, is most compatible with the data.

References

Dickel, J.R., Dickel, H.R. & Wilson, W.J., 1978, *Astrophys. J.*. **223**, 840.

Fischer, J., Sanders, D.B., Simon, M. & Solomon, P.M., 1985, *Astrophys. J.*, **293**, 508.

Forrest, W.J. & Shure, M.A., 1986, *Astrophys. J. Lett.*, **311**, L81.

Gear, W.K., Gee, G., Robson, E.I., Ade, P.A.R. & Duncan, W.D., 1986, *Mon. Not. R. astr. Soc.*, **219**, 835.

Gear, W.K., Robson, E.I. & Griffin, M.J., 1988, *Mon. Not. R. astr. Soc.*, **231**, 55P.

Harvey, P.M., Campbell, M.F. & Hoffman, W.F., 1977, *Astrophys. J.*, **211**, 786.

Haschick, A.D., Reid, M.J., Burke, B.F., Moran, J.M. & Miller, G., 1981, *Astrophys. J.*, **244**, 76.

Hasegawa, T., Kaifu, N., Inatani, J., Morimoto, M., Chikada, Y., Hirabayashi, H., Iwashita, H., Morita, K., Tojo, A. & Akabane, K., 1984, *Astrophys. J.*, **283**, 117.

Hildebrand, R., 1983, *Q. J. R. astr. Soc.*, **24**, 267.

Hodapp, K. -W., 1984, *Astr. Astrophys.*, **141**, 255.

Jackson, Ho, P.T.P., Haschick, A., 1988, *Astrophys. J. Lett.*, **333**, L73.

Kaifu, N., Suzuki, H., Hasegawa, T., Morimoto, M., Inatani, J., Nagane, K., Miyazawa, K., Chakada, Y., Kanzawa, T. & Akabane, K., 1984, *Astr. Astrophys.*, **134**, 7.

Königl, A., 1982. *Astrophys. J.*, **261**, 115.

Lada, C.J., Thronson, H.A., Jr, Smith, H.A., Schwarz, P.R. & Glaccum, W., 1984, *Astrophys. J.*, **286**, 302.

Little, L.T., Dent, W.R.F., Heaton, B., Davies, S.R. & White, G.J., 1985, *Mon. Not. R. astr. Soc.*, **217**, 227.

Margulis, M., & Lada, C.J., 1985, *Astrophys. J.*, **299**, 925.

Merrill, K.M. & Soifer, B.T., 1974, *Astrophys. J. (Lett.)*, **189**, L27.

Mezger, P.G., Chini, R., Kreysa, E. & Wink, J., 1987, *Astr. Astrophys.*, **182**, 127.

Moneti, A., Forrest, W.J., Pipher, J.L. & Woodward, C.E., 1988. *Astrophys. J.*, **327**, 870.

Moriarty-Schieven, G.H., Snell, R.L., Strom, S.E. & Grasdalen, G.L., *Astrophys. J. Lett.*, **317**, L95.

Pudritz, R.E. & Norman, C.A., 1983. *Astrophys. J.*, **274**, 677.

Reipurth, B., Bally, J., Graham, J.A., Lane, A.P. & Zealey, W.J., 1986. *Astr. Astrophys.*, **164**, 51.

Rieke, G.H., Harper, D.A., Low, F.J. & Armstrong, K.R., 1973, *Astrophys. J. (Lett.)*, **183**, L67.

Sato, S., Nagata, T., Nakajima, T., Nishida, M., Tanaka, M. & Yamashita, T., 1985, *Astrophys. J.*, **291**, 708.

Shibata, K. & Uchida, Y., 1986, *Publ. astr. Soc. Japan*, **38**, 631.

Snell, R.L., Scoville, N.Z., Sanders, D.B. & Erikson, N.R., 1984, *Astrophys. J.*, **284**, 176.

Takano, T., Stutzki, J., Fukui, Y & Winnewisser, G., 1986, *Astr. Astrophys.*, **158**, 14.

Torrelles, J.M., Rodriguez, L.S., Canto , J., Carral, P., Marcaide, J., Moran, J.M. & Ho, P.T.P., 1984, *Astrophys. J.*, **274**, 214.

Torrelles, J.M., Ho, P.T.P., Rodriguez, L.S., & Canto, J., 1989. *Astrophys. J.*, **343**, 222.

Wynn-Williams, C.G., Becklin, E.E. & Neugebauer, G., 1974, *Astrophys. J.*, **187**, 473.

Yamashita, T., Sato, S., Tamura, M., Suzuki, H., Kaifu, N., Takano, T., Mountain, C.M., Moore, T.J.T., Gatley, I. & Hough, J.H., 1987, *Publ. astr. Soc. Japan*, **39**, 809.

Yamashita, T., Sato, S., Tamura, M., Suzuki, H., Gatley, I., Hough, J.H., Mountain, C.M. & Moore, T.J.T., 1988, *Mon. Not. R. astr. Soc.*, **233** 899.

Chapter 5

Mid-infrared Observations in the W75N Region

To follow the change-over in dominance from scattered light to thermal emission from dust and to fill the gap in the continuum spectrum of W75N, mid-infrared mapping observations were required. These measurements would probe the intermediate temperature ($\sim$ 100K) dust around the strong heating sources in the region. Improved near-infrared spectroscopy of the hydrogen recombination lines from IRS-1, IRS-2 and HII(A) was obtained at the same time in order to confirm anomalous line strengths and ratios suggested by the data of Chapter 2.

The work in this chapter was done in collaboration with C.M. Mountain & T. Yamashita. the observations were partly made during PATT allocation U/L/17 and partly in discretionary time allocated by the Astronomer in Charge (UKIRT) for the commissioning of the reconditioned mid-infrared bolometer array UKT16.

Summary

5-arcsec resolution mapping observations are presented at 10 μm and 20 μm of the major young sources in W75N, completing the 1-μm to 1100-μm continuum flux distribution of the region. The bright near-infrared object IRS-2 and the dominant luminosity source HII(B) are detected for the first time in the mid-infrared and it is found that 20 μm is the shortest wavelength at which HII(B) is directly observable at current sensitivities. The 1-μm to 20-μm luminosity of IRS-2 is 540 $L_\odot$, a fair approximation to the total luminosity of this source. The total luminosity of the region is 1.4×10^5 $L_\odot$, mostly provided by the source within HII(B).

IRS-2 is unresolved at these wavelengths and the emission from the somewhat extended HII(A) is similar in extent to the observed radio continuum. Therefore the

mid-infrared radiation must originate in a narrow region, within $\sim$ 0.02 pc of IRS-2 and in a zone of about this depth bordering the ionised gas of HII(A).

Improved measurements of the near-infrared hydrogen recombination lines Brγ, Brα and Pfγ, compared with current models of massive neutral or ionised winds, support the conclusion that IRS-2 is undergoing significant mass loss.

5.1 Introduction

In Chapter 2 a small group of reddened near-infrared sources was found in W75N close to the ultra-compact OH maser source HII(B), along with extended molecular hydrogen emission likely to be associated with the CO outflow (mapped in detail in Chapter 3). Maps of the dense molecular gas surrounding the outflow showed a large self-contained clump of material to the southwest of the main cloud core. The main red-shifted outflow lobe appears to be impinging on this clump, causing disruption and dividing as a result of the interaction.

Polarisation observations by Yamashita *et al.* (1988) revealed a 2-μm reflection nebula surrounding the embedded objects which is further studied at high spatial resolution in Chapter 6. The source ionising HII(B) and illuminating the brightest reflection nebula is very deeply obscured by dense material and the second brightest 2-μm source, IRS-2, is a very young, BN-like object and a strong emitter of hydrogen recombination lines. The region was observed in the mid-infrared continuum by Wynn-Williams *et al.* (1974) who found a 20-μm source at the position of HII(A), the strongest and most evolved of the compact HII regions in the area (Haschick *et al.* 1981).

The following chapter presents new continuum observations of the W75N region at 10 μm and 20 μm along with improved Brγ, Brα and Pfγ recombination line detections toward IRS-2. The measurements in the mid-infrared, where the illuminating source first becomes directly visible, complete the 1-μm to 1100-μm continuum spectrum of the region and clarify the nature of the sources therein.

5.2 Observations

All observations were made with the 3.8m United Kingdom Infrared Telescope (UKIRT) on Mauna Kea, Hawaii. Mid-infrared mapping with effective resolution of $\sim$ 5 arcsec was done using the 4$\times$2 element bolometer array UKT16 during the nights of 14, 16, 18 July 1987. Sky chopping was used with beams separated by 30 or 50 arcsec east-west,

and calibrations were obtained from a number of mid-infrared standard stars.

Extensive commissioning observations were made with UKT16 before observing the target sources. The relative positions of each detector in the array were measured by centring each of the eight detectors in turn on the bright mid-infrared standard αBoo. The centre or peak-response position of each detector was found and a flux measurement taken at both 10 μm and 20 μm. The half-power size and the shape of the beam profile in each pixel (in both Right Ascension and Declination directions) were then measured by drifting the telescope at a fixed rate across the source. The mean values and standard deviations of the half-power beam widths of the detectors were found to be 4.9 ± 0.2 and 3.9 ± 0.2 arcsec in RA and Dec, respectively. The mean offset between pixels in the array is 5.1 ± 0.4 (RA) and 6.2 ± 0.4 (Dec) arcsec. The sampling within the array in the RA-direction was tested by placing a star as close as possible to the mid-point between the centres of detectors 6 and 7. The resulting flux measurement, combining the signals from the two detectors, showed only a 25 per cent loss. In terms of flux collection, therefore, the sampling in RA is almost complete. The declination direction was not tested in the same way but the coverage is obviously considerably poorer, given the mean half-power width and offset obtained above. The flux measurements were made in order to find the relative response of the eight detectors to a point source, for flat-fielding corrections. Relative responses to an extended source were also measured at both 10 μm and 20 μm by observing the same point on the disk of Jupiter through each detector in turn. The results of these commissioning observations are summarised in Figs 5.1 and 5.2.

Maps were made of the region around HII(B) at 10 μm and 20 μm and of the brighter source HII(A) at 20 μm by sampling on a diagonal grid. This strategy provided reasonable coverage of the observed region, but left the maps somewhat undersampled. The maps were later interpolated onto a 3-arcsec square grid for contouring and presentation. Flux calibration and airmass corrections were obtained from repeated observations throughout each night of 10-μm and 20-μm standard stars. Calculated airmass corrections were 0.2 mag per airmass at 10 μm (for the night of 14 July), 0.5 and 0.3 mag per airmass at 20 μm (for the nights of 16 and 18 July, respectively). 1σ calibration uncertainties were 6 per cent (10 μm), 25 and 15 per cent (20 μm: 16 and 18 July, respectively). Integration times of 60–100 seconds per point produced mean statistical errors in the maps of 1.1×10^{-15} Wm^{-2} μm^{-1} or 0.04 Jy at 10 μm, 1.3×10^{-15} Wm^{-2} μm^{-1} or 0.18 Jy and 2.8×10^{-15} Wm^{-2} μm^{-1} or 0.37 Jy per pixel

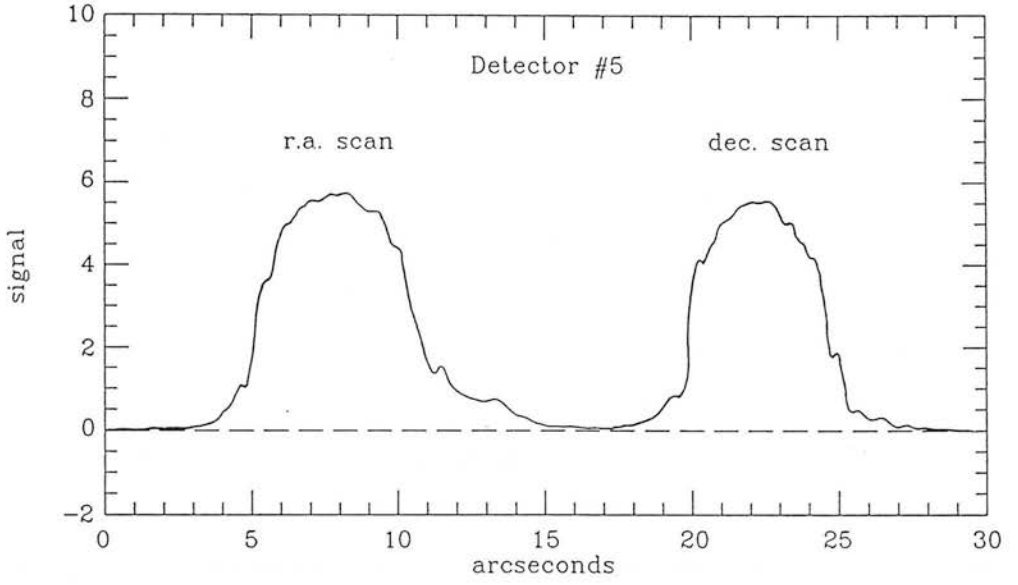

Figure 5.1: Result of the drift scan measurement of the beam profile of Detector 5 in the UKT16 array.

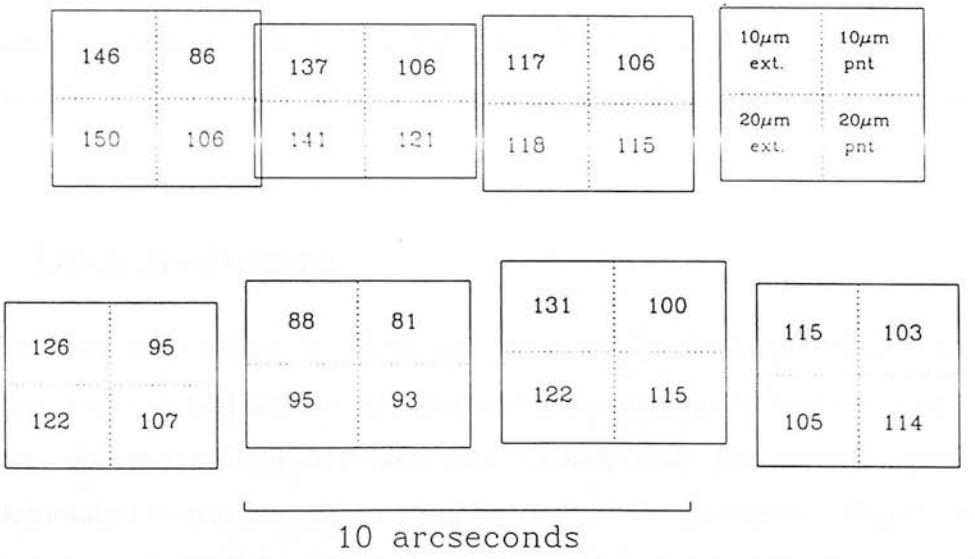

Figure 5.2: Schematic summary of the commissioning observations of UKT16. Indicated are the measured relative positions and sizes of the eight detectors. The figures are the relative responses (in per cent) of each detector, at 10 μm and 20 μm, to both a point source and to extended emission with respect to Detector 1.

at 20 μm on July 16 and 18, respectively. Relative positions within the maps and the absolute position of the offset zero are both accurate to ± 2 arcsec (rms).

Measurements at both wavelengths were also made towards the large dense condensation found in CS rotational lines to the southwest of the main cloud core (Chapter 3). This was done in order to look for signs of heating by hitherto undetected sources within this condensation which may have been severely dynamically affected by the impinging molecular outflow. An area of 42 arcsec (RA) $\times$ 18 arcsec (Dec.), centred on $20^h36^m45^s.3$ $+42°25'47''$ (1950) was mapped without fully sampling.

2-μm and 4-μm spectroscopy was done in a 5-arcsec beam with the cooled grating spectrometer CGS2 on UKIRT during 1987, 21 August and 19 July, respectively. East-west sky chopping was used with a 130-arcsec throw. Observations were made of IRS-2 and the 2-μm peak IRS-1, where Brγ was detected in a 20-arcsec beam in Chapter 2, and of the northern, more evolved HII region HII(A). The position observed at IRS-1 was that of the 2-μm peak as determined in Chapter 2, i.e. $20^h36^m50^s.4$ $+42°26'54''$ (1950). That in HII(A), which is considerable larger than the CGS2 beam was $20^h36^m51^s.3$ $+42°27'23''$

The 3.7-μm Pfγ measurement of IRS-2 was made as part of the UKIRT Service Observing Programme of 28 June 1987. Calibrations for the spectroscopic observations were made using stars from the UKIRT standards list and the measurements of absolute flux from Vega by Mountain *et al.* (1985). The positional accuracy of the spectroscopic observations was ± 1 arcsec (rms) with the point source IRS-2 used as the astrometric standard.

5.3 Data Reduction

Ground-based observations at 10 μm and 20 μm are particularly difficult since the telescope structure and sky are emitting into these wavebands from the peak of the ambient temperature blackbody spectrum. Consequently, the required signal from an astronomical source may be as small as 10^{-6} of the background signal. In this situation the very small flexures of the telescope that occur when changing position can significantly alter the background signal. Such flexures also mean that different areas of the mirror, with minutely differing emissivities, are being used. Another problem is that, especially when chopping and nodding with a significant component of movement in the Elevation direction, the sky emission gradient may be steep enough

to produce significant differences in sky signal between the on-source and sky positions and these differences will increase with increasing airmass (decreasing elevation) of the source and so vary with time. One or another of these problems may dominate in a given telescope, but the result is to produce changes in the background signal with position which are not removed by the standard chopping and nodding technique but which have to be corrected for later.

In the present observations, the signal baselines at both 10 μm and 20 μm developed quite rapid systematic drifts at lower source elevations. These drifts were occasionally large enough to produce baseline differences between 'pairs' (sets of integrations at the source and sky positions) which were larger than the signal. Consequently, the on-line basic reduction system used by UKIRT was unable to cope since the coadding, statistical error calculation and 'spike' rejection routines expected a flat baseline. As the observed drift was quite linear on the small timescale of one integration it was possible to re-process the data satisfactorily, without fitting polynomials to reproduce the baseline shape, by coadding odd (sky – object) and even (object – sky) pairs separately before obtaining the final result. Since, with a linear drift, all odd (even) pairs would possess an equal negative (positive) offset from their true value, this technique enabled the calculation of correct standard deviations of the mean coadded signal.

Finally, a non-circular effective beam profile required deconvolving from the raw maps. The asymmetry took the form of distinct elongation of the apparent shape of a bright point source, below the 15–20 per cent level, along the RA axis (Fig. 5.3). Since this was the direction of chopping throughout the observations the probable cause is a badly adjusted nodding cycle in which insufficient time was allowed for the telescope to settle before sampling began at the new position. To deconvolve the reconstructed asymmetrical beam, a simple adaptation of the CLEAN algorithm was applied. The basis of the method was to treat the contents of a map as the superimposition of many point sources. The peak in the map was found, a fractional (usually 10 per cent) strength point spread function was subtracted and the position and size of the subtraction recorded. The operation was then repeated until no peaks (positive or negative) stronger than 3σ remained. The deconvolved map, reconstructed from the recorded subtractions was then smoothed with a 2-D Gaussian filter to the nominal resolution (5 arcsec) of the detectors.

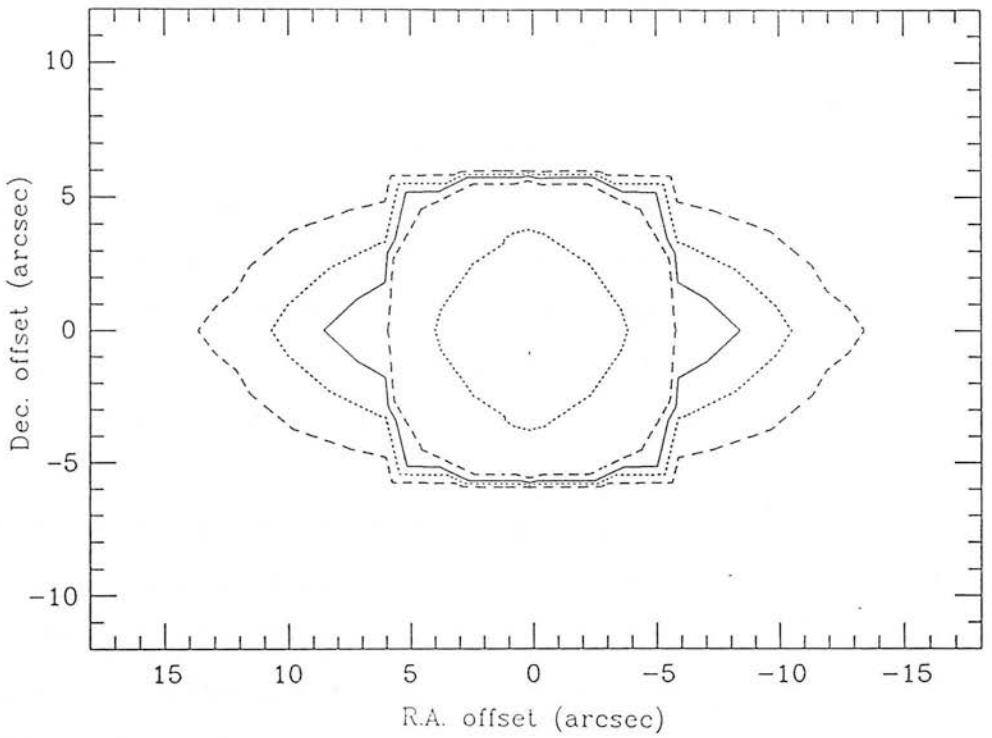

Figure 5.3: 10-μm effective point spread function at 10 μm, during the observations of 1987 July 16. The contours are at 10, 20, 30, 40 & 50 per cent of the peak.

5.4 Results

Figs 5.4 and 5.5 show the results of the 10-μm and 20-μm mapping observations, with positions given as offsets from $20^h36^m50^s.4$ $+42°26'51''$ (1950). Absolute calibration errors are estimated to be 10 per cent at 10 μm and about 25 per cent at 20 μm. Fig. 5.4 is limited to the area covered by the 2-μm observations of Chapter 2, while Fig. 5.5 extends to include the bright northern source HII(A). Strong emission at both wavelengths was found at the position of IRS-2 and from the dominant luminosity source HII(B). It can be seen that IRS-2 decreases in brightness towards longer wavelengths while the HII(B) flux density is increasing. A suggestion of weak emission at 10-μm was also found close to the fainter and less reddened near-infrared object, IRS-3.

Apart from a suggestion of low-level emission in the southwest corner of Fig. 5.4, IRS-2 is essentially unresolved at both 10 μm and 20 μm, but the emission encompassing IRS-1 and HII(B) is marginally extended in the northwest-southeast direction at both 10 μm and 20 μm. The extension is at a low level at 10 μm but it can be seen that the peak shifts by $\sim$ 7 arcsec to the northwest between 10 μm and 20 μm. HII(A) is extended, with a half power size of about 20 arcsec, and dominates the 20-μm emission in the region.

Total flux densities for HII(B), HII(A) and IRS-2 are given in Table 4.1, along with near- to mid-infrared integrated luminosities, calculated assuming a distance of 2 kpc (Dickel, Dickel & Wilson 1978). The continuum data available to date for the major sources in W75N are summarised in Fig. 5.6, including integrated flux densities from IRAS SKYFLUX maps of the region plus the near-infrared and submillimetre measurements presented in Chapters 2 and 4.

The under-sampled observations of the region containing the southwestern condensation detected no continuum source within the dense clump at either 10 μm or 20 μm. The 3σ upper limit to the 20-μm surface brightness obtained was 4×10^{-16} $\mathrm{Wm^{-2}\,\mu m^{-1}\,arcsec^{-2}}$ (0.05 Jy $\mathrm{arcsec^{-2}}$).

Results of the recombination line spectroscopy towards IRS-1, IRS-2 and the northern HII region HII(A) are listed in Table 4.2. As in Chapter 2, Brα was detected strongly towards IRS-2 and also weakly towards the nebula peak IRS-1 (the observed position was that of the 2-μm peak as determined in Chapter 2). Brγ was not detected at IRS-1, although it had been in the 20-arcsec beam used in Chapter 2. Pfγ was detected from IRS-2 where, because of high extinction, it has a higher flux than Brγ.

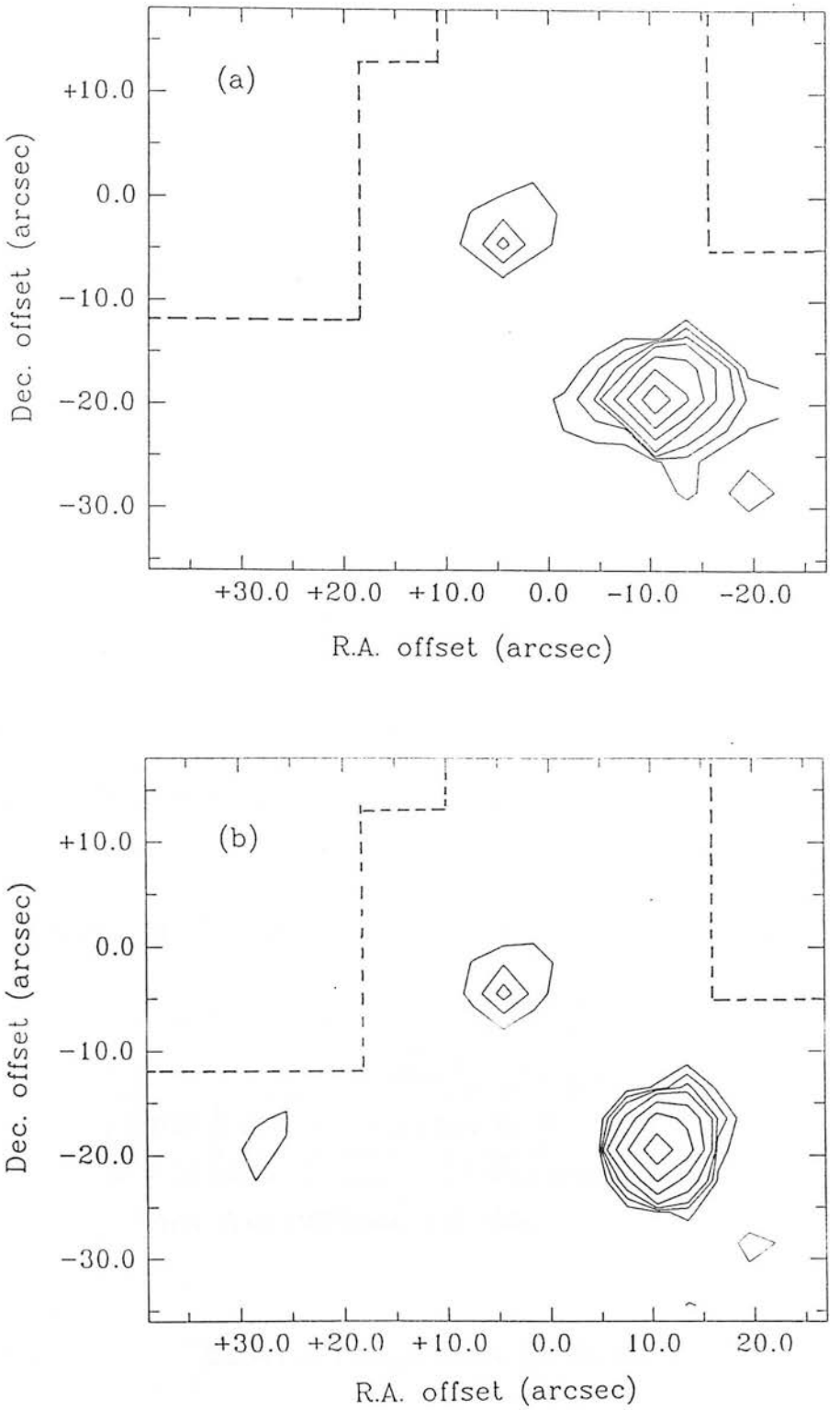

Figure 5.4: (a) Raw map at 10 μm of the region around HII(B) in W75N. The offset zero is at $20^h36^m50^s.0$ $+42°26'59''$ (1950) which is the position of HII(B). (b) The same map with the point spread function of Fig. 5.3 deconvolved, smoothed to the original resolution. Contours in both maps are drawn at (5.1, 10.2, 15.3, 25.5, 51, 85 & 170) $\times 10^{-13}$ Wm^{-2} μm^{-1}.

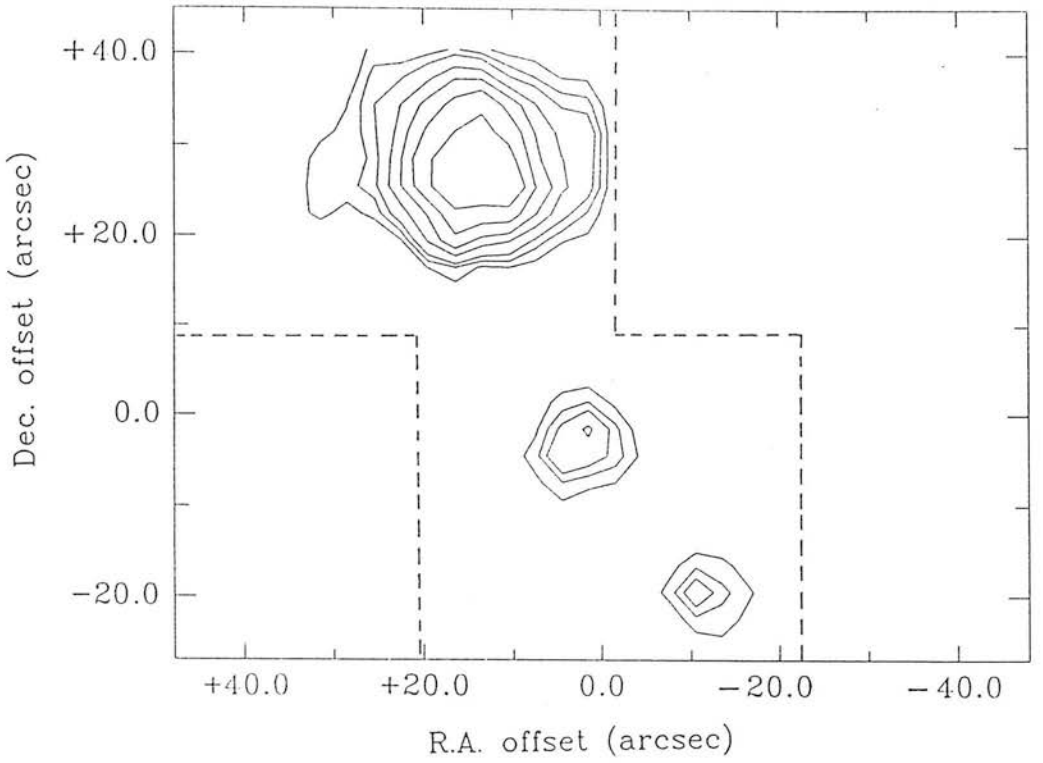

Figure 5.5: Deconvolved map at 20 μm of W75N, including the northern HII region HII(A). Contours are drawn at (1.5, 2.9, 4.4, 7.3, 10.3, 14.7 & 22.0) $\times 10^{-12}$ $Wm^{-2}\,\mu m^{-1}$. The dashed lines delineate the observed area.

Table 5.1: Mid-infrared flux densities and 1 μm to 20 μm luminosities

Object	S(10 μm) $Wm^{-2}\,\mu m^{-1}$	S(20 μm) $Wm^{-2}\,\mu m^{-1}$	1 μm–20 μm Luminosity
IRS-2	3.4×10^{-13}	6.7×10^{-14}	540 $L_\odot$
HII(B)	2.4×10^{-14}	1.52×10^{-13}	190 $L_\odot$
HII(A)	4.7×10^{-13}*	1.2×10^{-12}	1890 $L_\odot$

*From Wynn-Williams *et al.* 1974

Table 5.2: Recombination-line Fluxes

Object	Recombination Line Flux $/10^{-16}$ $Wm^{-2}\,\mu m^{-1}$		
	Brα(4.052 μm)	Brγ(2.166 μm)	Pfγ(3.754 μm)
IRS-2	10.1 ± 0.5	0.8 ± 0.2	1.8 ± 0.2
IRS-1	1.2 ± 0.3	$< 0.6(3\sigma)$	–
HII(A)	8 ± 1	0.8 ± 0.2	–

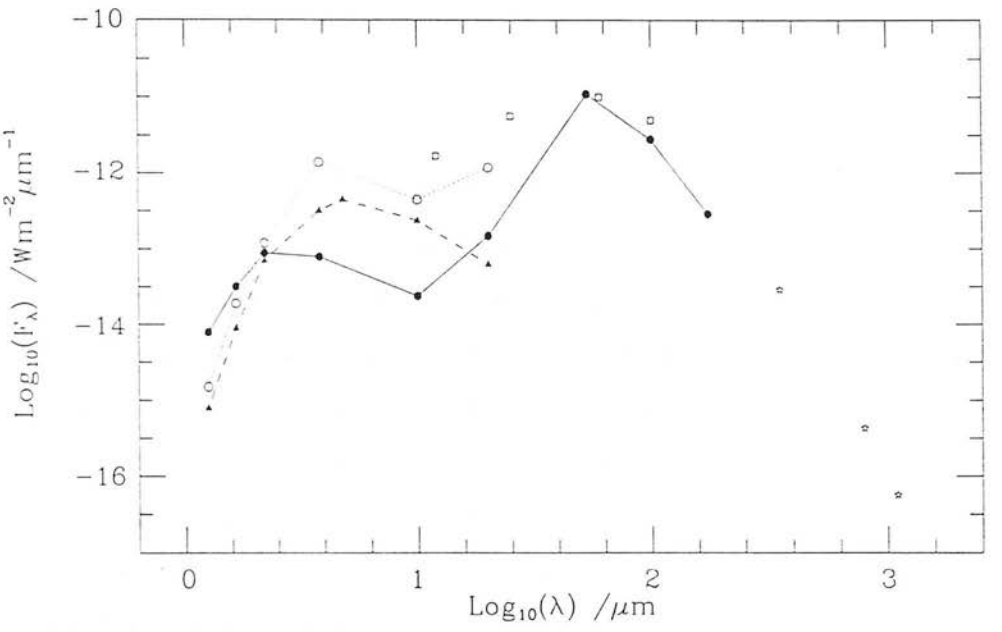

Figure 5.6: Composite spectral distribution of the major sources in W75N from 1 μm to 1100 μm. The filled circles represent data for IRS-1 and HII(B) (from Chapter 2, this chapter and Harvey *et al.* 1977). The filled triangles denote data for IRS-2 (from Chapter 2 and this chapter). The open circles represent data for HII(A) (from Yamashita *et al.* 1988, Wynn-Williams *et al.* 1974 and this chapter). The open squares are IRAS SKYFLUX data covering the whole region. The stars represent the submillimetre continuum data from Chapter 4.

Both Brγ and Brα were detected from HII(A).

5.5 Discussion

5.5.1 Mid-infrared Continuum

The compact 10-μm sources in Fig. 5.4 are coincident, within the quoted positional errors, with the bright near-infrared objects IRS-1 and IRS-2 found in Chapter 2. However, high polarisation fractions found in the 2-μm continuum towards IRS-1 by Yamashita *et al.* (1988) and in Chapter 6 have established that the apparent near-infrared source at this position is a peak in the reflected 2-μm light of the nebula. The 10-μm emission from the position of IRS-1, which is offset from the maser source by $\sim$ 7 arcsec, is therefore almost certainly associated with warm dust situated where the line-of-sight extinction is lower than to HII(B) itself. A model by Dent (1988) predicts a similar effect in the polar regions of dense dusty, edge-on disks around a heating source, in which the observed position of the emission peak begins to shift away from the source at shorter mid-infrared wavelengths as optical depths increase. Even though there is no evidence of a disk involved in the HII(B) system, the warm dust may be located close to the opening in the dense material through which near-infrared light escapes to illuminate the reflection nebula. Since no emission is detected at this wavelength direct from HII(B) itself, it is clear that the extinction at 10 μm is still extremely high toward the luminosity source.

At 20 μm, the 'IRS-1' emission has shifted so as to peak very close to the position of HII(B), leaving a weaker extension in the direction of the 10-μm peak (Fig. 5.5). This change indicates that between 10 μm and 20 μm the foreground extinction reduces sufficiently that the warm dust around the source begins to be directly detected. The 20 μm/10 μm colour temperature of the HII(B) emission is 150K at the position of the 10-μm peak and 120K close to HII(B) itself. Apart from the suggestion of low-level emission to the southwest, IRS-2 remains an unresolved source at all measured wavelengths. The mid-infrared continuum must therefore arise within about 0.02 pc of the central star. IRS-2 is decreasing in brightness beyond 10 μm while HII(B) becomes rapidly stronger, completely dominating the emission at submillimetre wavelengths (Chapter 4).

At 20 μm, the northern and more extended HII region HII(A) is the brightest object in the area, as expected since it corresponds to the peak found by Wynn-

Williams *et al.* (1974) which was then the only detectable 20-μm emission in W75N. HII(A) is extended at 20 μm on a scale ($\sim$ 20 arcsec) consistent with the size of the ionised region mapped by Haschick *et al.* (1981) and the mid-infrared radiation therefore must originate in the warm dust within the photo-dissociation zone bordering the ionised gas.

A complete spectrum of the 1-μm to 1100-μm emission from IRS-1/HII(B) is presented in Fig. 5.6, showing a double peaked flux-density distribution. This spectral shape can be most easily explained by a source embedded in a non-spherically symmetric distribution of extinguishing material. In this situation, strong scattering along less extinguished paths causes the near-infrared peak, while a high optical depth in the direct line of sight results in a large far-infrared hump in the spectrum containing most of the luminosity of the source and dominating the long-wavelength output of the whole region. Dent (1988) predicts spectral distributions of this form by modelling the continuum radiative transfer through edge-on or slightly inclined dense circumstellar disks which are optically thick well into the mid-infrared. The fractional luminosity emerging from IRS-1/HII(B) in the near-infrared is rather lower than in the specific models presented by Dent, suggesting that, in W75N, a significant amount of foreground extinction exists through the outer regions of the enveloping cloud. A visual extinction of $A_{\rm v} = 15$ mag applied to the model of a partly obscured hot dust photosphere (effective temperature 1000 K – 1500 K), approximately reproduces the spectral shape in Fig. 5.6. This is consistent with the photometric analyses of Chapters 2 and 6, which predict a large hot dust component to the near-infrared light and a foreground extinction component of about this order.

Integrating under the flux distribution in Fig. 5.6, the total luminosity of IRS-1/HII(B) is 1.4×10^5 $L_\odot$, assuming a distance of 2kpc (Dickel, Dickel & Wilson 1978), equivalent to a O7 ZAMS star (Thompson 1984). This luminosity source is likely to be the object that is ionising HII(B). However, Haschick *et al.* (1981) measured a radio flux density requiring only a B0.5 ZAMS or equivalent to provide the ionising radiation. The discrepancy is not likely to due to any unusual pre-Main Sequence property of the central star, since such a luminous (and therefore massive) object will have evolved very rapidly towards the Main Sequence. It may, however, be explained by large amounts of circumstellar material orbiting close to the star, which strongly attenuate the UV radiation. The re-radiation of the absorbed energy then also explains the hot dust spectrum known to dominate the stellar photosphere at near-infrared wavelengths.

The second of the strong 2-μm sources, IRS-2, is pointlike at both 10 μm and 20 μm (Figs 5.4 & 5.5). Its flux density spectrum decreases in the mid-infrared, the new data fitting smoothly with the existing near-infrared photometric points (Fig. 5.6). At a distance of 2 kpc the 1-μm to 20-μm luminosity of IRS-2 is 540 $L_\odot$, which may be assumed to be a moderately good estimate of the total output from this source. This implies an illuminating source of roughly 5.5 $M_\odot$ and indicates that the visual extinction value of > 34 mag, derived from the J–H colour in Chapter 2, is too high. $A_V = 34$ mag would require a dereddened 1-μm flux density equivalent to a ZAMS O7 star. Thus the 1.6-μm H-band flux density must be dominated, in this source also, by emission from a compact, optically thick envelope of hot dust around the young star, increasing the J–H colour and rendering it unusable as an estimate of extinction. This conclusion is consistent with the analysis of the near infrared spectrum in Chapter 6.

The upper limit to any 20-μm continuum emission from the southwestern CS clump indicates that there are no optically thick sources within this condensation with temperature greater than 50K. The timescale of the outflow is $\sim 10^5$ yr which is about comparable to the dynamical collapse time of a protostellar core (Lizano & Shu 1989). Therefore, any incipient condensations that may have been triggered into collapse rather than being disrupted by the impact may still have had insufficient time to become observable.

5.5.2 Recombination Line Ratios

The recombination lines detected from IRS-2 (Table 4.2) have the ratios Brα/Brγ = 12 ± 1 and Brα/Pfγ = 5.5 ± 0.7. Although the latter is an upper limit to the intrinsic Brα/Pfγ ratio (in the case of zero extinction), it is already 3σ less than the standard Case B value (7.47: Giles 1977). Since Brα and Pfγ are close together near 4 μm the ratio is in any case almost unaffected by moderate degrees of reddening and the observed value offers a fair estimate of the intrinsic intensity ratio. Recent modelling of recombination lines arising in massive, mainly neutral winds from young stars (Natta *et al.* 1988) predict intrinsic Brα/Brγ ratios close to unity, in cases where Brα/Pf$\gamma \simeq 5$. If this were the case with IRS-2, the direct visual extinction would be $A_V \simeq 36$ mag (from the extinction law of Rieke & Lebofsky 1985). Although it was mentioned above that the extinction towards the hot dust photosphere in IRS-2 is probably significantly less than this, the reddening to the inner regions of the stellar wind, where the recombination lines should form, may be considerably higher and so there is no conflict. In

the neutral wind model, the ratios mentioned above arise for high gas temperatures ($\sim 10^4$ K) and medium or low mass-loss rates ($10^{-7} - 10^{-8}$ $M_\odot$ yr^{-1}) or for low gas temperatures when mass-loss rates are high ($\sim 10^{-6}$ $M_\odot$ yr^{-1}). However, these models use stellar surface temperatures of around 4,500 K and may not be appropriate to a source with a total luminosity $\gtrsim 540$ $L_\odot$. Models of fully-ionised winds (*e.g.* Simon *et al.* 1983) produce similar line ratios.

The Brα/Brγ ratio towards HII(A) is 10 ± 3. Assuming that Case B conditions are more appropriate to this apparently more evolved HII region, this value implies an extinction of $A_V = 18 \pm 4$ mag. This amount of reddening is comparable to the 'foreground' values mentioned above and calculated in Chapter 6 and it may be appropriate to ascribe it to the general cloud material covering the whole area. Since the 5-arcsec aperture used in the observations is considerable smaller than the ionised region of HII(A), the value of Brα/Brγ above may not be fully representative of the whole object.

The detection of Brα towards the reflection peak IRS-1 confirms the reality of the Brγ detection in a 20-arcsec beam in Chapter 2, but does not help in explaining the source. HII(B) is too heavily extinguished to be the direct source although, as suggested in Chapter 2, the recombination line photons may be scattered in the nebula and are detectable close to IRS-1 where there is strong forward scattering. On the other hand, there is at least one true continuum source (albeit of relatively low luminosity: Chapter 6) close enough to IRS-1 to have been caught in the present observation.

5.6 Conclusions

5-arcsec resolution mapping observations in W75N at 10 μm and 20 μm have been made, tracing the continuum emission from warm ($\sim$ 100K) dust around the main heating sources. The bright near-infrared object IRS-2 and the dominant luminosity source HII(B) are detected for the first time at mid-infrared wavelengths and it is found that, because of the very high line-of-sight extinction, 20 μm is the shortest wavelength at which radiation can be detected directly from HII(B). The 1-μm to 20-μm luminosity of IRS-2 is 540 $L_\odot$, a fair approximation to the total luminosity of this source. The total luminosity of the region is 1.4×10^5 $L_\odot$, mostly provided by the source within HII(B).

No continuum source was found in the dense clump of molecular gas to the south-

west of the main core, which is interacting with the CO outflow. The upper limit to the surface brightness obtained at 20 μm was 4×10^{-16} Wm^{-2} μm^{-1} arcsec^{-2} (0.05 Jy arcsec^{-2}).

New near-infrared spectroscopy of Brγ, Brα and Pfγ toward IRS-2 show evidence of non-Case B line ratios which are consistent, in the absence of accurate knowledge of the extinction affecting the lines, with recombination in a massive stellar wind from the young star.

References

Dent, W., 1988. *Astrophys. J.*, **325**, 252.

Dickel, J.R., Dickel, H.R. & Wilson, W.J., 1978. *Astrophys. J.*, **223**, 840.

Draine, B.T. & Lee, H.M., 1984. *Astrophys. J.*, **285**, 89.

Fischer, J., Sanders, D.B., Simon, M. & Solomon, P.M., 1985. *Astrophys. J.*, **293**, 508.

Giles, K., 1977. *Mon. Not. R. astr. Soc.*, **180**, 57P.

Harvey, P.M., Campbell, M.F. & Hoffman, W.F., 1977. *Astrophys. J.*, **211**, 786.

Haschick, A.D., Reid, M.J., Burke, B.F., Moran, J.M. & Miller, G., 1981. *Astrophys. J.*, **244**, 76.

Lizano, S. & Shu, F.H., 1989. *Astrophys. J.*, **235**, 834.

Moore, T.J.T., Mountain, C.M., Yamashita, T. & Selby, M.J., 1988. *Mon. Not. R. astr. Soc.*, **234**, 95.

Mountain, C.M., Leggett, S.L., Selby, M.J., Blackwell, D.E. & Petford, A.D., 1985. *Astr. Astrophys.*, **151**, 589.

Natta, A., Giovanardi, C. & Palla, F., 1988. *Astrophys. J.*, **288**, 921.

Rieke, G.H. & Lebofsky, M.J., 1985. *Astrophys. J.*, **288**, 618.

Thompson, R.I., 1984. *Astrophys. J.*, **283** 165.

Wynn-Williams, C.G., Becklin, E.E. & Neugebauer, G., 1974. *Astrophys. J.*, **187**, 473.

Chapter 6

High Resolution 1-μm to 2-μm Imaging Polarimetry of W75N

In the preceding chapters, multi-wavelength observations of W75N at spatial resolutions of around 0.1 parsec and larger failed to provide information on the initial collimation state of the high-velocity outflow or any evidence of a dense ordered structure (i.e. a disk) on these scales which may influence that state. It was therefore necessary to find out whether structures exist with scale sizes < 0.1 pc which might strongly influence the morphology and energetics of the region. The advent of the new infrared camera systems provided the opportunity to probe the 0.01-pc scale physical structure around the luminosity sources and in the reflection nebulosity by examining the distribution of the dust-scattered light. The data analysed in this chapter were obtained during PATT allocation U/N/70 and the work is part of a collaboration including C.M. Mountain, T. Yamashita and I.S. McLean.

Summary

1.25-μm to 2.2-μm imaging polarimetry of W75N, with seeing-limited spatial resolution ($\sim$ 2 arcsec), shows that the diffuse 2.2-μm emission arises in two separate reflection nebulae. The bright 2-μm peak IRS-1 is found to be part of the larger nebula and is not a self-luminous object. The main illuminating source was not detected, implying direct obscuration of $A_V > 90$ mag. Analysis of the reflected light indicates much lower extinction ($A_V \simeq 16$ mag) along the reflection path and predicts significant emission from hot dust near the source.

Comparison of the surface brightness distribution in the main nebula with that in similar sources and with theoretical predictions shows that large grains in a narrow size range ($a = 0.5\,\mu$m to $1\,\mu$m) dominate the scattering of near-infrared radiation.

However, since the observed wavelength selects the size of the dominant scatterers, little can be inferred about the relative numbers of such grains within the overall distribution of sizes. The dominance of large grains in the near-infrared should produce anisotropic intensity phase functions in the reflected light, with strong forward scattering. This may contribute to the asymmetric appearance of many infrared reflection nebulae, in which the lobe directed away from the observer is often heavily suppressed.

The pattern of polarisation vectors close to the source of the CO outflow shows evidence of multiple scattering in dense material in front of the source, but there is no clear indication of any disk structure at the scale of the resolution or larger. The collimation of the W75N CO outflow probably arises on smaller scales or is achieved without the action of a disk.

The smaller reflection nebula around IRS-2 is symmetrically bipolar, only lightly collimated and appears to be orientated with its axis in the plane of the sky. The presence of this nebula indicates that IRS-2 is generating small-scale outflow of its own, apparently free of the significant interactions with a clumpy ambient medium that dominate the structure of the large outflow from the OH maser source. The presence of a massive stellar wind or outflow is consistent with the non-Case B hydrogen recombination lines previously measured towards IRS-2. The line-of-sight extinction toward IRS-2 is $A_V \simeq 25$ mag.

39 new low-luminosity sources have been detected at 2.2 μm within a 70-arcsec square region. The K luminosity function of these sources is consistent with that of a single cluster of young stars, showing no significant difference from the distribution found in the Orion cluster.

6.1 Introduction

2-μm polarimetry (Yamashita *et al.* 1988, hereafter Y88) and photometry (Chapter 2) of the W75N star-forming region revealed embedded infrared sources and reflection nebulosity close to the compact HII/OH maser HII(B). From those observations it was concluded that the brightest 2-μm object, IRS-1, is probably a compact part of that nebula and not self-luminous, despite being an apparent source of recombination line emission. However, the data presented were unable to provide enough evidence to rule out a true source at or near the position of IRS-1. The true picture was confused by the possibility of closely-associated, low-luminosity objects hidden in the diffuse emission.

Both infrared and visual reflection nebulae are generally associated with dust shells around the large-scale outflows of material from young sources (a similar explanation being first postulated by Elsässer & Staude 1978). In some cases the distribution of reflected light clearly traces cusped or looped structures suggesting limb-brightened swept-up shells or bubbles (e.g. R Mon: Yamashita *et al.* 1989; AFGL 2591: Forrest & Shure 1986). In W75N, however, the relationship between the complex molecular outflow (Chapter 3) and the compact but rather amorphous reflection nebulosity observed in Chapter 2 has not, up to now, been plain.

This chapter presents seeing-limited resolution imaging polarimetry at 1.25 μm, 1.65 μm and 2.2 μm within a $\sim$ 100-arcsec square region close to the OH maser source. The purpose of these observations was to examine the morphology of the reflection nebula with reference to the CO flow, to identify the dominant illuminating source and look for small-scale structure in the surrounding dense material (which may be affecting the initial collimation state of the outflow). In addition to this, it was intended to look for low-luminosity young stars in the bright diffuse emission (which might contribute to the Brγ line detected there) and to look for undiscovered, fainter members of a cluster to which the known, bright infrared sources might belong.

6.2 Observations

The observations were made on the night of 30 June, 1988, with the United Kingdom Infrared Telescope (UKIRT) on Mauna Kea, Hawaii, using the near-infrared camera system IRCAM and its companion polarimeter IRPOL (McLean 1987, McLean *et al.* 1989). Imaging polarimetry was done with the image scale set to 0.6-arcsec per pixel, so that a single frame covered a rectangular area 38 arcsec (RA) $\times$36 arcsec (Dec.) on the sky. All observations were carried out in 'stare' mode, that is, without sky chopping by the secondary mirror.

Using the IRCAM filters at J(1.25μm) and H(1.65μm), a single position was observed, centred close to the bright 2-μm peak IRS-1. With the K-filter (2.2μm) in the beam, a 110 $\times$ 106 pixel (68 $\times$ 66 arcsec) mosaic image was produced, using four additional frames diagonally offset, overlapping the centre frame and each other. An anomalous non-linearity in the response of the IRCAM detector array required correction before final reduction and calibration. After subtracting a bias or short dark frame (*i.e.* $<$ 10 sec exposure), each data frame was divided by the number of

coadds forming the image. The result (in C, or counts above bias per coadd) was multiplied, pixel by pixel, by the following correction polynomial, obtained from the measurement of known sources (M. Casali, private communication):

$$f(C) = 1.0 - 2.308 \times 10^{-9}C + 8.689 \times 10^{-11}C^2 + 2.281 \times 10^{-14}C^3$$
$$-1.687 \times 10^{-18}C^4 + 4.287 \times 10^{-23}C^5$$

Individual source frames were flat-fielded with images of nearby blank sky and then the mean sky surface brightness subtracted. The sky images were taken within a few minutes of the source frames since colour of the near-infrared sky changes with its brightness, being affected by differentially changing absorption-line depths, and so too does the wavelength-dependent relative response of the camera array pixels.

After fine adjustment of the zero levels to match frames, the five 2-μm images were combined into the large mosaic by averaging the values of corresponding overlapping pixels. The integrated signals from bright sources occurring in more than one constituent frame were measured, and the frame-to-frame response variation was found to be less than ± 7 per cent in all cases. Positive or negative spikes in the images, due to dead pixels in the 62×58 array or to cosmic ray hits, were replaced, where possible, with values of corresponding pixels in overlapping frames or by interpolating between neighbouring pixels in the same frame.

Polarisation information was obtained in the usual way by imaging each spatial position with four angular settings of the achromatic half-wave plate polariser in the sequence 0, 45, 22.5, 67.5 degrees. The instrumental offset in position angle of the electric vector was calibrated by observing S106 and adopting the 2-μm polarisation values obtained by Tokunaga *et al.* (1981) in a 6-arcsec beam. Flux density calibration at all three wavelengths was obtained by comparison with the 8-arcsec photometry of Chapter 2; associated calibration errors are around 10 per cent. Integration times of 120, 180 and 180 s per frame gave 1σ statistical uncertainties of 5.3×10^{-18}, 8.0×10^{-18} and 4.9×10^{-17} $\mathrm{Wm^{-2}}$ $\mu\mathrm{m^{-1}}$ per pixel at J, H and K, respectively. The spatial resolution of the observations was seeing-limited, and so the images are properly fully-sampled. The FWHM of a stellar image was typically 2 arcsec at all three wavelengths.

Photometry of the known and newly-identified objects was done by integrating inside circular apertures 5, 8 or 13 pixels in diameter (i.e. 3, 5 or 8 arcsec).

6.3 Results

The main results are contained in Figs 6.1–6.3, which show contours of sky-subtracted surface brightness at K, H and J with polarisation vectors superimposed on every second pixel. Logarithmic contours are used to show the presence of numerous small sources in this part of W75N. IRS-2 was used as the astrometric standard, at $20^h36^m49^s.0$ $+42°26'39'' \pm 1$ arcsec (1950). Fig. 6.4 shows the polarised intensity, and Fig. 6.5 the polarisation fraction, in the K mosaic. Cuts along the longitudinal axis of the IRS-1 reflection lobe are shown in Fig. 6.6 for K surface brightness and polarisation fraction plus H surface brightness and H–K colour.

The surface brightness map in Fig. 6.1 clearly follows the general form of the 8-arcsec observations of Chapter 2, while the large improvement in spatial resolution picks out many important details not previously accessible. Similarly, the size and orientation of the polarisation vectors are consistent with the 20-arcsec resolution measurements of Y88. The 2.2-μm emission from the peak of the bright nebula is $\sim$ 20 per cent polarised, increasing to $\sim$ 50 per cent towards the southeast and south. However, instead of there being just one large region of extended emission, illuminated by a single source, there is also a second, smaller and fainter reflection nebula centred on the bright source IRS-2 (offset −11, −20).

The objects IRS-2 and IRS-3 found in Chapter 2 are now seen as bright point sources at 2 μm, and the region denoted IRS-1 is revealed by the present observations to be highly structured, consisting of bright patches of extended emission. Virtually all the 2-μm flux from these nebulous patches is highly polarised and they therefore consist principally of scattered photons. The intensity peak at offset (+4, −5) (which hereafter inherits the name IRS-1) is itself also around 20 per cent polarised and is thus a knot of reflected light rather than a self-luminous object, confirming the postulation of Y88. On the other hand, at least three true sources do exist close to IRS-1, identified as such by coincident reductions in the polarisation fraction.

The H-band image of the central 38×36 arcsec (Fig. 6.2) shows overall similarity to the same area at K, with centro-symmetric polarisation up to 50 per cent in the diffuse emission around IRS-1, the brightest object at this wavelength. However, the new nebula associated with IRS-2 is much reduced both in brightness and extent, indicating large extinctions towards both source and nebula. At J, where the reddening may be very much greater than at K, only IRS-1 and one or two nearby sources show

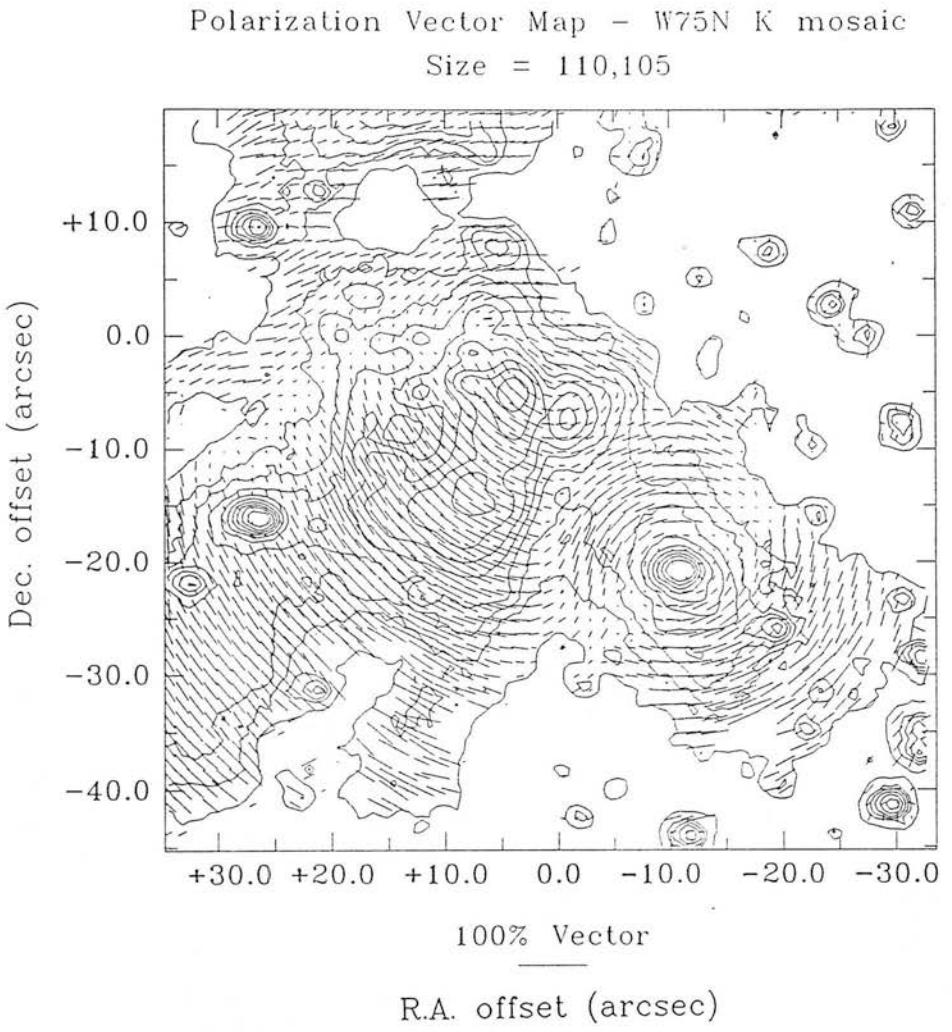

Figure 6.1: K(2.2-μm) continuum surface brightness and polarisation mosaic of W75N. The offset is at the position of the OH/HII source HII(B): $20^h36^m50^s.0$ $+42°26'59''$ (1950). Surface brightness contours are at $(0.09, 0.25, 0.45, 0.79, 1.41, 2.50, 4.45, 7.91, 14.07, 25.02)\times10^{-16}$ Wm^{-2} μm^{-1} per 0.6-arcsec pixel. The direction of the polarisation vectors indicates the orientation of the electric vector and the length is proportional to the degree of polarisation. 100 per cent polarisation would be represented by a vector of length 6 arcsec on the scale of the map. Vectors are plotted at every second pixel, for clarity. The enhancement in surface brightness to the north is emission from the compact HII region HII(A).

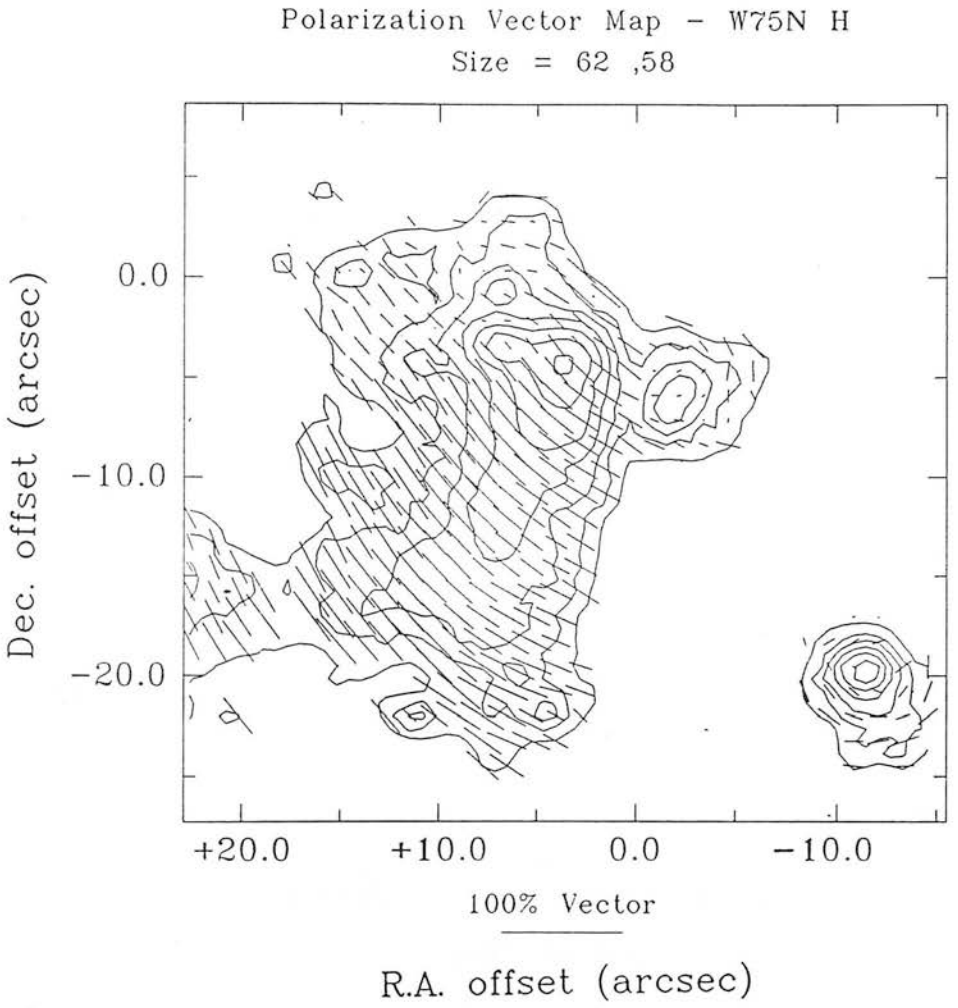

Figure 6.2: Continuum surface brightness and polarisation map of the central region at 1.65 μm. The offset centre is the same as in Fig. 6.1 Surface brightness contours are at (0.25, 0.46, 0.82, 1.46, 2.60, 4.62, 8.21)$\times 10^{-16}$ Wm^{-2} μm^{-1} per 0.6-arcsec pixel. Polarisation vectors are to the same relative scale as in Figure 6.1.

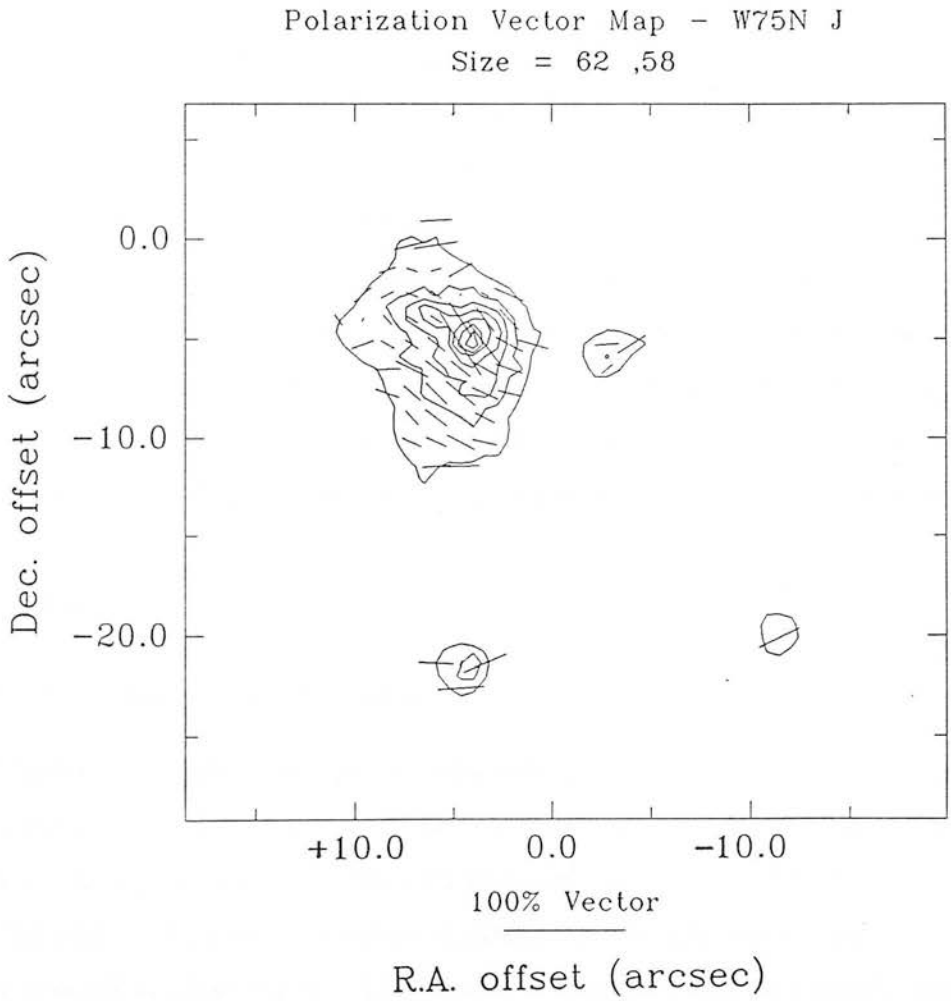

Figure 6.3: Continuum surface brightness and polarisation map of the central region at 1.25 μm. The offset centre is the same as in Fig. 6.1 Surface brightness contours are at (0.14, 0.33, 0.61, 0.84, 1.17, 1.63, 2.33)$\times 10^{-16}$ Wm^{-2} μm^{-1} per pixel.

up clearly, although IRS-2 and a source to the south of IRS-1 are marginally detected (Fig. 6.3). Most of the nebulous emission which dominates the picture at K is no longer present, and the polarisation is weaker and less ordered than at the longer wavelengths, probably due to line-of-sight extinction and the effects of multiple scattering through foreground material, randomising the polarisation angles.

In addition to the previously identified bright objects IRS-1, IRS-2 and IRS-3 there are a large number of weaker sources in the region. 39 new sources were detected within the area enclosed by Fig. 6.1 with K flux densities of 2.0×10^{-16} $\mathrm{Wm^{-2}\,\mu m^{-1}}$ (K= 15.8 mag) or more. The photometric results are listed in Table 6.1, along with standard J–H and H–K colours, where possible.

The actual number of background sources is uncertain, as no sky observations were made at a sufficiently large offset to ensure that any detected sources were not associated with the W75N cluster. However, the sky frames used (at an offset of +100 arcsec in R.A.) contained an average of 1.4 objects per square arcmin which were brighter than the above limit. This serves as an upper bound to the frequency of background stars and indicates a contamination fraction of no more than 5 per cent.

6.4 Discussion

6.4.1 The Reflection Nebulae

The characteristic polarisation pattern of a reflection nebula is centro-symmetric, with the normals to the electric vectors of the scattered radiation converging at the source position. In Fig. 6.1 there are two such points of convergence, the first is coincident with the peak of IRS-2 and the second occurs inside a roughly elliptical (12×6 arcsec) region centred at offset (–3, 0). This second convergence area is virtually coincident with the position of the OH maser source HII(B), and so the ionising star of this HII region is by far the most likely candidate for the source illuminating IRS-1 and the large reflection nebula.

6.4.1.1 IRS-1 – The Main Nebula

Like other reflection nebulae, W75N contains a high-velocity molecular outflow, first detected and mapped by Fischer *et al.* (1985). The outflow has subsequently been mapped in CO (J=1–0) at 15-arcsec resolution (Chapter 3), revealing a complex structure with a compact blue-shifted component peaking in the region between HII(B),

Table 6.1: Continuum data obtained for all sources detected at J, H or K

Object	Offset[a] /arcsec		F_λ(J) $/10^{-16}$ $Wm^{-2}\,\mu m^{-1}$	F_λ(H) $/10^{-16}$ $Wm^{-2}\,\mu m^{-1}$	F_λ(K) $/10^{-16}$ $Wm^{-2}\,\mu m^{-1}$	Aperture /arcsec	J–H /mag	H–K /mag
1	−32,	−36	-	-	14.3	3	-	-
2	−32,	−34	-	-	10.2	3	-	-
3	−32,	−28	-	-	21	5	-	-
4	−31,	−23	-	-	5.0	3	-	-
5	−31,	−7	-	-	5.4	3	-	-
6	−31,	+11	-	-	4.6	3	-	-
7	−29,	−41	-	-	32	5	-	-
8	−29,	+19	-	-	3.6	3	-	-
9	−28,	+1	-	-	3.3	3	-	-
10	−25,	+3	-	-	7.1	3	-	-
11	−23,	−31	-	-	5.8	3	-	-
12	−23,	−15	-	-	3.9	3	-	-
13	−23,	−9	-	-	2.5	3	-	-
14	−22,	−34	-	-	5.8	3	-	-
15	−19,	−25	-	-	41	5	-	-
16	−19,	+8	-	-	3.5	3	-	-
17	−13,	+6	-	-	2.2	3	-	-
18	−12,	−44	-	-	17	5	-	-
IRS-2	−11,	−20	4	73	681	5	3.75	3.50
20	−8,	+3	-	-	2.1	3	-	-
21	−8,	+16	-	-	4.7	3	-	-
22	−5,	0	-	-	3.7	3	-	-
23	−2	−42	-	-	2.6	3	-	-
24	−2,	−40	-	-	3.4	3	-	-
25	+5,	+8	-	-	13	3	-	-
26	+6,	+3	-	10	29	3	-	2.3
27	+6,	+16	-	-	8	3	-	-
28	+7,	−22	4.9	20.0	-	3	2.2	-
29	+8,	−3	10	77	157	3	2.8	1.9
30	+8,	0	-	19	54	3	-	2.3
31	+12,	−23	-	8.0	20.8	3	-	2.4
32	+12,	0	-	9	23	3	-	2.1
33	+15,	0	-	8	17	3	-	2.0
34	+17,	+4	-	3.7	10.8	3	-	2.3
35	+20,	+1	-	4.2	13.3	3	-	2.4
36	+21,	−31	-	-	7.9	3	-	-
37	+21,	−16	-	9	26	3	-	2.3
38	+21,	+13	-	-	10	3	-	-
IRS-3	+26,	−15	-	-	453	5	-	-
40	+27,	+10	-	-	46	5	-	-
41	+33,	−21	-	-	66	5	-	-
IRS-1 neb			205	1150	5800		2.5	2.9

[a] Offset from 0,0 (=$20^h36^m50^s.0$, $+42°26'59''$ (1950)) in Fig. 1.

IRS-2 and IRS-3 (Fig 6.4). This blue flow lobe thus coincides with the large reflection nebulosity around IRS-1 and the implication is that the nebula consists of light scattered from dust within a dense, swept-up shell around the outflow. Furthermore, the very low surface brightness emission at the southeastern extremity of this region shows a double-cusp structure as if tracing a limb-brightened shell. Formations of this kind associated with molecular outflows have been observed both in the infrared continuum (e.g. Mon R2: Yamashita *et al.* 1989) and in molecular lines. No extended near-infrared emission was detected coinciding with red-shifted molecular material, which appears in two discrete zones to the northeast and southwest of the source (Chapter 3).

No 2-μm source was detected at the position of HII(B), which is only a few arcsec away from the IRS-1 peak. Both the total and polarised surface brightnesses fall very rapidly to the north and northwest of IRS-1. In fact, there is at least a factor of 20 drop in intensity, corresponding to $A_V \gtrsim 30$ mag, over a projected distance of $\sim$ 12 arcsec, suggesting a similarly large column density gradient within the obscuring material. This situation may be consistent with the presence of a dense disk around the luminosity source, tilted so as to obscure the second reflection lobe, and such a model was suggested by Y88. In this general region, the polarisation pattern ceases to be centro-symmetric and is instead rather linear, the vectors aligning roughly perpendicular to the axis of the bright reflection lobe (Fig. 6.1). Such a pattern is predicted by Bastien & Ménard (1988) from multiple (or secondary) scattering from an approximately edge-on disk around the luminosity source. Since the extinction is so high in this direction, emission observed in the direct line of sight to HII(B) is likely to have suffered multiple scattering. However, the high optical depth material is not constrained to be arranged in a disk structure and will tend to produce a similar linear vector pattern, provided a front 'surface' exists containing the final scatterers and the primary scatterers are in a region of lower optical depth material away from this surface. Hence, the pattern may be produced by photons reflected back from the brightly illuminated dust shell and off any large obscuring slab in front of the source. In addition, a rather large disk ($\gtrsim$ 40 arcsec diameter) would be required to obscure the HII region and one complete half of a bipolar nebula, but no such structure has been detected, either in the submillimetre continuum (Chapter 4) or in the basic CS rotational transitions (Chapter 3). Further, no underlying velocity gradient that might indicate rotation of a large disk was found in the cloud core.

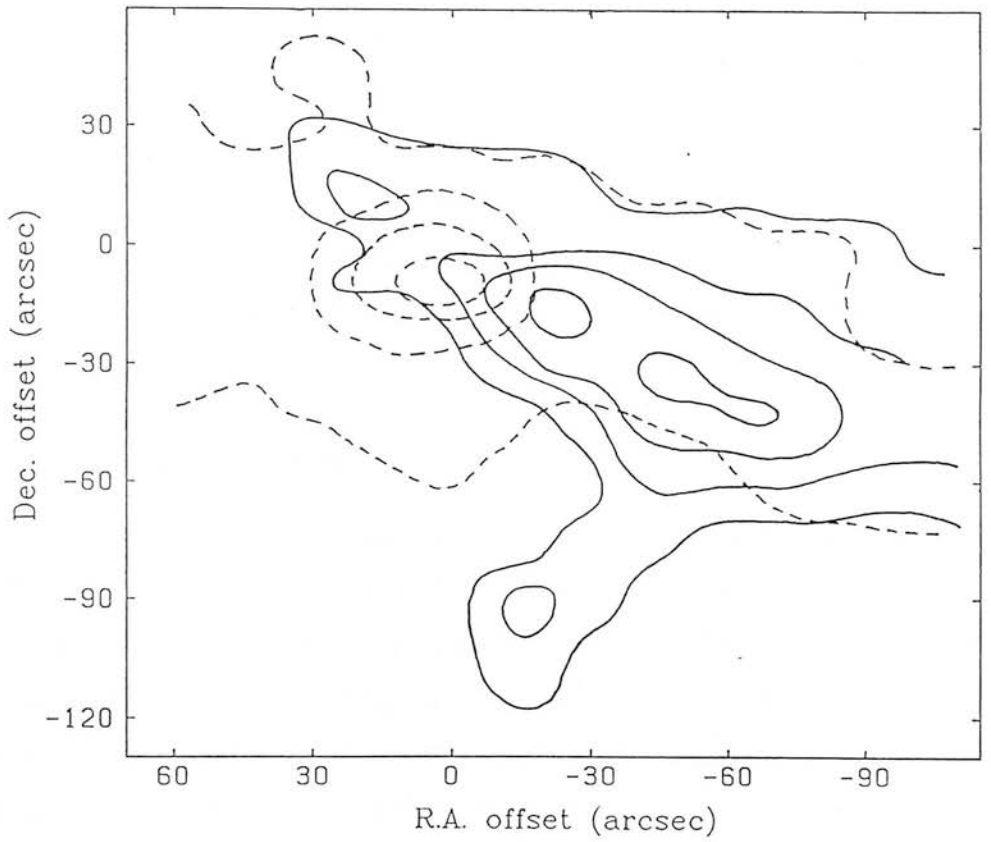

Figure 6.4: ^{12}CO (J=1–0) emission from the large molecular outflow in W75N. Solid contours represent the intensity in the red-shifted line wing, and the dashed contours show the blue-shifted emission. Taken from Chapter 3

The polarisation fraction in the IRS-1 nebula increases from $\sim$ 20 per cent, close to the luminosity source, to a maximum of $\sim$ 50 per cent (20 arcsec to the southeast). This pattern is a familiar one in infrared and visual reflection nebulae, and is generally consistent with polarisation by surface scattering from dust grains in a roughly paraboloid shell around an outflow, in which the degree of polarisation increases with scattering angle (Yamashita *et al.* 1987; see Fig. 6.7). Hence the light from IRS-1 is scattered from material near the line of sight to each source and larger polarisation fractions are produced by larger scattering angles further out in the reflection lobes. Castelaz *et al.* (1985: hereafter C85) regard a similar increase in polarisation fraction, observed in GSS30 in Ophiucus, as too great to be due solely to the change in scattering angle. However, it is clear from a detailed examination of scattering models that the polarisation fraction can increase from zero to nearly 100 per cent (less for non-spherical particles) at a scattering angle of 90 degrees (Bastien & Ménard 1988)

6.4.1.2 The IRS-2 Nebula

The small nebula around IRS-2 shows up in the total intensity map (Fig. 6.1) only as a limited diffuse component around the source. The morphology of the scattered light, and hence of the distribution of scattering dust, is much more clearly seen in the map of polarised intensity (Fig. 6.5) and polarisation fraction (Fig. 6.6). These show two symmetrical lobes of scattered light separated by a straight lane of low polarisation across the source. It therefore seems certain that IRS-2 is generating a limited, probably lightly-collimated bipolar outflow of its own.

It was found in Chapters 2 & 5 that the hydrogen recombination lines from IRS-2 are anomalously strong and have non-Case B ratios, implying the presence of a massive, optically thick wind. If this wind is largely neutral, as modelled by Natta *et al.* (1988) it may be responsible for driving a larger-scale outflow which has swept up the dust shells forming the bipolar reflection nebula.

The decreased polarisation in the band across IRS-2 may be caused simply by an absence of scattering material between the two reflection lobes. However, it could also be due to multiple scattering through an edge-on, flattened structure. In this case, the variation in polarisation fraction (along a northeast-southwest cut across the source) indicates a half-maximum thickness of 6 ± 1 arcsec. At a distance of 2 kpc (Dickel, Dickel & Wilson 1978), this implies a physical thickness of 0.06 pc for the

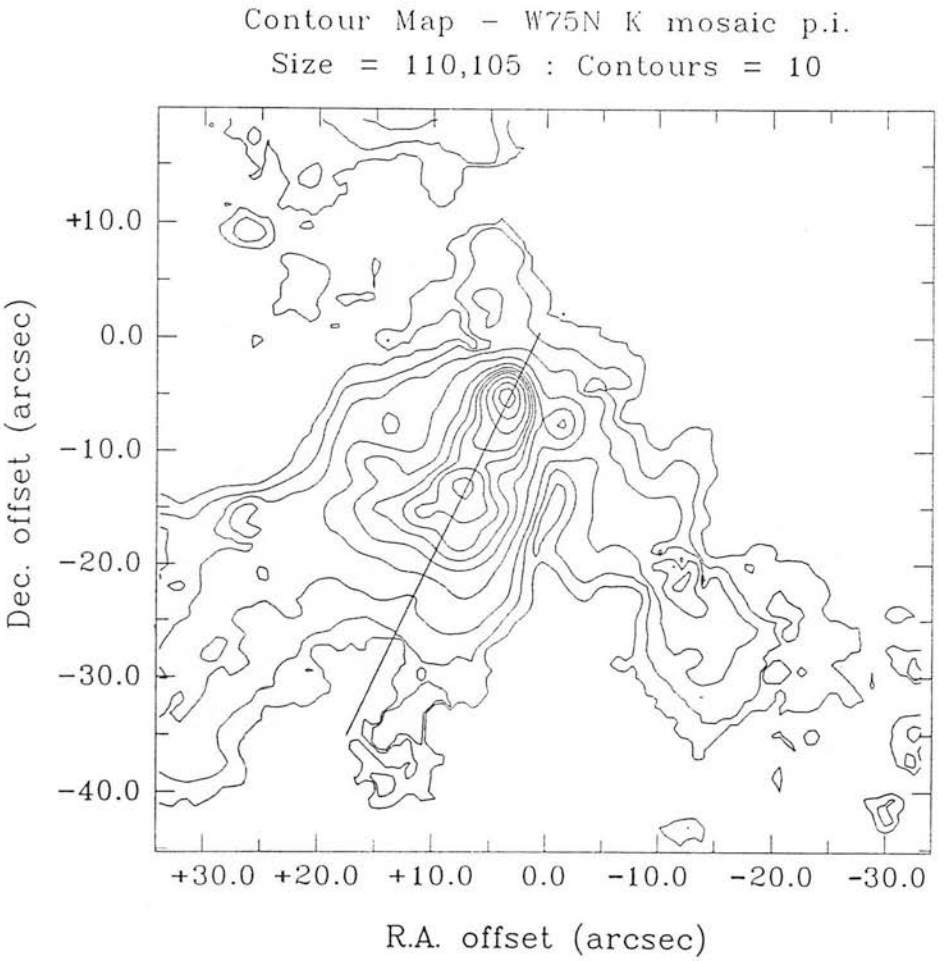

Figure 6.5: K-band polarised intensity in the region covered by Figure 6.1. The contours are Polarisation Fraction × Intensity and are placed at (0.05, 0.09, 0.18, 0.45, 0.89, 1.33, 1.78, 2.22, 3.11, 4.45, 5.79)$\times 10^{-16}$ Wm^{-2} $\mu\mathrm{m}^{-1}$ per pixel. The straight line represents the locus of the 1–D cut displayed in Fig. 6.7

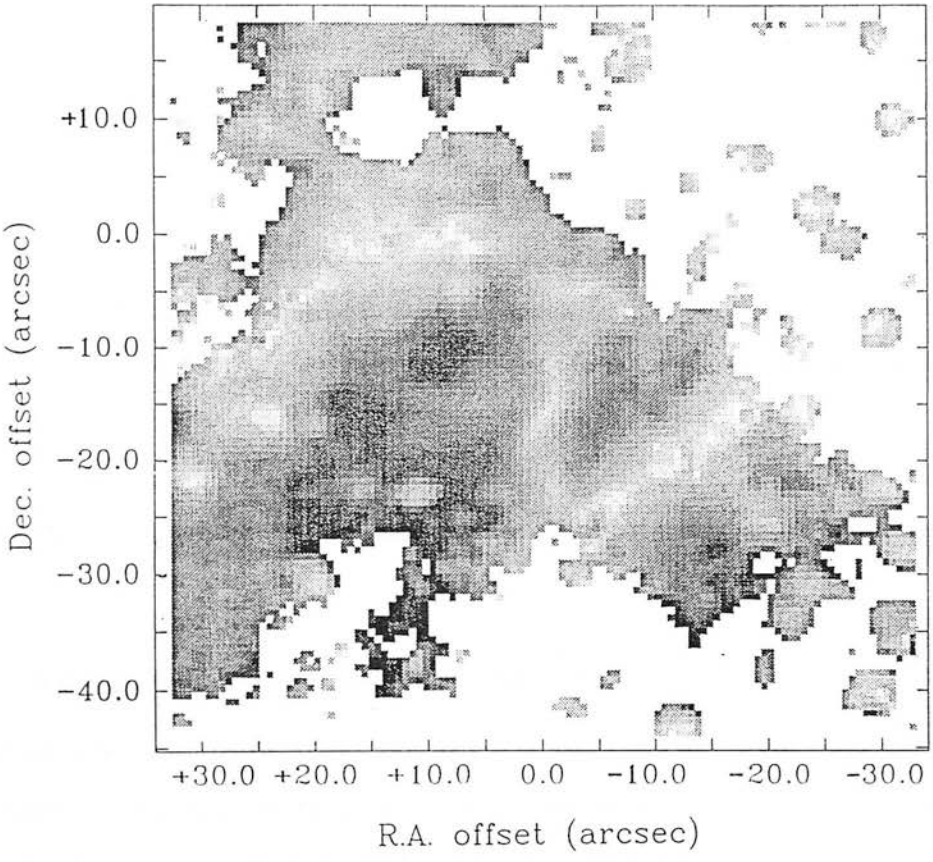

Figure 6.6: K-band polarisation fraction in the region covered by Figure 6.1. The variation is shown as a greyscale map from 0 per cent (white) to 50 per cent (black).

obscuring slab. Within this region the polarisation fraction is reduced by nearly a factor of 10, indicating $\tau_{sca}(2\mu\mathrm{m}) \simeq 2.3$. Assuming τ_{sca} is the main component of the reddening (*cf* the high albedo derived by Leinert & Haas 1987 for dust in the postulated disk around ZCMa), $A_V \simeq 22$ mag (if $A_V = 9A_K$), similar to the value of $A_V = 25$ mag derived from photometric data (see §5.4.3.1). If the slab is in the form of a flat cylinder of diameter ~ 0.12 pc, the total hydrogen column density conversion of Bohlin, Savage & Drake (1978) ($N_{H_2}/A_V = 9.36 \times 10^{24}$ m^{-2} mag^{-1}) yields a mass of only ~ 3 M$_\odot$ in this structure. This in turn implies a mean space density of about 6×10^{10} m^{-3}, if most of the gas is in molecular form. This is a relatively low particle density for such a formation and may mean that our hypothetical disk-like slab is not a dynamically active formation but perhaps a remnant of the density structure in the original cloud core which formed IRS-2. If the grain albedo at K were as low as 0.22, as predicted by Draine & Lee (1984: DL), the 2-μm optical depth would rise to ~ 10, which would be large enough to have completely obscured IRS-2. In this case, then, the modelled reduction in polarisation through increased column density would not be feasible, except that strong forward scattering from large grains (see §5.4.2) may significantly reduce the fraction of light scattered out of the beam, and produce a large 'effective' albedo.

6.4.2 Anisotropic Scattering from Large Grains

The present observations reveal a number of interesting features in the extended, reflected light. As well as a strong primary peak near the projected source position (i.e. IRS-1), where the polarisation fraction is still considerable but lower than in the rest of the nebula, there is a less bright and less compact secondary surface-brightness peak to the southeast (Fig. 6.1). This secondary peak, displaced ~ 15 arcsec down the projected outflow axis from IRS-1, is coincident with a local reduction in the polarisation fraction and a peak in both J–H and H–K colour (Fig. 6.7). At H (1.65 μm), the primary peak shifts a little away from the source position while the secondary moves 4–5 arcsec in the opposite direction.

Features similar to those described above can be found in other asymmetric or unipolar infrared reflection nebulae (*e.g.* GSS 30 in Ophiucus: C85; SGS 1 in NGC 1333: Castelaz *et al.* 1986, hereafter C86; GGD 27: Yamashita *et al.* 1987). C85 and C86 assume that secondary surface brightness peaks are density enhancements in the scattering material. However, while this explanation could also account for

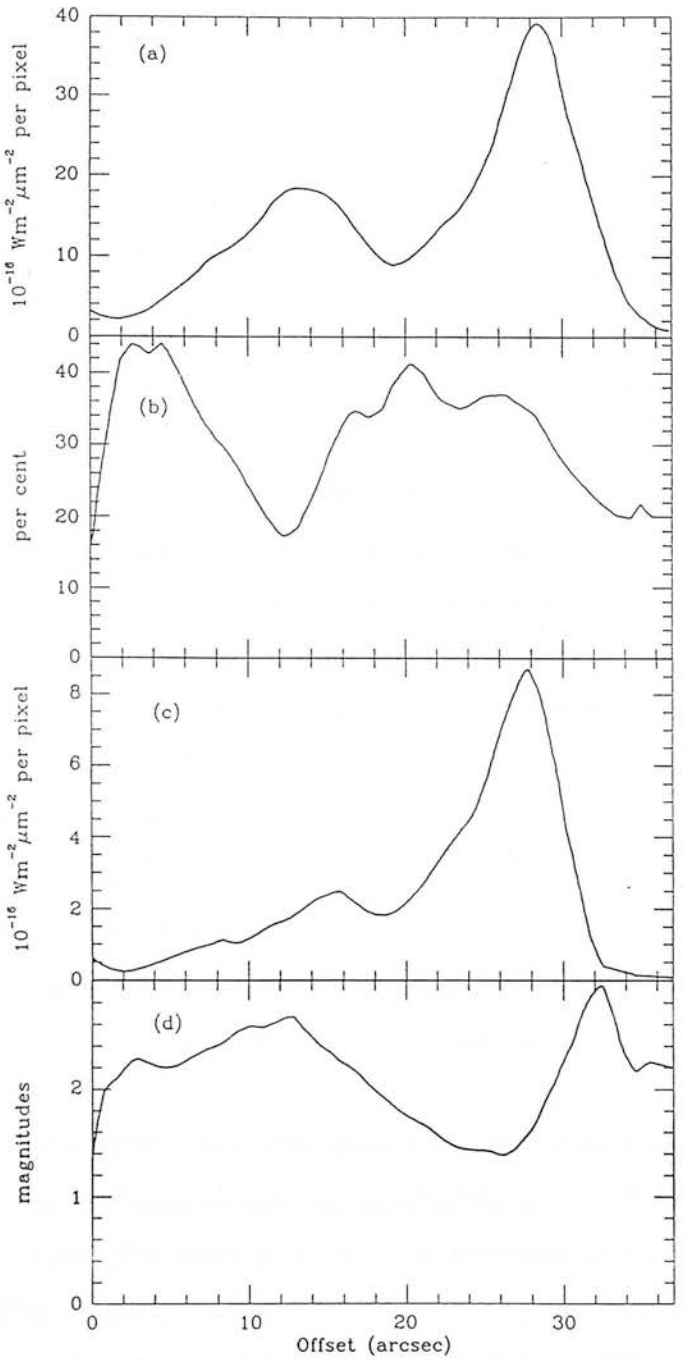

Figure 6.7: The variation of four quantities in the extended emission along a line from offset (+17, −36) to (0, 0) in Figure 6.1 (see Fig. 6.5). (a) K surface brightness; (b) K polarisation fraction; (c) H surface brightness; (d) H–K colour index.

the local colour change and the shift between the H and K peak positions through optical depth effects, it requires a remarkable similarity in physical structure between sources. Further, while an increase in the scattering optical depth, τ_{sca}, will increase the scattered intensity when τ_{sca} is low, in order to produce a drop in polarisation fraction by the same method multiple scattering must occur, which requires a high τ_{sca}. Unfortunately, an increase in density when τ_{sca} is already high would produce either no change in surface brightness (for grain albedo = 1, i.e. no absorption) or a *reduction* (for an albedo < 1). The existence of a patch of luminosity degrading the polarisation fraction is not a plausible explanation for the secondary surface brightness peaks since the polarised intensity does not change monotonically across the region (Fig. 6.4).

A sharp peak in the polarised light close to the source position in W75N was interpreted by Y88 as being due to strong forward scattering off material close to the line of sight to the luminosity source. Strong forward scattering is indicative of the anisotropic scattering functions of large grains with radii comparable to the observed wavelength (*e.g.* Van de Hulst 1957) while the small grain (Rayleigh) case produces a phase function which only varies very slowly with scattering angle. The presence of significant numbers of large grains ($a \sim 0.5\,\mu$m) in similar sources was concluded by C85 and C86 from the wavelength dependence of the scattered intensity (see also Yamashita *et al.* 1989). Despite the likely presence of a distribution of grain sizes, the dependence of the scattering cross-section on grain radius a means that light in the 1-μm to 4-μm region should be scattered preferentially by a very narrow range of large ($a \sim 1\,\mu$m) dust sizes.

The so-called MRN interstellar grain size distribution (Mathis, Rumpl & Nordsieck 1977) suggests the power-law size distribution $n \sim a^{-3.5\pm0.3}$ with an upper limit cut-off at $a \simeq 1\,\mu$m. The small-grain ($a \ll \lambda$) scattering cross-section is proportional to a^6, becoming proportional to a^3 for radii $a \gtrsim \lambda$ (Van de Hulst 1957). Hence the intensity scattered by grains of a particular size rises as $a^{\sim 2.5}$, then becomes nearly constant between about $\lambda/5$ and the upper cut-off radius of the distribution. Thus, when observed at $2.2\,\mu$m, the grains doing the majority of the scattering must lie in a very limited size range i.e. $a = 0.5\,\mu\text{m} - 1\,\mu\text{m}$. Since we see little or no light reflected by smaller grains, we can say little about the overall size distribution in the dust.

At longer wavelengths it thus appears that, dependent on the effective upper limit to the grain radius, large grains of nearly constant size scatter most of the ob-

served light. The angular scattering pattern from spheres with radii comparable to the incident wavelength is strongly affected by diffraction. The intensity phase function, $\phi(x, \theta_{sca})$ has a large peak in the forward (scattering angle $\theta_{sca} = 0$) direction and much smaller ancillary maxima and minima appearing as θ_{sca} increases (Van de Hulst 1957). A wide size range in the most efficient scatterers would average out the smaller features, as the pattern shifts shifts to smaller scattering angles with increasing $x = 2\pi a/\lambda$, but the mixture would remain strongly forward-scattering.

Since we have concluded that the dominant scatterers are large and we do not see a wide size range, anisotropic scattering effects may well be the cause of the observed surface brightness features. While the secondary maxima in theoretical scattering patterns are only a few per cent of the $\theta_{sca} = 0$ peak, the observed secondary peak in W75N is about 50 per cent as strong as the primary at K and 27 per cent at H (Fig. 6.6). However this is not difficult to explain, since the extinction along directions close to $\theta_{sca} = 0$ is extremely high (see §6.4.3.1) and the primary peak would be strongly suppressed (Fig. 6.8). The relative size of the secondary surface brightness peak is reduced at H, even though the extinction affecting the primary must be considerably larger than at K. This is consistent with increased averaging effects in the pattern at shorter wavelengths, where the size range of the effective scatterers is larger. Similarly, the shift of the second peak closer to the source is consistent with the expected shift of the scattering pattern to smaller θ_{sca} at shorter wavelengths. This shift also explains the characteristic peak in H–K colour slightly beyond the K secondary surface brightness maximum. The movement of the primary in the opposite direction can be simply explained by higher extinction close to $\theta_{sca} = 0$. Finally, a further characteristic feature of single-size, large-grain scattering is that minima in the intensity phase function $\phi(x, \theta_{sca})$ correspond to maxima in the polarisation phase function, just as is found in the current observations.

The IRS-2 reflection zone, as an example of an essentially symmetrical bipolar nebula, shows no strong peaks at all. This is understandable, in terms of the above discussion, if the outflow axis is roughly in the plane of the sky. In this case, the paraboloid or conical dust shells around the outflow which form the reflection nebula are orientated so that only a small range of large scattering angles are observed.

In conclusion, the surface brightness and polarisation fraction distributions in W75N and in other, similar sources support a theoretical expectation that observing reflected light in the 1 μm to 2 μm band will select large grains in a narrow size range

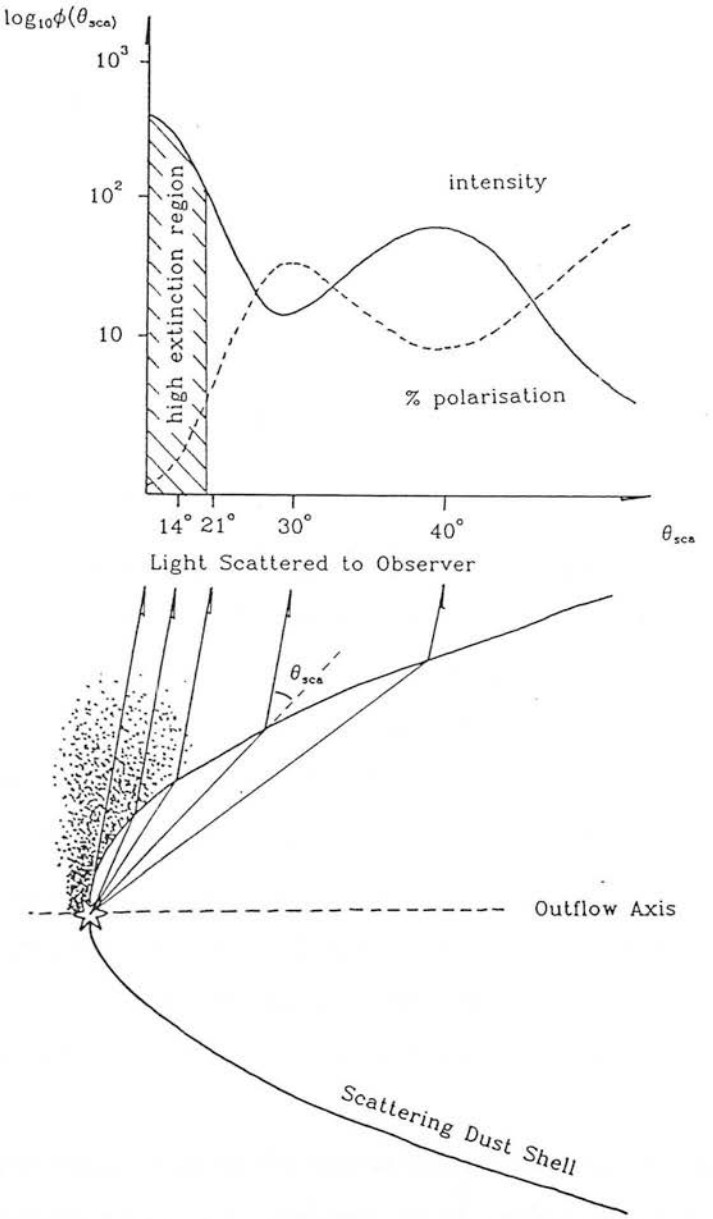

Figure 6.8: Schematic of the scattering in an optically thin, paraboloid dust shell around a molecular outflow, showing how the scattering angle increases with projected distance from the source. Also shown is an example of the approximate variation of intensity and polarisation phase functions with scattering angle (adapted from Van de Hulst 1957 for particles with refractive index $m \simeq 1.5$ and size parameter $a/\lambda \simeq 1$.

as the dominant scatterers. This dominance of large scatterers has no bearing on the relative numbers of such grains within the overall grain size distribution. However, the details of the angular scattering patterns of large particles are dependent on the optical properties of the scatterers. Hence, with careful observations it may be possible to obtain information on the grain shape and constitution in these regions. Strong forward scattering may also contribute to the apparent suppression of the backward-directed reflection lobe, corresponding to the red-shifted outflow, in many infrared reflection nebulae and the effect may not be the unambiguous signature of extinction through a large, tilted disk.

6.4.3 The Luminosity Sources

6.4.3.1 IRS-1 & IRS-2

The dominant object in the region is undoubtedly the ionising star within HII(B), since this is the main heating source (Chapter 4), the origin of the CO outflow (Chapter 3) and illuminates the bright reflection nebula. From the present observations it can be seen that, although IRS-1 is part of the reflection nebula and not a self-luminous object, the Brγ detection towards it (Chapter 2) included at least three true sources within the 20-arcsec beam. One of these (Object no. 29 in Table 6.1) was probably also included in the accompanying 5-arcsec resolution Brα observations. Thus, while HII(B) itself is too heavily extinguished to be a direct source of detectable recombination lines, we cannot now be certain of the origin of the observed lines without similarly high resolution observations and cannot use them to draw conclusions about the ionising source.

Although we cannot measure the near-infrared properties of the luminosity source directly, some information can be gathered via the reflected light in the associated nebula. Summing over the diffuse emission related to IRS-1, we obtain a total K flux density of 5.8×10^{-13} Wm^{-2} μm^{-1}. The mean colours in the nebula are J–H = 2.5 and H–K = 2.9. If the de-reddened source were a pure stellar ($\geq$ 10,000 K) photosphere, the extinction law of Reike & Lebofsky (1985: RL) predicts corresponding visual extinctions of 23 mag and 46 mag, respectively. Assuming the RL extinction law applies here, the large discrepancy indicates the presence of a much cooler photosphere, dominating the K-band emission and significantly affecting the H-band also. This cooler source must be a region of hot dust close to the central star or stars of

HII(B), reprocessing a significant fraction of the visible and UV photons.

The presence of large amounts of hot dust makes the job of deducing intrinsic source parameters very uncertain, especially without recombination line data to provide constraints on the line-of-sight extinction. If it is assumed that the observed J-band flux is not heavily contaminated by dust emission (i.e. that the dust temperature, T_d, is $< 1,000$ K, placing $\lambda = 1.25$ μm well down the Wien side of the Planck function) then the extinction along the path of the reflected light can be estimated. Taking the source to be a single ZAMS O7 (Chapter 2) and adopting the theoretical grain albedo of Draine & Lee (1984: DL), the total observed J flux density (2.05×10^{-14} $\mathrm{Wm^{-2}\,\mu m^{-1}}$) indicates a value for $A_V = 16$ mag. The RL extinction law in turn implies an intrinsic J–H colour of 1.0, i.e. an H-band flux density nearly 3 times larger than that of a ZAMS O7. Similarly, if $A_V = 16$ the intrinsic H–K colour is ~ 2.3 and the corresponding source colour temperature is $T_{H-K} \simeq 850$ K which may be taken as an estimate of T_{dust}. This solves a problem encountered in Chapter 2, in which A_V was calculated from J–H, assuming the H-band was also free of dust emission. This assumption resulted in over-estimates of A_V and yields intrinsic source luminosities an order of magnitude or more higher than any O-type star at all three wavelengths. A blackbody of T = 850 K with the calculated de-reddened and de-reflected K-band luminosity ($L_K = 690$ $L_\odot$) would contribute less than 20 per cent of the observed J-band emission, and so our assumption of a purely stellar photosphere at J is reasonable.

For a blackbody of T = 850 K, $L_K / L_{bol} \simeq 0.04$ and so L_{bol} for the reprocessed emission $\simeq 1.7 \times 10^4$ $L_\odot$. The dust responsible therefore either reprocesses around 7 per cent of the total radiative output from the central star or 7 per cent is the fraction that escapes via the reflection nebula. The high temperature of the dust indicates a location fairly close (< 100 A.U.) to the heating source: a spherical blackbody of 10^4 $L_\odot$ at 850 K would be ~ 60 A.U. in diameter. The fraction of light reprocessed may indicate non-symmetrical geometry in the absorbing material. For instance, a thick circumstellar disk whose longitudinal cross-section has an opening angle of ~ 8 degrees would intercept approximately 7 per cent of the light from a central star. The assumption of the DL albedos, RL extinction law and a central ZAMS O7 star therefore implies 16 mag of visual extinction along the path of the reflected light and a region of dust at ~ 850 K close to the star.

Unfortunately, the foregoing model contains many assumptions and is by no means unique; in particular, the choice of central source is not constrained. Table

6.2 lists the main features of three alternative models with hotter but less luminous dust emission and higher extinction. If the central star is equivalent to a B0.5 ZAMS (required for the ionisation of HII(B) – Haschick *et al.* 1981), the main difference is that a much larger fraction of the initial stellar luminosity must be reprocessed through heating of the dust. The choice of grain albedo also affects the calculated parameters, a wavelength-independent scattering efficiency with negligible absorption means higher foreground extinctions and temperatures but lower dust luminosities.

A lower limit for the direct line–of–sight extinction to HII(B) can be estimated by assuming the ionising star is a single B0.5 ZAMS star with a K magnitude of 8.7 at 2 kpc. The 3σ upper limit to the surface brightness of any source within HII(B) implies an extinction of $\geq$ 9.9 mag at 2.2 μm, or $A_{\rm v} \geq 89$ mag (from the RL extinction law). If the ionising star is as hot as O7, this rises to $A_{\rm v} \geq 102$ mag and, if the above model of an O7 star plus dust is accurate, the lower limit becomes $A_{\rm v} \geq 133$ mag.

The bright source IRS-2 was identified in Chapter 2 as a very young ionising source, possibly possessing a massive stellar wind and intrinsically anomalous (i.e. non-Case B) recombination line ratios. More recent spectroscopic data (Chapter 5) also show anomalous line ratios. The present observations have shown that the source has signs of a small bipolar outflow, perhaps driven by the mass-losing wind. Using a similar argument as employed for IRS-1 and assuming a total luminosity $L_{\rm bol} = 540$ $L_{\odot}$ (Chapter 5), estimates of $T_{dust} \simeq 1,000$K and $A_{\rm v} \simeq 25$ mag are obtained from the photometry of IRS-2 itself.

6.4.3.2 The W75N Cluster

A total of 39 new low-luminosity sources were detected within the region of sky covered by Fig. 6.1. The nine objects detected in the H-band frame (Fig. 6.2 & Table 6.1) all have very similar H–K colours (mean = 2.2 ± 0.2) and are therefore likely to be subject to similar reddening and occupy the same volume of space. since the fraction of new objects which consists of 'background' stars is probably less than 5 per cent, it is safe to assume that all the detected objects belong to a single cluster which has recently formed within the W75 cloud. The K luminosity distribution of all 39 objects is shown as a histogram in Fig. 6.8, along with the same function for the 440 known sources in the Trapezium cluster in Orion (McCaughrean 1988). In order to compare the two samples a Kolmogorov-Smirnov test was applied to calculate the probability that they arise from the same population, or from a luminosity distribution common to young

Table 6.2: Derived intrinsic parameters for the hot dust component illuminating IRS-1

ZAMS[a]	Albedo[b]	A_V^c /mag	F_K excess[d]	F_H excess[e]	T_{H-K}^f /K	L_{bol}(dust)[g] / $L_\odot$	$L_J/L_{J,star}^h$
07	DL	16.2	23	2.6	850	1.7×10^4	0.21
	1	19.4	8	1.7	1100	2.7×10^3	0.25
B0.5	DL	10.8	52	4.4	820	1.1×10^4	0.34
	1	14.0	16	2.7	950	1.9×10^3	0.44

[a]Adopted spectral type for central star

[b]Albedo model: DL = wavelength-independant graphite-silicate model of Draine & Lee (1984); 1 = wavelength-independant model, no absorption

[c]A_V derived from the observed J-band flux in the nebula, assuming no significant hot dust component and 100 per cent of the J-band luminosity escapes via the reflection nebula.

[d]Calculated intrinsic K flux relative to that from the adopted ZAMS type

[e]Intrinsic H-band flux, as above

[f]Colour temperature from calculated intrinsic H–K index

[g]Bolometric luminosity luminosity of the hot dust emission component implied by the de-reddened F_K and T_{H-K}

[h]J-band lumnosity implied by L_{bol}(dust) and T_{H-K} as a fraction of that from the adopted ZAMS type

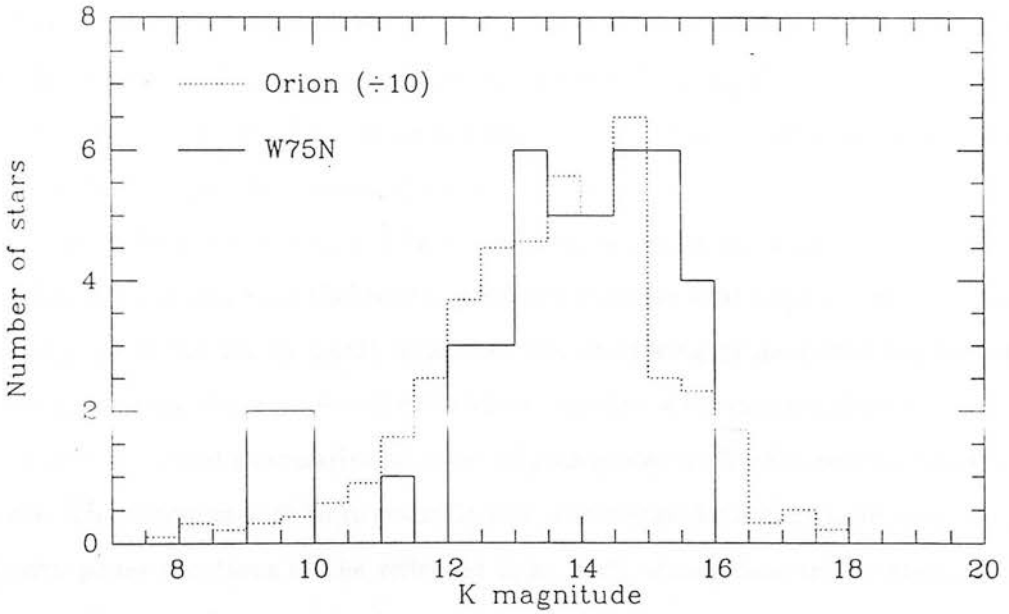

Figure 6.9: The K magnitude distribution in the detected members of the W75N cluster (solid lines). Superimposed (dotted lines) is the same distribution for the 440 sources detected at K in the Trapezium cluster in Orion (McCaughrean 1988). The Trapezium sample has been shifted by +2 mag to equalise the median values and is scaled by 1/10.

clusters. The W75N K magnitudes were binned in the same 0.5-mag intervals as used by McCaughrean. Since the Kolmogorov-Smirnov test is sensitive to median shifts, the Trapezium Sample was adjusted by adding 2 magnitudes to each bin, roughly equalising the median K magnitude with that of the W75N sample. This can be justified since account must be taken of (known) distance and (unknown) reddening differences. The test yielded a value for χ^2 of 1.1 with 2 degrees of freedom, which implies a probability of about 0.6 that the populations are the same. Thus, while the evidence is not conclusive that the underlying luminosity distributions are exactly the same, there is certainly no basis in the observations for rejecting this hypothesis. It is therefore quite plausible that the objects in W75N belong to a young cluster of stars similar to that already seen in Orion.

6.5 Conclusions

Seeing-limited 1.25-μm to 2.2-μm imaging polarimetry has revealed two separate infrared reflection nebulae in W75N. The larger and brighter nebula associated with HII(B) shows evidence of shell structure coincident with the blue-shifted lobe of the CO outflow. The 2.2-μm peak IRS-1 is found to be part of the reflection nebula and is not a self-luminous object, although a number of true sources do exist in close proximity. The obscuration of the luminosity source within HII(B) is highly direction-dependent, with A_V possibly greater than 130 mag along the direct line-of-sight but about 16 mag along the path of photons scattered in the nebula.

Comparison of the surface brightness distribution in the main nebula with that in similar sources and with theoretical predictions shows that large grains in a narrow size range ($a = 0.5\,\mu$m to $1\,\mu$m) dominate the scattering of near-infrared radiation. However, since the observed wavelength selects the size of the dominant scatterers, little can be inferred about the relative numbers of such grains within the overall distribution of sizes. The dominance of large grains in the near-infrared should produce anisotropic intensity phase functions in the reflected light, with strong forward scattering. This may contribute to the asymmetric appearance of many infrared reflection nebulae, in which the lobe directed away from the observer is often heavily suppressed.

There is no evidence in the distribution of scattered light for any large (> 0.02 pc) disk structure around the main luminosity source in W75N with which to associate the collimation of the CO outflow.

The small, bipolar reflection nebula around IRS-2 indicates that this source is generating a small-scale outflow of its own. There may be evidence of a 0.1-pc disk-like structure at the waist of the IRS-2 outflow but, if so, it appears to be of low mass ($\sim 2.5\ M_{\odot}$) and to be relatively diffuse ($\sim 5 \times 10^{10}\ m^{-3}$).

Photometric analysis shows that a significant amount of the observed near-infrared emission arises in regions of hot (800K to 1000K) dust close to the main luminosity sources. In the case of the dominant illuminating star, this dusty material does not appear to intercept and reprocess all the stellar emission, and may constitute the interior regions of a small disk. The likely presence, in the H-band, of significant emission from hot dust means that the J–H colour may not be a reliable indicator of extinction in these young objects.

39 new low-luminosity sources have been detected at $2.2\,\mu m$ within a roughly 70 arcsec square region around HII(B). Most of these objects appear to be part of a cluster of newly-formed stars associated with the main luminosity sources IRS-1, IRS-2 and IRS-3. Their K luminosity distribution shows no statistical evidence of deviation from that found in the large Orion cluster.

References

Bastien, P. & Ménard, F., 1988, *Astrophys. J.*, **326**, 334.

Bohlin, R.C., Savage, B.D. & Drake, J.F., 1978. *Astrophys. J.*, **224**, 132.

Castelaz, M.W., Hackwell, J.A., Grasdalen, G.L., and Gehrz, R.D., 1986, *Astrophys. J.*, **300**, 406.

Castelaz, M.W., Hackwell, J.A., Grasdalen, G.L., Gehrz, R.D. & Gullixson, C., 1985, *Astrophys. J.*, **290**, 261.

Dickel, J.R., Dickel, H.R. & Wilson, W.J., 1978, *Astrophys. J.*, **223**, 840.

Draine, B.T., & Lee, H.M., 1984. *Astrophys. J.*, **223**, 840.

Elsässer H. & Staude, H.J., 1978. *Astr. Astrophys.*, **70** L3.

Fischer, J., Sanders, D.B., Simon, M. & Solomon, P.M., 1985, *Astrophys. J.*, **293**, 508.

Forrest, W.J & Shure, M.A., 1986, *Astrophys. J. Lett.*, **311**, L81.

Haschick, A.D., Reid, M.J., Burke, B.F., Moran, J.M. & Millar, G., 1981, *Astrophys. J.*, **244**, 76.

Leinert, Ch. & Haas, M., 1987. *Astr. Astrophys.*, **182**, L47.

McCaughrean, M.J., 1988. *PhD Thesis* Edinburgh University.

McLean, I.S., 1987. *Infrared Astronomy with Arrays* ed. C.G. Wynn-Williams & E.E. Becklin. p. 180. University of Hawaii.

Mclean, I.S., Casali, M.M., Wright, G.S. & Aspin, C.A., 1989. *Proc. 3rd NASA-Ames Workshop on Infrared Detectors* ed. C. McCreight, in press.

Mathis, J.S., Rumpl, W. & Nordsieck, K.H., 1977. *Astrophys. J.*, **217**, 425.

Natta, A., Giovanardi, C. & Palla, F., 1988. *Astrophys. J.*, **332**, 921.

Reike, G.H., & Lebofsky, M.J., 1985. *Astrophys. J.*, **288**, 618 (RL).

Tokunaga, A.T., Lebofsky, M.J. & Reike, G.H., 1981, *Astr. Astrophys.*, **99**, 108.

Van de Hulst, H.C., 1957, *Light Scattering by Small Particles*, Wiley.

Yamashita, T., Sato, S., Nagata, T., Suzuki, H., Hough, J., McLean, I., Garden, R. & Gatley, I., 1987, *Astr. Astrophys.*, **177**, 258.

Yamashita, T., Sato, S., Tamura, M., Suzuki, H., Gatley, I., Hough, J.H., Mountain, C.M. & Moore, T.J.T., 1988, *Mon. Not. R. astr. Soc.*, **233**, 899.

Yamashita, T., Sato, S., Nagata, T., Gatley, I., Hayashi, S.S. & Fukui, Y., 1989, *Astrophys. J.*, **336**, 832.

Chapter 7

Conclusions

This thesis has been mainly concerned with an in-depth observational study of a single star formation region, W75N, undertaken in order to provide a comprehensive picture of the physical conditions in an environment that is forming high-mass stars. The importance of such studies lies in testing the detailed implications of generally-applicable models of the physics of the star formation process.

7.1 New Knowledge of W75N

Prior to this work, W75N was known to be a region of recent high-mass star formation lying in a large molecular cloud and containing a number of highly compact HII regions (and thus some young massive stars), one of which (HII(B)) has associated OH maser emission. A large (1-parsec scale) molecular outflow and a high-velocity H_2O maser source were also known to exist but the physical relationship between all these features was uncertain. The comprehensive set of data contained in the present work now allows the development of a detailed physical model of the region.

The two or three massive OB stars ionising the compact HII regions in W75N are part of an embedded young stellar cluster, revealed for the first time by near-infrared camera observations. The cluster consists largely of fainter, less luminous low-mass stars and the 2-μm luminosity distribution of the observed members contains no evidence of any significant difference (e.g. in the underlying mass distribution) from the Trapezium association in Orion.

From the submillimetre continuum observations, the dominant luminosity source (with $L_{bol} = 1.4 \times 10^5\ L_\odot$), responsible for heating most of the dust within the surrounding cloud core, is that within HII(B). This object is so heavily obscured by the overlying column of dust ($A_V \gtrsim 90$ mag) that it is not detected at near-infrared

wavelengths. The obscuration is, however, highly anisotropic and large amounts of near-infrared light escape via a bright reflection nebula.

Analysis of the emission in the reflection nebula shows that most of the scattered light originates in hot ($\sim$ 1000K) dust very close to the central star. The dust intercepts a significant fraction of the short-wavelength (optical and UV) photons from the star, is heated and re-radiates the energy into the near-infrared. The emission from this hot dust dominates the source continuum spectrum at wavelengths longer than 1.5 μm.

The dense circumstellar material containing the hot dust is unlikely to constitute a spherical cocoon, but may be distributed in a disk or disk-like configuration orbiting the star. Active accretion of mass may be continuing via such a disk, despite the presence of an energetic outflow and large amounts of ionising radiation. The size of such a structure would be no greater than a few times 100 A.U.

Surrounding the central source and the associated hot dust is the volume of ionised gas constituting HII(B). This compact HII region extends out to between 0.03 and 0.05 pc from the centre. The ionisation rate in this zone is significantly less than would be expected from the bolometric luminosity of the source. This may be explained by the interception of UV photons by the circumstellar dust and by large amounts of dust in the body of the HII region itself.

At the boundary between the ionised gas and the molecular cloud core there is a region of semi-dissociated, dense gas in which the dust is heated to a few $\times$ 100K. It is from this region that the OH maser emission is most likely to originate, since OH column densities here are considerably enhanced by the photo-dissociation of H_2O.

From the morphology of the high-velocity CO, HII(B) is the most probable generating source of the large molecular outflow. It is the blue-shifted lobe of this outflow that has created the bright reflection nebula illuminated from within HII(B). The fast-moving molecular gas has swept away the high-density ambient material, leaving a path for the escape of near-infrared radiation. Where it emerges from the dense cloud core, the flow has produced a shell of dusty swept-up material which forms the nebula.

Large grains are expected to dominate the scattering of near-infrared light and the distribution of surface brightness and polarisation fraction in the HII(B) nebula is consistent with the effects of anisotropic scattering by dust of equivalent size to the observed wavelength. These are chiefly interference effects and are manifested in strong forward-directed scattering and secondary maxima and minima in the angular pattern.

The polarisation vectors in the close vicinity of the main outflow source showed signs of the linear scattering pattern commonly thought to arise from scattering through an edge-on disk structure. However, this pattern should arise in any density distribution involving a flat 'surface' of final scatterers and there is no evidence in the 2-μm surface brightness distribution for any large ($\gtrsim$ 0.01 pc) disk-like formation.

About 25 arcsec to the northeast of HII(B) (a projected distance of about 0.25 pc) lies a somewhat more extended and probably more evolved ionised region known as HII(A), containing what may be a less massive ionising star (the ionisation rate is roughly equivalent to a ZAMS B0.5, but the 1-μm to 20-μm luminosity is more indicative of ZAMS B3). HII(A) is no longer closely surrounded by very large amounts of high-density gas since it does not heat a large column of dust and does not influence the distribution of submillimetre continuum emission, even though it dominates the region at 20 μm. This object is considerably less extinguished than HII(B), being a bright near-infrared source, but the ionised zone does not appear to have yet reached the edge of the cloud core or formed a 'blister' HII region.

Approximately 25 arcsec to the southwest of HII(B) lies another bright 2-μm source, IRS-2. This object is found to have a 1-μm to 20-μm luminosity of 540 $L_{\odot}$, which is likely to be a fair estimate of its total luminosity since the flux distribution is falling beyond 10 μm. Like HII(A), IRS-2 is considerably less reddened than HII(B) and may be situated closer to the front of the cloud core. This young object is a strong source of hydrogen recombination lines, despite being an intermediate-luminosity source and having no detected radio continuum emission. The recombination-line ratios observed are consistent with those expected to arise in a dense, optically thick, mass-losing wind which may be either fully or partially ionised. IRS-2 is illuminating a small bipolar reflection nebula of its own, which supports the implication of mass-loss in the hydrogen lines. The reflection lobes are rather wide with an uncollimated appearance, suggesting the wind or outflow expands into a low-density medium. The near-infrared colours of IRS-2 indicate that, as in HII(B), a considerable amount of hot dust is lying close to the source.

The mid-infrared emission detected from close to HII(A), HII(B) and IRS-2 trace narrow regions of warm ($\sim$ 100K) dust where the temperature is falling rapidly with distance into the cloud. These zones are likely to be associated with the photodissociation regions between the ionised gas and the surrounding molecular cloud.

Surrounding most or all of the stellar cluster is a dense core of molecular gas

and dust, traced by CS rotational transitions from the gas and by thermal submillimetre continuum from the dust. Here the dust is cool (20K to 30K) with a shallow temperature gradient. In W75N the CS emission and submillimetre continuum follow consistent morphologies in the cloud core, but the complementary submillimetre observations of AFGL 2591, which is a very similar type of source, apparently trace a quite different mass component to the CS lines. The latter appear to follow the more diffuse peripheral material and, presumably due to high opacities in the central regions, reveal little of the central structure of the core in that source.

The dense cloud core in W75N is very large, with a scale size of approximately 0.7 parsec and a mean density of about 1×10^{11} m^{-3}, and contains between 1800 $M_{\odot}$ and 2700 $M_{\odot}$ of material. The core is roughly symmetrical in overall shape with no sign of a large interstellar toroid or disk, or of any flattened structure. There is also no significant velocity gradient across the core that might be interpreted as rotation. However, there are clear physical features in the dense material that correspond directly to the morphology of the accompanying CO outflow and which illustrate how mutual interactions influence the structure and dynamics of both core and flow. The clearest of these features are the channel of reduced column density which contains the main red-shifted outflow lobe and the large clump of CS-traced gas which causes an apparent bifurcation in the flow where the fast-moving material impacts upon the clump.

A surprise was encountered in $C^{18}O$ observations of the densest parts of the central core region, when a dense condensation was found to the east of that associated with HII(B). The mean density of both condensations is about 1×10^{12} m^{-3} and although the new core contains a mass comparable to the original, it does not appear to have a central heat source. This object deserves closer study since it may be in a very early (i.e. pre-collapse) stage of the star formation process.

In observations of CO it was found that the outflow is asymmetrical and possibly multi-polar, but that the individual flow lobes are well-collimated. Dynamical calculations showed that the dense core, as traced by CS emission, is able to contain and re-collimate the high-velocity material if the outflow were initially isotropic or expanding freely before it first impinges on the cloud. The width and opening angle of the flow at its base plus its irregular large-scale form indicate that it is not initially highly-directed, or that it soon loses any initial collimation. These conclusions suggest that the outflow structure is determined chiefly by the density distribution in the surrounding cloud, as the fast-moving material takes the path of least resistance down

the steepest density gradients.

The internal structure of the outflow is not that of a thin shell of material around a hot, expanding wind-blown bubble. Instead, molecular material fills the outflow channel, with slow-moving dense material near the sides (presumably mostly existing in clumps recently ablated from the channel walls). Faster-moving material, containing fewer regions of high enough density to excite CS, occupy the centre of the channel (suggesting that the dense clumps have been disrupted and accelerated as they move into the flow). Temperatures in the flow were found to be low ($\sim$ 15K) and similar to those in the ambient cloud, but the temperatures increased somewhat towards the central flow axis.

No sign of rotation was found in the CS core and it is unlikely that the observed large-scale (> 0.1 pc) flow could be driven by rotation-powered magneto-hydrodynamic generating mechanisms, especially since the flow is not cylindrically symmetric. Although a stellar-wind driven model appears much more likely, it may be that rotational energy-driven mechanisms, which also provide a means of shedding angular momentum, operate on a small scale ($\ll 0.1$ pc) close to the source and supply the initial kinetic energy.

7.2 Some Implications for the General Case

Among the conclusions for the general picture of star formation that can be drawn from the present observations is that large interstellar disks or toroids are unnecessary for the production of collimated molecular outflows. On the largest scales, flow collimation or re-collimation can be achieved through containment be the ambient core material. There is therefore no strict requirement for flows to be bipolar on such scales. Bipolarity may occur where overall toroidal symmetry has been induced in the cloud by significant rotation and, since all clouds must possess some angular momentum, bipolar flows may constitute the majority case.

Since fast-moving, cold molecular material is found to fill the outflow channel in W75N, molecular outflows cannot in general be energy-driven by hot bubbles created by stellar winds. Furthermore, since the ubiquity of the outflow phenomenon points to a single, universal generating mechanism, it is more likely that all outflows are momentum-driven and consist of molecular material accelerated and swept along initially by an energetic stellar wind. The initial driving process is still open to question,

however, and may be violent stellar surface activity producing a fast massive wind, or acceleration may occur on small scales through a magnetic-torque or centrifugally-driven process which also allows the young star to lose angular momentum.

The large, toroidal configurations of dense matter that have been observed in other sources probably have no dynamical relationship to the accompanying flows, except that they may be the remains of flattened structures that were already present in the pre-collapse clouds (formed either at random, or in the presence of rotation or ordered magnetic fields). The complementary observations of AFGL 2591 show that care must be taken in interpreting isolated molecular line observations. Saturation is easy to achieve in the lower rotational levels of CS and they cannot always be relied upon to trace the mass distribution in the central regions of cloud cores. Dynamically active disks are more likely to exist on very small scales where they would have a much larger specific energy and could play a part in driving outflows. Consistent with this, there is considerable circumstantial evidence for significant amounts of circumstellar material very close to the studied sources.

If the near-infrared photons from the reflection nebulae are scattered mostly from large grains (with radius $\simeq \lambda$) and the observed features in the surface brightness and polarisation fraction distributions are due to diffraction effects in the scattering phase functions then, although little can be deduced concerning the overall grain size distribution, it may be possible to gain much-needed information on intrinsic grain properties (e.g. shape and refractive index) upon which the scattering pattern depends. Large grains are strongly forward-scattering which will naturally tend to enhance the brightness of the nearer reflection lobe (associated with the blue-shifted outflow) in a bipolar source and reduce that of the further (red-shifted) lobe. It is clear that it is not necessary to invoke large obscuring, tilted disks to explain the ubiquitous suppression of the far lobe in such sources, as has often been done. A linear pattern in the polarisation vectors across the source is often taken as the signature of multiple scattering in an edge-on dense disk. However, it is possible to reproduce such a pattern with any roughly planar, high opacity 'surface' containing the secondary or final scatterers above which is a reduced-density 'atmosphere' of primary or penultimate scatterers. The presence of linear polarisation patterns is not, therefore, proof of the presence of a disk.

The finding that the H-band continuum emission can be severely contaminated by hot dust implies that J–H colour cannot be reliably used to measure the extinction in

such young objects. This creates a non-trivial problem, since hydrogen recombination-line ratios cannot be used either for this purpose because classical Case B predictions may not be relevant, as shown by the spectroscopic observations of IRS-2.

The study of the W75N cluster is incomplete but its presence supports ideas of formation of high-mass stars within such groups. There may be evidence in W75N that high-mass star formation does not necessarily spell the end of star formation within a cloud, since the W75N cloud core is largely intact after approximately 10^5 yr of molecular outflow from the dominant source.

7.3 Thoughts for the Future

Further observational studies such as this will be needed to extend the existing knowledge of physical conditions in star-forming sources. It will be important to probe closer to the source of the molecular outflows for clues to the generating mechanism. High spatial resolution studies of the flows themselves with millimetre-wave array telescopes will eventually reveal the collimation state on 0.01-pc scales. High sensitivity spectroscopy in the near-infrared (with new instruments and large-mirror telescopes) of hydrogen recombination lines and of the 2-μm and 4-μm CO vibrational transitions will probe the physics of the atomic and molecular flows in the close vicinity of the sources. A rather more distant hope is that stellar structure theory (perhaps aided by space-vehicle observations of the Sun) may improve knowledge of stellar surface activity in relation to mass loss and outflow generation in very young stars.

Many young massive objects are heavily obscured in the near-infrared and studies of the scattering properties of interstellar grains may prove invaluable since scattered light is often contains the only information 'direct' from a source.

A number of questions still require answers in the larger picture of high-mass star formation which could be answered through imaging observations of young clusters. Information is required on the distribution of stellar masses soon after formation and whether this is correlated with the core temperature or density. Also, it is not known if clusters form all at once or sequentially and, if the latter, whether high- or low-mass stars form first and in what part of the cloud this happens.

Appendix A

Derivation of the Radiation Transport Equations used in Molecular Line LTE Analysis

The majority of this sequence of derivations was compiled from the literature by C.J. Chandler (personal communication)

The absorption coefficient for a transition between the rotational states $J = j \rightarrow i$ is

$$\kappa(\nu_{ji}) = \frac{h\nu_{ji}}{4\pi}[n_i B_{ij} - n_j B_{ji}]\phi(\nu_{ji})$$

where $\phi(\nu_{ji})$ is the line profile phase function of the transition. Therefore

$$\kappa(\nu_{ji}) = \frac{h\nu_{ji}}{4\pi} n_i B_{ij} \left[1 - \frac{n_j B_{ji}}{n_i B_{ij}}\right] \phi(\nu_{ji}).$$

But $g_i B_{ij} = g_j B_{ji}$, where g_i and g_j are the statistical weights of the two levels. Hence,

$$\kappa(\nu_{ji}) = \frac{h\nu_{ji}}{4\pi} n_i B_{ij} \left[1 - \frac{n_j g_i}{n_i g_j}\right] \phi(\nu_{ji}). = \frac{h\nu_{ji}}{4\pi} n_i B_{ij} \left[1 - e^{-h\nu_{ji}/kT_{ex}}\right] \phi(\nu_{ji}).$$

if local thermodynamic equilibrium (and so the Boltzmann population distribution) is assumed. T_{ex} is the excitation temperature characterising the distribution and is defined by $n_j g_i / n_i g_j = \exp(-h\nu_{ji}/kT_{ex})$. We also know that the Einstein transition coefficients are related by

$$A_{ji} = \frac{2h\nu_{ji}^3}{c^2} B_{ji} = \frac{g_i}{g_j} B_{ij} \frac{2h\nu_{ji}^3}{c^2}$$

and therefore that

$$B_{ij} = \frac{g_j}{g_i} \frac{c^2}{2h\nu_{ji}^3} A_{ji}$$

and so

$$\kappa(\nu_{ji}) = \frac{h\nu_{ji}}{4\pi} n_i \frac{g_j}{g_i} \frac{c^2}{2h\nu_{ji}^3} A_{ji} \left[1 - e^{-h\nu_{ji}/kT_{ex}}\right] \phi(\nu_{ji}).$$

$$= \frac{c^2}{8\pi} \frac{g_j}{g_i} n_i \frac{A_{ji}}{\nu_{ji}^2} \left[1 - e^{-h\nu_{ji}/kT_{ex}}\right] \phi(\nu_{ji}). \tag{A.1}$$

Generally, where the total number of particles is n,

$$\frac{n_i}{n} = \frac{g_i}{\mathcal{Z}} e^{-h\nu_{i0}/kT_{ex}} \tag{A.2}$$

where $\mathcal{Z}$ is the partition function:

$$\mathcal{Z} = \sum_{J=0}^{\infty} (2J+1) \exp\left[\frac{-hBJ(J+1)}{kT_{ex}}\right]$$

where the substitution $\nu_{J,0} = BJ(J+1)$ has been made. $B = h/8\pi^2\mathcal{I}$ is the rotation constant and $\mathcal{I}$ is the moment of inertia of the molecule.

For $hB \ll kT_{ex}$, the expression for $\mathcal{Z}$ can be approximated as an integral:

$$\mathcal{Z} \simeq \int_0^{\infty} (2J+1) \exp\left[\frac{-hBJ(J+1)}{kT_{ex}}\right] dJ$$

which solves to give

$$\mathcal{Z} \simeq \frac{-kT_{ex}}{hB} \left[\exp\left(\frac{-hBJ(J+1)}{kT_{ex}}\right)\right]_0^{\infty}$$

$$= \frac{-kT_{ex}}{hB} \tag{A.3}$$

NOTE: this assumes that T_{ex} is the same for all transitions.

We can now substitute for $n_i g_j / g_i$ in equation 1. From equations 2 and 3,

$$n_i \frac{g_j}{g_i} = \frac{g_j}{g_i}\frac{g_i}{\mathcal{Z}} n e^{-h\nu_{i0}/kT_{ex}} = g_j \frac{hB}{kT_{ex}} n e^{-h\nu_{i0}/kT_{ex}}$$

so equation 1 becomes

$$\kappa(\nu_{ji}) = \frac{c^2}{8\pi} g_j \frac{hB}{kT_{ex}} e^{-h\nu_{i0}/kT_{ex}} \frac{A_{ji}}{\nu_{ji}^2} \left[1 - e^{-h\nu_{ji}/kT_{ex}}\right] n\phi(\nu_{ji}).$$

The optical depth of the radiation is given by

$$d\tau(\nu) = \kappa(\nu) dx$$

$$\tau(\nu) = \int \kappa(\nu) dx \simeq \kappa(\nu) L$$

where L is the extent of the emittion region along the line of sight. Therefore

$$\tau(\nu_{ji}) \simeq \frac{c^2}{8\pi} g_j \frac{hB}{kT_{ex}} e^{-h\nu_{i0}/kT_{ex}} \frac{A_{ji}}{\nu_{ji}^2} \left[1 - e^{-h\nu_{ji}/kT_{ex}}\right] \phi(\nu_{ji}) N.$$

N is the column density of material contributing to the line emission. If we substitute $g_j = 2j + 1$ and $\nu_{i0} = Bi(i + 1)$,

$$\tau(\nu_{ji}) = \frac{c^2}{8\pi}(2j+1) \frac{hB}{kT_{ex}} e^{-hBi(i+1)/kT_{ex}} \frac{A_{ji}}{\nu_{ji}^2} \left[1 - e^{-h\nu_{ji}/kT_{ex}}\right] \phi(\nu_{ji}) N. \tag{A.4}$$

We can also substitute for A_{ji}:

$$A_{ji} = \frac{16\pi^3}{3\varepsilon_o h c^3} \nu_{ji}^3 |\mu_{ij}|^2$$

where $|\mu_{ij}|$ is the dipole moment matrix element for the transition, summed over the three perendicular directions in space. It can be shown that $|\mu_{ij}|^2 = \mu^2 j/(2i+3)$ for $j \rightarrow i$, $j = i+1$ (Townes & Schawlow 1955). Then,

$$\tau(\nu_{ji}) = \frac{2\pi^2}{3\varepsilon_o hc}(2j+1)\frac{hB}{kT_{ex}}\nu_{ji}|\mu_{ij}|^2 e^{-hBi(i+1)/kT_{ex}}\left[1-e^{-h\nu_{ji}/kT_{ex}}\right]\phi(\nu_{ji})N. \qquad (A.5)$$

In order to obtain an expression for the peak line optical depth, we can approximate $\int \tau(\nu)d\nu \simeq \tau_o \Delta\nu$, where τ_o is the peak optical depth and $\Delta\nu = \sqrt{\pi/(4\ln 2)}\times$ FWHM $= 1.064 \times$ FWHM for a Gaussian line. For a Doppler broadened line, FWHM $= \Delta\nu = \nu_{ji}V/c$.

For two adjacent transitions of the same species, $J+1 \rightarrow J$ and $J \rightarrow J-1$, it is possible to calculate the ratio of line optical depths. From equation 5, since $\int \phi(\nu)d\nu = 1$:

$$\tau(J+1,J) = \frac{2\pi^2}{3\varepsilon_o hc}(2J+3)\frac{hB}{kT_{ex}}\frac{c}{V}\mu^2\frac{(J+1)}{2J+3}e^{-hBJ(J+1)/kT_{ex}}\left[1-e^{-h2B(J+1)/kT_{ex}}\right]N.$$

$$\tau(J,J-1) = \frac{2\pi^2}{3\varepsilon_o hc}(2J+1)\frac{hB}{kT_{ex}}\frac{c}{V}\mu^2\frac{J}{2J+1}e^{-hBJ(J-1)/kT_{ex}}\left[1-e^{-h2BJ/kT_{ex}}\right]N.$$

Hence the ratio of optical depths is

$$\frac{\tau(J+1,J)}{\tau(J,J-1)} = \frac{(J+1)}{J}e^{-2hBJ/kT_{ex}}\frac{\left(1-e^{-2hB(J+1)/kT_{ex}}\right)}{\left(1-e^{-2hBJ/kT_{ex}}\right)}$$

$$= \frac{J+1}{J}\frac{\left(1-e^{-2hB(J+1)/kT_{ex}}\right)}{\left(e^{2hBJ/kT_{ex}}-1\right)}. \qquad (A.6)$$

Radiation temperature T_R is given by

$$T_R = \frac{c^2}{2k\nu^2}(I_\nu - I_{bg})$$

where I_{bg} is the intensity of the microwave background at the frequency of the line and

$$I_\nu = \frac{2h\nu^3}{c^2}\frac{1}{\left(e^{h\nu/kT_{ex}}-1\right)}\left(1-e^{-\tau(\nu)}\right).$$

Hence

$$T_{\rm R} = \frac{h\nu}{k}\left[\frac{1}{(e^{h\nu/kT_{ex}}-1)} - \frac{1}{\left(e^{h\nu/kT_{bg}}-1\right)}\right]\left(1-e^{-\tau(\nu)}\right). \tag{A.7}$$

For $\tau(\nu) \ll 1$ and $h\nu \ll kT$, this becomes

$$T_{\rm R} \simeq \tau(\nu)(T_{ex} - T_{bg})$$

and for $T_{ex} \gg T_{bg}$,

$$T_{\rm R} \simeq \tau(\nu)T_{ex}.$$

Thus equation 6 can be used to find the ratio of $T_{\rm R}(J+1, J)$ to $T_{\rm R}(J, J-1)$:

$$\frac{T_{\rm R}(J+1,J)}{T_{\rm R}(J,J-1)} \simeq \left(\frac{J+1}{J}\right)\frac{2hB(J+1)/kT_{ex}}{2hBJ/kT_{ex}}$$

$$= \left(\frac{J+1}{J}\right)^2$$

which is true for optically thin transitions in the high excitation temperature limit.

From Equation 4, it is easy to obtain an expression for the column density of gas emitting in the measured line, in terms of the line temperature $T_{\rm R}$.

$$N_{ji} = \frac{8\pi}{(2j+1)c^2}\frac{kT_{ex}}{hB}e^{hBi(i+1)/kT_{ex}}\frac{\nu_{ji}^2}{A_{ji}}\left[1-e^{-h\nu_{ji}/kT_{ex}}\right]^{-1}\int\tau(\nu_{ji})d\nu \tag{A.8}$$

and from above,

$$\int\tau(\nu)d\nu \simeq \frac{1}{T_{ex}}\int T_{\rm R}(\nu)d\nu = \frac{\nu}{cT_{ex}}\int T_{\rm R}(V)dV.$$

To correct for optical depth, the factor $\tau/(1-e^{-\tau})$ is applied to the right hand side of equation 8.

In the case of $J = 1-0$ transitions the expression simplifies to

$$N_{10} = \frac{16\pi}{3c^3}\frac{k}{h}\frac{\nu_{10}^2}{A_{10}}\left[1 - e^{-h\nu_{10}/kT_{ex}}\right]^{-1}\int T_{\rm R}(V)dV.$$

References

Townes, C.H. & Schawlow, A.L., 1955. *Microwave Spectroscopy*, McGraw-Hill Publications, Inc., New York.

Appendix B

Gravitational Force on a Gaussian-distributed Cloud Core Around a Central Star

The radial distribution of density within an idealised cloud core is given by:

$$\rho(r) = \rho_o e^{-r^2/2\sigma^2}$$

Where ρ_o is the density at the centre of the core and σ is the variance of the Gaussian distribution. Hence, for a central star of mass M_*, the gravitational force exerted by the star on the core is:

$$F_* = -4\pi\rho_o G M_* \int_0^\infty e^{-r^2/2\sigma^2} dr = -4\pi\rho_o G M_* \sqrt{\frac{\pi}{2}}\sigma,$$

since, when $m = 0$ and $a = 1/2\sigma$:

$$I_m = \int_0^\infty x^m e^{-ax^2} dx = \frac{\Gamma[(m+1)/2]}{2a^{(m+1)/2}} = \sqrt{\frac{\pi}{2}}\sigma.$$

The total cloud core mass $M_{\rm cl}$ is given by

$$M_{\rm cl} = 4\pi\rho_o \int_0^\infty r^2 e^{-r^2/2\sigma^2} dr = \rho_o (2\pi)^{3/2}\sigma^3,$$

since

$$\int x^2 e^{-ax^2} dx = \frac{\Gamma(3/2)}{2a^{3/2}} = \frac{\sqrt{\pi}/2}{2a^{3/2}}.$$

Thus, the expression for the gravitational binding force on the cloud core material due to the star becomes:

$$F_* = -4\pi G M_* \frac{M_{\rm cl}}{(2\pi)^{3/2}\sigma^3}\sqrt{\frac{\pi}{2}}\sigma = -4\pi G M_* \frac{M_{\rm cl}}{\sigma^2}.$$

This can be expressed in terms of the radius at half-maximum density in the core, $r_{1/2}$, since $\sigma = r_{1/2}/\sqrt{2\ln 2}$. Hence,

$$F_* = -2\ln 2 \frac{G M_* M_{\rm cl}}{r_{1/2}^2}$$

Secondly, the self-gravity or binding force within the core itself is given by:

$$F_{\rm cl} = (4\pi)^2 G \int_0^\infty \rho(r) \int_0^r r'^2 \rho(r') dr' dr.$$

This expression is easily approximated numerically, by assuming $F_{\rm cl} = C.GM_{\rm cl}^2/r_{1/2}^2$ where C is a constant. C can be found by means of the following algorithm (C.J. Chandler, personal communication):

1. Initialise values of radius in the cloud (r) and radial mass distribution $M(r)$.

2. Select step size Δr and total number of steps.

3. For simplicity, assume $r_{1/2}^2/\ln 2 = 2\sigma^2 = 1$ and calculate the value of the following sum

$$M(r) = M(r - \Delta r) + r^2 e^{-r^2} \Delta r$$

4. Calculate the value of the following sum

$$I(r) = I(r - \Delta r) + M(r) e^{-r^2} \Delta r.$$

5. Increase the value of r by one step: $r = r + \Delta r$ and return to Step 3. Repeat until the maximum number of steps is reached.

6. Since, from above,

$$M_{\rm cl} = \left(\frac{\pi}{\ln 2}\right)^{3/2} \rho_{\rm o} r_{1/2}^3$$

and so

$$\frac{GM_{\rm cl}^2}{r_{1/2}^2} = G\left(\frac{\pi}{\ln 2}\right)^3 \rho_{\rm o}^2 r_{1/2}^4 = \frac{G\pi^3\rho_{\rm o}^2}{\ln 2},$$

the constant C is given by

$$C = \frac{(4\pi)^2 G\rho_{\rm o}^2 I(r_{\rm max})}{G\pi^3\rho_{\rm o}^2/\ln 2} = \frac{16\ln 2}{\pi} I(r_{\rm max}).$$

If Δr is chosen to be very small and the number of steps is very large, the calculated value of C approaches 0.252 asymptotically. Hence, the total gravitational binding force on the core is given by

$$F_{\rm grav} \simeq \frac{GM_{\rm cl}}{r_{1/2}^2}\left[(2\ln 2)M_* + 0.25M_{\rm cl}\right].$$

This expression is a factor of 4 smaller than that given by Davidson & Jaffe (1984) and by Gear *et al.* (1986) in the same terms. This difference is easily accounted for if the latter authors mistakenly defined $r_{1/2}$ as the full width at half maximum of the Gaussian density distribution, rather than the half-width or radius.

References

Davidson, J.A. & Jaffe, D.T., 1984. *Astrophys. J., Lett.*, **277**, L13.

Gear, W.K., Gee, G., Robson, E.I., Ade, P.A.R. & Duncan, W.D., 1986. *Mon. Not. R. astr. Soc.*, **219**, 835.

Appendix C

Calculation of Integrated Flux from the Map of an Extended Source, Using a Single-point Calibration

The ideal way of finding the total flux from the map of an extended source is to make an identical map of the flux calibrator. The problem is then a trivial one of aperture photometry, with the maps as the effective aperture. This method requires no knowledge of the effective beam shape during the observations, nor assumptions of the source distribution and the sampling within the maps is accounted for. If the flux (density) of the point source standard is F_{st} and the uncalibrated surface brightnesses at each point i in the maps of object and standard are $V_i(\mathrm{obj})$ and $V_i(\mathrm{st})$ (in units of millivolts or 'counts'), then the calibration for the target source is given by

$$\mathrm{Cal} = \frac{F_{\mathrm{st}}}{\sum_i V_i(\mathrm{st})}$$

and so the target flux is

$$F_{\mathrm{obj}} = \sum_i V_i(\mathrm{obj}) \times \mathrm{Cal} = \sum_i V_i(\mathrm{obj}) \times \frac{F_{\mathrm{st}}}{\sum_i V_i(\mathrm{st})}.$$

If the map of the flux calibrator (usually an unresolved standard star). were sampled so that the central point fell on the position of the star, the strength at that point $V_{\mathrm{peak}}(\mathrm{st})$ would measure the total flux of the standard. A calibration can be obtained in this case without mapping the star:

$$\mathrm{Cal(single\ point)} = \frac{F_{\mathrm{st}}}{V_{\mathrm{peak}}(\mathrm{st})}$$

therefore,

$$F_{\rm obj} = \frac{\sum_i V_i({\rm obj}) \times {\rm Cal(single\ point)}}{\sum_i V_i({\rm st}) \div {\rm V_{peak}(st)}}.$$

The denominator is simply the ratio of the total coadded to the peak surface brightness in the hypothetical map of the standard. Since, if the beam profile is known accurately, it is possible to calculate this factor without actually making the map we can obtain an accurate total source flux for an extended target with just a single point calibration observation. With a Gaussian beam and full Nyquist sampling (at HPBW/2 frequency), the factor is

$$\sum_i \exp(-x_i y_i / 2\sigma^2) = 4.51.$$

In this case the source flux is given by

$$F_{\rm obj} = \frac{\sum_i V_i({\rm obj})}{4.51} \times {\rm Cal(single\ point)}.$$

and only a single point calibration observation is required. Since many calibration measurements are usually necessary, this saves a large amount of observing time. One map of a point source may be required if the beam shape is not well known.

Mon. Not. R. astr. Soc. (1988) **234**, 95–105

New near-infrared sources and reflection nebulosity in W75N

T. J. T. Moore *Edinburgh University, Astronomy Department, Blackford Hill, Edinburgh EH9 3HJ*

C. M. Mountain *Royal Observatory, Blackford Hill, Edinburgh EH9 3HJ*

T. Yamashita *Nobeyama Radio Observatory, Nobeyama, Minamisaku, Nagano 384-13, Japan*

M. J. Selby *Department of Physics, Imperial College, Prince Consort Road, London SW7 2AZ*

Accepted 1988 February 16. Received 1988 January 18; in original form 1987 November 5

Summary. Near-infrared observations around the OH maser source in W75N reveal new embedded sources, an infrared reflection nebula and extended molecular hydrogen emission. The brightest 2 μm continuum source, IRS-1, may be either a peak in the reflection nebula or a self-luminous object, although the former requires very large near-infrared continuum and recombination brightness from the true luminosity source. Confirmation of either model requires observations with higher spatial resolution. A second source, IRS-2, is a very young object with strong recombination lines but no accompanying 5 GHz continuum emission. Photometry indicates a visual extinction of $\geqslant$34 mag towards IRS-2, assuming a hot stellar photosphere. The source of luminosity in the reflection nebula has a ZAMS stellar type between B0.5 and O7 or equivalent, and is probably coincident with the ultracompact H II region W75N(OH).

We have also mapped molecular hydrogen v=1–0 $S(1)$ emission in a slightly undersampled 1.5×2 arcmin^2 area. The total reddened luminosity detected in the line is $\sim 0.3\,L_\odot$. Energetics calculations show that either UV photons or CO outflow mechanical energy are sufficient to account for the H_2 emission by fluorescence or shock-excitation. H_2 line ratios fall between the values expected for the two mechanisms, suggesting that both may contribute.

Simple dynamical time-scales suggest that the various sources in this region are the result of coeval formation, if a north-south density gradient of around 10 per cent may be assumed in the original cloud.

1 Introduction

W75N is a bipolar CO outflow source and infrared-luminous region of recent star formation with an integrated *IRAS* SKYFLUX luminosity of over $10^5\,L_\odot$. It is embedded in a large molecular

cloud with average radial velocity near +9 km s^{-1} (Dickel, Dickel & Wilson 1978), at a distance of 2 kpc (Dickel, Wendker & Bieritz 1969) and is part of the Cygnus-X complex of dense molecular clouds. There are a number of radio, infrared and molecular line sources associated with the W75N region and Dickel *et al.* (1978), who have mapped the large-scale structure of this area in ^{12}CO and ^{13}CO, suggest that these sources may be the products of an interaction between the W75N and nearby DR-21 molecular clouds.

The region contains a bright OH maser source W75N(OH) identified with a faint ultracompact H II region, H II(B), lying 25 arcsec to the south and 15 arcsec to the west of a more extended H II region, H II(A) (Habing *et al.* 1974; Haschick *et al.* 1981). H II(A) coincides with a 20 μm continuum peak (Wynn-Williams, Becklin & Neugebauer 1974) and is also a source of molecular hydrogen emission (Fischer, Righini-Cohen & Simon 1980). However, H II(B), relatively less studied in the infrared, is also close to a high-velocity H_2O maser (Genzel & Downes 1977) and to the peak of the far-infrared emission that probably dominates the luminosity of this region (detected at 53 μm by Harvey, Campbell & Hoffmann 1977). It has been shown that H II(B) is also a source of molecular hydrogen emission (Mountain *et al.* 1985a).

Fischer *et al.* (1985) have reported ^{12}CO J=1–0 line profiles from W75N with a full width, at 0.1 K antenna temperature, of about 35 km s^{-1}. This satisfies the criterion of Lada (1985) defining the presence of a high-velocity cold molecular outflow, i.e. that the full width at T_A^* (^{12}CO)=0.1 K should be greater than 10 km s^{-1}. These authors also mapped the region in the high-velocity wings of ^{12}CO and discovered an apparently lightly collimated bipolar outflow centred near to the H II(A) and H II(B) sources, and extending out to about 1.2 pc from it.

In this paper we present new near-infrared observations of the W75N region including a 2.2 μm continuum map covering a 64×48 arsec^2 area centred near to W75N(OH). This map reveals a cluster of previously unobserved near-infrared continuum sources and an extensive 2 μm reflection nebula. Using photometry and Brackett line detections we estimate the extinction towards these sources and discuss the detailed structure of the region and the nature of the individual objects found. An undersampled map of molecular hydrogen v=1–0 S(1) detections is also presented covering a 1.5×2 arcmin^2 area. The strength, distribution and location of the emission is discussed in comparison with excitation models and the constraints they place on the energetics of the source.

2 Observations and results

All observations were made on the 3.8-m United Kingdom Infrared Telescope (UKIRT) on Mauna Kea, Hawaii. The 4 μm spectroscopy was done with a 5 arcsec aperture using the cooled grating spectrometer CGS2 as part of the UKIRT Service Observing Programme of 1986 October 10. The 2 μm mapping, photometry and spectroscopy were carried out with the UKIRT CVF spectrophotometer UKT-9 during three half nights of 1985 July 28–30. Photometry was done in a 7.8 arcsec beam for the UKIRT filter set J, H, K, and L' and in a 5 arcsec beam for M. The H_2, v=1–0 S(1) line was mapped with a 'Queensgate' 2 μm Fabry–Perot etalon with a resolution of ~120 km s^{-1}, used in an uncollimated f/36 beam in front of UKT-9 with a 19.6 arcsec sky aperture. Sky chopping was used in all observations, the beams being separated ~130 arcsec east–west. The telescope pointing was accurate to about ±3 arcsec throughout the observations.

Spectrometric and flux calibrations were obtained using NGC 7027 and standard stars from the UKIRT standards list. We assumed a line strength, in H_2 v=1–0 S(1), of (2.5±0.5)×10^{-15} Wm^{-2} for NGC 7027, obtained by integrating the map of Beckwith *et al.* (1980) over the 19.6-arcsec aperture used for the 2 μm spectroscopic observations.

The 2.2 μm continuum flux density map, made on a 4 arcsec grid with the 7.8 arcsec circular beam, is shown in Fig. 1. The offset centre is at 20^{h}36^{m}50^s.5 +42°26′56″ (1950). This is the peak of

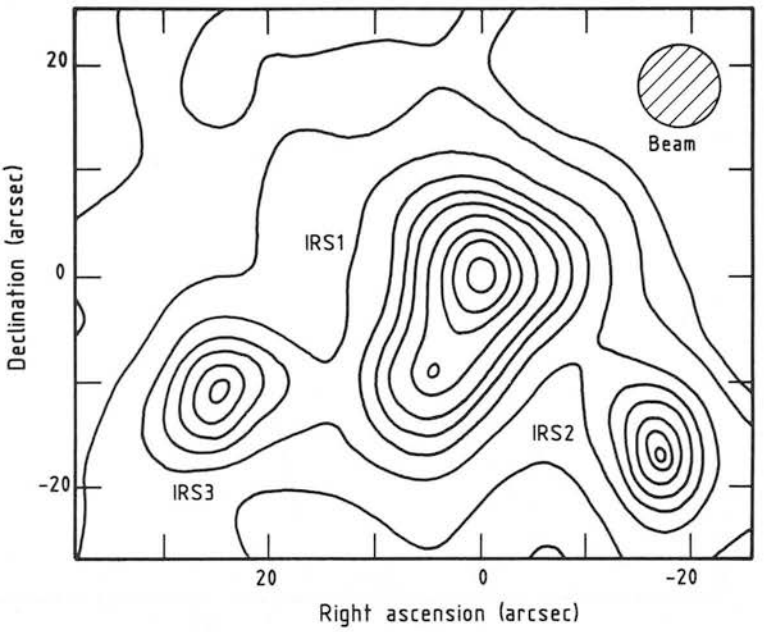

Figure 1. K continuum map. Contours are at 2, 4, 10, 20, 30, . . . , 80×10^{-15} Wm$^{-2}\mu$m^{-1} per 7.8 arcsec beam. The offset centre is at $20^h36^m50^s5$; +42° 26′ 56″ (1950). The map is oversampled at 4 arcsec intervals.

the 2 μm emission, and is about 3 arcsec south and 6 arcsec east of the position of W75N(OH). The image has been slightly smoothed using a 2D Gaussian function with a sampling radius equivalent to the beam size. The map reveals a small cluster of previously undetected near infrared sources which we have designated (in order of 2 μm brightness) IRS-1, IRS-2, IRS-3. The latter two sources are pointlike while IRS-1 appears extended by ~15 arcsec towards the south-east, with other slight extensions to the west and north-east. Fig. 1 also shows the existence of diffuse 2 μm emission extending over almost the whole area covered by the map, with low-level emission ($<2\times10^{-15}$ Wm$^{-2}\mu$m^{-1} per beam) extending beyond the limits set by our observations.

Results of photometry measurements are given in Table 1 and Fig. 2 for IRS-1, IRS-2, IRS-3 and a representative point in the extended nebula at offset 20 arcsec east, 12 arcsec north. IRS-1 and IRS-2 are highly reddened, IRS-2 having an H–K=3.5 and K–L'=3.8, and typical points in the nebula have H–$K\simeq$2.3, similar to IRS-1. Flux calibrations were obtained using standard stars and the measurements of absolute flux from Vega by Mountain *et al.* (1985b).

Brγ and Brα line strengths toward IRS-1 and IRS-2 are listed in Table 2. Two 2.05–2.30 μm CVF spectra taken at separate points in the extended nebula are displayed in Fig. 3(a) and (b) and

Table 1. 1–5 μm photometry.

Source	Offset (arcsec)		Magnitude					Implied A_V (from J–H)
			J	H	K	L'	M	
IRS-1	0	0	14.0	11.3	9.2	7.0	–	25
IRS-2	16W	16S	16.4*	12.8	9.3	5.5	4.3	≥34
IRS-3	24E	12S	12.7	10.9	9.6	–	–	17
Diffuse nebula	20E	12N	17.6*	15.0	12.7	–	–	≥24

*3σ upper limit.
– indicates that no measurement was made.

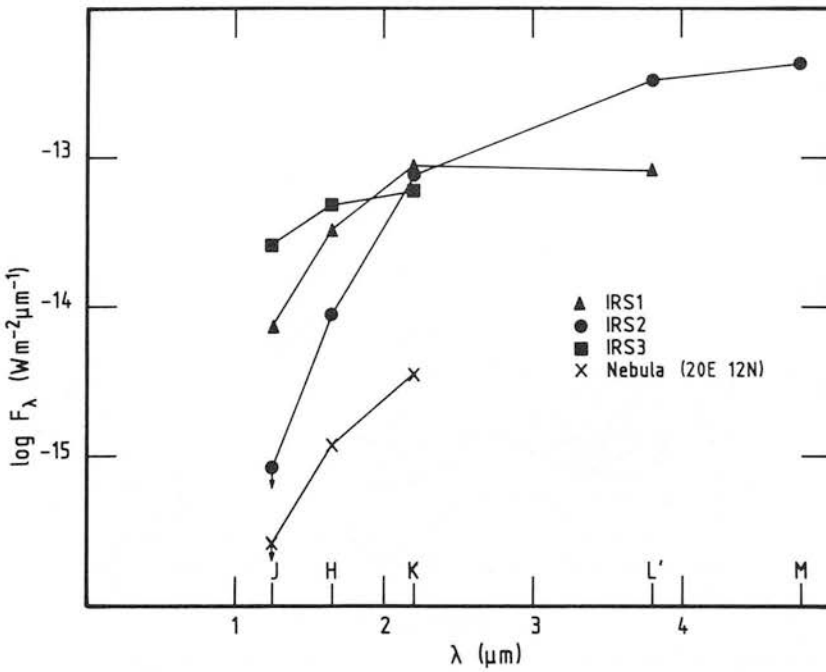

Figure 2. Results of *JHKL'M* photometry towards IRS-1, IRS-2, IRS-3 and a position in the diffuse nebula. The *J* measurements of IRS-2 and the diffuse nebula are upper limits. Typical 1σ errors are around 10 per cent.

Table 2. Recombination line strengths.

Source	Observed line fluxes (10^{-16}Wm^{-2})	
	Brγ: 2.166μm (20 arcsec beam)	Brα: 4.052μm (5 arcsec beam)
IRS-1	1.0 (±0.2)	1.2 (±0.2)
IRS-2	1.2 (±0.2)	9 (±1)

each clearly shows the v=1–0 $S(1)$ (2.122μm), v=1–0 $S(0)$ (2.223μm) and v=2–1 $S(1)$ (2.248μm) lines of molecular hydrogen.

To determine the extent and magnitude of the molecular hydrogen emission in the vicinity of H II(B) the v=1–0 $S(1)$ line was mapped with a circular 19.6 arcsec beam on a 20 arcsec grid. At each point the line and continuum contributions were measured by stepping the Fabry–Perot (F.P.) off the line centre to a suitable continuum point, determined from initial CVF and F.P. scans. The total line-plus-continuum integration time per point was 8 s. The $S(1)$ line strengths are accurate to about 20 per cent, most of the error arising from uncertainties in the calibration. The results are shown in Fig. 4, overlayed on the 6-cm VLA map of Haschick *et al.* (1981). The H_2 emission is extended on a scale of order 120 arcsec which corresponds to 1.2 pc at 2 kpc. The $S(1)$ peak flux in Fig. 4 agrees well with 3×10^{-16} Wm^{-2}, obtained from the CVF spectrum taken at IRS-1 with the same aperture.

3 Discussion

3.1 COMPACT CONTINUUM SOURCES AND DIFFUSE NEBULA

The low-level, diffuse 2μm continuum emission in Fig. 1 clearly arises from an infrared reflection nebula. The alternative possibility of extended free–free emission is excluded since the 2μm CVF

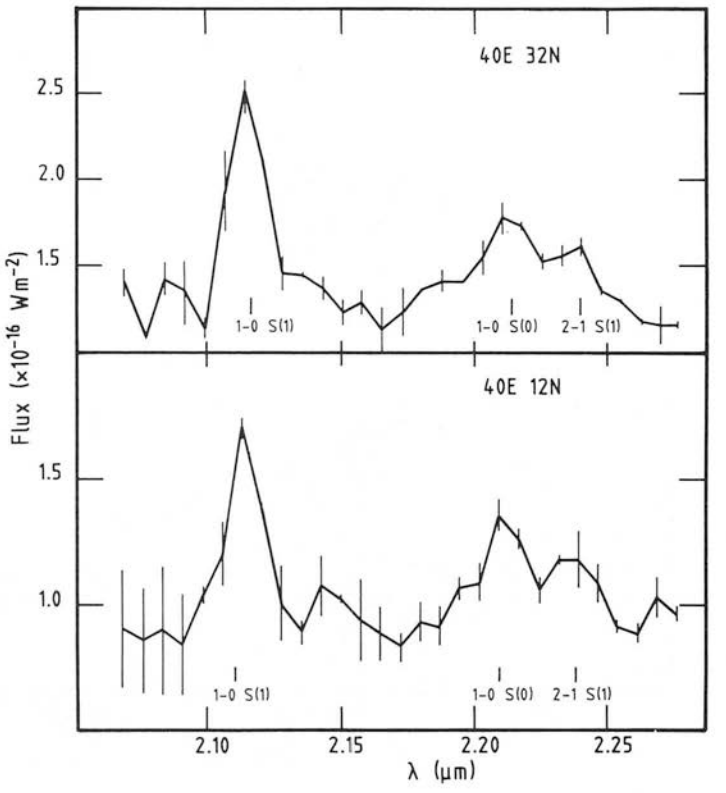

Figure 3. 20 arcsec resolution 2.05–2.30 μm spectra showing molecular hydrogen lines originating from two points in the continuum reflection nebula.

spectra (Fig. 3a and b) show an absence of Brγ recombination lines in the nebula, and since no complementary extended radio emission is observed (Haschick *et al.* 1981, and Fig. 4). This conclusion is supported by continuum polarization observations at 2 μm by Yamashita *et al.* (1988) revealing polarization fractions of up to 50 per cent throughout the region of Fig. 1. Strong polarization (20 per cent) was observed towards the *K* continuum peak, IRS-1, hinting that this may actually be a bright portion of the reflection nebula and not the source of illumination. The extended appearance of IRS-1 may indicate the presence of separate associated sources or patchy extended emission to the west, north-east and especially towards the south-east of the peak.

If IRS-1 were a hot ($T>10^4$ K) self-luminous source then the *J–H* colour of 2.7 mag (Table 1) would imply a visual extinction of $A_V \simeq 25$ mag. Hence the Brα detected in a 5-arcsec beam towards IRS-1 would require a total Lyman continuum luminosity from the associated ionizing source of 3.7×10^{45} ($\pm$30 per cent) photon s^{-1} (assuming 10^4 K, 10^{10} m^{-3} and Menzel's Case B: Brocklehurst 1971; Giles 1977). This is indicative of a B1/B0.5 ZAMS star (Thompson 1984), compatible with the type predicted for the star ionizing H II(B) (Haschick *et al.* 1981). However, the displacement of IRS-1 from H II(B) (Fig. 4) is well outside the telescope pointing error and the H II region may coincide instead with the slight Western extension of IRS-1. The 2 μm peak is therefore more likely to be associated with a separate cluster member or with bright, extended emission.

No small-beam Brγ flux is available to examine properly the Brα/Brγ intensity ratio towards IRS-1. The line was detected in a 20-arcsec aperture during these observations, but we cannot say if the emitting source is IRS-1, H II(B), extended reflected emission in the nebula or a combina-

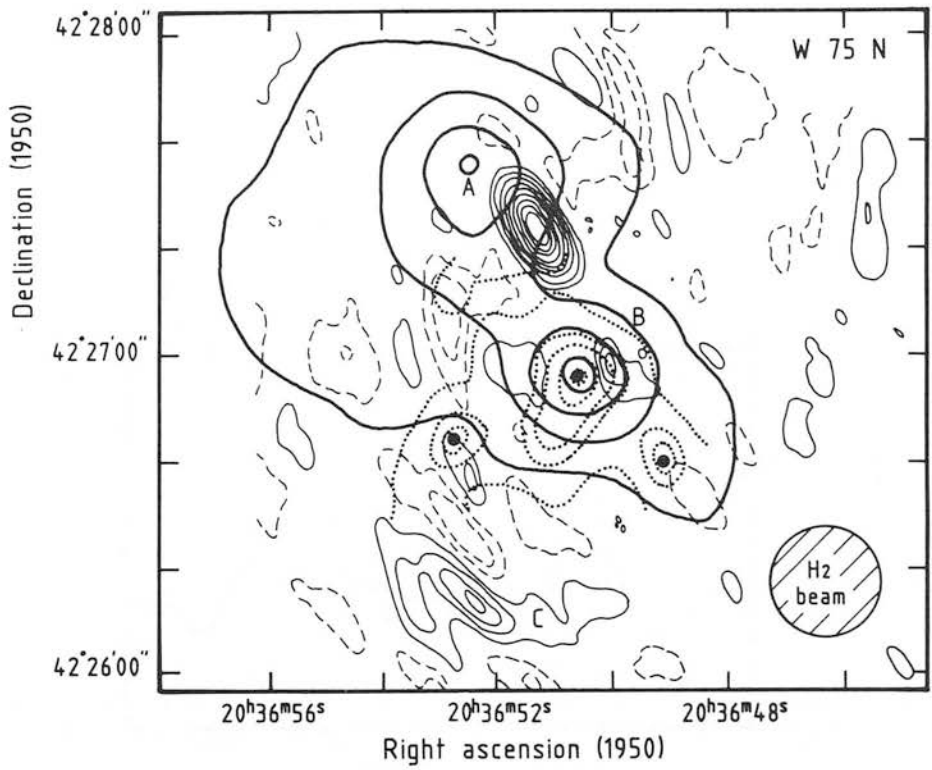

Figure 4. Map of the $v=1$–0 $S(1)$ line of molecular hydrogen (thick contours) superposed on the 6-cm radio continuum map of Haschick *et al.* (1981). Contour levels are at 0.3, 1.1, 1.9 and 2.7×10^{-16} Wm^{-2} per 19.6 arcsec beam. The sampling grid is 20×20 arcsec^2. Dotted contours show the 2μm continuum from Fig. 1.

tion of these. However, if the emission were solely from a single point source at IRS-1, the observed Brackett line ratio would be highly anomalous, being close to unity even without dereddening corrections. This makes it more likely that the Brγ flux is contaminated by H II(B), or that the measured recombination lines are due to extended scattered emission in the nebula. Considering also the 20 per cent polarization fraction observed toward IRS-1 (Yamashita *et al.* 1988), we might argue that the source is dominated by, or is purely, reflected light. In this case the illuminating object is considerably extinguished at 2μm, and would be most probably associated with the ionizing source in or near H II(B). This location is consistent with the pattern of polarization vectors observed in the nebula (Yamashita *et al.* 1988).

Since the assumption of a single point source at IRS-1 creates problems in interpreting the recombination line ratio, we should also examine whether the source can plausibly consist of scattered light. The main difficulty with such an analysis is the assumption of a suitable scattering efficiency or grain albedo for the reflecting material. Estimated parameters for a source at H II(B) illuminating IRS-1 are shown in Table 3 for two contrasting cases. The first uses the theoretical graphite/silicate mix albedos calculated by Draine & Lee (1984) and the second assumes 100 per cent scattering efficiency, independent of wavelength. The 'pre-reflection' values of J–H colour and implied visual extinction (columns 1 and 2) are not greatly affected either way, but the Brα/Brγ ratio and its associated extinction estimate are strongly altered by adopting the Draine & Lee albedos, as these fall rapidly between 2 and 4μm. The photometric extinction estimate should therefore be the most reliable, especially since the source is identified in this case with a

Table 3. Calculated parameters for a source illuminating IRS-1, coincident with H II(B).

Albedo	Pre-reflection					Log (N_{Ly})	ZAMS[c]	M_K
	$J-H$	A_V ($J-H$)[a]	Brα/Brγ	A_V (Case B)[b]		from Brα		
Draine & Lee	2.9	27	37 (±9)	33–40		48.2±30%	O8	−9.3
Unity at all λ	2.7	25	10 (±3)	13–22		47.0±30%	B0/B0.5	−7.4

[a] Assumes source is an extinguished stellar photosphere, with $T_{eff}>10^4$ K, and the extinction law of Rieke & Lebofsky (1985).

[b] Intrinsic ratio assumed to be 2.82 for 10^4 K and 10^{10} m^{-3} (Giles 1977).

[c] ZAMS spectral type required to produce predicted number of Lyman continuum photons N_{Ly} (Thompson 1984).

hot ionizing star. With better line data we would be able to say more about the grain scattering properties in this wavelength range. A flat albedo gives a Case B reddening estimate from Brα/Brγ which is too small in comparison with $A_V(J-H)$, while the Draine & Lee value is rather too high (columns 3 and 4). An intermediate 2μm/4μm albedo ratio of ~1.6 would provide better agreement; however, if a significant fraction of the reddening occurs within the reflecting material itself, optical depth effects will distort the $J-H$ colour and the Brα/Brγ ratio. Such a distortion would increase the Brα/Brγ value of A_V relative to the $J-H$ value by about the amount observed (10 mag) and may explain the mismatching of these estimates. This will be discussed in more detail in a later paper.

Columns 5 and 6 of Table 3 contain Case B Lyman continua and associated ZAMS spectral types for a source at H II(B), calculated from the Brα towards IRS-1 and assuming a projected separation of 6 arcsec (reddening corrections are taken from the $J-H$ colours and the Draine & Lee 4μm albedo is taken to be 0.06). In the first case the predicted spectral type is consistent with the *IRAS* far-infrared luminosity of the region but not with the 5 GHz continuum measurements of Haschick *et al.* (1981), which imply an ionizing source for H II(B) of type B0.5; the ionization required in the second case is much more compatible with these radio data.

We may estimate an apparent K magnitude for the central source by using Hubble's relation for reflection nebulae, in the form given by Castelaz *et al.* (1985), which assumes 100 per cent scattering efficiency at the wavelength in question:

$$m_*(\lambda) = -2.75 + m'_{\rm neb}(\lambda) - 5\log_{10}\theta.$$

Here $m_*(\lambda)$ is the derived apparent magnitude (at wavelength λ) of the illuminating star, $m'_{\rm neb}(\lambda)$ is the measured surface brightness of a point in the nebula (in mag arcsec^{-2}) and θ is the distance between nebula and source in arcsec. The relation yields absolute K magnitudes for the illuminating object in the final column of Table 3. The value of −9.3 obtained using the Draine & Lee 2μm albedo of 0.22 is implausibly bright, since the total *IRAS* luminosity of the whole W75N region is $1.3\times10^5\,L_\odot$: the latter luminosity, if from a dominant single source, limits the ZAMS spectral type to O7 at most, with absolute K magnitude of −4.3. This problem may be resolvable in terms of a source with a low effective temperature (i.e. a few thousand K) which could be separate from the ionizing star. If the majority of the extinction occurs before reflection, it is also possible that the 2μm source photosphere is spatially extended on a 0.01–0.1 pc scale and that the solid angle correction contained in Hubble's relation is inapplicable. However, the corrections available are only just sufficient and must be viewed with caution; we cannot fully account for the Brα luminosity required by reflection which remains (in the Draine & Lee case) about an order of magnitude too large in comparison to the 5 GHz flux measurement of Haschick *et al.* (1981). This requires an optical depth of ~2.5 at 5 GHz which is not unusual in ultracompact H II regions of the kind studied by Garay, Reid & Moran (1985), but may be hard to accept in a considerably larger H II region such as this. The assumption of a high and roughly constant albedo for this dense

cloud-core environment appears to obviate the bulk of the foregoing problems; however, this produces a disagreement between extinction estimates which is opposite to that expected from optical depth effects within extended reflecting material.

It is clear that the present data will not allow us to draw positive conclusions on the nature of IRS-1 and it may be that the situation is confused by the presence of multiple sources coexisting in a very small region. Further observations are certainly necessary, including high spatial resolution maps of the continuum polarization and mid-infrared emission plus small-beam Brγ observations around IRS-1 and H II(B).

IRS-2 is a deeply embedded, pointlike source with $J-H>3.6$ implying $A_V \geqslant 34$ mag along the line-of-sight. An ionization rate of $(3.8\pm0.4)\times10^{46}$ s^{-1} is implied by the Brα flux (3.0×10^{-15} Wm^{-2}, dereddened according to Rieke & Lebofsky 1985), and is equivalent to the Lyman flux expected from a ZAMS B0.5–B0 star (Thompson 1984). However, no 5 GHz continuum source has been detected at the position of IRS-2 to a 2.7 mJy limit (Haschick *et al.* 1981 and Fig. 4). Standard Case B recombination theory predicts a radio continuum flux density of ~120 mJy at 5 GHz from an optically thin ionized region producing this amount of Brα emission.

As IRS-2 appears unresolved, we have made no beam-size correction to the Brα/Brγ intensity ratio. Comparing the diffuse 2 μm continuum emission near IRS-2 with that at IRS-1, contamination of the large-beam Brγ measurement by scattered photons should be an order of magnitude less than the observed flux. The intensity ratio for IRS-2 is thus 8 ± 2, implying a Case B extinction of $A_V=11$–18 mag, much lower than the value obtained from the $J-H$ colour. If the $J-H$ extinction value is correct, then the intrinsic Brα/Brγ ratio is around 0.8 (*cf.* the usual case B value of 2.82). Anomalous recombination line ratios are predicted by Simon *et al.* (1983) for very young, medium to low luminosity sources due to self-absorption of the Brα line in very dense ionized material. IRS-2 thus appears to be an extremely young, highly reddened stellar source, possibly having a very compact ionized region with a high continuum optical depth at cm wavelengths.

Little information has been gained on the third near-infrared source, IRS-3, except that it appears to be a somewhat less reddened ($A_V \geqslant 17$ mag from the $J-H$ colour), point-like luminosity source. It is, however, close to an enhancement in the radio continuum map of Haschick *et al.* (1981) (see Fig. 4), but no recombination line observations were made toward this object.

3.2 H_2 EMISSION

By integrating over the map in Fig. 4, the total observed luminosity in the $v=1$–0 $S(1)$ line is ~0.3 $L_\odot$. If we use the arguments of Beckwith *et al.* (1980) and Fischer *et al.* (1985) and assume that most of the H_2 vibrational radiation results from cooling behind an isothermal shock, then the power radiated in these lines should be approximately equal to the rate at which bulk energy is deposited in the gas. From the results of Fischer *et al.* (1985) the total energy in the CO flow should be $\sim1\times10^{40}$ J. If the flow has been steady, its age (t_f) is $\sim2.3\times10^4$ yr, and the total H_2 energy radiated in all lines (taking the vibration–rotation temperature as $T_{v\text{-}r}=2000$ K) during this time is $\sim1\times10^{39}$ J. This assumes that the total power emitted in all H_2 lines is 10–17 times that in the $v=1$–0 $S(1)$ line (Shull & Hollenbach 1978). Thus the ratio of total energies is:

(Total H_2 luminosity$\times t_f$)/(CO flow energy)~0.1.

Hence the outflow is energetic enough to power the H_2 emission by shock excitation. For this ratio to exceed unity, there would have to be an average 1 μm extinction of >2.5 mag across the whole region, and the likelihood of this is linked to the previous discussion of the nature of IRS-1. However, there are many assumptions made in calculating this ratio, as discussed by Fischer *et al.* (1985), and before we can ascribe the molecular line emission to post-shock cooling it is necessary to examine other excitation mechanisms.

As the line emission appears predominantly near an infrared reflection nebula, it is necessary to examine the possibility that the H_2 could be fluorescent, as reported by Gatley *et al.* (1987) in the visual reflection nebula NGC 2023 and by Sellgren (1986) for other visual reflection nebulae. Following the argument of Longmore, Robson & Jameson (1986), about 1 per cent of the total luminosity of a B0.5 star will be emitted in the non-ionizing 912–1108 Å range responsible for fluorescence in H_2. If 75 per cent of the emitted photons go into heating dust and the conversion efficiency into 1–0 $S(1)$ photons is about 2 per cent (Black & Dalgarno 1976; Black & van Dishoeck 1987), then the total energy in the 2.122 μm line should be about 1.3 $L_\odot$. If the star is hotter than B0.5, then this figure increases rapidly. In fact, we observe $\sim$0.3 $L_\odot$ and so fluorescent emission is energetically feasible. The short-fall in the observed emission could be due a higher UV absorption rate by dust or missed emission due to undersampling, but is most likely to be accounted for by extinction.

Calculations by Black & Dalgarno (1976) for fluorescent H_2 predict [2–1 $S(1)$]/[1–0 $S(1)$] and [1–0 $S(0)$]/[1–0 $S(1)$] line ratios of 0.52 and 0.64 respectively. These values are generally consistent with the results of the more detailed strong field models of Black & van Dishoeck (1987). From the spectra in Fig. 3, the observed ratios are 0.3±0.1 and 0.5±0.1. If we assume a shock velocity of $V_s \sim 15\,\mathrm{km\,s^{-1}}$ and a density $n(H_2) \sim 3\times10^{11}\,\mathrm{m^{-3}}$ (the latter value calculated from CS line observations by Moore *et al.*, in preparation) the H_2 shock-heated models of Kwan (1977) and Shull & Hollenbach (1978) give values of 0.2 for both ratios. The present data fit rather better to the UV fluorescence model, but not sufficiently so to rule out shock-excitation. The low ratios may suggest that the observed spectra are a 'mixture' of fluorescent and shock heated gas. Until further observations are made and more sophisticated H_2 excitation codes developed it may be difficult to unambiguously differentiate between the two mechanisms from limited line ratio studies. The presence of a second strong peak coincident with the larger H II(A) seems to point toward fluorescent emission there, due to UV radiation from the B0.5 ionizing star (Haschick *et al.* 1981) or to non-ionizing radiation from H II(B) impinging on enhanced density material surrounding H II(A).

3.3 CLUSTER EVOLUTION AND MORPHOLOGY

W75N contains a cluster of young sources, spread over a region about 0.6 pc in size, which appear to display a sequence in relative age. The more extended, less embedded and so probably more evolved H II region, H II(A) appears in the north, the more compact OH maser source H II(B) is central, and on the south end of this 'line' is the very young BN-type object, IRS-2 (see Fig. 4).

To examine if these sources are the result of sequential or coeval formation we can calculate the dynamical ages (τ_d) of the H II regions assuming an expansion rate of the order of the thermal sound speed $\sim 10\,\mathrm{km\,s^{-1}}$ (Ho, Haschick & Israel 1981), this also being the apparent expansion velocity of the maser spots near H II(B), (Baart *et al.* 1986). This gives, for H II(A): $\tau_d \sim 8\times10^3$ yr; H II(B): $\tau_d \sim 4\times10^3$ yr and for IRS-2: $\tau_d < 10^3$ yr. The upper limit on the IRS-2 age is calculated assuming the maximum size an optically thick 4.9 GHz emission region can have without being detected on the VLA map of Haschick *et al.* (1981) (0.1 arcsec or $\sim$200 AU), allowing for a departure from the assumed sound speed up to a factor $\sim$5 (Ho *et al.* 1981). If these age differences are the result of sequential star formation, the formation times (τ_f) would have to be of the same order as the differences in dynamical age.

A lower limit to the formation time can be set by the placental cloud free-fall time (τ_{ff}) as given by Ho *et al.* (1981):

$$\tau_f > \tau_{ff} = 4.3\times10^{10}\,[n(H_2)]^{-1/2}\,\mathrm{yr}.$$

The differences in the observed dynamical time-scales are $\sim 4\times10^3$ yr, requiring substantial pre-

formation densities greater than $10^{14}\,m^{-3}$, whereas the observed central density in the W75N region is only about $3\times10^{11}\,m^{-3}$ (Moore *et al.*, in preparation) and there is no reason to suppose this figure was significantly higher in the past. Density inhomogeneities or a density gradient of only 10 per cent of the present-day value could, however, have produced formation times that differ by the range of observed dynamical ages. This suggests that the initial collapse to form these objects occurred at the same time, with differences in their dynamical ages resulting from a shallow north–south density gradient.

4 Conclusions

(i) Near-infrared observations of W75N have revealed a number of embedded objects in a region ~0.6 pc in extent, close to the ultracompact H II region and OH maser source. Surrounding them is an extensive infrared reflection nebula.

(ii) The brightest 2 μm source, IRS-1, may be a reflection peak in the nebula, but this model requires a large excess near infrared continuum and recombination line luminosity from a purely stellar source coincident with the OH maser. It is possible to reconcile this excess with the total *IRAS* luminosity of the region by assuming that the source has a considerably extended photosphere with a temperature of only a few thousand degrees, but the required recombination line output remains difficult to explain. The opposing conclusion that IRS-1 is a real source or a cluster of sources is equally probable, based on the present data. The limits on the ZAMS spectral type of the central source are B0.5 to O7.

(iii) The second brightest 2 μm continuum source, IRS-2, is highly reddened ($A_V \geqslant 34$ mag) with a large recombination line flux although it has no associated 5GHz continuum emission. This object appears to be extremely young, possibly possessing a very dense and compact ionized region.

(iv) The extended molecular hydrogen $v=1$–0 $S(1)$ emission has an observed luminosity of $\sim 0.3\,L_\odot$. This can be accounted for by the post-shock cooling energy available from the CO flow in W75N. However, the H_2 line ratios and energetics suggest a significant UV-fluorescence component to the excitation.

(v) The dynamical ages of the H II regions are surprisingly small and differ by only a few per cent of possible free-fall formation times. This might be explained by coeval formation in a shallow density gradient (~10 per cent over the region) running north–south.

Acknowledgments

We would like to thank Ian Gatley for invaluable help with the observations and Sandy Leggett for access to additional observing time. We also thank Andy Longmore for valuable discussion and Marjorie Fretwell for patiently preparing our figures. UKIRT is operated by the Royal Observatory, Edinburgh on behalf of the UK Science and Engineering Research Council. TJTM acknowledges a SERC studentship.

References

Baart, E. E., Cohen, R. J., Davies, R. D., Norris, R. P. & Rowland, P. R., 1986. *Mon. Not. R. astr. Soc.*, **219,** 145.
Beckwith, S., Neugebauer, G., Becklin, E. E., Matthews, K. & Persson, S. E., 1980. *Astr. J.*, **85,** 886.
Black, J. H. & Dalgarno, A., 1976. *Astrophys. J.*, **203,** 132.
Black, J. H. & van Dishoeck, E. F., 1987. *Astrophys. J.*, **332,** 412.
Brocklehurst, M., 1971. *Mon. Not. R. astr. Soc.*, **153,** 471.
Castelaz, M. W., Hackwell, J. A., Grasdalen, G. L., Gehrz, R. D. & Gullixson, C., 1985. *Astrophys. J.*, **290,** 261.
Dickel, H. R., Wendker, H. & Bieritz, J. H., 1969. *Astr. Astrophys.*, **1,** 270.

Dickel, J. R., Dickel, H. R. & Wilson, W. J., 1978. *Astrophys. J.*, **223,** 840.
Draine, B. T. & Lee, H. M., 1984. *Astrophys. J.*, **285,** 89.
Fischer, J., Righini-Cohen, G. & Simon, M., 1980. *Astrophys. J.*, **238,** L155.
Fischer, J., Sanders, D. B., Simon, M. & Solomon, P. M., 1985. *Astrophys. J.*, **293,** 508.
Garay, G., Reid, M. J. & Moran, J. M., 1985. *Astrophys. J.*, **289.** 681.
Gatley, I., Hasegawa, T., Suzuki, H., Garden, R., Brand, P., Lightfoot, J., Glencross, W., Okuda, H. & Nagata, T., 1987. *Astrophys. J.*, **318,** L73.
Genzel, R. & Downes, D., 1977. *Astr. Astrophys. Suppl.*, **30,** 145.
Giles, K., 1977. *Mon. Not. R. astr. Soc.*, **180,** 57P.
Habing, H. J., Goss, W. M., Matthews, H. E. & Winnberg, A., 1974. *Astr. Astrophys.*, **35,** 1.
Harvey, P. M., Campbell, M. F. & Hoffmann, W. F., 1977. *Astrophys. J.*, **211,** 786.
Haschick, A. D., Reid, M. J., Burke, B. F., Moran, J. M. & Miller, G., 1981. *Astrophys. J.*, **244,** 76.
Ho, P. T. P., Haschick, A. D. & Israel, F. P., 1981. *Astrophys. J.*, **243,** 526.
Kwan, J., 1977. *Astrophys. J.*, **216,** 713.
Lada, C. J., 1985. *Ann. Rev. Astr. Astrophys.*, **23,** 267.
Longmore, A. J., Robson, E. I. & Jameson, R. F., 1986. *Mon. Not. R. astr. Soc.*, **221,** 589.
Mountain, C. M., Selby, M. J., Zadrozny, A. & Hartquist, T. W., 1985a. *Mon. Not. R. astr. Soc.*, **216,** 13P.
Mountain, C. M., Leggett, S. K., Selby, M. J., Blackwell, D. E. & Petford, A. D., 1985b. *Astr. Astrophys.*, **151,** 399.
Rieke, G. H. & Lebofsky, M. J., 1985. *Astrophys. J.*, **288,** 618.
Sellgren, K., 1986. *Astrophys. J.*, **305,** 399.
Shull, J. M. & Hollenbach, D. J., 1978. *Astrophys. J.*, **220,** 525.
Simon, M., Felli, M., Cassar, L., Fischer, J. & Massi, M., 1983. *Astrophys. J.*, **266,** 623.
Thompson, R. I., 1984. *Astrophys. J.*, **283.** 165.
Wynn-Williams, C. G., Becklin, E. E. & Neugebauer, G., 1974. *Astrophys. J.*, **187,** 473.
Yamashita, T., Sato, S., Tamura, M., Suzuki, H., Gatley, I., Hough, J. H., Mountain, C. M. & Moore, T. J. T., 1988. *Mon. Not. R. astr. Soc.*, in press.

Publ. Astron. Soc. Japan 39, 809–820 (1987)

Geometric Configuration around GL 2591: An Infrared Reflection Nebula and a CS Molecular Disk*

Takuya YAMASHITA,† Shuji SATO,‡ and Motohide TAMURA

Department of Physics, Faculty of Science, Kyoto University, Kitashirakawa, Sakyo-ku, Kyoto 606

Hiroko SUZUKI, Norio KAIFU, and Toshiaki TAKANO

Nobeyama Radio Observatory, Minamimaki-mura, Minamisaku-gun, Nagano 384–13

Charles M. MOUNTAIN

Royal Observatory, Blackford Hill, Edinburgh EH9 3HJ, U. K.

Toby J. T. MOORE

Astronomy Department, University of Edinburgh, Blackford Hill, 9EH 3HJ, U.K.

Ian GATLEY§

United Kingdom Infrared Telescope Unit, 665 Komohana St., Hilo, Hawaii 96720, U.S.A.

and

James H. HOUGH

Physics Department, Hatfield Polytechnic, Hatfield, Hertfordshire AL10 9AB, U.K.

(Received 1986 November 14; accepted 1987 May 21)

Abstract

We present observations of K band ($\lambda=2.2$ μm) polarization and CS $J=2$–1 and 1–0 emission around GL 2591. The polarization map reveals an infrared reflection nebula extended ($2' \times 1'$) to both east and west. The maps of CS lines delineate a dense disk ($50'' \times 80''$). The infrared reflection nebula and the bipolar CO flow are parallel to each other, and perpendicular to the CS disk. The density and the mass of the disk are derived to be 1×10^5 cm^{-3} and $1000 M_\odot$, respectively. The velocity gradient in the CS emission is nearly perpendicular to the major axis of the disk; this can be interpreted either as rotation about an axis tilted from the disk axis, or as contraction of the disk toward the central source.

* Based partly on observations made at the Nobeyama Radio Observatory (NRO). NRO, a branch of the Tokyo Astronomical Observatory, University of Tokyo, is a facility open for general use by researchers in the field of astronomy, astrophysics, and astrochemistry.

† Present address: Nobeyama Radio Observatory, Minamimaki-mura, Minamisaku-gun, Nagano 384–13.

‡ Present address: Tokyo Astronomical Observatory, University of Tokyo, Mitaka, Tokyo 181.

§ Present address: National Optical Astronomy Observatories, 950 N. Cherry Av., P.O. Box 26732, Tucson, Arizona 85726–6732, U.S.A.

Key words: Disks; Molecular lines; Polarization; Reflection nebulae; Star formation.

1. Introduction

The infrared source GL 2591 has been found to be typical of protostellar sources associated with large infrared polarization and a bipolar molecular flow. The anisotropy of this source was first noticed with the discovery of large K band polarization of 9.0% (Oishi et al. 1976). Recent CO measurements show that GL 2591 is associated with a bipolar molecular flow with lobes to the northeast and west of GL 2591 (Lada et al. 1984). Hodapp (1984) and Sato et al. (1985) showed, based on the fact that the direction of the bipolar CO flow is perpendicular to that of the infrared polarization of the central source for each object, that the infrared polarization of GL 2591, similar to that of a number of other young stellar objects, most likely arose from the anisotropic scattering of radiation.

More recent observations have shown further anisotropy to be present in the form of an infrared unipolar bubble in the K band (Forrest and Shure 1986) and a complex nebulosity in the I band [$\lambda=1.0$ μm; Lenzen (1987)] extended in the direction of the blueshifted lobe of the bipolar molecular flow. In this paper, we present observations of CS $J=2$–1 and 1–0 emission and K band polarization maps and discuss the geometrical relation among the disk, the outflow, and the reflection nebulae.

2. Observations

2.1. *K Band Polarimetry*

Infrared observations were made on 19 August 1985 using the Kyoto polarimeter and the UKT 9 photometer equipped with an InSb photovoltaic detector on the 3.8-m United Kingdom Infrared Telescope (UKIRT). The polarimeter consisted of a rotating half-wave plate and a fixed wire-grid analyzer. The observational efficiency of polarization degree was measured to be 93% by a laboratory experiment. Position angles were calibrated by taking the position angle of polarization of GL 2591 itself as 171° in the K band (Lonsdale et al. 1980). We used a beam size of 20″ with a chopping throw of 220″ in the E-W direction. We made measurements on grid points with a spacing of 20″ centered on the K band flux peak [R.A. (1950)$=20^{h}27^{m}35^{s}.8$, Decl. (1950) $=40°01'14''$]. In order to check contamination from field stars in the reference beam, we measured each grid point twice, with a reference at both east and west.

2.2. *CS Line Mapping*

The $J=2$–1 and 1–0 transitions of CS at 98 and 49 GHz, respectively, and the $J=$ 1–0 transition of $C^{34}S$ at 48 GHz were observed during 24–27 May 1986, using the 45-m millimeter-wave telescope of the Nobeyama Radio Observatory (NRO). All three transitions were observed simultaneously using the open-beam polarization splitter, the 100-GHz cooled mixer receiver, and the 35–50-GHz cooled mixer receiver with a 2-GHz instantaneous band width. The T_{sys} (SSB) of the 40-GHz and 100-GHz band receivers were 700–800 K and 500–700 K, respectively, including atmospheric effects

at the zenith. The half-power beam width and the beam efficiency for the $J=2$–1 transition were 18″ and 0.53, respectively, and 36″ and 0.85 for the $J=1$–0 transition. The spectral resolution was 0.12 and 0.24 km s^{-1} for lines at 98 and 49 GHz, respectively.

A total of 99 points in the 90″ (R.A.)×110″(Decl.) area around GL 2591 were observed with a grid spacing of 10″, with the center position (0, 0) at R.A. (1950)=$20^{h}27^{m}35^{s}.2$, Decl. (1950)=40°01′09″. The pointing accuracy was checked by observing the SiO maser source χ Cyg at 86 GHz every 1 or 2 hr and the error was found to be typically less than 5″ and 10″ in the worst case. A position switching method was employed with one reference position [R.A. (1950)=$20^{h}30^{m}$, Decl. (1950)=40°27′] for every three on-positions. Intensity calibrations using a rotating hot load were performed every 24 min.

3. Results

3.1. IR Polarization Mapping

The surface brightness and the polarization in the K band are shown in figure 1. The surface brightness (solid contours) obviously extends in the E-W direction and the western lobe is much brighter than the eastern one. The shape of the western lobe is similar to that of the I band image (Lenzen 1987) and the oval loop (8″ diameter) in the K band (Forrest and Shure 1986), except for the fine structures.

Our polarization map shows the polarization vectors to be centrosymmetric

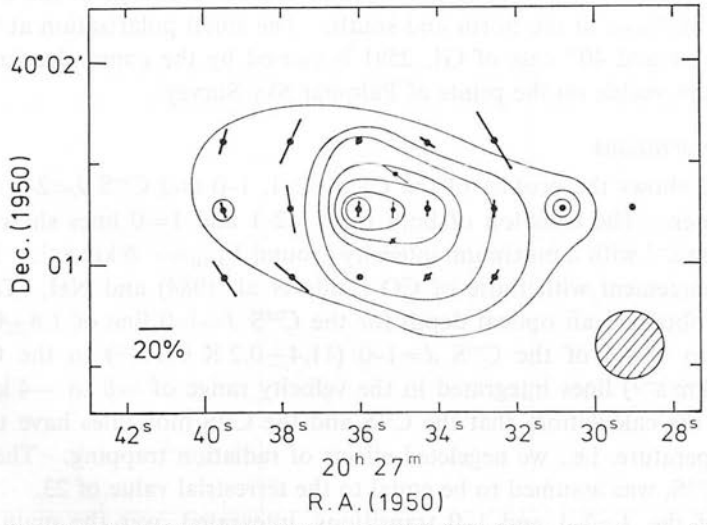

Fig. 1. Surface brightness and polarization map of GL 2591 in the K band. Surface brightness is shown by the solid contours. Contour levels are 2, 5, 10, 20, 50, 100, 200×10^{-21} W cm^{-2} μm^{-1} arcsec^{-2}. GL 2591 itself is located at an intensity peak [R.A. (1950)=$20^{h}27^{m}35^{s}.8$, Decl. (1950)=40°01′14″ (Lada et al. 1984)]. Each bar indicates the degree and the direction of polarization at the position denoted by a filled circle. A polarization of 20% is displayed by the bar in the lower left corner. The beam size of 20″ is indicated by the hatched circle. The thin bars are from Hodapp et al. (1984).

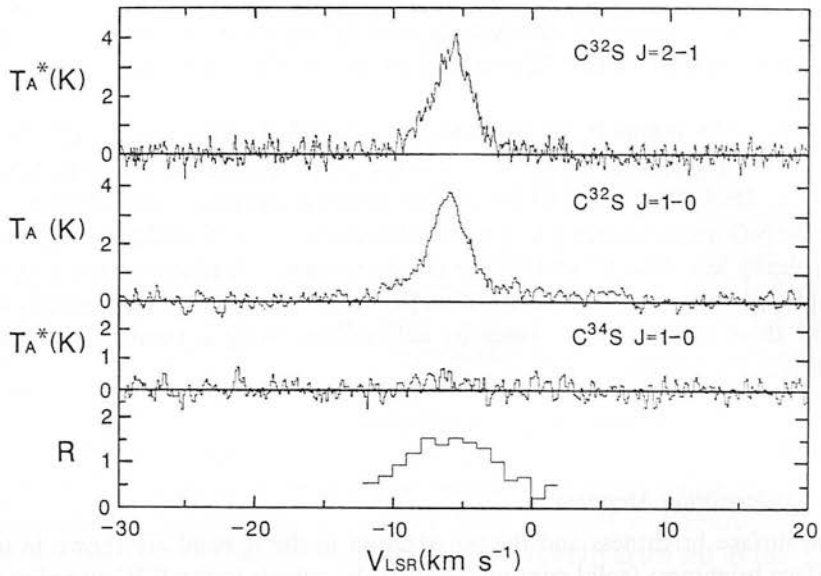

Fig. 2. Upper three: The profiles of $C^{32}S$ $J=2$–1, $J=1$–0, and $C^{34}S$ $J=1$–0 lines at the map center. Bottom: The intensity ratio of the CS $J=2$–1 line to the 1–0 line after correction for different beam sizes and beam efficiencies.

centered on GL 2591 itself. The polarization degrees are large in the east and west compared with those in the north and south. The small polarization at the intensity peaks 60″ west and 40″ east of GL 2591 is caused by the contamination from field stars which are visible on the prints of Palomar Sky Survey.

3.2. *CS Observations*

Figure 2 shows the profiles of the CS $J=2$–1, 1–0 and $C^{34}S$ $J=2$–1 lines toward the map center. The emission of both the $J=2$–1 and $1=0$ lines shows a FWHM of about 3 km s^{-1} with a maximum intensity around $V_{LSR}=-6$ km s^{-1}. This velocity is in good agreement with those of CO (Lada et al. 1984) and NH_3 (Takano et al. 1986). We obtained an optical depth for the $C^{32}S$ $J=1$–0 line of 1.8 ± 0.6 using an intensity ratio 13 ± 3 of the $C^{32}S$ $J=1$–0 (11.4 ± 0.2 K km s^{-1}) to the $C^{34}S$ $J=1$–0 (0.9 ± 0.2 K km s^{-1}) lines integrated in the velocity range of -8 to -4 km s^{-1}. We assumed, in the calculation, that the $C^{32}S$ and the $C^{34}S$ molecules have the same excitation temperature, i.e., we negelcted effects of radiation trapping. The abundance ratio, $C^{32}S/C^{34}S$, was assumed to be equal to the terrestrial value of 23.

Maps of the $J=2$–1 and 1–0 transitions, integrated over the main component (-8 to -4 km s^{-1}), are shown in figures 3a and 3b. A slight displacement ($<5''$) between the intensity peaks of the $J=2$–1 and 1–0 transitions may probably be due to the squint of the two beams. Figure 3c displays the wing component of the $J=$ 1–0 transition, which extends to the north as in the case of CO molecular emission (figure 7). The size of the compact CS emission is $50''\times80''$ (figure 3a), which corresponds to a linear size of 0.5 pc$\times$0.8 pc at a distance of 2 kpc (Merrill and Soifer

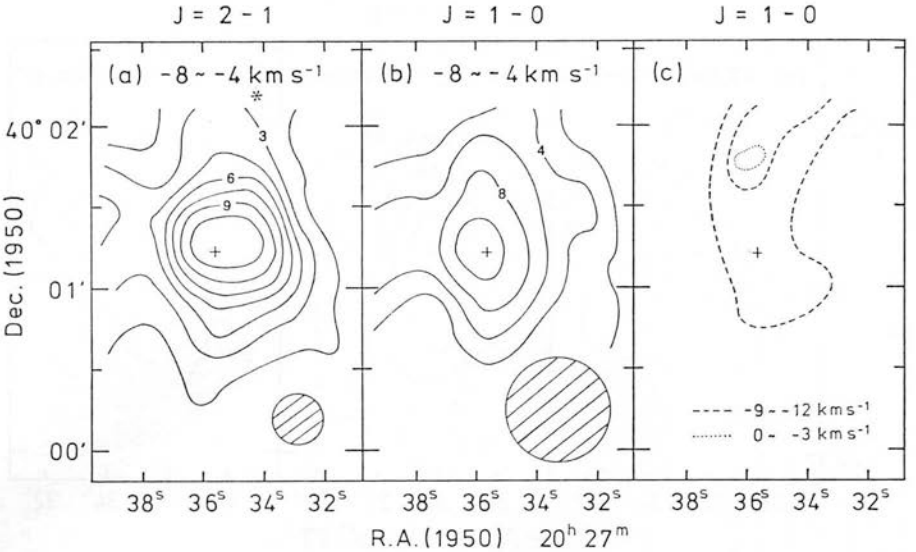

Fig. 3. (a) Map of the CS $J=2$–1 emission integrated over the velocity range from -8 to -4 km s^{-1} (main component). The contours are spaced by 1.5 K km s^{-1}. The beam size is shown by the hatched circle. (b) Map of the $J=1$–0 emission. Designations are the same as in (a) except for a contour interval of 2 K km s^{-1}. (c) Map of the wing components. The blueshifted component (-12 to -9 km s^{-1}) and redshifted component (-3 to 0 km s^{-1}) are indicated by the dashed and the dotted contours, respectively, spaced by 1 K km s^{-1}.

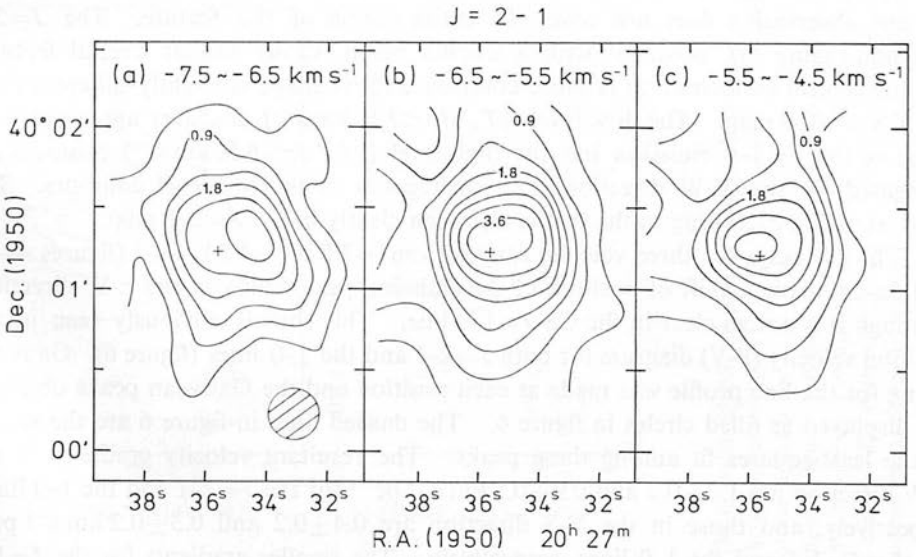

Fig. 4. $\int T_A^* dv$ map of the CS $J=2$–1 emission for velocity ranges of (a) $V_{LSR}=-7.5$ to -6.5 km s^{-1}, (b) $V_{LSR}=-6.5$ to -5.5 km s^{-1}, and (c) $V_{LSR}=-5.5$ to -4.5 km s^{-1}. Contours are spaced by 0.45 K km s^{-1}. The position of the infrared source, R.A.(1950) $=20^h27^m35^s.6$, Decl.(1950) $=40°01'16''$ (Lada et al. 1984), is indicated by the cross. The beam size is shown by the hatched circle.

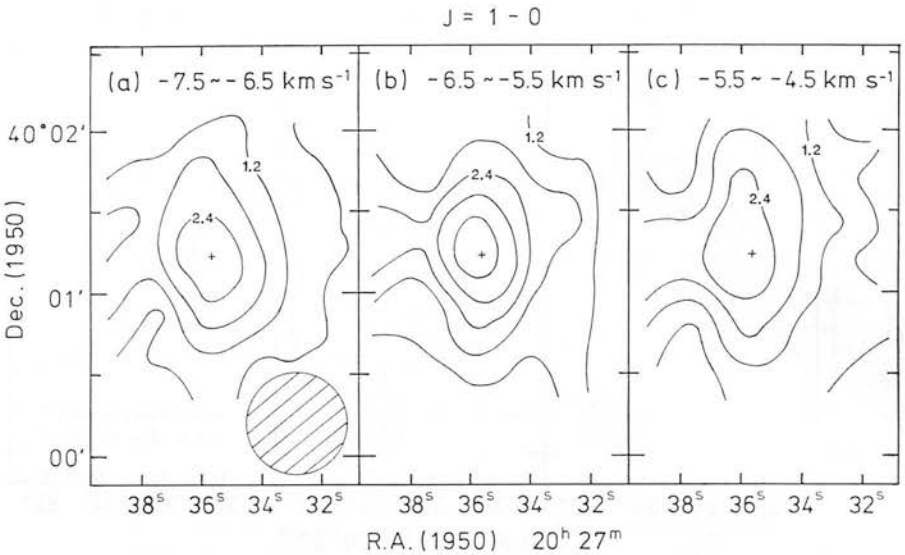

Fig. 5. $\int T_A^* dv$ map of the CS $J=1$–0 emission. Designations are the same as for figure 4 except for a contour interval of 0.6 K km s^{-1}.

1974), comparable with that of the NH_3 condensation observed with a 40″ beam (Takano et al. 1986). The high-resolution CS maps reveal interesting structures which are not seen in the NH_3 maps. The $J=1$–0 contours (figure 3b) are elongated in the N-S direction. A weak emission extending to the east is seen, although the present observation does not cover the entire region of the feature. The $J=2$–1 emission (figure 3a), observed with a smaller beam, shows similar overall features but the central condensation is more compact and its shape is slightly different from the CS $J=1$–0 map. The low-level ($\int T_A^* dv < 3$ K km s^{-1}) contours agree well with those of the $J=1$–0 emission but the high-level ($\int T_A^* dv > 6$ K km s^{-1}) contours are elongated in the E-W direction, i.e., orthogonal to the low-level contours. The weak emission extending to the east is also seen clearly in the $J=2$–1 map.

The CS maps for three velocity ranges from -7.5 to -4.5 km s^{-1} (figures 4a–4c and 5a–5c) show a shift of position of the emission peak nearly in the E-W direction, although it is not so clear in the CS $J=1$–0 line. This shift is obviously seen in the position velocity (P-V) diagram for both $J=2$–1 and the 1–0 lines (figure 6). Gaussian fitting for the line profile was made at each position and the Gaussian peaks obtained are displayed as filled circles in figure 6. The dashed lines in figure 6 are the results of the least-squares fit among these peaks. The resultant velocity gradients in the E-W direction are 1.2 ± 0.2 and 0.9 ± 0.3 km s^{-1} pc^{-1} for the $J=2$–1 and the 1–0 lines, respectively, and those in the N-S direction are 0.4 ± 0.2 and 0.3 ± 0.2 km s^{-1} pc^{-1} for the $J=2$–1 and the 1–0 lines, respectively. The smaller gradients for the $J=1$–0 line than those for the $J=2$–1 would be due to larger beam size for the $J=1$–0 line. Therefore, we adopt the larger gradients of the $J=2$–1 line hereafter in this paper. The velocity gradient in the plane of the sky is 1.3 ± 0.2 km s^{-1} pc^{-1} with a position angle of $70°\pm10°$, which is smaller than and nearly orthogonal to that of the NH_3

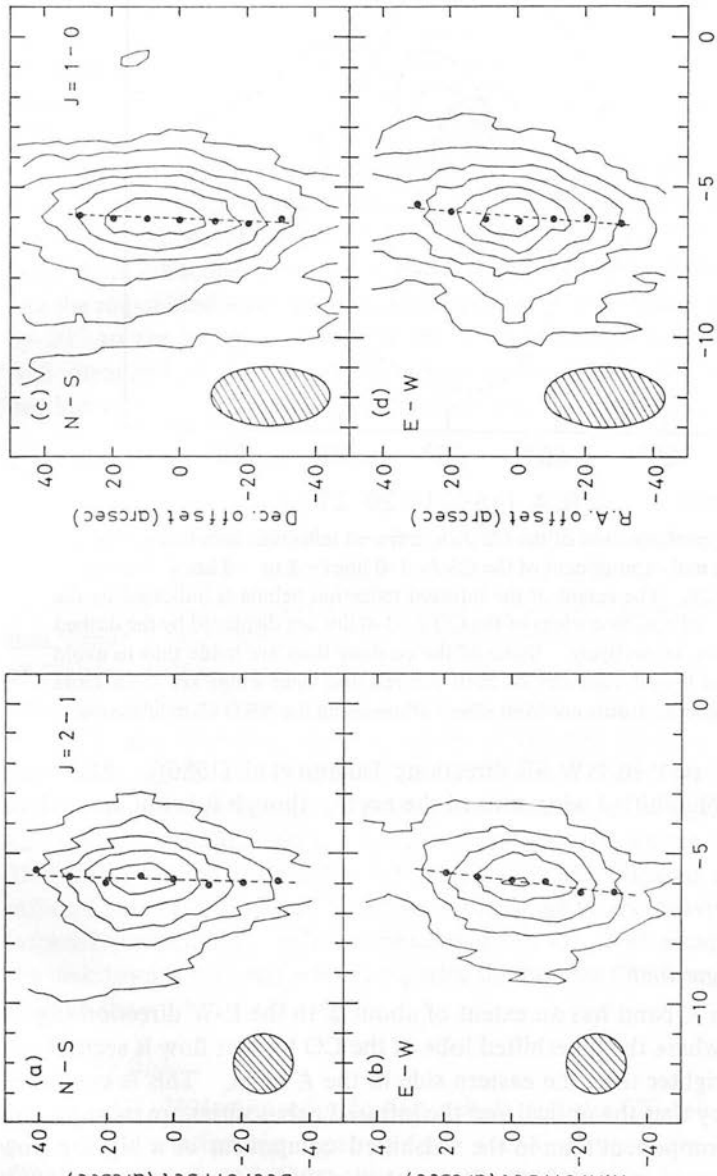

Fig. 6. The position-velocity diagrams of the CS $J=2$–1 and $J=1$–0 lines through the map center. Three scans, that through the map center and those on both sides of that through the center, are added in order to improve the S/N ratio. (a) Scan along the N-S direction (major axis of the disk) for the $J=2$–1 line. (b) Scan along the E-W direction (minor axis of the disk) for the $J=2$–1 line. (c) Scan along the N-S direction for the $J=1$–0 line. (d) Scan along the E-W direction for the $J=1$–0 line. Contours are spaced by 0.75 K for the $J=2$–1 line and by 0.5 K for the $J=1$–0 line. Gaussian fits for the profile at each position along the scan are made and the peak velocities are shown by filled circles. The dashed lines indicate velocity gradients obtained by the least-squares fit for the velocity peaks along the scan. Effective resolutions are displayed by hatched ellipses. These velocity resolutions are not those of the observations themselves but those due to smoothing during the mapping procedure in order to improve the S/N ratio.

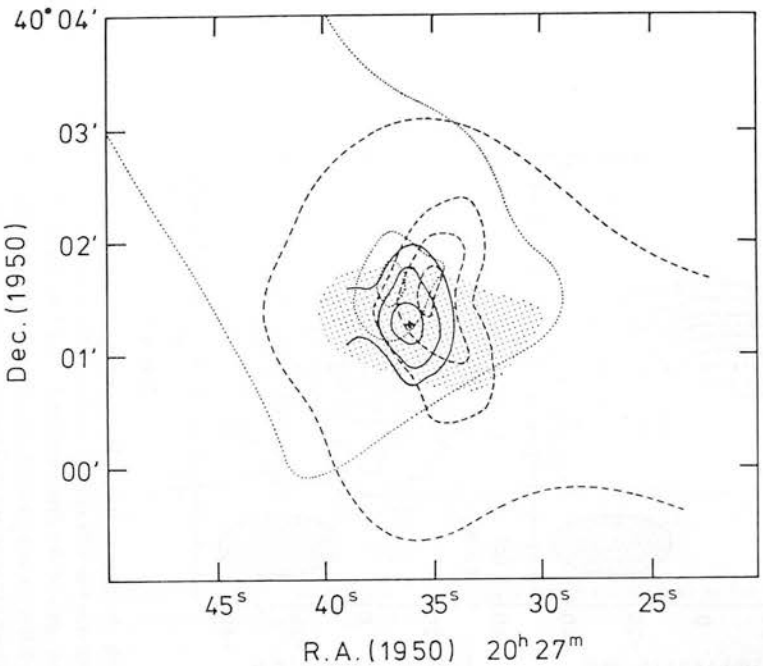

Fig. 7. The schematic configuration of the CS disk, infrared reflection nebula, and the CO bipolar flow. The main component of the CS $J=1$–0 line (-8 to -4 km s^{-1}) is shown by the solid contours. The extent of the infrared reflection nebula is indicated by the shaded area. The red and blue wings of the CO $J=1$–0 line are displayed by the dashed and dotted contours, respectively. Some of the contour lines are made thin to avoid complication. The lowest contours of both the red and blue wings are from Lada et al. (1984) and higher contours are from observations using the NRO 45-m telescope.

observations [2.3 km s^{-1} pc^{-1} in NW-SE direction; Takano et al. (1986)]. Also these diagrams show a weak blueshifted wing toward the north, though it is not so obvious in the CS 1–0 line.

4. Discussion

4.1. Geometrical Configuration

The emission in the K band has an extent of about 2′ in the E-W direction (figure 1). The western side, where the blueshifted lobe of the CO bipolar flow is seen (Lada et al. 1984), is much brighter than the eastern side in the K band. This is consistent with the general tendency that the optical and the infrared nebulosities are more prominent in the blueshifted component than in the redshifted component of a bipolar flow [e.g., L1551 IRS 5: Draper et al. (1985); Strom et al. (1985); Nagata et al. (1986); Kaifu (1986)]. This tendency is explained by the presence of a tilted disk, which obscures the nebula on the redshifted side. The degrees of polarization are large in the direction of the extension (E-W) compared with those in the N-S direction. Multiple scattering, which reduces the degree of polarization,will occur in a dense region, while single scattering, which produces large polarization, will occur in a diffuse region

(Yamashita et al. 1987). Therefore, the surface brightness and the polarization of GL 2591 in the K band indicate the presence of a dense material, which is probably disk-shaped, extends in the N-S direction, and tilts with respect to the line of sight.

Contour maps of both the CS $J=2$–1 and the 1–0 emission lines show an elongated shape in the N-S direction (figures 3a and 3b). This orientation of the CS condensation, perpendicular both to the direction of the CO bipolar flow and to the extension of the reflection nebula, is consistent with the geometry found in several star forming regions, as revealed by Kaifu et al. (1984), Hasegawa et al. (1984), Takano et al. (1984), Kawabe et al. (1984), and Kaifu (1986).

The CO outflow data presented by Lada et al. (1984) do not show bipolarity in the E-W direction; the blueshifted lobe extends to the west, but the red one does to the northeast. However, our recent high-resolution (17″) CO observations with the NRO 45-m telescope show that in the vicinity (on a scale of 100″) of GL 2591, the blue- and the red-shifted lobes are separeted in the E-W direction with a flow center displaced by 20″ to the north of GL 2591 (figure 7). Thus, the anisotropic phenomena are well arranged in this star forming region; the bipolar CO flow and the infrared reflection nebula are parallel to each other and are perpendicular to the CS disk.

4.2. *The Illuminating Source*

Polarization mapping has been used to identify the illuminating source in star forming regions [Ori BN/KL: Werner et al. (1983) and Hough et al. (1986), Cep A: Lenzen et al. (1984), S140: Joyce and Simon (1986), GSS 30: Castelaz et al. (1985), GGD27 IRS: Yamashita et al. (1987)] from the convergence of normals to the polarization vectors. The normals of the polarization vectors of our map, together with that of Hodapp (1984), point to an area around the infrared source GL 2591 within an accuracy of 10″. There exist an infrared source, an H_2O maser (Wynn-Williams et al. 1977), and four compact H II regions (Campbell 1984) in this area. None of the four radio sources is coincident with GL 2591 and there appears to be no strong 2-μm or 10-μm source at any of the positions of the radio and H_2O maser sources (Lada et al. 1984). Since GL 2591 is a unique strong infrared source, it is most likely that GL 2591 is the source responsible for illuminating the infrared reflection nebula, unless infrared sources associated with the radio sources are heavily obscured even at the infrared wavelengths. Infrared photons from GL 2591 escape through the cavity of the disk toward east and west along with the bipolar CO flow, and are scattered by the dust on the wall of the cavity.

4.3. *The Disk*

The GL 2591 infrared reflection nebula and the CS disk are found to satisfy the geometrical relationship expected for a star forming region. We now examine the CS disk in detail, and discuss the velocity gradient which exists in a direction nearly orthogonal to the major axis of the disk.

In figure 3 the map of the CS $J=1$–0 line delineates a shape elongated in the N-S direction, while that of the $J=2$–1 line shows an elongation in the E-W direction near the peak with the overall structure extending in the N-S direction. This E-W elongation could be an optical depth effect resulting from the presence of the velocity gradient.

Generally speaking, optical thickness of the CS $J=2$–1 line is larger than that of the $J=1$–0 line due to larger intrinsic line strength of the former. In addition, the large velocity gradient in the E-W direction might relieve the saturation of $J=2$–1 line, allowing us to see warmer inner part, and resulting in the E-W elongation near the peak.

The density of the disk is derived from the intensity ratio of the CS $J=2$–1 line to the 1–0 line using an LVG model (Linke and Goldsmith 1980) and assuming a kinetic temperature of 50 K derived from the $T_{\rm rot}$ of NH_3 (Takano 1986). The ratios [$R=T_{\rm R}(2\text{–}1)/T_{\rm R}(1\text{–}0)$] at the map center are calculated after the convolution of the beam sizes and correction for the beam efficiencies for both the $J=2$–1 and the 1–0 lines, and are plotted against the LSR velocity at the bottom of figure 2. The typical value of R is 1.5 ± 0.2 for $V_{\rm LSR}=-4$ to -8 km s^{-1}, leading to an H_2 density of 1×10^5 cm^{-3}. The size of the disk is estimated to be $50''\times80''$ (thickness$\times$diameter), or 0.5 pc$\times$0.8 pc assuming the distance to GL 2591 of 2 kpc, at the half intensity levels of the CS $J=1$–0 map. Then the mass of the disk is calculated to be about $1000M_\odot$ assuming a filling factor of unity.

This mass is about one order of magnitude larger than that derived from the NH_3 observations by Takano et al. (1986), assuming the abundance ratio of NH_3 to be 10^{-8}. However, this ratio may vary by an order of magnitude because of the changes in the production efficiency of NH_3 in interstellar clouds (Graedel et al. 1982). Although the filling factor for CS is not known, we take 1000 $M_\odot$ as the disk mass for the remainder of this paper.

The velocity gradient is found to be 1.4 ± 0.2 km s^{-1} pc^{-1} with a position angle of $70°\pm10°$, approximately orthogonal to the elongation (P.A.$\sim0°$) of the CS disk. We will examine three possible interpretations of this velocity gradient: (1) very low velocity components of a CS bipolar flow or an expanding motion of the disk influenced by an outflow, (2) rotation of the disk about an axis tilted from the geometrical axis of the disk, and (3) contraction of the disk.

The first case, that the E-W velocity gradient may be due to a CS flow with very low velocity (<1 km s^{-1}), does not require an unfamilier kinematical model. Such a low velocity flow might occur in the interacting region between the disk and the CO flow. However, the velocity gradient under discussion represents a motion of the dense core, not of the wing. In addition, the relatively dense part of the flow is actually seen 20″ north of the map center in the CS emission (figure 3c), whose spatial extent is similar to that of the CO wing (figure 7). Then this spatial displacement excludes the possibility that the dense core is dynamically affected by the flow, unlike an expanding torus around Orion IRc 2 (Plambeck et al. 1982). In addition, the direction of the gradient corresponds to a contraction, if we assume it to represent a radial motion of the disk. Therefore, the observed velocity gradient is not likely to be due to emission from dense gas in the flow nor to expanding motion of the disk.

Second, the velocity gradient may be produced by a rotation of the disk with the rotation axis tilted from the disk axis. The mechanism of the disk formation is not yet known and the disk shape is not necessarily resulted from rotational equilibrium. The rotation velocity of $0.4/\sin i$ km s^{-1} at a distance of 0.3 pc implies a virial mass of $(10/\sin^2 i)M_\odot$, much smaller than the disk mass. The rotation velocity also cor-

responds to the rotational period of 4×10^{9} yr, which is more than one order of magnitude longer than the dynamical time scale of 7×10^{4} yr for the CO bipolar flow associated with GL 2591 (Lada et al. 1984). Therefore, the observed flow phenomena do not contradict the assumption of the rotation axis tilted with respect to the geometrical axis. The axis of rotation (P.A.$=160^\circ\pm10^\circ$) is nearly parallel to that of the galactic rotation (P.A.$=135^\circ$) in favor of the rotation origin of the velocity gradient.

Third, if we interpret the velocity gradient to be radial motion of the disk, the velocity gradient can be understood as the combination of the contraction (1.2 ± 0.2 km s^{-1} pc^{-1} in the E-W direction) and the slight rotation (0.4 ± 0.2 km s^{-1} pc^{-1} in the N-S direction), if present, with an axis in the E-W direction. If this is the case, the velocity of the contraction is $0.4/\sin i$ km s^{-1} at a distance of $0.3/\cos i$ pc from the infrared source, where i is the inclination of the axis of the disk with respect to the line of sight. This velocity is smaller than the free-fall velocity of $5.5\cos^{1/2} i$ km s^{-1} in the gravitational field of 1000 $M_\odot$ for $16^\circ<i<86^\circ$. The rotation with an axis in the E-W direction implies a virial mass of $(1.0/\sin^2 i)$ $M_\odot$, much smaller than the mass of 1000 $M_\odot$ obtained above. Therefore, the rotation, if present, does not rule out the contraction.

Thus, we conclude that either rotation (with the rotation axis tilted from the disk axis) or contraction of the disk is a plausible interpretation of the velocity gradient.

5. Conclusions

We carried out both the K band polarization and the CS $J=2$–1 and $J=1$–0 line mapping around GL 2591. The main results are summarized as follows:

1. We have found an infrared reflection nebula and a CS disk around GL 2591.
2. These phenomena, together with the previously discovered bipolar CO flow, show distinct geometrical relationship: the bipolar flow and the infrared reflection nebula are parallel to each other and are perpendicular to the CS disk.
3. The size, the density, and the mass of the disk are estimated to be 0.5 pc$\times$0.8 pc (thickness$\times$diameter), 1×10^{5} cm^{-3}, and 1000 $M_\odot$, respectively.
4. The velocity gradient of 1.4 ± 0.2 km s^{-1} pc^{-1} with a P.A. of $70^\circ\pm10^\circ$ can be interpreted either as rotation of the disk, with the rotation axis tilted from the disk axis, or as contraction of the disk toward the central source.

We thank the staff of the United Kingdom Infrared Telescope and Nobeyama Radio Observatory for their support and hospitality. We also acknowledge Professor H. Hasegawa for his continuous encouragement. We appreciate Dr. M. Ohishi for his careful reading of this manuscript. This work was supported by the Ministry of Education, Science, and Culture of Japan and Science and Engineering Research Council of United Kingdom.

References

Campbell, B. 1984, *Astrophys. J.*, **287**, 334.
Castelaz, M. W., Hackwell, J. A., Grasdalen, G. L.,Gehrz, R. D., and Gullixson, C. 1985, *Astrophys.*

J., **290**, 261.
Draper, P. W., Warren-Smith, R. F., and Scarrott, S. M. 1985, *Monthly Notices Roy. Astron. Soc.*, **216**, 7P.
Forrest, W. J., and Shure, M. A. 1986, *Astrophys. J. Letters*, **311**, L81.
Graedel, T. E., Langer, W. D., and Frerking, M. A. 1982, *Astrophys. J. Suppl.* **48**, 321.
Hasegawa, T., Kaifu, N., Inatani, J., Morimoto, M., Chikada, Y., Hirabayashi, H., Iwashita, H., Morita, K., Tojo, A., and Akabane, K. 1984, *Astrophys. J.*, **283**, 117.
Hodapp, K.-W. 1984, *Astron. Astrophys.*, **141**, 255.
Hough, J. H., Axon, D. J., Burton, M. G., Gatley, I., Sato, S., Bailey, J., McCaughrean, M. J., McLean, I. S., Nagata, T., Allen, D., Garden, R. P., Hasegawa, T., Hayashi, M., Kaifu, N., Morimoto, M., and Walther, D. 1986, *Monthly Notices Roy. Astron. Soc.*, **222**, 629.
Joyce, R. R., and Simon, T. 1986, *Astron. J.*, **91**, 113.
Kaifu, N. 1986, in *Star Forming Regions, IAU Symp. No. 115*, ed. M. Peimbert and J. Jugaku (Reidel, Dordrecht), p. 275.
Kaifu, N., Suzuki, S., Hasegawa, T., Morimoto, M., Inatani, J., Nagane, K., Miyazawa, K., Chikada, Y., Kanzawa, T., and Akabane, K. 1984, *Astron. Astrophys.*, **134**, 7.
Kawabe, R., Ogawa, H., Fukui, Y., Takano, T., Takaba, H., Fujimoto, Y., Sugitani, K., and Fujimoto, M. 1984, *Astrophys. J. Letters*, **282**, L73.
Lada, C. J., Thronson, H. A., Jr., Smith, H. A., Schwartz, P. R., and Glaccum, W. 1984, *Astrophys. J.*, **286**, 302.
Lenzen, R. 1987, *Astron. Astrophys*, **173**, 124.
Lenzen, R., Hodapp, K.-W., and Solf, J. 1984, *Astron. Astrophys.*, **137**, 202.
Linke, R. A., and Goldsmith, P. F. 1980, *Astrophys. J.*, **235**, 437.
Lonsdale, C. J., Dyck, H. M., Capps, R. W., and Wolstencroft, R. D. 1980, *Astrophys. J. Letters*, **238**, L31.
Merrill, K. M., and Soifer, B. T. 1974, *Astrophys. J. Letters*, **189**, L27.
Nagata, T., Yamashita, T., Sato, S., Suzuki, H., Hough, J. H., Garden, R., and Gatley, I. 1986, *Monthly Notices Roy. Astron. Soc.*, **223**, 7P.
Oishi, M., Maihara, T., Noguchi, K., Okuda, H., and Sato, S. 1976, *Publ. Astron. Soc. Japan*, **28**, 175.
Plambeck, R. L., Wright, M. C. H., Welch, W. J., Bieging, J. H., Baud, B., Ho, P. T. P., and Vogel, S. N. 1982, *Astrophys. J.*, **259**, 617.
Sato, S., Nagata, T., Nakajima, T., Nishida, M., Tanaka, M., and Yamashita, T. 1985, *Astrophys. J.*, **291**, 708.
Strom, S. E., Strom, K. M., Grasdalen, G. L., Capps, R. W., and Thompson, D. 1985, *Astron. J.*, **90**, 2575.
Takano, T. 1986, *Astrophys. J.*, **303**, 349.
Takano, T., Fukui, Y., Ogawa, H., Takaba, H., Kawabe, R., Fujimoto, Y., Sugitani, K., and Fujimoto, M. 1984, *Astrophys. J. Letters*, **282**, L69.
Takano, T., Stutzki, J., Fukui, Y., and Winnewisser, G. 1986, *Astron. Astrophys.*, **158**, 14.
Werner, M. W., Dinerstein, H. L., and Capps, R. W. 1983, *Astrophys. J. Letters*, **265**, L13.
Wynn-Williams, C. G., Becklin, E. E., Forster, J. R., Matthews, K., Neugebauer, G., Welch, W. J., and Wright, M. C. H. 1977, *Astrophys. J. Letters*, **211**, L89.
Yamashita, T., Sato, S., Nagata, T., Suzuki, H., Hough, J. H., McLean, I. S., Garden, R., and Gatley, I. 1987, *Astron. Astrophys.*, **177**, 258.

Mon. Not. R. astr. Soc. (1988) **231**, 887–895

Mainline OH masers near young H II regions: a correlation with *IRAS* far-infrared flux density

T. J. T. Moore *Astronomy Department, University of Edinburgh, Royal Observatory, Blackford Hill, Edinburgh EH9 3HJ*

R. J. Cohen *University of Manchester, Nuffield Radio Astronomy Observatories, Jodrell Bank, Macclesfield, Cheshire SK11 9DL*

C. M. Mountain *Royal Observatory, Blackford Hill, Edinburgh EH9 3HJ*

Accepted 1987 October 23. Received 1987 October 23; in original form 1987 August 6

Summary. Examination of the *IRAS* data for Type I OH/H II region maser sources in the galactic plane shows that a correlation exists between OH 1665-MHz peak flux density and far-infrared flux density. The form of the correlation suggests that a minimum far-infrared flux density is required for a given OH maser strength. This can be interpreted as evidence for pumping by far-infrared photons with a maximum efficiency in the *IRAS* 60-μm band of about 10 per cent. An alternative, but less plausible, possibility is that the OH and infrared emissions depend separately on the strength of the radiation field in the photodissociation zones close to compact H II regions.

1 Introduction

Mainline 1665- or 1667-MHz OH masers have long been known to be associated with sites of recent star formation. Habing *et al.* (1974), and later Turner (1982), concluded that possibly all Type I OH/H II maser sources occur near compact H II regions, i.e. those smaller than about 0.1 pc, with implied dynamical ages less than about 10^4 yr and electron densities above about 3×10^9 m^{-3}. High OH abundances are needed to produce strong OH maser emission, and masers should form easily in the photodissociation zones close to compact OH/H II regions, where strong ultraviolet fields efficiently convert H_2O to OH (e.g. Elitzur & de Jong 1978). Indeed, the close association of OH maser spots with the edges of compact H II regions has been established by studies such as those of Ho *et al.* (1983), Garay, Reid & Moran (1985) and Gaume & Mutel (1987).

For masers to be a useful probe of their parent regions, a reliable determination of both the molecular formation chemistry and the dominant pumping mechanism is required. For OH masers, pumping by collisions in enhanced density regions (with H_2 or by ion streaming) or by absorption of far-infrared photons has been proposed (e.g. Elitzur 1982, 1985), along with other mechanisms such as a chemical pump inherent in the formation reactions (Andresen 1986). The

far-infrared pump model, investigated by Elitzur (1978) and by Bujarrabal *et al.* (1980a) for OH/IR sources, requires excitation of the $^2\Pi_{3/2}$, and $^2\Pi_{1/2}$ rotational levels of OH, principally by 35, 53, 79 and 119 μm photons, followed by radiative relaxation preferentially into the upper half of the lambda-doubled ground state. The maser transitions then occur between the hyperfine levels of the ground state (Fig. 1). Previous investigations appeared to rule out far-infrared pumping of OH/H II masers on the grounds that too few far-infrared photons were indicated by the 10- and 20-μm emission (Wynn-Williams, Becklin & Neugebauer 1972; Evans *et al.* 1979). For this and other reasons Elitzur (1985) favours a collisional pumping mechanism. It has recently emerged, however, that all OH/H II sources have a far-infrared spectrum peaking at ~100 μm, in agreement with the results of Thronson & Harper (1979). In the present paper we use the *IRAS Point Source Catalog* (IRPS) to study the mid- and far-infrared emission from the counterparts of known Type I OH maser sources, and readdress the possibility of far-infrared pumping.

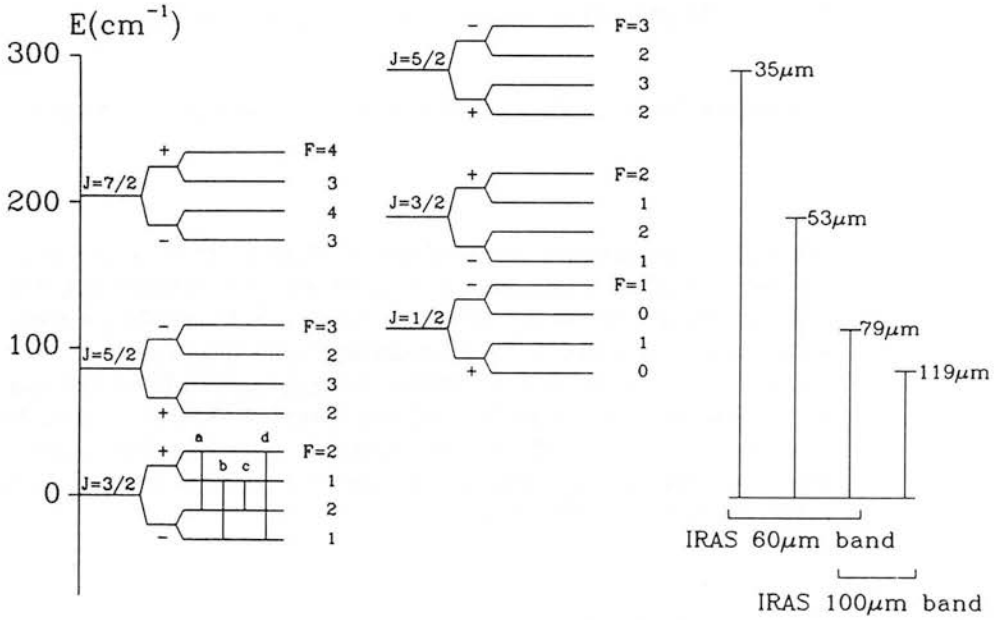

Figure 1. The rotational levels of OH which couple radiatively to the $^2\Pi_{3/2}$ (J=3/2) ground state. Each state is split by Λ-doubling and hyperfine interactions. The splitting is not drawn to scale. The maser transitions occur between the ground state levels: F-conserving (main line) transitions at (a) 1667 MHz and (b) 1665 MHz; F-changing (satellite line) transitions at (c) 1612 MHz and (d) 1720 MHz. The far-infrared transitions to and from the ground state, which may create the maser inversion, are shown to the right.

2 The sample and results

The starting point for the investigation is the sample of 144 OH/H II maser sources observed by Caswell, Haynes & Goss (1980) and Caswell & Haynes (1983a, b). The southern Galaxy sources between galactic longitudes 326° and 2° were found in a systematic survey of the galactic plane, and represent an unbiased, radio-selected sample complete to a 1665-MHz detection limit of ~1 Jy. The northern Galaxy sources are a less homogeneous group: they consist of all OH/H II masers known (in 1982) between longitudes 3° and 60°, which Caswell & Haynes (1983b) remeasured. We have repeated all investigations with and without this last data set, and the

results are not affected by its inclusion. The OH measurements for all 144 sources have positional uncertainties of typically 20 arcsec, up to a maximum of 60 arcsec.

The IRPS was searched for objects within 2 arcmin of each maser. 128 of the 144 maser sources were found to have *IRAS* detections and, despite the generous 2-arcmin matching criterion, only seven were associated with more than one *IRAS* source. The typical positional offset between the OH and *IRAS* positions is about 30 arcsec. Inspection of the 5-GHz survey of the galactic plane by Haynes, Caswell & Simons (1978) showed that maser sources with no *IRAS* association tend to occur near large H II complexes and so may be too confused to be included as point sources in the IRPS. Sources associated with known stars in the *IRAS* database were removed, leaving a final sample containing 120 OH maser sources with peak maser flux densities, kinematic distances and *IRAS* 12, 25, 60 and 100 μm non-colour-corrected flux densities. Six of the final sample had double *IRAS* associations.

The main result is shown in Fig. 2 where peak OH (1665 MHz) flux densities are plotted against *IRAS* flux densities, revealing a sharp cut-on distribution at 60 and 100 μm. The form of the distribution suggests that, at these wavelengths, a minimum infrared flux density is required for a given maser line strength (Fig. 2c and d). A weaker cut-on is seen at 25 μm but none is present at 12 μm (Fig. 2a and b).

No correlation was found between the $F(\mathrm{OH})/F(60\,\mu\mathrm{m})$ ratio and *IRAS* colours [$F(60\,\mu\mathrm{m})/F(25\,\mu\mathrm{m})$, $F(25\,\mu\mathrm{m})/F(12\,\mu\mathrm{m})$ etc.]; the flux density ratios of all the objects are similar. The mean value of log $[F(100)/F(60)]$ is 0.5 and that of log $[F(60)/F(25)]$ is 1.1 (with

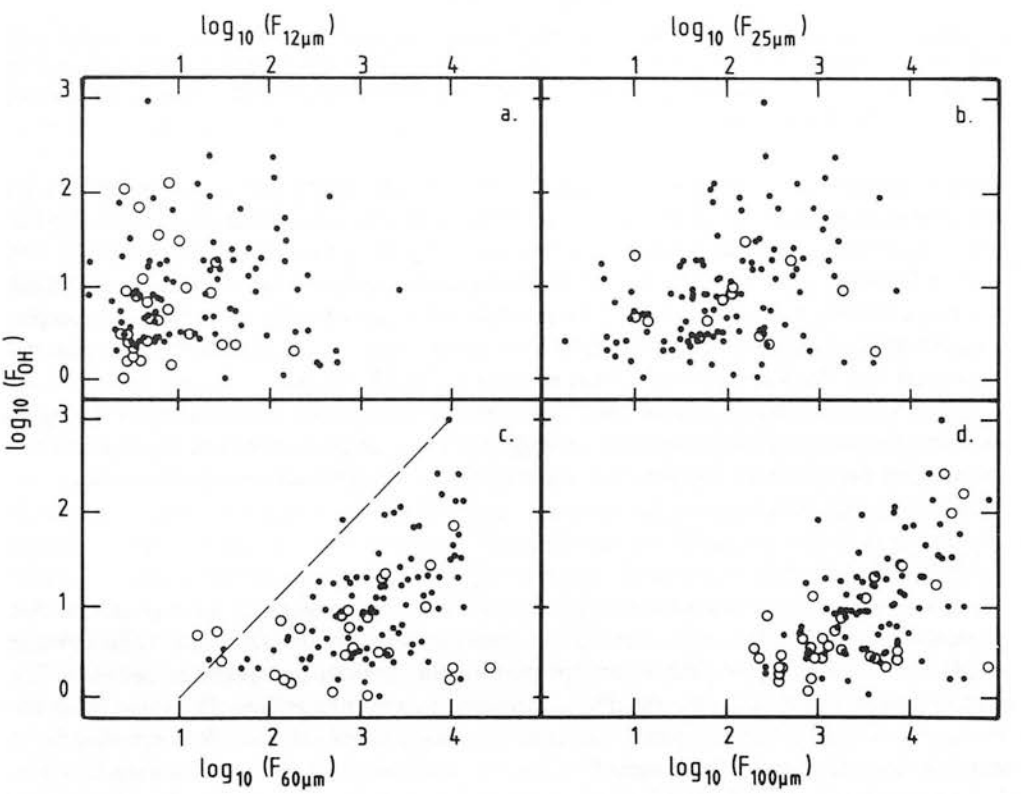

Figure 2. 1665-MHz OH maser peak flux density plotted against far-infrared flux density in the four *IRAS* non-colour-corrected wavebands. A correlation appears at 60 and 100 μm, (c) and (d), less clearly at 25 μm and not at all at 12 μm. Open circles have been used for detections flagged as low quality in the *IRAS* database. The dashed line in Fig. 2(c) represents $F(\mathrm{OH})/F(\mathrm{IR})=0.1$.

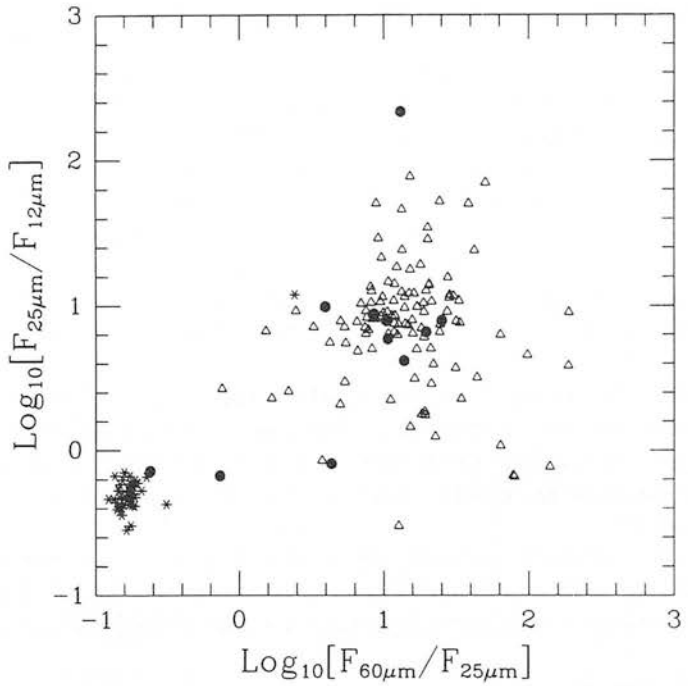

Figure 3. *IRAS* two-colour diagram of OH masers. OH/H II sources are represented by open triangles (where maser emission is dominated by the 1665-MHz line) or filled circles (where the 1667-MHz line dominates). OH/IR stars are represented by asterisks. It is possible that one or two of the 1667-MHz-dominated OH/H II objects are misclassified, and may be Type I OH/IR stars.

standard deviations 0.4 and 0.5, respectively). These are the typical cool or warm dust colours expected from young H II regions still embedded in dense dusty molecular cloud cores. Similar results on the *IRAS* colours of OH/H II sources were found by Braz & Sivagnanam (1987) and Braz & Epchtein (1987). The colours of these objects are quite distinct from those of OH/IR sources, as shown in Fig. 3. Here we give a colour–colour plot for the OH/H II maser sample, together with a sample of Type I OH/IR stars taken from the Engels (1979) catalogue and associated with *IRAS* sources in the same way as the OH/H II objects.

The distribution of the $F(\mathrm{OH})/F(60)$ ratio within the sample is shown as a histogram in Fig. 4, including the sources having 60-μm values flagged as low-quality detections in Fig. 2. From this diagram the cut-on can be recognized at $F(\mathrm{OH})/F(60)\approx 0.1$; the median value is ~ 0.01.

3 Discussion

Fig. 2 shows that there is a minimum far-infrared flux density required for a given OH line strength from the OH/H II maser sources. This, together with the favourable ratio of far-infrared to OH flux densities, suggests far-infrared photon pumping of the masers, as we argue below. The relation shown in Fig. 2 cannot readily be explained by selection effects. The OH masers are strong sources and cover ~ 3 orders of magnitude in luminosity in all four *IRAS* wavebands, so any selection effect would be expected to manifest itself in all four bands. The correlation is, however, only seen clearly at 60 and 100 μm, and not at all at 12 μm. The Spearman rank correlation coefficients for the data in Fig. 2 are 0.150, 0.341, 0.489, 0.471 for 12, 25, 60 and 100 μm respectively. These indicate that the observed correlations are significant at a level less than 10^{-5} at 60 and 100 μm, at about the 10^{-4} level at 25 μm but that there is no significant

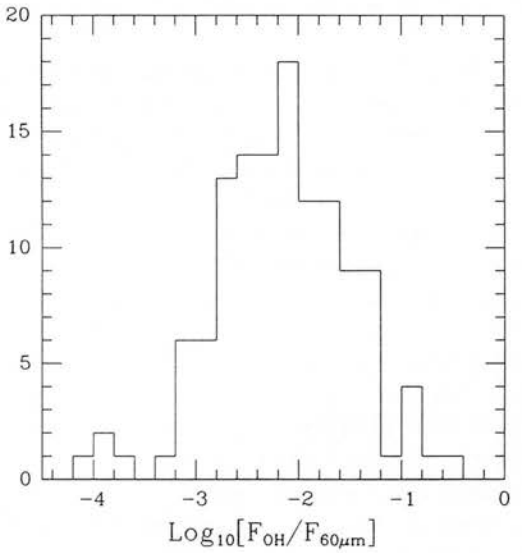

Figure 4. Distribution of the $F(\mathrm{OH})/F(60\,\mu\mathrm{m})$ ratio within the sample of OH/H II sources. Low-quality detections flagged in Fig. 2 are included.

deviation from random distribution at 12 μm. The sharp upper limit to the 60-μm flux densities in Fig. 2(c) appears to be a saturation limit in the *IRAS* detectors. Thus an apparently real cut-on correlation occurs which is strongest in the *IRAS* wavebands containing the ground state rotational transitions at 35, 53, 79 and 119 μm, which may cause the OH inversion (Fig. 1).

3.1 FAR-INFRARED PHOTON PUMPING

It has long been accepted that far-infrared pumping of the OH 1612-MHz line is feasible in Type II OH/IR stars. Observations by Evans & Beckwith (1977) and Werner *et al.* (1980) showed that sufficient 35-μm photons are present in such objects to account for the OH maser output. The latter authors also found that the $F(\mathrm{IR})/F(\mathrm{OH})$ flux ratio remains roughly constant in time in these variable sources.

Previous 'pre-*IRAS*' conclusions of insufficient 30–60 μm pumping photons for OH main lines in OH/H II regions (Wynn-Williams *et al.* 1972; Evans *et al.* 1979) relied on extrapolations from 10- and 20-μm measurements and are clearly superseded by the *IRAS* results. Crawford & Rowan-Robinson (1986) have recently fitted a hot-centred dust cloud model to *IRAS* data from a sample of compact, embedded H II regions. They find that the 12-μm emission does not fit their model in many sources and conclude that high optical depths cause deviations from the assumed spherical symmetry to become important. The far-infrared emission is stronger than might be predicted from 10- and 20-μm data, as also found by Thronson & Harper (1979). For example, in W3(OH) the flux density rises from ~200 Jy at 20 μm (Wynn-Williams *et al.* 1972) to ~4000 Jy at 40 μm, an increase by a factor of 40 in photon luminosity and in the IR/OH photon ratio. Thus there are ample infrared photons available to pump the OH masers.

One objection which is often raised to far-infrared pumping is that the photons measured originate at a radius r_{FIR} greater than that of the OH masers r_{OH}. This introduces a dilution factor of order $(r_{\mathrm{OH}}/r_{\mathrm{FIR}})^2/4$ (Gaume & Mutel 1987, and references therein). However, this analysis ignores the fact that, for an optically thick source, essentially the same number of photons per unit velocity will be available for pumping at r_{OH}, albeit at a shorter wavelength. Hence, provided

that most of the flux seen by *IRAS* comes from the maser source itself, then far-infrared pumping is certainly viable.

The triangular distributions of Fig. 2c and d show that the OH peak flux density is always less than 10 per cent of the 60-μm flux density. These numbers can therefore be interpreted as upper limits to the infrared pumping efficiency. The apparent spread in efficiency over about three orders of magnitude could be due in part to source multiplicity in the *IRAS* beam ($\sim$1 arcmin at 60 μm). Young, embedded infrared sources tend to occur in groups with individual components separated by about 0.1 pc (Beichman, Becklin & Wynn-Williams 1979). If only one member of such a cluster is a maser source, then the apparent efficiency might be diluted by a factor of up to a few hundred. We find no relation between the $F(\mathrm{OH})/F(60\,\mu\mathrm{m})$ ratio and apparent kinematic distance (from the OH survey). This may indicate either that clustered sources are compact enough to appear completely within the *IRAS* beam, even at small distances, or that the efficiency range is, to a large extent, intrinsic to the sources. This needs further investigation using infrared data with high angular resolution. The highest efficiency members of the sample are, in any case, assumed to be single infrared sources in which the maser is saturated.

When a radiatively pumped maser saturates, each absorbed pump photon is converted to maser emission. This is therefore the most efficient state of the system. A saturated maser produces a roughly linear variation of maser intensity with pump rate (e.g. Elitzur 1982). Such a linear variation is consistent with the shape of the cut-on line in Fig. 2, if it is assumed that all the maser regions have similar OH column densities, i.e. that variations in maser emission from source to source are due only to differences in the pump rate. Supporting this, the photodissociation zone models of Sternberg (1986) show that, at ultraviolet levels (912–1100 Å) applicable to compact H II regions (i.e. at least 10^5 times the mean interstellar field), the increase of OH column density with ultraviolet flux is rather slow. In fact, this relation eventually becomes approximately logarithmic, $N(\mathrm{OH})\sim\ln\,[F(\mathrm{UV})]$ (Sternberg, private communication). Because of this, in younger and more compact sources, $F(\mathrm{OH})$ should vary very little with source age and luminosity, leaving the variation with pump rate dominant.

The apparent maser efficiency is given by $\varepsilon=R_\mathrm{m}/R_\mathrm{p}$, where R_m and R_p are the maser and pump photon rates within the emitting volume. If the velocity widths of maser and pump lines are similar, then this becomes $\varepsilon=F_\mathrm{m}/F_\mathrm{p}$, where F_m and F_p are maser and pump flux densities. Evans *et al.* (1979) introduce two further factors $(\Omega_\mathrm{em}/4\pi)$ and $(1/f_\mathrm{abs})$ into the right-hand side of the efficiency equation. The former represents the beaming of the OH emission and the latter f_abs is the fraction of potential (and detectable) pump photons emitted globally by the infrared source which is physically available to the masing region.

In this paper we ignore beaming of the maser emission, on the assumption that the observed number and strength of the sub-arcsecond maser sources would be similar from all directions and are dependent on general conditions in the gas exterior to the H II region. Hence, the maser emission can be taken as isotropic in the large scale, even though individual clumps may produce highly beamed radiation (Alcock & Ross 1985). We can therefore globally take $\Omega_\mathrm{em}\sim4\pi$. In any case, $(\Omega_\mathrm{em}/4\pi)$ and $(1/f_\mathrm{abs})$ will tend to cancel each other out since, for individual OH spots, both Ω_em and f_abs become $\ll1$. The maximum pump efficiency is thus given by $F_\mathrm{m}/F_\mathrm{p}\approx0.1$, from inspection of the 60-μm cut-on line in Fig. 2(c) and from Fig. 4. The median value within our sample is $\sim$0.01. These values agree well with the results of far-infrared pumping calculations by Bujarrabal *et al.* (1980a) who found a pumping efficiency of $\sim$1 per cent, which could be increased to 10 per cent by far-infrared line overlap (Bujarrabal *et al.* 1980b). Line overlap arises naturally in the expanding envelopes of OH/IR sources, the case considered by those authors. It is likely that similar effects can be produced in H II regions either by systematic motions or by turbulence.

The far-infrared pump model predicts increased 1665-MHz inversions in hotter regions, whereas no significant difference appears to exist (Fig. 3) between the colours of masers strongest

at 1665 MHz and those strongest at 1667 MHz. No colour difference has been found either in OH/IR stars (Kirrane 1987), and so this effect must either be easily masked (by factors other than optical depth – OH/IR stars are expected to be generally optically thin in the infrared continuum) or the model in question is not accurate in detail. The efficiency ratio distribution found in our data is also consistent with that for Type I OH/IR stars (Dickinson 1987). This may indicate that the two phenomena of stellar and H II region OH masers are more closely related than previously assumed, with similar local conditions fortuitously existing in the maser-producing regions of each.

The presence of a weakened, but statistically significant, cut-on distribution between OH emission and 25-μm flux density (Fig. 2b) can be explained simply by the constancy of the 60/25 μm colours throughout most of the sample. It is also possible that cascades from levels higher than $J=5/2$ may contribute to the inversion. Higher frequency rotational transitions from the ground state are forbidden by the $\Delta J=0, \pm 1$ selection rule, but these upper states may be populated by multiple radiative excitation. This is possible since the natural lifetimes of the lower excited levels are rather long (1–500 s, Destombes *et al.* 1977) and so, although most secondary excitations are in the 60-μm band, transitions such as $^2\Pi_{3/2}(J=7/2)$–$^2\Pi_{1/2}(J=9/2)$ at 25 μm may be minority contributors to the population inversion.

3.2 THE ULTRAVIOLET FIELD IN PHOTO-DISSOCIATION ZONES

An alternative explanation for the correlation in Fig. 2 may be that the far-infrared continuum and OH maser line emissions depend separately on the luminosity of the embedded young stars. The column density of OH in the gas adjacent to an H II region will depend on the H_2O photodissociation rate and on the local H_2 density. The gain length available over which stimulated emission can occur (and hence the emitted maser intensity) is therefore determined by the strength of the non-ionizing ultraviolet field present. The ultraviolet flux from the central source is also primarily responsible for heating the dust which produces the far-infrared emission. Thus we might expect a relationship between the far-infrared continuum and the strength of the maser lines that does not arise through any pumping mechanism. Such a mutual dependence on the ultraviolet field might appear to select particular wavebands if optical depths in the mid-infrared can produce sufficient scatter to hide the correlation at shorter wavelengths.

Sternberg (1986) has produced detailed photodissociation zone models, and has calculated the variation of OH abundance with H_2 column density for various densities and non-ionizing ultraviolet strengths. The results obtained show that the column density of OH increases rapidly at first with ultraviolet flux, but tends to slow towards higher field strengths. At local densities around $n(H_2)=10^{12}$ m^{-3} and ultraviolet fluxes 10^5 times stronger than the mean interstellar field (equivalent to a location ~0.1 pc from a B0 ZAMS star), Sternberg's model predicts OH densities greater than 10^6 m^{-3} over a length of about 10^{13} m into the cloud. Theoretical calculations (Field 1985) show saturation of maser emission occurring at gain lengths greater than 2×10^{12} m for OH densities of $\sim 8\times10^6$ m^{-3}. Thus this linear, equilibrium chemistry model predicts that ideal conditions for saturated OH masers exist in typical photodissociation zones around compact H II regions.

From the constant density cases examined by Sternberg (1986), the OH column density rises quickly at first with incident ultraviolet flux but begins to flatten in strong fields. If $F(\mathrm{OH})\sim$gain length, for saturated emission, and (to first order) $F(\mathrm{IR})\sim$UV field, then a correlation of the form $F(\mathrm{OH})\sim F(\mathrm{IR})^{\alpha}$ might arise. However, α would be close to unity only for a relatively narrow band of moderate ultraviolet fields ($\sim 10^5\times$mean interstellar value). Since the increase of OH column density with ultraviolet flux tends towards a logarithmic rate when the incident field strength increases to values more typical for compact H II regions, α should be considerably less

than 1, generally. In this case it would require the extra linear dependence of $F(\mathrm{OH})$ on the pump rate to reproduce the exponent observed in Fig. 2, i.e. close to unity.

4 Conclusions

A correlation has been established between the peak 1665-MHz flux from a galactic plane sample of Type I OH masers and the far-infrared flux densities from associated *IRAS* sources. The correlation takes the form of a minimum far-infrared luminosity required for a given maser strength. The observed relationship is most suggestive of direct pumping of the masers by far-infrared photons with efficiencies of up to 10 per cent. The efficiencies agree well with those predicted by Bujarrabal *et al.* (1980a, b) for OH/IR sources. The apparently large range of efficiencies may be due in part to the occurrence of multiple sources in the *IRAS* beam, a possibility which should be investigated further.

An alternative explanation for the OH/far-infrared relation might be provided by mutual dependence of the OH column density and far-infrared flux upon the strength of the incident ultraviolet fields in photodissociation zones, with a third mechanism responsible for the maser pump, but recent calculations of the photochemistry in these regions seem to indicate against this.

Acknowledgments

The authors thank Tom Hartquist and Amiel Sternberg for helpful discussion and encouragement, and Jon Fairclough and IPMAF for providing *IRAS* software. TJTM acknowledges a SERC studentship.

References

Alcock, C. & Ross, R. R., 1985. *Astrophys. J.*, **299,** 763.
Andresen, P., 1986. *Astr. Astrophys.*, **154,** 42.
Beichman, C. A., Becklin, E. E. & Wynn-Williams, C. G., 1979. *Astrophys. J.*, **232,** L47.
Braz, M. A. & Epchtein, N., 1987. *Astr. Astrophys.*, **176,** 245.
Braz, M. A. & Sivagnanam, P., 1987. *Astr. Astrophys.*, **181,** 19.
Bujarrabal, V., Destombes, J. L., Guibert, J., Marlière-Demuynck, C., Nguyen-Q-Rieu & Omont, A., 1980a. *Astr. Astrophys.*, **81,** 1.
Bujarrabal, V., Guibert, J., Nguyen-Q-Rieu & Omont, A., 1980b. *Astr. Astrophys.*, **84,** 311.
Caswell, J. L. & Haynes, R. F., 1983a. *Aust. J. Phys.*, **36,** 361.
Caswell, J. L. & Haynes, R F., 1983b. *Aust. J. Phys.*, **36,** 417.
Caswell, J. L., Haynes, R. F. & Goss, W. M., 1980. *Aust. J. Phys.*, **33,** 639.
Crawford, J. & Rowan-Robinson, M., 1986. *Mon. Not. R. astr. Soc.*, **221,** 923.
Destombes, J. L., Marliere, C., Baudry, A. & Brillet, J., 1977. *Astr. Astrophys.*, **60,** 55.
Dickinson, D. F., 1987. *Astrophys. J.*, **313,** 408.
Elitzur, M., 1978. *Astr. Astrophys.*, **62,** 305.
Elitzur, M., 1982. *Rev. Mod. Phys.*, **54,** 1225.
Elitzur, M., 1985. In: *Masers, Molecules & Mass Outflows in Star Forming Regions*, p. 299, ed. Haschick, A. D., Haystack Observatory.
Elitzur, M. & de Jong, T., 1978. *Astr. Astrophys.*, **67,** 323.
Engels, D., 1979. *Astr. Astrophys. Suppl.*, **36,** 337.
Evans, N. J. Jr. & Beckwith, S., 1977. *Astrophys. J.*, **217,** 729.
Evans, N. J. Jr., Beckwith, S., Brown, R. L. & Gilmore, W., 1979. *Astrophys. J.*, **227,** 450.
Field, D., 1985. *Mon. Not. R. astr. Soc.*, **217,** 1.
Garay, G., Reid, M. J. & Moran, J. M., 1985. *Astrophys. J.*, **289,** 681.
Gaume, R. A. & Mutel, R. L., 1987. *Astrophys. J. Suppl.*, **65,** 193.
Habing, H. J., Goss, W. M., Matthews, H. E. & Winnberg, A., 1974. *Astr. Astrophys.*, **35,** 1.
Haynes, R. F., Caswell, J. L. & Simons, L. W. S., 1978. *Aust. J. Phys. (Astrophys. Suppl.) No. 45,* 1.
Ho, P. T. P., Haschick, A. D., Vogel, S. N. & Wright, M. C. H., 1983. *Astrophys. J.*, **265,** 295.

Kirrane, T., 1987. *MSc thesis,* Victoria University of Manchester.
Sternberg, A., 1986, *PhD thesis,* Columbia University.
Thronson, H. A. Jr. & Harper, D. A., 1979. *Astrophys. J.*, **230,** 133.
Turner, B. E., 1982. In: *Regions of Recent Star Formation,* p. 425, eds Roger, R. S. and Dewdney, P. E., Reidel, Dordrecht, Holland.
Werner, M. W., Beckwith, S., Gatley, I., Sellgren, K., Berriman, G. & Whiting, D. L., 1980. *Astrophys. J.*, **239,** 540.
Wynn-Williams, G. G., Becklin, E. E. & Neugebauer, G., 1972. *Mon. Not. R. astr. Soc.*, **160,** 1.

Mon. Not. R. astr. Soc. (1988) **233,** 899–905

Infrared reflection nebula in W75N

Takuya Yamashita,* Shuji Sato† and Motohide Tamura *Department of Physics, Kyoto University, Kyoto 606, Japan*

Hiroko Suzuki *Nobeyama Radio Observatory, Nobeyama, Minamisaku, Nagano 384-13, Japan*

Ian Gatley *National Optical Astronomical Observatories, 950 N. Cherry Avenue, PO Box 26732, Tucson, Arizona 85726-6732, USA*

James H. Hough *Physics Department, Hatfield Polytechnic, Hatfield, Hertfordshire AL10 9AB*

Charles M. Mountain *Royal Observatory of Edinburgh, Blackford Hill, Edinburgh EH9 3HJ*

Toby J. T. Moore *Astronomy Department, University of Edinburgh, Blackford Hill, Edinburgh EH9 3HJ*

Accepted 1988 February 16. Received 1988 January 18; in original form 1987 September 28

Summary. We identify a new infrared reflection nebula in the W75N region. The K-band polarization map shows a centrosymmetric pattern of the vectors extending over a region 2 arcmin in size, with large values of degrees of polarization, up to 50 per cent. The illuminating source is identified with the ultracompact H II region W75N(B) which is located at the centre of polarization pattern. The intensity peak, IRS-1, is not a self-luminous source but is rather a bright knot in the reflection nebula. The northern peak, IRS-4, located on a second ultracompact H II region, W75N(A), extends for more than 30 arcsec and is less polarized (5–10 per cent). We attribute the near-infrared light of IRS-4 to thermal emission from small ($a \sim 10$ Å) dust grains. The different polarization and spatial distribution of the near infrared emission around these two ultracompact H II regions are explained by the different dust densities around them, probably due to their different evolutionary stages.

1 Introduction

The W75N region is one of the sites of active star-formation which belongs to the molecular cloud complex DR21–W75. This molecular cloud complex consists of three star-forming regions DR21,

*Present address: Nobeyama Radio Observatory, Nobeyama, Minamisaku, Nagano 384-13, Japan.
†Present address: Tokyo Astronomical Observatory, Mitaka, Tokyo 181, Japan.

W75S and W75N, each of which includes radio continuum sources, OH masers, and near- and far-infrared sources. Dickel, Dickel & Wilson (1978) mapped the W75-DR21 region in ^{12}CO and ^{13}CO lines and revealed the presence of two large molecular clouds at radial velocities of -3 and $+9\,km\,s^{-1}$. The feature at $+9\,km\,s^{-1}$ peaks on W75N and that at $-3\,km\,s^{-1}$ on DR21 and W75S. They suggested that the two clouds were interacting with each other. Radio continuum observations around the W75N region have revealed three ultracompact H II regions, W75N(A), (B) and (C) (Wynn-Williams 1971; Harris 1974; Lo 1974; Haschick *et al.* 1981), one of which, W75N(B), coincides with an OH maser source within the positional error (Rydbeck, Ellder & Kollberg, 1969). Recently, Moore *et al.* (1988) found three near-infrared sources (IRS-1, 2 and 3) and molecular hydrogen emission within the W75N region.

The present observations show that the two ultracompact H II regions, W75N(A) and (B), are different from each other in their near-infrared appearance, both in polarization and surface brightness. We will discuss the nature of the near-infrared emission and its origin around these two ultracompact H II regions.

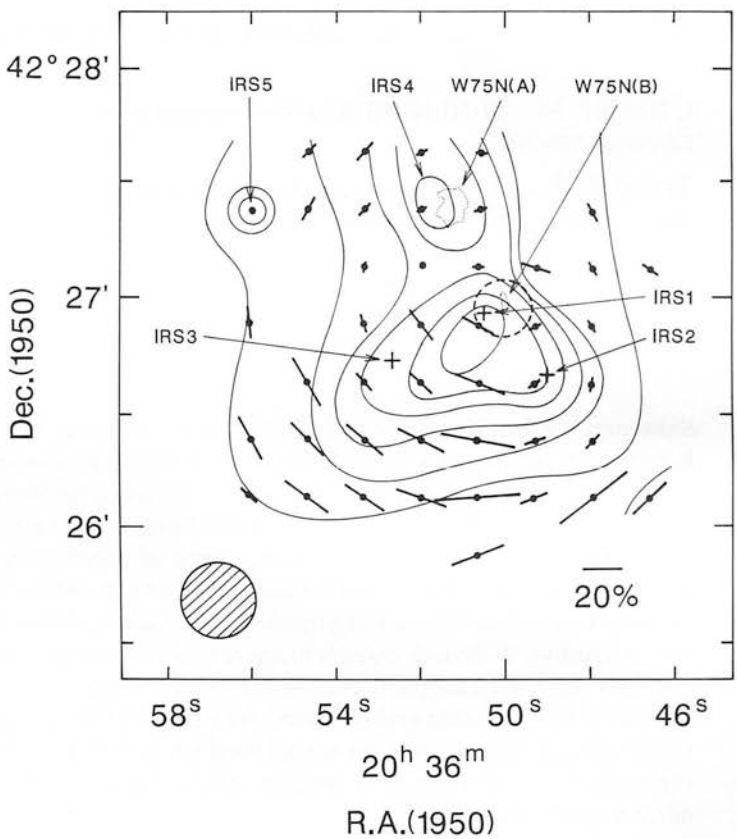

Figure 1. *K*-band surface brightness and polarization map of the W75N region. The beam size of 20 arcsec is indicated by the hatched circle. Contour levels are 0.5, 1, 2, 4, 6 and $10\times10^{-20}\,W\,cm^{-2}\,\mu m^{-1}\,arcsec^{-2}$. The direction and the length of each bar indicates the degree and the direction of a polarization at the position of its centre. A polarization degree of 20 per cent is displayed by the bar in the lower right-hand corner. A dashed open circle indicates an approximate polarization centroid. The positions of the near-infrared sources IRS-1–5 and those of compact H II regions W75N(A) and (B), are also indicated.

2 Observations and results

Polarimetric observations were made on 1985 August 22 on the 3.8-m United Kingdom Infrared Telescope (UKIRT). We used the Kyoto polarimeter together with the standard UKIRT photometer, UKT 9. The polarimeter consists of a rotating half-wave plate made of MgF_2 and a fixed wire grid polarizer. Instrumental polarization was measured to be less than 0.2 per cent. The efficiency of the polarimeter was determined by laboratory experiments and the absolute position angles were calibrated by using GL2591, whose position angle was taken as 171° in the *K*-band (Lonsdale *et al.* 1980). The beam size employed was 20 arcsec with a chopper throw of 220 arcsec in the E–W direction. In order to check the contamination from field stars in the reference beam, we measured each grid point twice with both an east and a west reference beam. The polarization and the surface brightness map is displayed in Fig. 1. The positions of these sources are summarized in Table 1 together with those of other relevant sources.

Additional two aperture photometry of IRS-4 at *J*, *H*, *K* and *L'* was performed on 1986 December 16–17 using the Agematsu Infrared Observatory (AIRO) 1-m telescope in order to investigate spatial variation of colour. We used 24 and 36 arcsec beams and the chopping throw

Table 1. Source positions.

Source	RA (1950) (h m s)	Dec. (1950) (° ′ ″)	Note	Reference
IRS-1	20 36 50.5±2″	42 26 56±2″		1
IRS-2	20 36 49.0±2	42 26 40±2		1
IRS-3	20 36 52.7±2	42 26 44±2		1
IRS-4	20 36 51±8	42 27 26±8	extended	2
IRS-5	20 36 57±8	42 27 26±8		2
IR(53μm)	20 36 50.7	42 26 56		3
IR(20μm)	20 36 51.1	42 27 19		4
W75N(A)	20 36 51.2	42 27 23	B0.5V	5
W75N(B)	20 36 50.03	42 26 58.4	B0.5V	5
H_2O maser	20 36 50.45	42 27 00.1		6
OH maser	20 36 49.98	42 26 57.9		5

References:
1. Moore *et al.* 1988.
2. This paper.
3. Harvey *et al.* 1977.
4. Wynn-Williams *et al.* 1974.
5. Haschick *et al.* 1981.
6. Genzel & Downes 1977.

Table 2. Near-infrared magnitudes of IRS-1 and 4.

Source	Beam (arcsec)	*J*	*H*	*K*	*L'*	Reference
IRS-1	8	14.0	11.3	9.2	7.0	1
	36	12.8	9.9	7.6	4.6	2
IRS-4	24	13.7	10.9	9.0	5.9	2
	36	13.3	10.5	8.6	5.4	2

References:
1. Moore *et al.* 1988.
2. This paper.

was 90 arcsec in the E–W direction. The results are summarized in Table 2 together with previous observations of IRS-1 (Moore *et al.* 1988). Errors for our photometry are less than 0.1 mag at every wavelength.

3 Discussion

The diffuse near-infrared emission extends for about 2 arcmin and is divided into two components, one of which peaks in the north (IRS-4) while the other peaks in the south (IRS-1). The shape of the northern emission is elliptical and that of southern one is triangular. Since each component is not on the symmetrical axis of the other, the whole emission is not a single infrared reflection nebula with two lobes like GGD27 IRS (Yamashita *et al.* 1987). Although the degrees of polarization are relatively small (5–10 per cent) around IRS-4 and large (20–50 per cent) to the south of IRS-1, the normals of the polarization vectors cross near IRS-1. Therefore, the polarization is caused by scattering of light from a single source near IRS-1. In addition, the small polarization around IRS-4 indicates that the *K*-band flux in this region is dominated by unpolarized light.

3.1 THE ILLUMINATING SOURCE

The illuminating source of the infrared reflection nebula is expected to be located at the convergence of normals of the polarization vectors. Here we notice, however, that the polarization vector does not point to the illuminating source from the centre of the beam where large gradient of surface brightness is seen because the integrated polarization within the beam is more largely affected by brighter part. In the present case, this is applicable to the eastern and western edge of the southern nebula. Taking this effect into consideration, an approximate centre of convergence is indicated by a dashed circle in Fig. 1. Its centre is displaced to the NW by about 8 arcsec from IRS-1, suggesting that the illuminating source is not situated on the intensity peak, IRS-1.

The large polarization (20 per cent) of IRS-1 itself supports this idea. Previous observations of this kind showed that the polarization degree of diffuse component in the vicinity of the illuminating source, not on the source, was about 20 per cent (GSS 30 in the Ophiucus dark cloud, Castelaz *et al.* 1985; Cep A and S140, Joyce & Simon 1986) SGS 1 in NGC 1333, Castelaz *et al.* 1986; GGD27 IRS, Yamashita *et al.* 1987). According to Yamashita *et al.* (1987), apparently small polarization of 20 per cent (not 100 per cent) for pure scattering is due to a scattering angle near 0° or 180°. Moreover, Cep A (Lenzen, Hodapp & Solf 1984) and GGD27 IRS (Yamashita *et al.* 1987) show near-infrared peaks separated from their illuminating sources. L1551 IRS-5, whose polarization at *K* is about 20 per cent, was thought to be an illuminating source of the associated reflection nebula but Strom *et al.* (1985) suggested that the near-infrared light from IRS-5 is scattered based on their high-resolutiuon (0.6 arcsec) images. These facts suggest that the polarization degree of 20 per cent of IRS-1 would not be diluted by the direct unpolarized light from the central star but be due to pure reflected light. In this picture, the illuminating source is located to the north-west of IRS-1 and is heavily obscured by a dense dust cloud with a cavity which opens towards IRS-1.

We then consider the most plausible candidate of the illuminating source as the ultracompact H II region W75N(B) which is located to the north-west of IRS-1 and within the dashed circle in Fig. 1. The fact that both a peak of 350 μm continuum emission (Moore *et al.* in preparation) and OH maser sources (Haschick *et al.* 1981) are located on W75N(B) indicates that it is the most active young source in this region and hence make our suggestion plausible. Therefore, we identify the illuminating source with W75N(B), or more precisely with the exciting source of W75N(B).

The dust cloud which extinguishes the illuminating source would be a disc or torus which is a similar phenomenon found with molecular line observations such as CS (e.g. L1551, Kaifu *et al.* 1984). In this picture, small polarization along the direction of elongation (NE–SW) of the suspected disc would be due to multiple scattering, as suggested for GGD27 IRS by Yamashita *et al.* (1987).

We next estimate an extinction through the disc according to the method employed by Lenzen *et al.* (1984). The *K*-band flux at the position of W75N(B) is known to be $<4\times10^{-18}$ W cm^{-2} μm^{-1} from the 8 arcsec resolution map (Moore *et al.* 1988). If we consider this measured flux on W75N(B) to be the remnant of the intrinsic flux of 1.2×10^{-15} W cm^{-2} μm^{-1}, obtained from integrated flux over south of W75N(B) assuming an albedo of 22 per cent and a solid angle of illumination of 3.6 sr, after suffering from extinction through the disc, comparison of the two fluxes leads to a *K*-band extinction of >6.0 mag or a visual extinction of >70 mag for the disc. In the present estimation, we neglect the convolution due to the visual extinction of 27 mag (Moore *et al.* 1988) because it can occur either through the foreground cloud or through the disc. This crude estimation is subject to large uncertainties but serves to demonstrate the high column density in the disc.

3.2 IRS-4

IRS-4 is an extended near-infrared source located to the north of IRS-1. Since IRS-4 envelopes the compact H II region W75N(A), IRS-4 must be excited by the source which excites W75N(A). As before, the radio observations demand the presence of at least a B0.5 ZAMS star (Haschick *et al.* 1981). The slight displacement between the peaks of IRS-4 and W75N(A) can probably be attributed to the low spatial resolution (15 arcsec) of our map. The small polarization indicates that the reflected light is dominated by the unpolarized light as discussed at the beginning of Section 3.

Then what is the dominant process for the diffuse near infrared light of IRS-4? The contribution to the *K* flux from free–free emission is negligible (36 mJy versus 200 mJy) and the source is much larger at *K* than in the radio (>30 arcsec versus 8 arcsec). The observed brightness temperature (~240 K) throughout IRS-4 is much higher than the blackbody equilibrium temperature predicted for grains at 0.15 pc (15 arcsec at the distance of 2 kpc) surrounding a B0.5 ZAMS star (*cf.* Sellgren *et al.* 1983).

A likely mechanism to radiate near-infrared light effectively is thermal emission by small (a~10 Å) grains as proposed for visual reflection nebulae by Sellgren *et al.* (1983). A small grain is heated up to 1000 K temporarily by absorbing a single UV photon of about 1000 Å (thermal fluctuation mechanism). This mechanism can also explain the large size of IRS-4 relative to W75N(A) because photons longer than 912 Å can penetrate into a neutral hydrogen region. The colour temperature is expected to remain constant with radius for this mechanism because the temperature of the small grains depends only on the energy of a single UV photon and the size of the grain (Sellgren 1984). Two aperture photometry for IRS-4 (Table 2) gives the following colours, $J-H$=2.8, $H-K$=1.9, and $K-L'$=3.1, for a 24 arcsec beam and 2.8, 1.9 and 3.2 for a 36 arcsec beam, identical within the errors.

We will next examine the colours themselves. The colours should not only be spatially constant but also should be equal to those for visual reflection nebulae when corrected for reddening. The near-infrared colours for visual reflection nebulae are $J-H$=1.0, $H-K$=0.8, and $K-L'$=2.0 mag (NGC 7027, 2023 and 2068; Sellgren *et al.* 1983; Sellgren 1984). Then if we assume that the intrinsic colours of IRS-4 are the same as visual reflection nebulae, the reddening here is found to be $A(J-H)=1.8\pm0.1$, $A(H-K)=1.1\pm0.1$ and $A(K-L')=1.1\pm0.1$ mag, respectively. These amounts of reddening correspond to the visual extinctions of 17 ± 1, 18 ± 3 and 21 ± 3 mag, respectively, using an extinction law by Rieke & Lebofsky (1985). Therefore, we regard the near-

infrared colours for IRS-4 to be consistent with those of the thermal fluctuation model after the correction of the reddening for $A_V=18$ mag. It should be noted that the flux contribution at K from a B0.5 ZAMS star at distance of 2 kpc is less than 10 per cent of the observed flux in a 20 arcsec beam, assuming a visual extinction of 18 mag.

3.3 NEAR INFRARED EMISSION AROUND W75N(A) AND (B)

W75N(B) is considered to be at an earlier evolutionary stage than W75N(A) because of its compactness and its association with OH and H_2O masers (Rydbeck *et al.* 1969; Lo, Burke & Haschick 1975). In the following, we will compare the near infrared emission from these two ultracompact H II regions.

The diffuse component south of W75N(B) was shown in Section 3.1 to be the reflected light from W75N(B). Therefore, the near-infrared light is not emitted in the diffuse (~1 pc) area but emitted thermally in the vicinity of the central 'star'. On the other hand, in Section 3.2 we have attributed the diffuse near-infrared light of IRS-4 (W75N(A)) to be due to thermal emission from small dust grains in the extended area (~0.5 pc).

We interpret this difference in the near-infrared emission around the two ultracompact H II regions as a result of the difference in the mean-free-path of UV photons, which is determined by dust densities around these H II regions; this difference in densities is directly attributable to the difference in evolutionary stages. Far-infrared and molecular line observations also suggest a higher dust density around W75N(B) than W75N(A). The peak of the 53 μm emission (Harvey, Campbell & Hoffmann 1977) lies close to W75N(B), whereas that of 20 μm emission (Wynn-Williams, Becklin & Neugebauer 1974) is coincident with W75N(A). Thus the colour temperature around W75N(A) is higher than that around W75N(B), suggesting that the dust grains around W75N(A) are exposed to larger UV flux than those around W75N(B), due to lower dust density. The CS $J=2$–1 and 1–0 observations (Moore *et al.*, in preparation) also indicate that the CS cloud around W75N(B) is denser than that around W75N(A).

Thus in W75N(B) the UV flux is converted into near-infrared photons in the immediate vicinity of the central source. These photons then scatter from dust on a scale of a parsec. In W75N(A) UV photons travel about a parsec before being converted into the near-infrared photons by the thermal fluctuation mechanism in small grains.

4 Conclusions

We studied the new infrared reflection nebula in the W75N region by polarization mapping at K. The main conclusions are summarized as follows.

(i) The illuminating source of this infrared reflection nebula is identified with the ultracompact H II region, W75N(B).

(ii) IRS-1, the brightest source at K, is not a self-luminous source but is the brightest knot of the infrared reflection nebula.

(iii) The excess K-band flux surrounding W75N(A) can be explained by thermal emission from small (a~10 Å) grains.

(iv) The different polarization and spatial distributions of the diffuse near-infrared emission around the two compact H II regions W75N(A) and (B) is a direct consequence of their difference in an evolutionary stage.

Acknowledgments

We would like to thank the staff of the UKIRT for their support. We acknowledge Mr C. Kim for his support at AIRO. We are also grateful to Dr M. Tanaka for his careful reading of this

manuscript and Miss C. Saruya for drawing the figure. We would like to acknowledge Professor H. Hasegawa and Dr N. Kaifu for their continuous encouragement. This work was supported by the SERC and the Ministry of Education, Science, and Culture of Japan.

References

Castelaz, M. W., Hackwell, J. A., Grasdalen, G. L. & Gehrz, R. D., 1986. *Astrophys. J.*, **300,** 406.
Castelaz, M. W., Hackwell, J. A., Grasdalen, G. L., Gehrz, R. D. & Gullixson, C., 1985. *Astrophys. J.*, **290,** 261.
Dickel, J. R., Dickel, H. R. & Wilson, W. J., 1978. *Astrophys. J.*, **223,** 840.
Genzel, R. & Downes, D., 1977. *Astr. Astrophys. Suppl.*, **30,** 145.
Harris, S., 1974. *Mon. Not. R. ast. Soc.*, **166,** 29P.
Harvey, P. M., Campbell, M. F. & Hoffmann, W. F., 1977. *Astrophys. J.*, **211,** 786.
Haschick, A. D., Reid, M. J., Burke, B. F., Moran, J. M. & Miller, G., 1981. *Astrophys. J.*, **244,** 76.
Joyce, R. R. & Simon, T., 1986. *Astr. J.*, **92,** 113.
Kaifu, N., Suzuki, S., Hasegawa, T., Morimoto, M., Inatani, J., Nagane, K., Miyazawa, K., Chikada, Y., Kanzawa, T. & Akabane, K., 1984. *Astr. Astrophys.*, **134,** 7.
Lenzen, R., Hodapp, K.-W. & Solf, J., 1984. *Astr. Astrophys.*, **137,** 202.
Lo, K. Y., 1974, *PhD thesis,* Massachusetts Institute of Technology.
Lo, K. Y., Burke, B. F. & Hashick, A. D., 1975. *Astrophys. J.*, **202,** 81.
Lonsdale, C. J., Dyck, H. M., Capps, R. W. & Wolstencraft, R. D., 1980. *Astrophys. J.*, **238,** L31.
Moore, T. J. T., Mountain, C. M., Yamashita, T. & Selby, M. J., 1988. *Mon. Not. R. astr. Soc.*, in press.
Rieke, G. H. & Lebofsky, M. J., 1985. *Astrophys. J.*, **288,** 618.
Rydbeck, O. E., Ellder, J. & Kollberg, E., 1969. *Astrophys. J.*, **156,** L141.
Sellgren, K., 1984. *Astrophys. J.*, **291,** 708.
Sellgren, K., Werner, M. W. & Dinerstein, H. L., 1983. *Astrophys. J.*, **271,** L13.
Strom, S. E., Strom, K. M., Grasdalen, G. L., Capps, R. W. & Thompson, D., 1985. *Astro. J.*, **90.** 2575.
Wynn-Williams, C. G., 1971. *Mon. Not. R. astr. Soc.*, **151,** 397.
Wynn-Williams, C. G., Becklin, E. E. & Neugebauer, G., 1974. *Astrophys. J.*, **187,** 473.
Yamashita, T., Sato, S., Nagata, T., Suzuki, H., Hough, J., McLean, I., Garden, R. & Gatley, I., 1987. *Astr. Astrophys.* **177,** 258.

Mon. Not. R. astr. Soc. (1988) **231**, *Short Communication*, 47P–54P

Submillimetre observations reveal that DR21 (OH) is a double source

W. K. Gear *Royal Observatory, Blackford Hill, Edinburgh EH9 3HJ*

C. J. Chandler and T. J. T. Moore *Astronomy Department, Edinburgh University, Blackford Hill, Edinburgh EH9 3HJ*

C. T. Cunningham *Rutherford Appleton Laboratory, Chilton OX11 0QX*

W. D. Duncan *Joint Astronomy Centre, 665 Komohana Street, Hilo Hawaii 96720, USA*

Accepted 1988 January 13. Received 1988 January 12

Summary. We have scanned the region around the OH maser source DR21 (OH) with a 20-arcsec beam at a wavelength of 350 μm and discovered a hitherto unknown double structure, with two peaks of roughly equal mass separated by 40 arcsec (0.1 pc) in declination. The northernmost peak is coincident with the OH maser position and the centroid of the far-infrared emission, while the southern source has not previously been found at any wavelength. Both sources are extremely dense and deeply embedded, with optical depths of order unity even in the far-infrared. The southern source may be one of the densest molecular cores yet found, and is a candidate protostar. These results confirm that OB star formation can occur deep within molecular clouds, and not just at their edges.

1 Introduction

The DR21/W75 complex in the Cygnus-X region has been extensively studied in molecular lines (e.g. Dickel, Dickel & Wilson 1978; Richardson *et al.* 1986a) and far-infrared continuum (e.g. Harvey *et al.* 1986). Dickel *et al.* conclude that it consists of two colliding clouds, the DR21 cloud with a velocity of $-3\,\mathrm{km\,s^{-1}}$ and the W75 cloud with a velocity of $11\,\mathrm{km\,s^{-1}}$. There are several extensive regions of star formation, namely DR21, DR21 (OH), W75N and a region to the north of DR21 (OH) close to an H_2O maser position. Detailed observations have concentrated on DR21 and the northern maser source, while DR21 (OH) has been relatively neglected.

The DR21 (OH) position has also been referred to in the literature as W75-S and W75 (OH), but Dickel *et al.* conclude that it is part of the $-3\,\mathrm{km\,s^{-1}}$ DR21 cloud rather than the $11\,\mathrm{km\,s^{-1}}$ W75 cloud, so we shall use the name DR21 (OH). We observed this source as part of a programme of observations of dense molecular cores at 350 μm (Cunningham *et al.* 1984; Cunningham, Griffin & Gee, in preparation; Gear *et al.* 1986; Richardson *et al.* 1986b). Submillimetre continuum

observations are an excellent tracer of the column density in such regions (Hildebrand 1983) since the emission is almost always optically thin and, on the long-wavelength side of the thermal spectrum, is not sensitive to temperature variations, unlike far-infrared observations.

It is a remarkable fact that, for the small number of dense molecular cores for which submillimetre continuum maps are available, a previously unknown cool dense protostellar condensation has been found in almost every case (Keene, Hildebrand & Whitcomb 1982; Gezari 1982; Jaffe *et al.* 1983, 1984; Cunningham *et al.* 1984, and in preparation). In this paper we present a high-resolution scan at 350 μm through DR21 (OH) which reveals a double structure which had remained previously undiscovered despite the region having been mapped with similar resolution in the far-infrared (Harvey *et al.* 1986). Despite the uncertain temperature of the two sources, it is clear that they are amongst the densest such cores so far discovered.

2 Observations

Preliminary observations revealing the double structure of DR21 (OH) were made during daylight observing in 1986 April. More detailed observations confirming this result were made during night-time observing in 1986 July. All observations were made using the common-user submillimetre photometer UKT14 on the United Kingdom Infrared Telescope on Mauna Kea, Hawaii. Calibration was performed against Jupiter and Saturn.

The aperture was 21 mm corresponding to a beamsize of 20 arcsec, measured against Mars. These are the first published observations with such a small beam at 350 μm. First, we made a fully sampled scan of the DR21 (OH) region in the north–south direction. At distances of 90 arcsec north and south the emission becomes contaminated by the contributions from the H_2O maser source and DR21 respectively (see Rieke *et al.* 1973; Harvey *et al.* 1986). We then made east–west scans at the positions of the two peaks found in the declination scan. The pointing uncertainty in these scans was approximately 2 arcsec.

3 Results

The results of our north–south scan photometry are given in Table 1 and displayed in Fig. 1. The uncertainties quoted for all fluxes are statistical, and we estimate the absolute uncertainty in the

Table 1. 350 μm declination scan through DR21 (OH).

Dec. offset	Flux (Jy)
+70	48±9
+60	51±11
+50	75±8
+40	101±3
+30	115±6
+20	203±6
+10	434±13
0	500±12
−10	368±6
−20	238±8
−30	288±6
−40	318±6
−50	201±4
−60	102±5
−70	57±6
−80	45±3
−90	29±6
−100	36±4

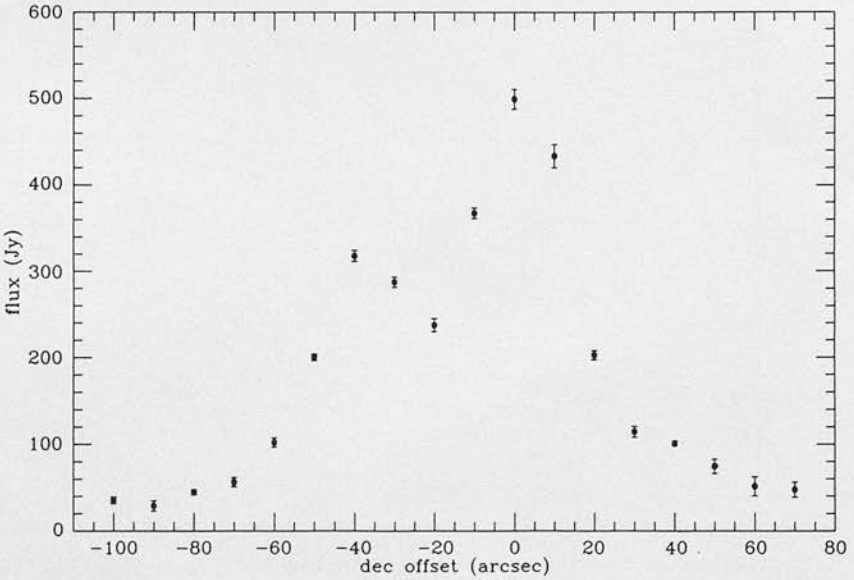

Figure 1. A declination scan through the DR21 (OH) region, revealing a clear double structure.

calibration to be approximately 20 per cent. The positions are given as declination offsets from the map centre which was at RA=$20^h37^m14^s.9$, Dec.=+42° 12′ 10″ (1950). It is clear that the emission is not symmetric and that there is an extension to the south with a secondary peak at around −40 arcsec.

In order to separate the contributions of the two peaks we first used a non-linear least-squares fitting programme (Bevington 1969) to fit the four points at +20, +10, 0 and −10 assuming

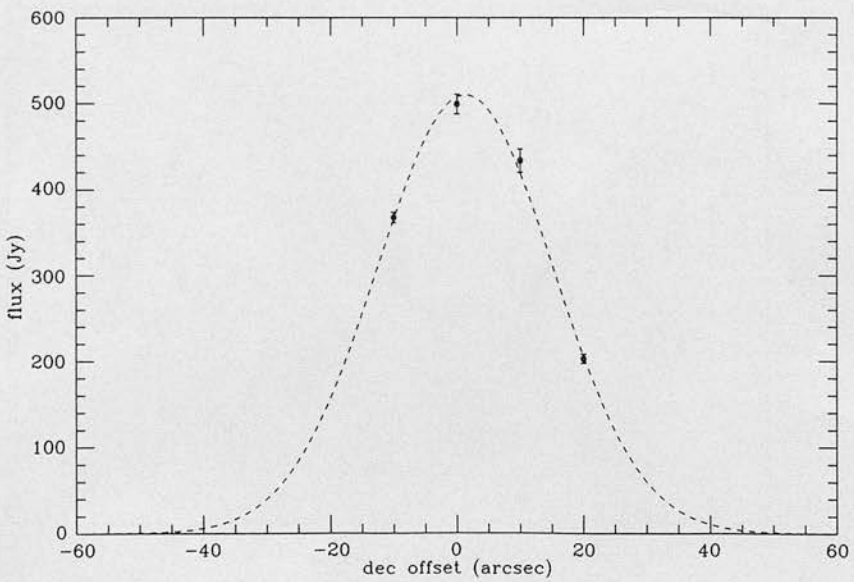

Figure 2. Best fit to the four points defining the DR21 (OH) peak, shown as a broken line. The fit is a Gaussian of FWHM 33 arcsec, which after deconvolving the beamwidth of 20 arcsec, gives a source size of 26 arcsec.

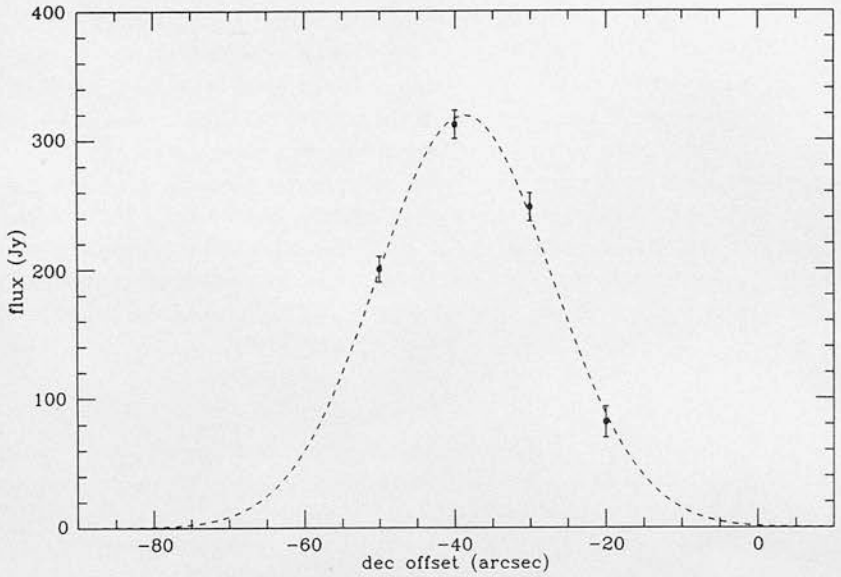

Figure 3. The best fit to the points defining the southern peak which were obtained by subtracting the fit shown in Fig. 2 from the fluxes given in Table 1. The fit is a Gaussian of FWHM 27 arcsec, which after deconvolving the beamwidth of 20 arcsec, gives a source size of 19 arcsec.

Gaussian source and beam distributions, and allowing the peak flux, position and FWHM as free parameters. The resulting best fit is shown in Fig. 2. The fitted FWHM gives a source width, after deconvolving the beamwidth, of 26±1 arcsec and a fitted peak flux of 510±10 Jy. This fit was then subtracted from the fluxes at −50, −40, −30 and −10 and the resultant derived fluxes fitted. This

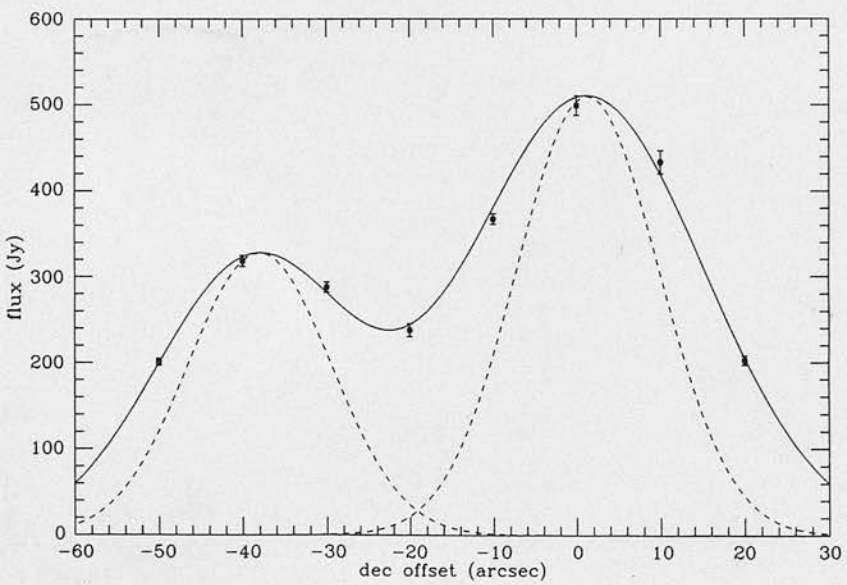

Figure 4. The full declination scan through the DR21 (OH) region, together with the sum of our two best fits shown by a solid line. The broken lines indicate the telescope beam, plotted at the position of the two peaks.

Table 2. RA scan at declination offset 0.

Offset	Flux (Jy)
−50	65±20
−40	103±7
−30	189±25
−20	347±4
−10	458±9
0	397±16
+10	230±13
+20	73±15
+30	45±21
+40	5±24
+50	36±10

fit is shown in Fig. 3. The best fit gave a peak flux of 320±10 Jy and a source width, after deconvolving the beam, of 19±3 arcsec. In Fig. 4 we show the whole scan through the source, with the dark line being the sum of the two fits and the broken lines indicating the beamwidth, plotted at the positions of the two peaks. We have clearly obtained a good fit to the scan.

The results for the east–west scan at a declination offset of 0 are given in Table 2. A fit was made to the points at RA offsets −30, −20, −10, 0, +10, +20. The resultant best fit, shown in Fig. 5, gave a source width, after deconvolving the beam, of 31±1 arcsec. The results for the east–west scan at a declination offset of −40 are given in Table 3. The best fit to the points at −30, −20, −10, 0, +10, +20 and +30 is shown in Fig. 6. The fitted source size, after deconvolving the beam is 41±8 arcsec.

Based on the RA and Dec. scans, the best-fit positions are $20^h37^m14\overset{s}{.}2$, +42° 12′ 11″ for the DR21 (OH) maser source and $20^h37^m14\overset{s}{.}6$, +42° 11′ 31″ for the newly discovered southern source.

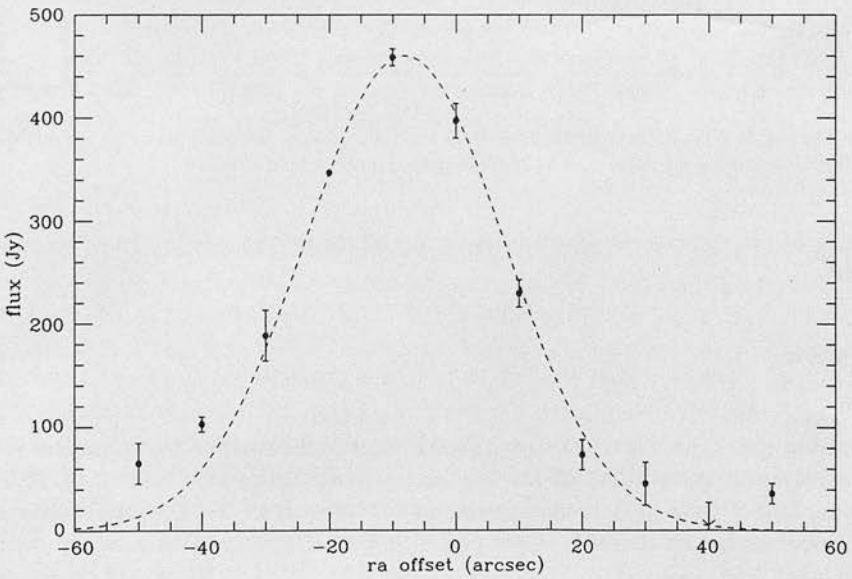

Figure 5. The best fit to the RA scan through the DR21 (OH) position. The fit is a Gaussian of FWHM 37 arcsec, which after deconvolving the beamwidth of 20 arcsec gives a source size of 31 arcsec.

Table 3. RA scan at declination −40.

Offset	Flux (Jy)
−50	62±28
−40	104±12
−30	142±23
−20	235±16
−10	306±31
0	360±14
+10	256±19
+20	171±22
+30	88±10
+40	34±32
+50	34±26

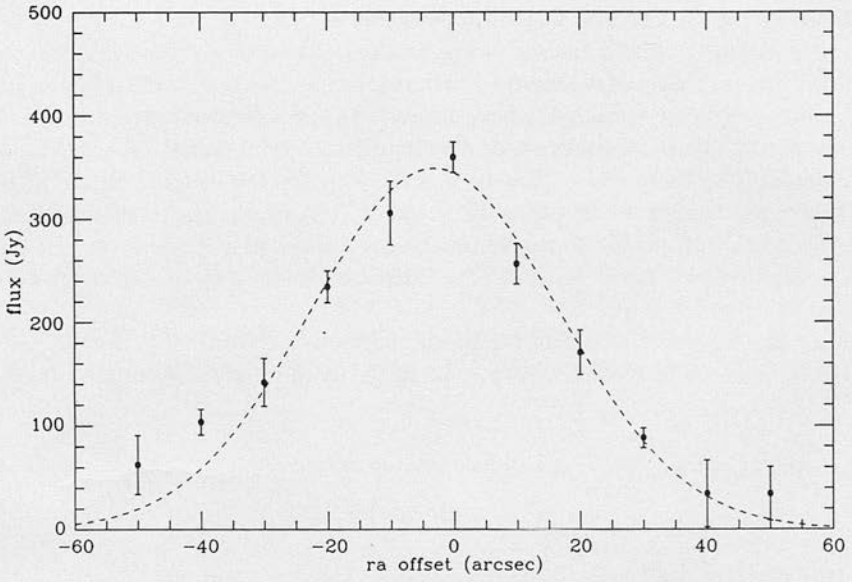

Figure 6. The best fit to the RA scan through the southern source positon. The fit is a Gaussian of FWHM 46 arcsec, which after deconvolving the beamwidth of 20 arcsec gives a source size of 41 arcsec.

The value of the reduced chi-squared statistic for all the fits discussed was 1 or less, indicating good fits.

4 Discussion

4.1 THE OH MASER SOURCE

The best-fitting position for the northern and stronger of the two peaks is coincident within the uncertainties with the position of the OH maser source given by Dickel *et al.* (1978). The centroids of the 50- and 100-μm maps presented by Harvey *et al.* (1986) were also identical with this position, indicating that the source powering the OH maser is the most luminous in the region.

Harvey *et al.* derive a temperature of 36 K for this source, assuming a λ^{-1} dust emissivity law, and using this value and the size derived in Section 3 we find a 350-μm optical depth for the central

position of 0.24. This is much higher than typical values for regions of star formation (e.g. Cunningham 1982; Jaffe *et al.* 1984) and is comparable with the dense condensation we have previously discovered at W51 (main) (Cunningham *et al.* 1984). Using a value of A_V/τ_{350} of 4700 (Gear *et al.* 1986) this corresponds to a visual extinction of 1100 mag! This explains why the strongest near-infrared source in this region is at W75 IRS1 (Garden *et al.* 1986); the extinction at the maser position is simply too great, even in the near-infrared. In fact this source will have an optical depth of unity even at 100 μm. Note that this high extinction could result in an underestimate of the temperature by several degrees.

Using the relations between τ_{350} and hydrogen column density derived by Hildebrand (1983) from the results of Whitcomb *et al.* (1981), but modified for Gaussian geometry (Gee 1987), we find a peak column density $N(H+H_2)=1.2\times10^{24}\,cm^{-2}$ and, assuming a distance of 3 kpc, a local peak density of $n(H+H_2)=8.6\times10^5\,cm^{-3}$. The total derived mass for this source is $5.0\times10^3\,M_\odot$.

4.2 THE SOUTHERN SOURCE

The southern, weaker source does not show up at all on the 50- and 100-μm maps of Harvey *et al.* (1986), and it must therefore be considerably cooler than the maser source, but without more spectral information we are unable to constrain its temperature. We can nevertheless still set useful lower limits on its density and mass. Assuming $T<30$ K we find a lower limit to the optical depth at 350 μm of 0.23 and to the column density $N(H+H_2)$ of $1.1\times10^{24}\,cm^{-2}$, corresponding to $A_V>1100$ mag. The lower limit to the local density is approximately $10^6\,cm^{-3}$, making this souce one of the densest cloud cores yet found. If the temperature of this source is significantly cooler than 30 K it will in fact be optically thick even at 350 μm. Provided the 350-μm emission is not optically thick, the derived mass is only linearly dependent on its temperature; for $T<30$ K we estimate $M>10^4\,M_\odot$.

We also note that, unlike the maser source position, this source is considerably elongated in the east–west direction; this may indicate a disc-like structure, or alternatively observations at even higher resolution may reveal a further subdivision into more than one source.

It is clear that further observations of this extremely interesting source are required in both submillimetre continuum, with even higher spatial resolution, and in molecular line tracers which may be able to probe the extremely dense conditions which appear to be found there. Such observations may also shed light on the evolutionary status of this source, which is certainly cool enough and dense enough to be a candidate accreting protostar.

5 Conclusions

The remarkable success of submillimetre continuum observations in discovering previously unknown cool dense condensations has been noted previously by Jaffe *et al.* (1984). DR21 (OH) joins the list of NGC 6334I (Gezari 1982), W3, OMC1 and S255 (Jaffe *et al.* 1984), W51 (Cunningham *et al.* 1984) and Sgr B2 (Cunningham *et al.*, in preparation) which have been mapped in the submillimetre continuum and all of which have been found to contain closely-spaced condensations. As Jaffe *et al.* have pointed out, the submillimetre optical depths of these regions also imply that they are deeply embedded within their parent clouds, rather than forming at the edges. Our results for DR21 (OH) in this paper confirm this conclusion, and the two sources are among the most deeply embedded condensations yet found.

The DR21 region appears to be particularly active in forming stars, with the condensations discovered in this paper and also the cool young source further to the north first discovered at 1 mm by Werner *et al.* (1975) and coincident with an H_2O maser. Further investigations of these regions are required, in particular high spatial resolution submillimetre observations at more than

one wavelength are essential for determining the temperature and luminosity of the two sources. In order to investigate fully the structure and evolutionary status in the DR21 (OH)–south source, measurements in both continuum and molecular lines will be required at even higher spatial resolution.

Acknowledgments

The UKIRT is operated by the Royal Observatory, Edinburgh on behalf of the SERC. TJTM and CJC acknowledge the support of SERC studentships. We thank Pat Roche and Matt Mountain for useful discussions and Ian Robson for encouragement.

References

Bevington, P. R., 1969. *Data Reduction and Error Analysis for the Physical Sciences,* McGraw-Hill, New York.
Cunningham, C. T., 1982. *PhD thesis,* University of London.
Cunningham, C. T., Griffin, M. J., Gee, G., Ade, P. A. R. & Nolt, I. G., 1984. *Mon. Not. R. astr. Soc.,* **210,** 891.
Dickel, J. R., Dickel, H. R. & Wilson, W. J., 1978. *Astrophys. J.,* **223,** 840.
Garden, R., Geballe, T. R., Gatley, I. & Nadeau, D., 1986. *Mon. Not. R. astr. Soc.,* **220,** 203.
Gear, W. K., Gee, G., Robson, E. I., Ade, P. A. R. & Duncan, W. D., 1986. *Mon. Not. R. astr. Soc.,* **219,** 835.
Gee, G., 1987. *PhD thesis,* University of London.
Gezari, D. Y., 1982. *Astrophys. J.,* **259,** L29.
Harvey, P. M., Joy, M., Lester, D. F. & Wilking, B. A., 1986. *Astrophys. J.,* **300,** 737.
Hildebrand, R. H., 1983. *Q. Jl. R. astr. Soc.,* **24,** 267.
Jaffe, D. T., Hildebrand, R. H., Keene, J. & Whitcomb, S. E., 1983. *Astrophys. J.,* **273,** L89.
Jaffe, D. T., Davidson, J. A., Dragovan, M. & Hildebrand, R. H., 1984. *Astrophys. J.,* **284,** 637.
Keene, J., Hildebrand, R. H. & Whitcomb, S. E., 1982. *Astrophys. J.,* **252,** L11.
Richardson, K. J., White, G. J., Phillips, J. P. & Avery, L. W., 1986a. *Mon. Not. R. astr. Soc.,* **219,** 167.
Richardson, K. J., White, G. J., Gee, G., Griffin, M. J., Cunningham, C. T., Ade, P. A. R. & Avery, L. W., 1986b. *Mon. Not. R. astr. Soc.,* **216,** 713.
Rieke, G. H., Harper, D. A., Low, F. J. & Armstrong, K. R., 1973. *Astrophys. J.,* **183,** L67.
Werner, M. W., Elias, J. H., Gezari, D. Y., Hauser, M. G. & Westbrook, W. E., 1975. *Astrophys. J.,* **199,** L185.
Whitcomb, S. E., Gatley, I., Hildebrand, R. H., Keen, J., Sellgren, K. & Werner, M. W., 1981. *Astrophys. J.,* **246,** 416.

Mon. Not. R. astr. Soc. (1989) **237**, *Short Communication*, 1P–6P

CS($J=7-6$) from heated gas near the embedded sources in NGC 2024

T. J. T. Moore and C. J. Chandler *Department of Astronomy, University of Edinburgh, Blackford Hill, Edinburgh EH9 3HJ*

W. K. Gear and C. M. Mountain *Royal Observatory, Blackford Hill, Edinburgh EH9 3HJ*

Accepted 1988 November 21. Received 1988 November 3

Summary. CS ($J=7-6$) observations of NGC 2024, at 15-arcsec resolution, show strong emission closely associated with the recently identified submillimetre continuum sources. Significant excitation of this line indicates the presence of localized regions of dense, heated molecular gas and implies that the continuum peaks contain heavily-obscured luminous stellar cores. A lower limit of 28 K is obtained for the line excitation temperature from the observed line strengths. A re-analysis of existing continuum data predicts an effective dust temperature of $T_d=47$ K over the whole region. Lower limits of $\sim 3\times10^{26}$ m^{-2} are derived for the column density of heated molecular hydrogen toward each continuum source, assuming $T_{ex}=T_d$ and optically thin lines. There is some evidence for significant optical thickness in $J=7-6$ toward at least two of the sources.

1 Introduction

In a recent paper, Mezger *et al.* (1988) (hereafter M88) presented high-resolution maps of the 1300-μm dust emission from the cloud core region of NGC 2024 and reported six new sources, previously undetected by far-infrared and low-resolution molecular line studies. By using a three-component model of the 12-μm to 1300-μm continuum, these new objects were interpreted as high-density ($n_H\sim10^{14}$–10^{15} m^{-3}), cold ($T_d\sim16$ K), isothermal condensations without luminous stellar cores, i.e. true protostars.

The time-scale for the isothermal phase of protostar development (e.g. Nakano 1985) is likely to be significantly shorter than the sound-crossing time of the cloud ($\sim10^6$ yr). The presence of six sources in roughly the same evolutionary state thus implies simultaneous formation, presumably by contraction and fragmentation of the entire cloud. To find out more about the evolutionary state of the new sources and the physical conditions in their vicinity, we have observed the region at 15-arcsec resolution in the $J=7-6$ transition of CS (detected in a large beam by Evans *et al.* 1987), mapping the distribution of warm gas and determining its relationship to the submillimetre cores.

2 Observations and results

The observations were made with the 15-m James Clerk Maxwell Telescope (JCMT) on Mauna Kea, Hawaii, during the nights of 1988 September 8–11, with the common-user, 345 GHz Schottky receiver and a 1024-channel AOS backend. Fully sampling with an 8-arcsec regular grid, we have mapped an area containing all six FIR sources identified by M88 and covering most of the dark cloud core region. The beam size at 343 GHz was 15 arcsec. The results are shown as maps of integrated antenna temperature (T_A^*) in Fig. 1(a)and peak T_A^* in Fig. 1(b). It should be noted that the portion of the map covering the northernmost continuum source, FIR 1, is not well sampled. Only two data points were obtained to the north of this object.

The values of peak T_A^* toward each of the M88 sources covered by Fig. 1 are listed in Table 1. For conversion to the T_R^* scale, the forward scattering efficiency is $\eta_{fss} = 0.8$. Total on-source integration time per point was 60–90 s, yielding mean rms noise levels of 1.2 K per 488-kHz channel. The 1σ noise in Fig. 1(a) is 0.3 K kms^{-1}. Calibration was done via an internal rotating hot load. Absolute pointing was checked at intervals of about 45 min against the molecular line peak in OMC-1 (Masson *et al.* 1987) and the rms error was less than 3 arcsec throughout.

3 Discussion

3.1 THE WARM MOLECULAR GAS

Fig. 1 shows clearly that the warm molecular gas traced by CS($J=7-6$) ($J=7$ is at $E/k=66$ K above the ground state) is localized at or very near the positions of the submillimetre condensations reported by M88. This implies that there are discrete regions of heated gas associated with each of FIR 2–6, and hence that there are probably self-luminous heating sources within each core. A relatively advanced state of evolution in FIR 6 is also inferred by its close proximity to the origin of an extensive bipolar molecular outflow (Sanders & Willner

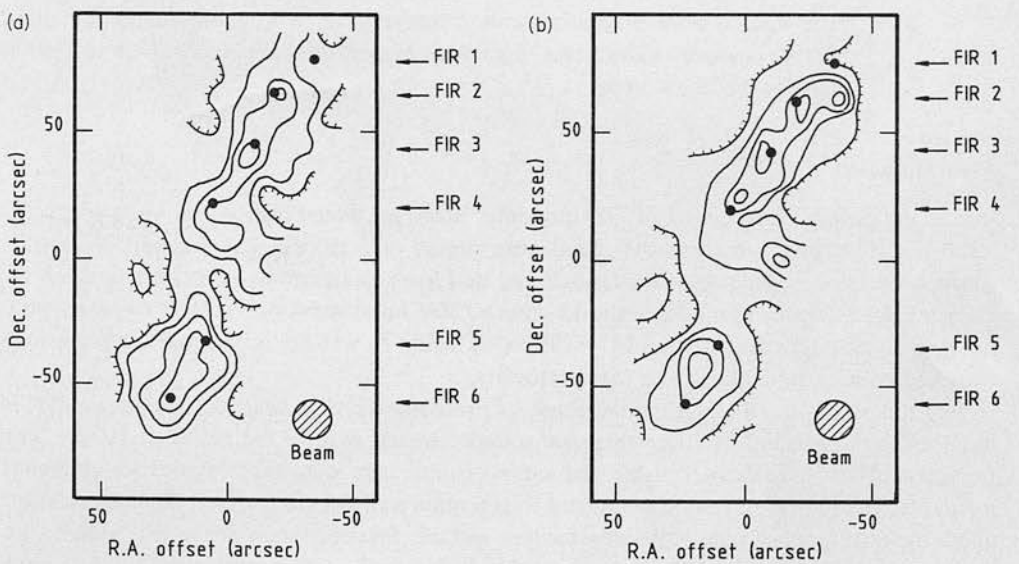

Figure 1. (a) Integrated CS($J=7-6$) emission ($\int T_A^*(V)\,dV$) in NGC 2024. Contours are drawn at 5, 10, 15 and 20 K km s^{-1}. The 1σ noise level is around 0.3 K km s^{-1}. The offset centre is $5^h39^m12\overset{s}{.}2 - 1°56'30''$ (1950). (b) Contours of peak T_A^* at intervals of 1.5 K from 3 K. The mean 1σ noise level is ~0.8 K.

Table 1. Observed and derived parameters toward FIR sources.

source	peak T_A^* /K	$\int T_A^*(\mathrm{V})\mathrm{dV}$ /Kkms^{-1}	T_{ex}^c /K	N_{7-6}^{CS} /$10^{17}m^{-2}$	V_0 /kms^{-1}	m^d (1300 μm) /$M_\odot$
FIR 1	2.9	6.0	13.9	0.9	8.2	1.9
FIR 2	7.9[a]	20.2[a]	27.2	3.1	8.0	2.0
FIR 3	8.4[a]	21.8[a]	28.5	3.3	10.0	6.5
FIR 4	8.1[a]	16.8[b]	27.7	2.5	8.3	4.9
FIR 5	5.8	20.0[a]	21.7	3.0	9.3	10.5
FIR 6	6.1	22.3	22.5	3.4	11.2	4.3

[a]Value from nearest peak (Fig. 1) if within one beam radius. [b]Values from peak T_A^* position. [c]Lower limit for high optical depth and filling factor (see text). [d]Hydrogen masses from M88, adjusted for $T_d = 47$ K, $\beta = 1.60$.

1985) and an H_2O maser (Genzel & Downes 1977), the latter being frequently associated with energetic outflow sources. The only continuum source without a nearby peak in T_A^* or $\int T_A^*(V)\,dV$ is the faintest (at 1300 μm) and most northern object, FIR 1. This may indicate a lack of warm gas at this position, but the map is not well-sampled in this area and further observations may be required of this object.

A lower limit to the effective line excitation temperature (T_{ex}) can be estimated from the LTE formula for radiation temperature:

$$T_R = \frac{h\nu}{k}[(e^{h\nu/kT_{ex}}-1)^{-1}-(e^{h\nu/2.7k}-1)^{-1}]\times(1-e^{-\tau}),$$

which means that for CS($J = 7-6$):

$$T_{ex} \simeq \frac{16.5}{\ln[1+16.5(1-e^{-\tau})/T_R]}.$$

T_R can be derived from $T_R = T_R^*/\eta_c$, where η_c is the source coupling efficiency and contains the beam filling factor f. Since the true value of f is very uncertain, assuming a value for η_c of 0.5 provides a reliable lower limit of $T_{ex} \geq 28$ K towards the line peak near FIR 3, the equality holding where the transition optical depth is large and f is close to unity. $T_{ex} \geq 28$ K is thus consistent with the average 60/100 μm colour temperature of 45 K calculated by Thronson *et al.* (1984), but not with the dust temperature of 16 K inferred by M88 for the submillimetre cores.

Evans *et al.* (1987), observing in a 73-arcsec beam, find $T_R(7-6)/T_R(6-5) \simeq 0.7 \pm 0.2$. If the optical depth in the lines is low this implies a value for T_{ex} of 25^{+15}_{-10} K. The optically thin, high-temperature limit to the line ratio is 1.36, so a low value (< 1) can be explained by: (i) cool optically thin gas; (ii) a steep, inward-increasing temperature gradient in hot ($T_{ex} \gg 50$ K), optically thick gas; (iii) a steep, outwardly increasing temperature gradient in cool ($T_{ex} < 50$ K), optically thick gas or (iv) dilution in the large beam. The latter possibility is the most likely, especially if the $J = 6-5$ emission is more extended than the $J = 7-6$. The value of T_{ex} derived from the line ratio therefore serves as a lower limit to the effective value for the compact FIR sources. Since the critical density of the $J = 7-6$ transition is $n_{crit} \simeq 2 \times 10^{13}\,\mathrm{m}^{-3}$, it is likely that the gas and dust are thermally well coupled where this line is detectable. We therefore find

it reasonable to assume that $T_d \simeq T_{ex}$ and adopt $T_{ex} = 47$ K from the dust temperature obtained below. This value implies optical depths of $\tau_{7-6} \simeq 0.7$ from the measured line strengths, if no self absorption is present.

The LTE formula for the CS column density producing the $J = 7 - 6$ line is:

$$N^{CS}_{7-6}(m^{-2}) = 1.79 \times 10^{15} \times (1 - e^{-16.5/T_{ex}})^{-1} \times \frac{1}{\eta_c \eta_{fss}} \int T^*_A(V)\, dV.$$

This produces values in the range $(2.5\text{–}3.4) \times 10^{17}\,m^{-2}$ for FIR 2–6 and total molecular hydrogen column density estimates of $(2.5\text{–}3.4) \times 10^{26}\,m^{-2}$ (see Table 1), assuming a relative CS abundance of 10^{-9} (Snell *et al.* 1984) and a filling factor of unity. In order to produce space densities of order n_{crit} for significant excitation of optically thin $J = 7 - 6$, the linear extent of the emitting regions must be as small as $\sim 10^{13}$ m. However, if the line is significantly optically thick, the density need not be as high as n_{crit} since radiative trapping maintains the level population above the collisional excitation rate. Evans *et al.* (1987) obtained beam-averaged densities of around $10^{12}\,m^{-3}$ by modelling the radiative transfer in the LVG approximation. If these densities are appropriate to the compact sources, τ_{7-6} may be as high as 10. If this is the case, then $T_{ex} = 28$ K must apply to the cooler outer layers of the emitting gas in the cores.

While the line emission from the northern part of the cloud (associated with FIR 1–4) is essentially unresolved (Fig. 1), the southern emission around FIR 5 and 6 seems to be slightly larger than the beam. A relatively large source size and low derived H_2 column density therefore implies either a low CS abundance or high optical depth in the line. There is some evidence for high τ_{7-6} toward FIR 5 and 6 in the comparison of integrated T^*_A (Fig. 1a), which peaks on or close to the continuum in each case, and peak T^*_A, which does not. This may be caused by self-absorption in the line emission toward the source positions; self-reversal in the foreground material is likely to affect an optically thick emission line. High line optical depths mean that N_{H_2} is under-estimated by a factor $\tau/(1 - e^{-\tau})$ and self-reversal produces under-estimates of T_{ex} when derived from the peak line temperature.

3.2 THE (SUB)MILLIMETRE CONTINUUM

M88 fitted a three-component greybody to the available continuum data for NGC 2024, setting the dust emissivity exponent at $\beta = 2.0$. In the resulting model the integrated emission at 350 μm and beyond is dominated by a large 16 K component. All the warm dust is assumed to be in a diffuse envelope surrounding cold cloud cores, contributing little to the mass and column density. Adopting a value for T_d as low as 16 K for the discrete sources implies large submillimetre optical depths, H_2 column densities and masses; however, the model adopted by M88 for the flux density distribution is not unique. If the constraint that the dust emissivity be proportional to $\nu^{2.0}$ is lifted, it is possible to obtain a very good fit (reduced $\chi^2 = 0.4$) to the same data using a simple, single-temperature model, parameterized by $T_d = 47$ K, $\beta = 1.60$ and a 350-μm optical depth of 0.06 (Fig. 2).

Since NGC 2024 contains visible hot stars, a large blister H II region and an extended CO outflow, it is evident that the disruptive formation of, and heating by massive stars has been occurring for a considerable period of time. It is likely, therefore, that warm gas and dust will have pervaded the entire region. In addition, cloud cores in regions of massive star formation are observed to be considerably warmer ($T \sim 40$ K) than those forming exclusively low-mass stars (see Shu, Adams & Lizano 1987 for a review). Since no spectral data are available for the individual FIR objects, we can only model source-averaged parameters from the integrated emission across the whole cloud. A single-temperature model, while not being any more of a unique physical description, is less subject to detailed ambiguities than a multi-component fit.

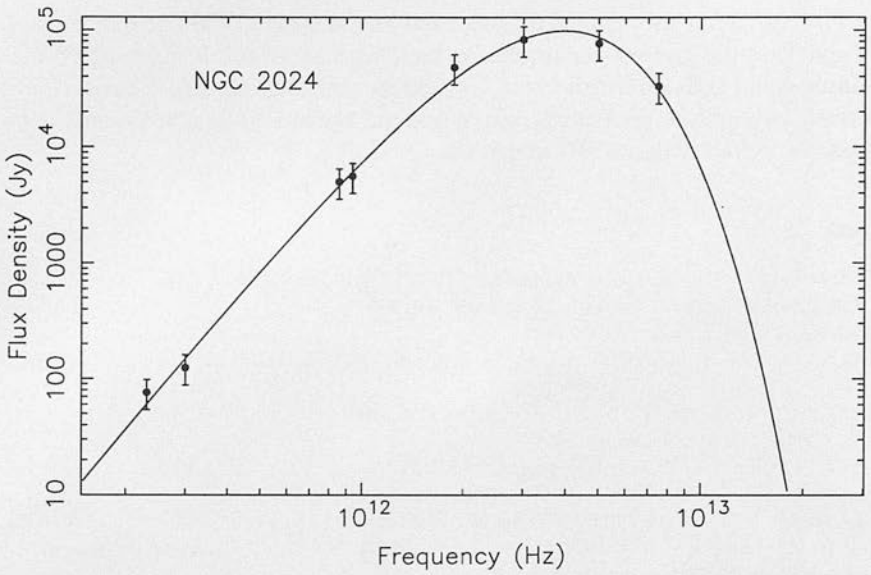

Figure 2. Single-temperature greybody fit to the integrated flux density distribution of NGC 2024. The fit parameters are $T_d = 47$ K, $\beta = 1.60$, $\tau_{350\,\mu m} = 0.06$. The data points are from Mezger *et al.* (1988) (M88). Related χ^2 for the fit is 0.4.

Using the dust-to-gas conversion from Hildebrand (1983), a 47 K single-temperature model with $\beta = 1.6$ reduces the optical depths and hydrogen column densities, derived by M88 from their 1300 μm and 350 μm data, by factors of 5.9 and 8.2, respectively (see Table 1). M88, assuming $T_d = 16$ K, find hydrogen column densities in the extended emission up to six times larger than derived from previous molecular observations (especially Snell *et al.* 1984). This discrepancy, interpreted as a decrease in molecular abundances and an increase in dust cross-section in cold, dense regions, is virtually eliminated by adopting a dust temperature near 50 K.

Further observations (e.g. in other high-excitation lines of CS and high-resolution submillimetre continuum mapping) would help to fill in the unknowns encountered above, especially the uncertain line optical depths, effective excitation temperatures and the variation in temperature and density conditions between the embedded FIR sources.

4 Conclusions

We have mapped the cloud core region of NGC 2024 in the $J = 7 - 6$ line of CS. Strong emission, closely associated with five out of the six known millimetre continuum sources, indicates localized regions of heated dense gas. Consequently, the compact continuum cores are likely to contain self-luminous heating sources and be in a rather more advanced evolutionary state than previously thought. A lower limit of 28 K is obtained for the CS($J = 7 - 6$) excitation temperature from the observed line strengths. A re-analysis of existing continuum data predicts an effective dust temperature of $T_d = 47$ K over the whole region. Lower limits of $\sim 3 \times 10^{26}$ m^{-2} are derived for the molecular hydrogen column density toward five continuum sources, assuming $T_{ex} = T_d$ and optically thin lines. There is some evidence for significant optical depth in $J = 7 - 6$ toward at least two of the sources.

Acknowledgments

Thanks are due to Saeko Hayashi and Takuya Yamashita for discussing the observations with us, and to Charles Cordell for excellent help during the observing run. Rachael Padman and

Richard Prestage are acknowledged for provision and support of the line reduction package SPECX and Marjorie Fretwell for producing the diagrams. JCMT is operated by the Royal Observatory, Edinburgh, on behalf of the UK Science and Engineering Research Council, the Netherlands Organisation for Pure Research and the National Research Council of Canada. TJTM and CJC acknowledge SERC studentships.

References

Evans, N. J., Mundy, L. G., Dais, J. H. & Vanden Bout, P., 1987. *Astrophys. J.*, **312,** 344.
Genzel, R. & Downes, D., 1977. *Astr. Astrophys. Suppl.*, **30,** 145.
Hildebrand, R., 1983. *Q. Jl R. astr. Soc.*, **24,** 267.
Masson, C. R., Lo, K. Y., Phillips, T. G., Sargent, A. I., Scoville, N. Z. & Woody, D. P., 1987. *Astrophys. J.*, **319,** 446.
Mezger, P. G., Chini, R., Kreysa, E., Wink, J. E. & Salter, C. J., 1988. *Astr. Astrophys.*, **191,** 44.
Nakano, T., 1985. *Publs astr. Soc. Japan,* **37,** 69.
Sanders, D. B. & Willner, S. P., 1985. *Astrophys. J.*, **293,** L39.
Shu, F. H., Adams, F. C. & Lizano, S., 1987. *Ann. Rev. Astr. Astrophys.*, **25,** 23.
Snell, R. L., Mundy, L. G., Goldsmith, P. F., Evans, N. J. & Erickson, N. R., 1984. *Astrophys. J.*, **276,** 625.
Thronson, H. A., Lada, C. J., Schwartz, P. R., Smith, H. A., Smith, J., Glaccum, W., Harper, D. A. & Loewenstein, P. F., 1984. *Astrophys. J.*, **280,** 154.